Summer 2014

Novel Energy Efficient Electrohydraulic Steer-By-Wire Technology

Naseem Daher
Purdue University

Graduate School ETD Form 9
(Revised 01/14)

PURDUE UNIVERSITY
GRADUATE SCHOOL
Thesis/Dissertation Acceptance

This is to certify that the thesis/dissertation prepared

By NASEEM A DAHER

Entitled
NOVEL ENERGY EFFICIENT ELECTROHYDRAULIC STEER-BY-WIRE TECHNOLOGY

For the degree of Doctor of Philosophy

Is approved by the final examining committee:

MONIKA IVANTYSYNOVA

JOHN H. LUMKES

GREGORY M. SHAVER

ANDREA VACCA

To the best of my knowledge and as understood by the student in the Thesis/Dissertation Agreement, Publication Delay, and Certification/Disclaimer (Graduate School Form 32), this thesis/dissertation adheres to the provisions of Purdue University's "Policy on Integrity in Research" and the use of copyrighted material.

MONIKA IVANTYSYNOVA

Approved by Major Professor(s): _____

_____

Approved by: GANESH SUBBARAYAN 08/27/2014

Head of the Department Graduate Program Date

NOVEL ENERGY EFFICIENT ELECTROHYDRAULIC STEER-BY-WIRE TECHNOLOGY

A Dissertation

Submitted to the Faculty

of

Purdue University

by

Naseem Daher

In Partial Fulfillment of the

Requirements for the Degree

of

Doctor of Philosophy

December 2014

Purdue University

West Lafayette, Indiana

I dedicate this work to my family members. I am grateful to my dear wife, Behan, and my two wonderful daughters, Batool and Amaal, for their love, support, and company that made this journey possible and tolerable. I am also thankful to my loving parents, Ahmad and Amal, who continually support me in each step that I take in my life. I thank my brother, Raafat, and my sister, Hayfaa, for their persistent encouragement and inspiration throughout this entire process.

I also dedicate this dissertation to my relatives and friends, who supported my decision to go back to graduate school and pursue a doctorate degree, and who kept cheering me on to get to the finish line!

Finally, I praise the God Almighty for looking over my family, guiding us towards the right path, and empowering us to fulfill our aspirations.

ACKNOWLEDGEMENTS

I thank my major professor, Monika Ivantysynova, for her clever guidance, incessant support, prudent mentorship, and kind understanding. Professor Ivantysynova has been influential in my studies, research, and career prospect, and for that I will forever be indebted to her.

I also acknowledge my PhD advisory committee members: Prof. John Lumkes, Prof. Greg Shaver, Prof. Andrea Vacca, and Prof. Bin Yao. I really appreciate their input and feedback, which helped improve my research and this dissertation.

I also thank the entire Maha team, which made going to (and staying at) the lab a fun and educational experience. I thank Enrique Busquets for his help in the instrumentation and experimental setup on the prototype machine, and for the productive discussions on control theory, application, and implementation. Last but certainly not least, a special thanks to Anthony Franklin for his instrumental role in helping me implement my research concept on a test vehicle and turn it into a reality.

TABLE OF CONTENTS

Page

Page

Page

Page

LIST OF TABLES

Table Page

LIST OF FIGURES

Figure Page

Figure Page

Figure Page

Figure Page

Figure Page

LIST OF SYMBOLS

a	Distance between Front C.G. and Front Axle
a_0	Adaptive Control Parameter
a_1	Adaptive Control Parameter
a_y	Lateral Acceleration
b	Distance between Front C.G. and Articulation Joint
b_0	Adaptive Control Parameter
b_1	Adaptive Control Parameter
c	Distance between Rear C.G. and Articulation Joint
d	Distance between Rear C.G. and Rear Axle
d_v	Viscous Damping Coefficient
k	Spring Stiffness Rate
k_{FF}	Feedforward Gain
k_{FB}	Feedback Gain
k_p	Proportional Feedback Gain
l	Length
m	Mass
g	Gravity Constant
n	Speed (engine / pump)
p	Pressure
p_i	Pole
r	Radius
r_j	Normal distance between the articulation joint and the steering actuator force line of action
s	Laplace Operator

u	Local Longitudinal Velocity
u_{sys}	System Input Vector
v	Local Lateral Velocity
wb	Wheelbase
x	Actuator Position
x_f	Front Frame Local Abscissa
y_f	Front Frame Local Ordinate
y_{sys}	System Output Vector
A	Area
A_{AC}	Adaptive Control Transfer Function Denominator Polynomial
A_m	Adaptive Control Model Transfer Function Denominator Polynomial
A_{sys}	State-space Matrix
B^+	Adaptive Control Polynomial
B^-	Adaptive Control Polynomial
B_{AC}	Adaptive Control Transfer Function Numerator Polynomial
B_m	Adaptive Control Model Transfer Function Numerator Polynomial
B_{sys}	State-space Matrix
C_{aj}	Articulation Joint Torsional Damping
C_{eq}	Equivalent Torsional Damping Coefficient
C_H	Hydraulic Capacitance
C_{LP}	Low Pressure System Linear Flow Gain
C_{sys}	State-space Matrix
C_α	Tire Lateral Force Coefficient
$C_{M\alpha}$	Tire Aligning Moment Coefficient
D	Dissipative Function
D_{sys}	State-space Matrix
F	Force
F_{sys}	State-space Matrix
G	Shear Modulus
G_{sys}	Process Noise Matrix

H	Steering Actuator Total Stroke
I	Moment of Inertia
J	Polar Moment of Inertia
J_O	Observer Gain Matrix
J_{PP}	Pole Placement Observer Matrix
K	Fluid Bulk Modulus
K_e	Optimal Observer Gain
K_{aj}	Articulation Joint Equivalent Torsional Stiffness
K_{Li}	Coefficient of Internal Leakage of Actuator
K_Q	Volumetric Loss Coefficient
K_{US}	Understeer Gradient
K_T	Torque Loss Coefficient
L	Lagrangian Function
M_Z	Tire Aligning Moment
N	Normal Force
P_e	Algebraic Riccati Equation Solution
Q	Flow Rate
Q_i	Generalized Force and Moment
R	Radius
R'	Adaptive Control Polynomial
R_{AC}	Adaptive Control Polynomial
S_{AC}	Adaptive Control Polynomial
T	Kinetic Energy
T_{AC}	Adaptive Control Polynomial
TSO	Transformation Matrix
U	Potential Energy
V	Volume
V_{LQE}	LQE Measurement Noise Matrix
V_{sys}	Measurement Noise Matrix
W	Work

W_C	Controllability Matrix
W_{LQE}	LQE Process Disturbances Matrix
W_O	Observability Matrix
W_{OC}	Output Controllability Matrix
W_{sys}	Process Noise Matrix
X	Global Abscissa
X_{sys}	System State Vector
Y	Global Ordinate
α	Actuator Area Ratio
α_D	Orifice Discharge Coefficient
α_s	Tire Slip Angle
β	Pump Swash Plate Angle (Normalized)
γ	Conversion Factor Between Steering Actuator Linear Motion and Vehicle Articulation Motion
γ_{AC}	Estimation Tuning Factor
ζ	Damping Ratio
δ	Differential
Δ	Difference
ε	Twist Angle
η	Volumetric Efficiency
θ	Rear Frame Yaw Angle
θ_{AC}	Parameter Vector
θ_{SW}	Steering Wheel Angle
λ	Fading Integrator Tuning Parameter
μ	Fluid Dynamic Viscosity / Friction Coefficient
μ_f	Friction Coefficient
v	Fluid Kinematic Viscosity
ξ	Estimation Tuning Factor
ρ	Density
τ	Time Constant

τ_{str}	Steering Torque
τ_{SW}	Torsional Stress
τ	Torque
φ	Regression Vector
ϕ	Articulation Angle
ψ	Front Frame Yaw Angle
ω	Natural Frequency

LIST OF ABBREVIATIONS

AFS	Articulated Frame Steering
AHS	Automated Highway System
AHV	Articulated Heavy Vehicle
DC	Displacement Control
DOF	Degree(s) of Freedom
ECU	Electronic Control Unit
GPS	Global Positioning System
HP	High Pressure
kph	kilometers per hour
LP	Low Pressure
LQE	Linear Quadratic Estimator
LQR	Linear Quadratic Regulator
LTI	Linear Time Invariant
MDPP	Minimum Degree Pole Placement
mph	miles per hour
MR	Magneto-Rheological
OEM	Original Equipment Manufacturer
OS	Overshoot
PE	Persistent Excitation
POCV	Pilot-Operated Check Valve
PP	Pole Placement
RLS	Recursive Least Squares
SbW	Steer-by-Wire

SISO	Single-Input Single-Output
SLC	Single Lane Change
SS	Steady State
STR	Self-tuning Regulator
TFD	Tactile Feedback Device

ABSTRACT

Daher, Naseem A., Ph.D., Purdue University, December 2014. Novel Energy Efficient Electrohydraulic Steer-by-Wire Technology. Major Professor: Monika Ivantysynova, School of Mechanical Engineering and Department of Agricultural and Biological Engineering.

Improving energy efficiency, productivity, safety, and comfort of mobile machines is of utmost priority to original equipment manufacturers, suppliers, and consumers given the escalating fuel prices and increased awareness to the environment and workplace hazards. A major breakthrough in the realm of high power motion control is pump displacement controlled (DC) actuation, which does away with hydraulic valves for motion control and uses a variable displacement pump as both a flow source and final control element, thus eliminating throttling losses associated with hydraulic control valves. This work deals with researching and implementing DC technology for realizing the steering function of articulated frame steering mobile machines; however, the technology can be easily adapted to accommodate other applications and industries (aerospace, automotive, commercial, etc.) as well.

To realize the new steering technology, high fidelity dynamic models of the entire system including the electro-hydraulics and vehicle dynamics are first derived. Two controllers, linear and nonlinear (adaptive), are designed and validated in

simulation and experimentally. System sizing and hardware implementation are then completed on a representative prototype test vehicle. Experimental testing results of a steering-only cycle performed on a compact wheel loader reveal a substantial improvement over the baseline machine in regards to fuel consumption reduction (-14.5%), productivity increase (+22.6%), and overall fuel efficiency improvement (43.5%).

A yaw stability control algorithm is developed to investigate the technology's capacity to increase the machine's safety via active steering control. The stability controller monitors the driver's desired trajectory, quickly intervenes when a deviation is detected, and smoothly relinquishes control back to the driver when the disturbance is attenuated. Advanced modern estimation techniques are employed to develop a virtual (soft) sensor for estimating the vehicle's yaw angle rate by combining available sensory data with the derived high-fidelity mathematical model. The output of the virtual yaw rate sensor is compared against that of an installed yaw rate sensor, and excellent correlation is obtained under various operating conditions.

CHAPTER 1. INTRODUCTION

1.1 Background

Power steering systems were first developed to assist operators in overcoming steering wheel resistance for pursuing a desired direction of travel, and have since been ubiquitous in almost all moving vehicles. Today's industrial applications that incorporate power steering span a large spectrum starting from small on-highway vehicles to large off-highway machines and everything in between. While primitive power steering systems were designed with the prior context in mind, today's requirements differ substantially especially in the areas of efficiency, response, controllability, operator feel and comfort, and several other demanding indices.

Power steering systems are mainly classified into hydraulic, electric, or electro-hydraulic architectures depending on the energy source, energy transmission, and energy management schemes that are employed. In hydraulic power steering systems, the energy source is typically a prime mover that drives a hydraulic pump responsible for generating the required power assist. Steering gain level and directional bias are controlled via a manually-actuated proportional control valve based on operator input to the steering wheel. Electric power steering systems utilize electric motors to drive the steering gear set and actuator;

speed and direction are controlled via frequency controllers based on measured operator input (steering wheel torque, angle, and speed). Electro-hydraulic power steering systems take advantage of the high power density and efficiency of fluid power systems, but use electronically controlled valves to control the power assist level. While this latter approach yields superior controllability, it still results in considerable inefficiencies due to metering losses that are incurred as the control valve throttles fluid flow across its ports.

This work introduces a novel scheme of an electro-hydraulic power steering system, steer-by-wire (SbW) in particular, that utilizes a proven energy-efficient actuation technology, known as Displacement Control (DC), which eliminates throttling losses associated with hydraulic control valves by controlling a variable displacement pump instead. The circuit shown in Figure 1 was first introduced in (Rahmfeld & Ivantysynova, 1998).

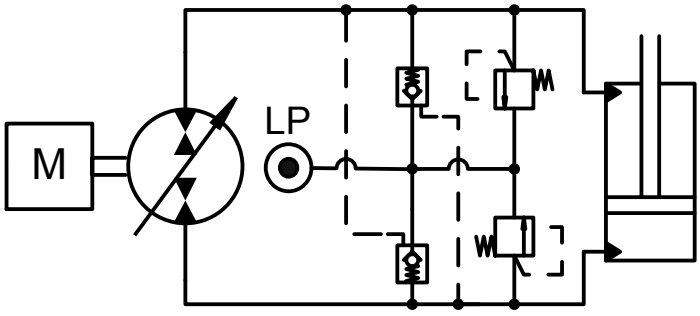

Figure 1: Pump Displacement Controlled (DC) Actuation.

In this arrangement, a constant- or variable-speed prime mover may be used to drive a variable displacement pump. The cylinder velocity is controlled by adjusting the pump speed, pump displacement, or both. The pilot operated check valves (POCV) keep the low pressure (LP) side of the cylinder connected

to a low pressure source, which can either provide or absorb flow as needed to account for the differential fluid flow introduced by the single rod cylinder. Not shown in the circuit is a proportional control valve used to control a double-rod cylinder that adjusts the pump displacement mechanism.

1.2 Motivation

The motivation behind this research work is to increase machines' efficiency, safety, intelligence, and productivity by offering the following features and benefits:

- Active safety
- Adaptability to environment and operating conditions
- Adjustability of steering ratio and feel
- Remote and/or autonomous operation
- Sensor fusion
- Improved fuel efficiency

1.3 Power Steering Architectures

The need for power steering stemmed from the fact that vehicles kept growing in size and mass, requiring larger tires that eventually became too hard to steer manually without supplemental power assist. Steering wheel effort required by a vehicle operator increases with the vehicle's mass, size, suspension system geometry, steering linkages placement, tire sizes and properties, and various other factors. While manual steering systems were adequate during early development stages, the industrial trend to make vehicles larger, safer, faster, and smoother required an additional power boost to assist the driver in the

steering effort, which precipitated the advent of power steering systems. Numerous power steering system designs have been proposed and produced, yet they can all be broadly categorized into the groups detailed in the following sections.

1.3.1 Hydrostatic Power Steering

In hydrostatic power steering systems the power is transmitted from the prime mover to the steered components via a hydraulic fluid flowing through pipes and hoses. A hydraulic pump is typically driven by an engine, and the pump flow is metered by a proportional control valve that delivers the required flow rate to the steering actuator(s) downstream. Typically, the operator's steering wheel input is transmitted via a lead-screw (torsion bar) to a proportional linear (rotary) valve that connects the steering actuator ports to the pump flow ports. The hydro-mechanical valve usually has two sections: a fluid metering section and a fluid control section. The fluid metering section meters flow to the steering actuator, hence maintaining the relationship between the steering wheel rotational angle and the steered components position. The valve's control section directs flow to and from the metering section, to and from the actuator, and regulates the pressure supplied to the actuator.

In hydrostatic steering architectures, the steering wheel is mechanically decoupled from the steered components thus inhibiting manual steering, and therefore it does not provide an adequate failsafe mode in case of a power failure, which can result in loss of steering function. To overcome this limitation, a manual pump (gear set) is typically installed as an emergency back-up solution in

case of a power loss. The pump can be directly rotated by the operator's turning action of the steering wheel. Given its adequate control, acceptable comfort level, and high boost capacity, this system architecture is common in agricultural and construction machinery.

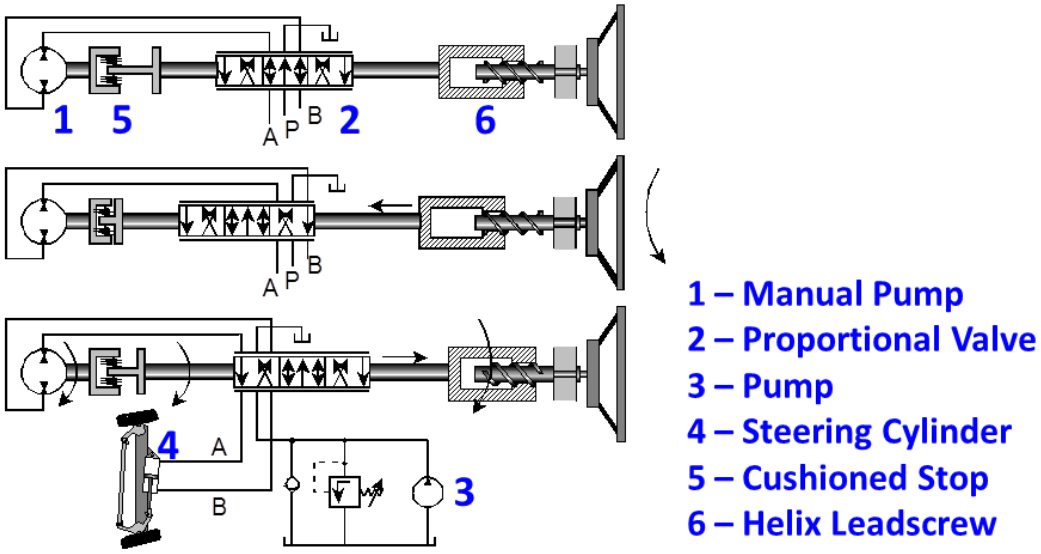

Figure 2: Example of a Hydrostatic Power Steering System.

1.3.2 Hydro-mechanical Power Steering

Hydro-mechanical power steering architectures incorporate a mechanical connection between the steering wheel and the steered components, where manual power from the operator and supplementary boost from the power steering system combine at one of the linkage system components (column / gearbox / rack). The assist level is determined based on the steering wheel input (torque / angle), which controls a proportional valve that varies the pressure in the actuator(s) coupled to the steered components. Such a system has an advantageous failsafe mode since the operator can still control the steering, to a

certain degree, depending on the vehicle's speed and load. However, this system is usually suitable for small to medium size applications where power demand is not very high.

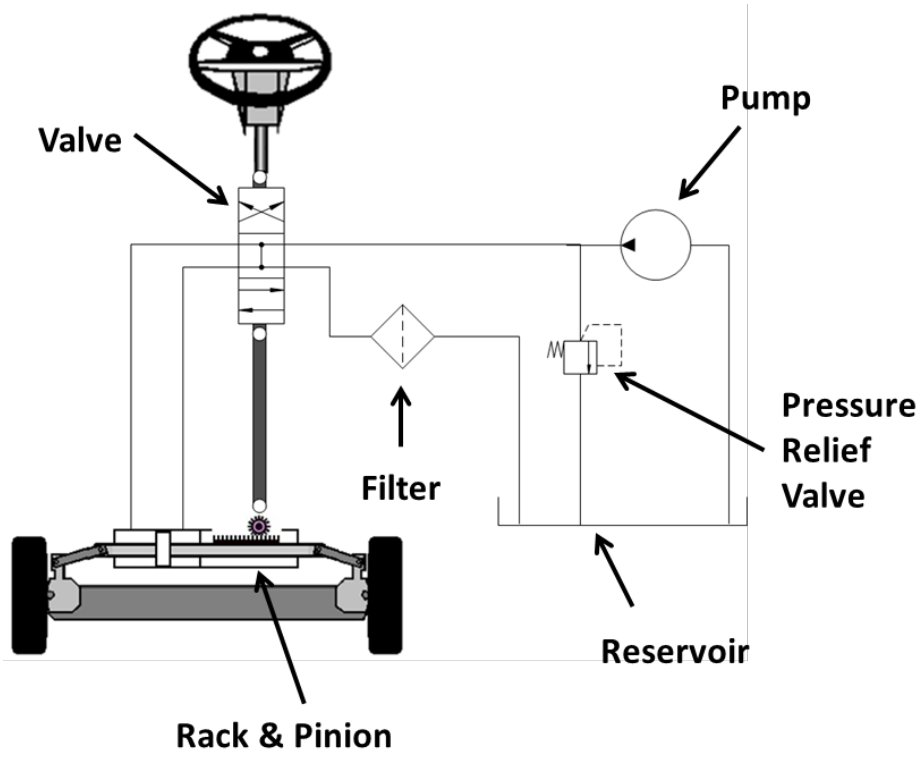

Figure 3: Example of a Hydro-mechanical Power Steering System.

1.3.3 Electro-hydraulic Power Steering

Electro-hydraulic power steering makes use of modern electronics (sensors, actuators, electronic control units) and control algorithms to perform the power steering function. The operator steering wheel input (torque, rotation, or both) are sensed via torque / angular position sensors, whose outputs are fed back to a controller that controls fluid flow to the actuators accordingly. In certain cases, the vehicle speed is also fed back to the controller to provide progressive steering, which provides speed-dependent assist level and steering effort.

Electro-hydraulic power steering systems that use electric motors also allow for on-demand power delivery since the motor is commanded to drive the pump only when steering input is present. The result is improved energy efficiency due to minimizing engine parasitic losses. However, energy efficiency is not optimized due the high throttling losses associated with flow metering across the electro-hydraulic control valve.

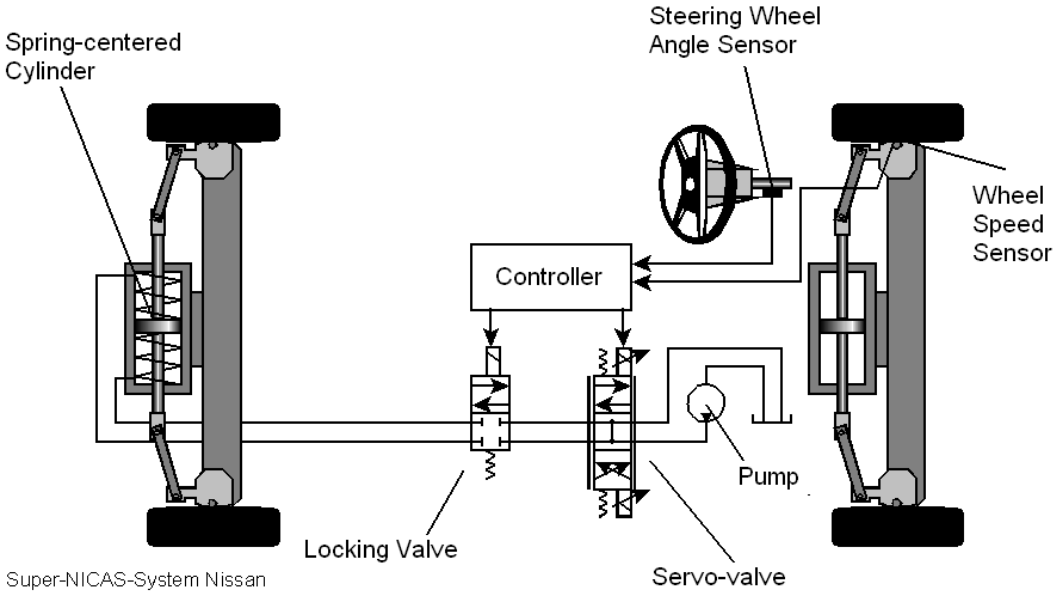

Figure 4: Example of an Electro-hydraulic Power Steering System.

1.3.4 Electric Power Steering

In the past decade or so, electric power steering systems gained favorability, especially in the automotive industry, due to the elimination of engine parasitic losses associated with the continuous driving of the power steering pump regardless of steering input. Several electric power steering designs exist and they typically vary by the mounting location of the electric motor (column / pinion / rack). Nevertheless, the operating principle is the same in the sense that the

electric motor provides an additional torque to the operator's input torque to help rotate the steering gear connected to the steered components. One drawback of electric power steering systems is their limited applicability to small-to-medium size vehicles; the high power requirement of larger vehicles results in massive direct current (DC) motor sizes that make the technology inappropriate. To reduce the motor size in larger vehicle applications, the steering system can utilize a higher voltage source (typically 42 Volts) than the standard system (typically 12 Volts), which necessitates the installation of DC converters to step-up the voltage in conventional powertrain vehicles or step-down the voltage in electric hybrid vehicles. The added cost, packaging constraints, mass, and volume make this alternative very challenging.

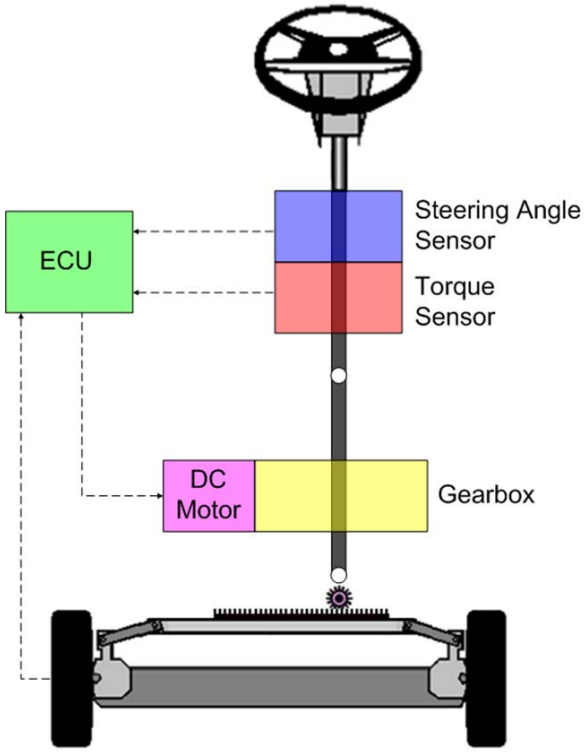

Figure 5: Example of an Electric Power steering System.

1.4 Vehicle Steering Architectures

Several steering geometries and kinematics are available for inducing steering in moving vehicles. The architectures vary based on the chassis components that are actuated, which are covered in the subsequent sections.

1.4.1 Wheel Steering

Wheel steering systems induce vehicle turning by pivoting the front and/or rear wheels about their respective axes. Most modern automobiles make use of this specific architecture, specifically front wheel steering. Ample research and published literature can be found on this architecture given the high level of attention and scrutiny paid by the automotive industry to front wheel steering systems relative to vehicle handling, comfort, safety, and design optimization.

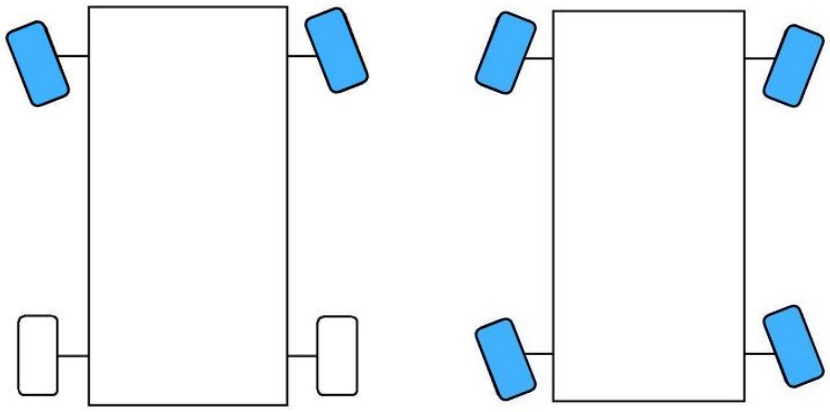

Figure 6: Wheel Steering Geometry.

1.4.2 Axle Steering

Axle steering systems induce vehicle turning by pivoting the front and/or rear axles about a vertical pin joint. This architecture is not very common, but has been used in various yard maintenance and agricultural equipment.

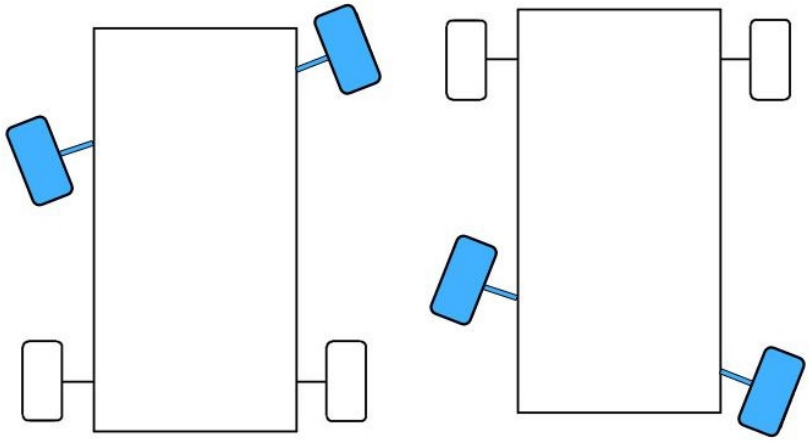

Figure 7: Axle Steering Geometry.

1.4.3 Skid Steering

In skid steering architectures, the wheels and/or axles are not pivoted about a vertical hinge joint, but rather steering is achieved by driving the wheels or tracks on opposite sides in reverse directions causing the vehicle to skid, that is to rotate about its vertical axis. Zero turning radius is possible with this configuration.

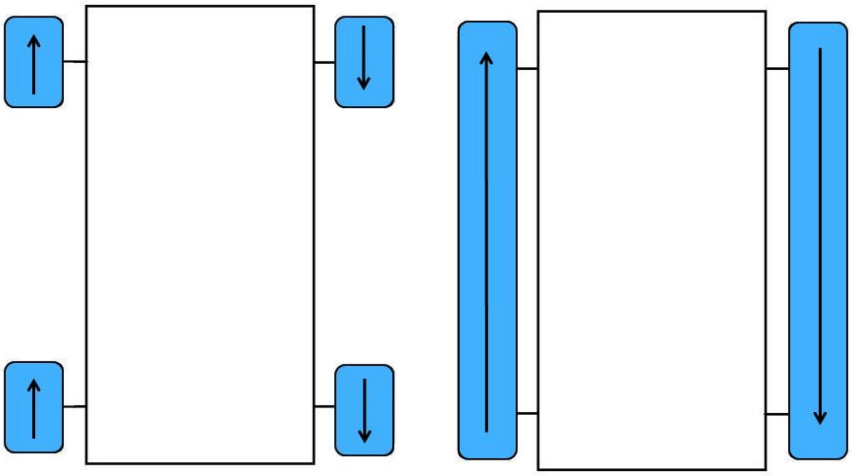

Figure 8: Skid Steering Geometry.

1.4.4 Articulated Frame Steering

As stated in the Abstract, this dissertation focuses on a special type of steering architecture, known as articulated frame steering. Articulated frame steering systems induce vehicle turning by pivoting the front and rear frames about an articulation joint. This architecture is widely used in mobile machinery because of the advantages it offers relative to its capacity to support large axle payloads and superior maneuverability that allows for negotiating corners with small turning radii. However, this architecture faces stability related issues with the possibility of a tip-over under certain combinations of steering angle, payload magnitude and distribution, and grade. A key design factor in articulated frame steering is the location of the articulation joint, which determines the relative paths of the front and rear axles. For instance, placing the hinge equidistantly between the front and rear axles circumvents the need for a central differential since both axles travel along the same path with the same speed.

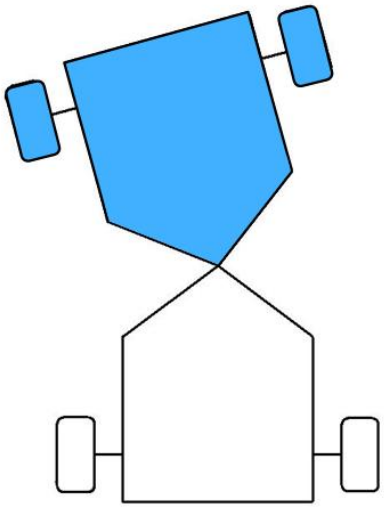

Figure 9: Articulated Frame Steering Geometry.

Figure 10 and Eq. (1) illustrate how for a joint placed at the midpoint between the front and rear axles, the two axles turn about the same center and the inner and outer wheels each trace their own circular paths.

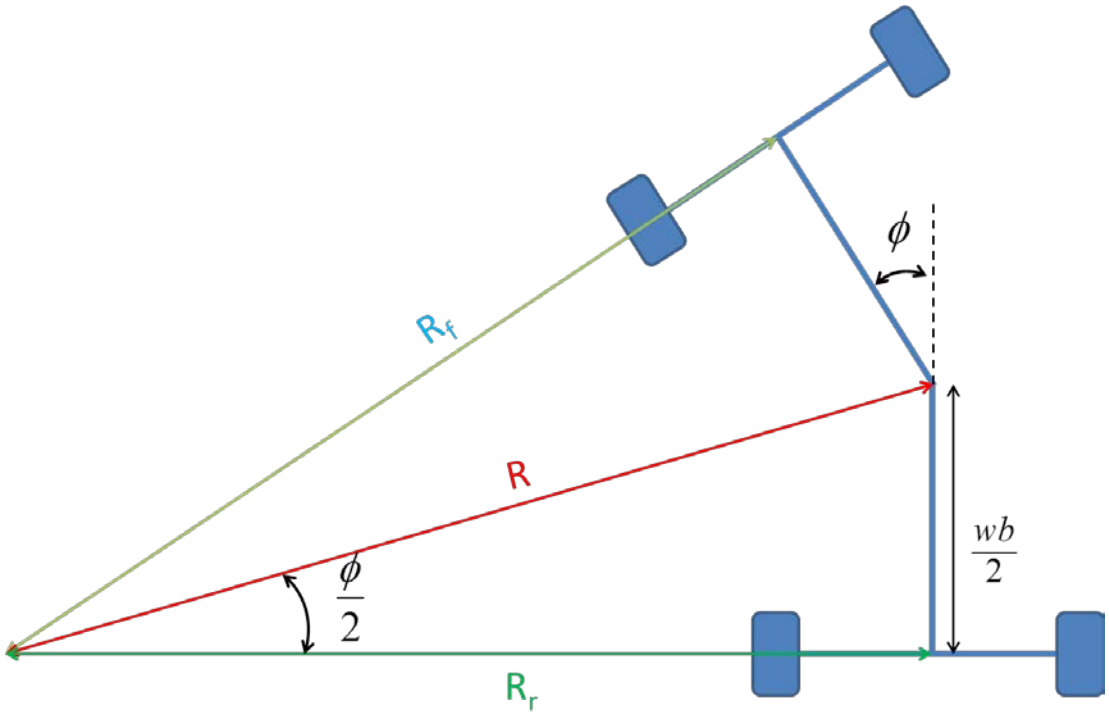

Figure 10: Articulated Steering Kinematics.

$$R_f = R_r = \frac{wb}{2}\cot\left(\frac{\phi}{2}\right). \tag{1}$$

where R_f and R_r are the front and rear axle turning radii respectively, wb is the vehicle wheelbase, and φ is the steering (articulation) angle.

The resulting turning radius of the articulation joint, R, is calculated via Eq. (2).

$$R = \frac{wb}{2}\sqrt{1+\cot^2\left(\frac{\phi}{2}\right)}. \tag{2}$$

1.5 Research Aims

The aims of this work are to research, propose, and verify a displacement controlled (DC) steer-by-wire (SbW) architecture, including controls, which offer the following:

- Active safety
- Adaptability to environment and operating conditions
- Sensor fusion
- Variable-rate & variable-effort steering
- Improved line holding capability
- Potential for remote and full autonomous operation
- Improved fuel efficiency

1.6 Original Contributions

Over the course of this research work, the following original contributions were made and are included in this dissertation:

- Researched and designed a novel SbW technology based on DC actuation, which is the world's first and only 'throttle-less' electrohydraulic SbW system in articulated frame steering (AFS) vehicles.
- Proposed an advanced model-based controller for realizing accurate motion control by combining feedforward control with full-state feedback control based on state errors estimation.
- Researched and implemented an adaptive control algorithm that allows the machine to adapt to operating conditions and variations.
- Implemented a DC SbW system on a prototype test vehicle.

- Proposed a yaw stability control system via active steering intervention by the new DC SbW system.
- Researched and designed a virtual sensor that estimates the vehicle's yaw rate based on available sensory data and model input/output.

1.7 Dissertation Organization

After having introduced the scope of this work in Chapter 1, a literature review of state-of-the-art technologies is presented in Chapter 2. The proposed system architecture is detailed in Chapter 3. Dynamic models of the associated components, subsystems, and the entire system are derived and validated in Chapter 4. Chapter 5 presents two controllers: a linear controller based on the derived linearized plant model and a nonlinear (adaptive) controller that copes with parametric uncertainties and unmodeled nonlinearities. Hardware implementation of the new system components and instrumentation of the required sensors on a prototype test vehicle are denoted in Chapter 6. Baseline measurements performed on the stock machine and testing results on the overhauled machine retrofitted with DC steering are furnished in Chapter 7. A yaw stability control system via active steering is developed in Chapter 8, and a virtual yaw rate sensor is designed in Chapter 9. The dissertation ends with conclusions and future work as outlined in Chapter 10.

CHAPTER 2. STATE OF THE ART LITERATURE REVIEW

The main findings of the state-of-the-art literature review are categorized into two main segments: one that studies displacement control (DC) technology and its implementation on non-steering related functions; and a second that reviews current technologies and prior work done on steering systems, in general, and focusing on articulated frame geometries and x-by-wire systems, in particular.

2.1 Articulated Steering Instabilities

Many on-highway vehicles (e.g. semi-trailer trucks) and off-highway machines (e.g. articulated trucks and wheel loaders) feature one type or another of articulated steering geometries, and for that reason researchers in the past have extensively studied their dynamics in order to characterize their stability margins. The main lateral instabilities that articulated vehicles suffer from are known as jackknifing and snaking. Snaking occurs when both front and rear frames become unstable and start oscillating (weaving) relative to one another as illustrated in Figure 11.

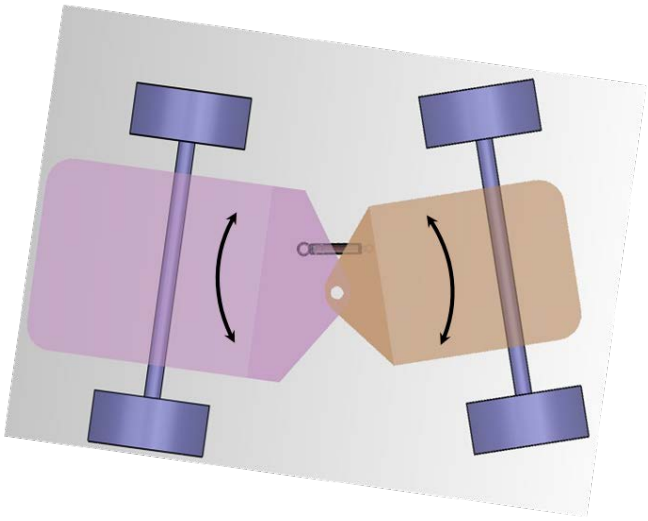

Figure 11: Snaking Mode of an Articulated Frame Steering Vehicle.

In jackknifing mode, one of the frames becomes unstable and folds onto the other stable end (like a pocket knife) as illustrated in Figure 12. Jackknifing of semi-trailer trucks prompts major safety and traffic congestion concerns.

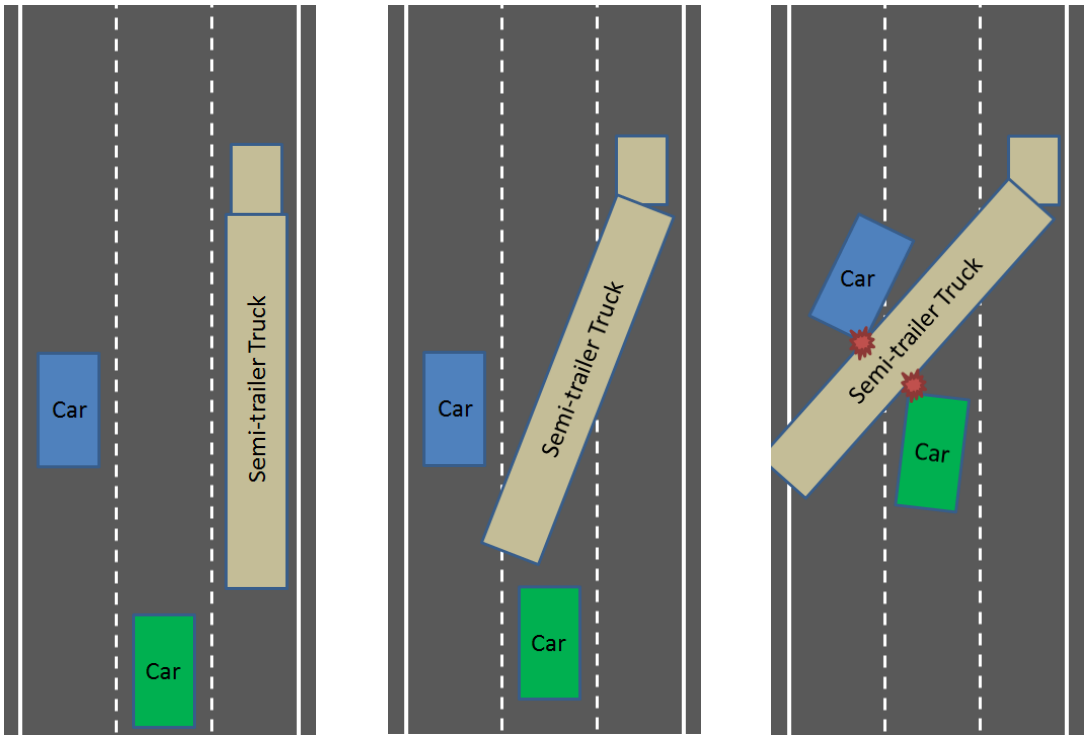

Figure 12: Illustration of a Semi-trailer Truck Undergoing Jackknifing.

2.2 Articulated Vehicle Dynamics and Control

Various dynamic models of articulated vehicles have been derived by previous researchers, who focused their attention on distinct aspects of the modeling approach based on their particular research interests and aims. In (Scholl & Klein, 1971), the authors studied the effect of the steering system on the stability of an articulated vehicle, in which they concluded that the oil mass resonance was the most critical phenomenon affecting the system closed loop stability. The work presented in (Crolla & Horton, 1983) detailed the derivation of a theoretical 3-DOF dynamics model that describes the handling behavior of articulated vehicles both on- and off-road in order to investigate stability at higher speeds. For simplification and practical purposes, the model is linearized and the hydraulic steering actuators are modeled as an equivalent torsional spring and damper combination at the articulation joint. This model, however, is only useful for analyzing the dynamic behavior of the vehicle without any steering input. Hence to complete their prior work, the researchers' later publication (Horton & Crolla, 1986) included a model of the steering system based on linearized pressure build-up equations to allow for stability analysis while incorporating the steering system effects. Simulation results revealed the impact that the steering system characteristics have on the stability of articulated vehicles, and identified leakage across the hydraulic cylinders as a critical design parameter to control stability, with higher leakage leading to reduced snaking oscillations. Their findings also confirmed the fact that increasing articulation joint friction results in reduced oscillations due to the increased structural damping effect that friction introduces.

More than a decade later, (Chen & Tomizuka, 1997) proposed a control oriented dynamic modeling approach based on the Lagrange mechanics, mainly for tractor-semitrailer vehicles in an Automated Highway System (AHS) with lateral control as their primary focus. Two types of dynamic models were utilized: the first type was a complex nonlinear simulation model, whereas the second type consisted of two simplified control models that were derived from the complex nonlinear model. Their report concluded with the design of two control algorithms for lateral guidance: the first was a baseline steering control algorithm and the second was a coordinated steering and independent braking control algorithm. Another linearized dynamics model was later presented in (He, Khajepour, McPhee, & Wang, 2005), where the authors devised a linear model of the steering system using a rotary proportional valve instead of the linear valve, which was considered by Horton and Crolla. Their work remains valuable given the wide adoption of rotary valves as the preferred control element for hydrostatic steering systems in most machines today. The research was carried on by (Azad, 2006) where the author investigated the lateral stability of articulated machines with a rear-mounted load interacting with the ground, such as forestry skidders, and investigated the impact of locking the front and rear differentials on stability. From an active safety standpoint, the author also investigated the concepts of engine torque vectoring and differential braking to help stabilize the otherwise unstable vehicle via the design of robust control algorithms.

2.3 Hydrostatic Steering Systems

The most common type of power steering architectures used in mobile machines is hydrostatic steering, in which there is no mechanical connection between the steering column and the steered components. Multiple hydrostatic steering designs and variations exist with open-center and load-sensing systems being the most common. Open-center hydrostatic steering systems require their own fixed displacement pump to supply the steering unit with fluid flow. Open-center systems result in increased engine parasitic losses since the pump is constantly running and flow is being circulated through the hydro-mechanical valve. On the other hand, load-sensing systems only require one pump to supply both the steering system and the working hydraulics (implement functions), which results in slightly better energy efficiency. However, the latter architecture requires the addition of a priority valve to give precedence to the steering system ensuring ample flow is always available to safely steer the vehicle. Figure 13 shows a load-sensing hydrostatic steering system of the baseline wheel loader, which is used to validate the derived analytical plant models and control algorithms in this work. As highlighted in the figure, the fluid flow from the main pump passes through a priority valve then a proportional valve; this flow metering results in significant energy dissipation into heat due to throttling losses across the edges of the spools. In a hydrostatic steering system, the driver's applied torque to the steering wheel results in twisting a torsion bar, which corresponds to an equivalent orifice area opening that in turn determines the flow rate to the steering actuator(s). In the event of a power loss, a gear set integrated within the

steering unit could be manually rotated by turning the hand wheel, which provides adequate fluid flow to the steering actuator. In normal operation, the gear set plays the role of a metering section that meters flow to the steering actuator in order to maintain the relationship between the hand wheel rotational angle and the steered components position.

As previously stated, the new pump displacement controlled steering system gains its fuel efficiency advantage over the state-of-the-art valve controlled systems by eliminating hydraulic control valves as final control elements, and using a variable displacement pump to directly channel the appropriate fluid flow to the actuators, without throttling.

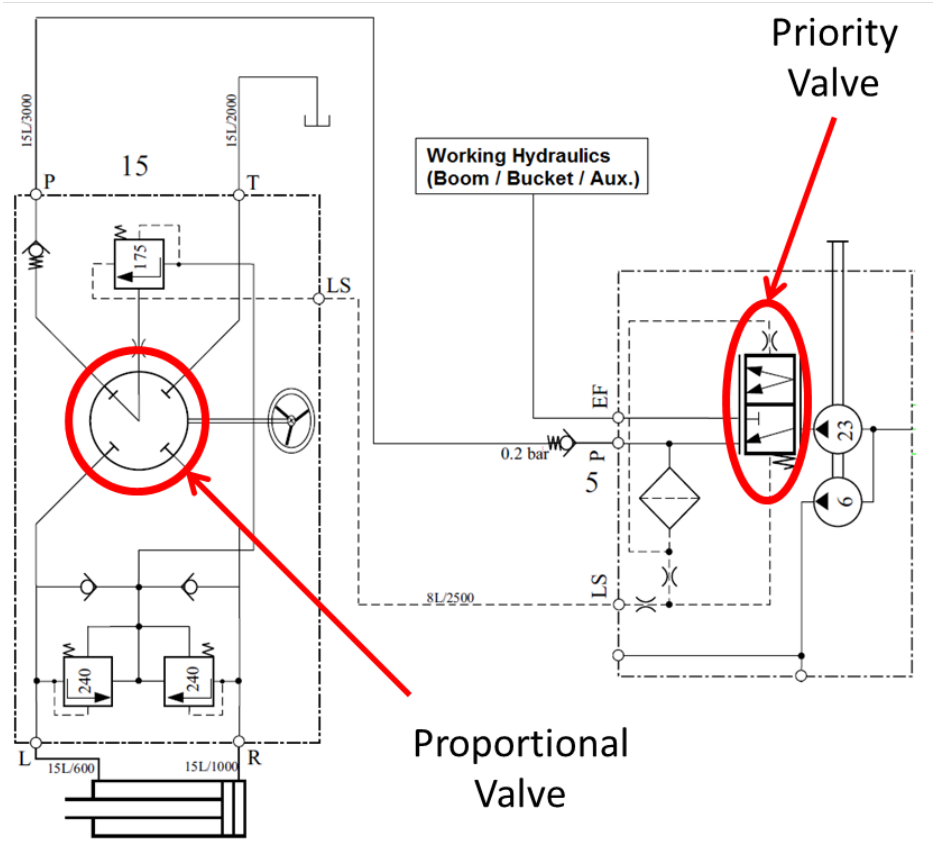

Figure 13: Hydrostatic Steering System of the Baseline Prototype Machine.

2.4 Steer-by-wire Systems

The new DC steering system is classified as a steer-by-wire (SbW) system since it decouples the vehicle operator from the steered structures, and uses electrical signals to sense the desired input and command the corresponding output. X-by-wire systems, where the X can be fly, drive, brake, and steer, have seen steady proliferation in the aerospace and automotive industries as a result of the latest advances in electronic control systems. Fly-by-wire systems dramatically improved and revolutionized air travel experience, and in some instances made it possible to fly inherently unstable planes without loss of control. Drive-by-wire systems are almost standard on most modern automobiles, in which an electronic sensor reads the accelerator pedal position and a controller commands an actuator that adjusts the throttle plate. Brake-by-wire systems are not widely used yet, but they have started to appear on the market. Consequently, it is safe to presuppose that SbW technology will be the steering choice of the future and many vehicles will feature this technology soon. SbW systems have in fact been researched by the academic community for various industries including the automotive sector as in (Yih, 2005), and for earth-moving machines as in (Haggag, 2002) and (Abd-Elaziz, 2007). As for industry, numerous publications by original equipment manufacturers and system suppliers can be found on the topic of SbW, mainly geared towards the automotive industry published by the Society of Automotive Engineers (SAE).

2.5 Pump Displacement Controlled Actuation

Varying the output flow of displacement machines has been used for decades now. For instance, hydrostatic transmissions offer infinitely variable transmission (IVT) ratios by varying the displacement of the pump and/or motor units coupled to the engine and wheels respectively. Another technology that works on a similar principle is Electro-hydrostatic actuation (EHA), which was introduced by the aerospace industry as a solution to reduce system mass by eliminating the need for long hydraulic hoses used for transmitting power from a central power supply. EHA can be categorized into two main classes: a variable displacement pump driven by a constant speed prime mover arrangement, which offers fast dynamics due to the low inertia of the pump adjustment mechanism; and a fixed displacement pump driven by a variable speed motor arrangement, which uses a less expensive pump but requires more advanced motor speed control algorithms and more expensive electronic drive circuits.

Pump controlled actuation was first applied to actuate hydraulic (rotary) motors and double-rod (linear) actuators, both of which have equal volumes on the opposing actuator sides. However, to actuate single-rod (linear) actuators, solutions had to be devised to overcome the challenge of having unequal volumes on the actuator sides. In surveying the available literature, several solutions are found including the incorporation of a servo-valve (Berbuer, 1988) and (Ziegler, 1990); a tandem-unit hydraulic transformer (Lodewyks, 1994); a flushing valve (Hewett, 1994); a single-rod cylinder with equal chamber volumes (Pastrakulijic, 1995) and (Habibi & Goldenberg, 1999); a three-port pump with

two working ports and a tank port (Stephenson & Rajput, 2010); a pilot-operated three-way valve connected to a low pressure source (Lawrence, et al., 1995); and two pilot-operated check valves in conjunction with a low pressure flow source (Rahmfeld & Ivantysynova, 1998). A pump controlled system employing the latter solution, whose circuit is shown in Figure 1, is known as displacement control (DC) in literature. The new steering system under investigation in this work adopts this last solution with two pilot-operated check valves.

Since its introduction DC technology has been implemented and successfully demonstrated considerable fuel efficiency increase on multiple mobile machines such as wheel loaders (Rahmfeld & Ivantysynova, 2004) resulting in 15% fuel savings, skid steer loaders (Williamson & Ivantysynova, 2007) resulting in 15-20% fuel savings, and excavator (Zimmerman, 2008) resulting in 40% fuel savings. DC has also been researched and implemented for realizing active vibration damping on a wheel loader (Rahmfeld & Ivantysynova, 2003) and a skid steer loader (Williamson, Lee, & Ivantysynova, 2009). More recently, DC actuation was investigated for employing total machine power management schemes (Williamson & Ivantysynova, 2010) resulting in additional machine efficiency improvements. Nevertheless, DC actuation has never been researched nor implemented on the steering function of mobile machines. The only reference found in literature for applying DC technology on a steering system was in a patent by (Ivantysynova, Weber, & Grabbel, 2011).

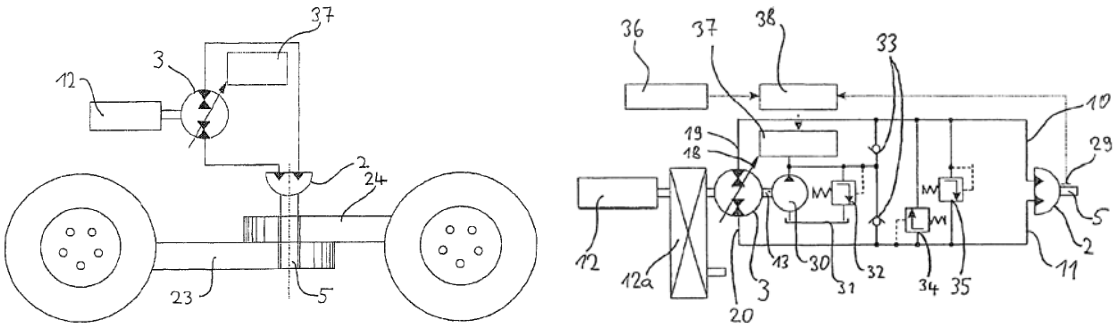

Figure 14: Sample Figures Taken from U.S. Patent No. 7,786,125 B2.

Another research that involved the implementation of pump displacement control for designing a dual-path front hydrostatic drive-by-wire system for an off-road vehicle was presented in (Lumkes Jr. & Van Doorn IV, 2008), where the authors developed a mathematical model, generated control algorithms, and validated their work by retrofitting the drive-by-wire system in an agricultural windrower.

CHAPTER 3. DC STEERING SYSTEM

DC steering is classified as electro-hydrostatic power steering, in which the steering wheel torque and/or angle, and vehicle speed in some instances, are sensed and fed back to a controller that adjusts the displacement of a variable displacement pump as opposed to controlling a proportional valve. Figure 15 is provided for identification of the proposed steering system components, which is based on the circuit introduced in Figure 1. The actuator (8) motion is controlled by adjusting the pump (2) speed, displacement, or both. The pump inlet/outlet ports are connected to the piston/rod sides of the actuator. The differential fluid flow between the actuator's uneven sides is overcome by means of pilot-operated check valves (6), which keep the low pressure side of the actuator connected to a low pressure source that can either provide or absorb flow to prevent evacuation. The low pressure source has its own fixed displacement charge pump (4), driven by the same prime mover (1), providing continuous flow to the cylinder's low pressure side. The low pressure level setting is adjusted via a pressure relief valve (5). An accumulator (not shown) could also be used to provide high flow rate spikes when sudden high speed cylinder movements are incurred, if the charge pump flow is not sufficient. The system is protected from over-pressurization by means of pressure relief valves (7) installed on both sides

of the actuator. The pump control system (3), sketched in Figure 16, uses a proportional control valve that meters flow to a double rod actuator that is mechanically coupled to the pump swash plate. The actuator linear displacement determines the angular position of the swash plate, and therefore the effective instantaneous pump displacement volume per revolution.

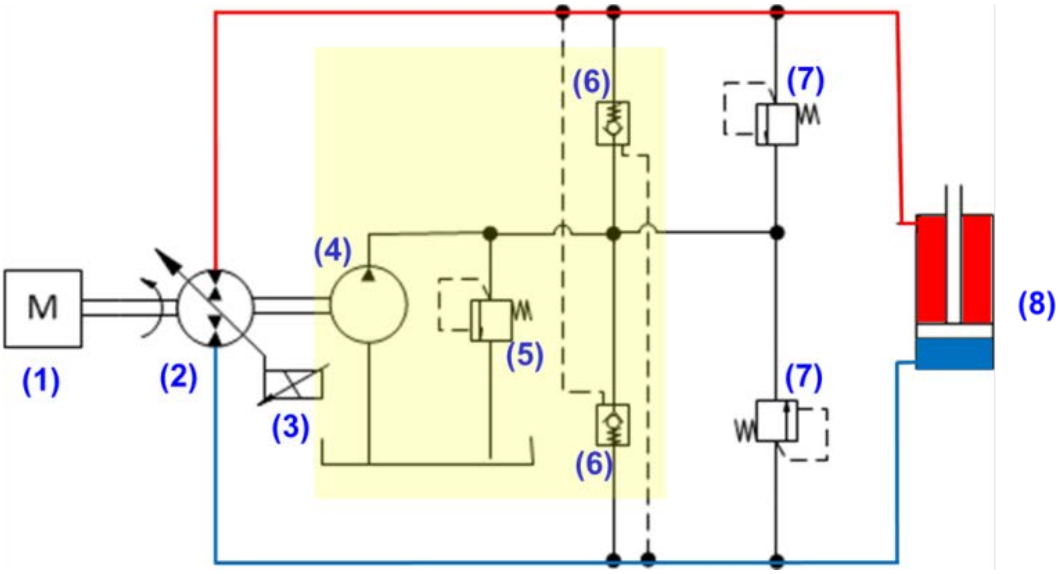

Figure 15: DC Steering Hydraulic Schematic.

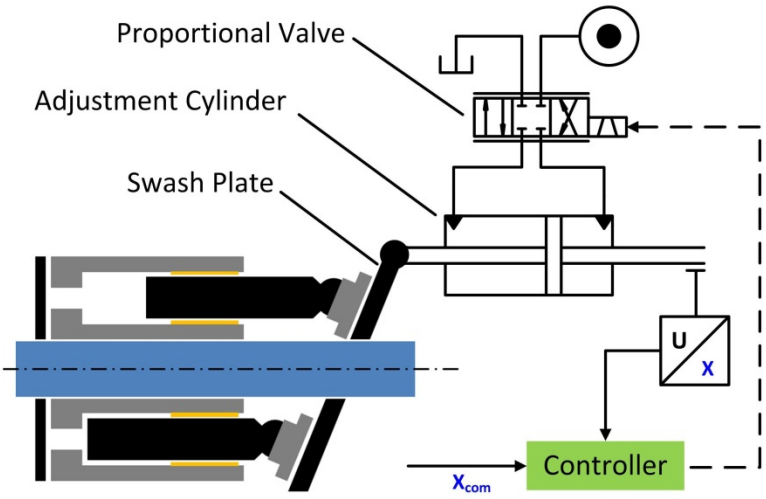

Figure 16: Electro-hydraulic Pump Swash Plate Control System.

3.1 Advantages of the New DC Steering System

The new DC steering system promises multiple advantages over its state-of-the-art hydrostatic steering counterpart, shown in Figure 13 above. These advantages, combined, address the main concerns that vehicle manufactures are facing today, and produce a technological leap that advances machines into the future by meeting the ever-increasing demanding requirements.

3.1.1 Fuel Efficiency

First and as previously explained, pump controlled actuation is an energy efficient technology that promises significant fuel savings and increased machine productivity, which have been demonstrated in field tests on prototype machines. Therefore, improved efficiency results are expected when employing pump controlled actuation to the steering function of mobile machines.

3.1.2 Adjustability

The DC steering system offers the ability to vary the steering sensitivity (gain) and effort based on operating conditions. Most present day machines have a fixed steering ratio, which is the relationship between the hand wheel number of revolutions and the corresponding vehicle steering angle; and a fixed steering feel, which is the level of tactile feedback experienced by the operator at the steering wheel. With the new DC technology, both features could be made variable based on the operating conditions. For instance, at low vehicle speeds the number of steering wheel turns is reduced resulting in increased machine productivity (more work done per unit time), and the level of torque feedback is also reduced resulting in reduced operator fatigue (fewer operator breaks and

extended machine uptime). On the other hand, at high speeds the number of steering wheel turns and the level of torque feedback are both increased to prevent abrupt steering wheel perturbations from destabilizing the machine while traveling at high speeds, since the steering wheel feels stiffer and the steering ratio (sensitivity gain) is lower.

3.1.3 Active Safety

Pump controlled actuation has been successfully demonstrated for realizing active vibration damping on the boom function of a wheel loader (Rahmfeld & Ivantysynova, 2003) and a skid steer loader (Williamson, Lee, & Ivantysynova, 2009), in which rapidly varying loads and disturbances were attenuated, proving that DC has desirable dynamics and relatively high bandwidth frequencies. This capability can be carried over to the steering system, which upon the detection of instabilities can command the steering actuator to take corrective actions for stabilizing the vehicle especially when traveling at higher speeds.

3.1.4 Straight Line Holding

Backlash between the steering shaft and the steering valve, as well as the drift of hydro-mechanical valves prevalent in hydrostatic steering systems, are the main culprits behind the inability to maintain straight line driving without continuous corrections made at the steering wheel. Minimizing hand wheel corrections is a highly desirable feature since less operator input is required to maintain straight-line driving, and the machine can safely travel at higher speeds. The new system uses closed loop control, which results in improved line holding capability.

3.1.5 Tele-operation and Full Autonomous Operation

The new DC steering system takes advantage of x-by-wire technologies that do not require physical input to induce motion control. As such, vehicles equipped with the new DC steering system can be either remotely operated by entering appropriate input signals (e.g. joystick), or autonomously operated with the inclusion of proper sensors (e.g. GPS, Radar, LiDAR, and Laser). The trend for autonomous operation has been gaining steady momentum amongst original equipment manufacturers, and a DC steering system aptly fits this new paradigm.

3.1.6 Diagnostics and Health Monitoring

Last but not least, with the integration of electronic control units (ECU), sensors, and communication protocols, the new DC steering system can benefit from the latest advances in the area of health monitoring, diagnostics, and prognostics. Model based algorithms could be implemented granting access to vehicle states that are not (or could not) be otherwise physically sensed.

3.2 System Sizing

A key requirement for the successful implementation of any new technology starts with a properly sized system. The new DC steering system is no exception. The following sections provide basic formulations for sizing the DC steering pump and the proportional control valve of the pump control system. The given sizing methodology assumes that the operating pressure range, maximum loads, basic vehicle parameters, and duty cycles are given. However, if not all of the above information is available, certain estimations can still be made to allow for moving forward in the analysis and design processes.

3.2.1 DC Steering Pump Sizing

This section deals with sizing the pump for a DC steering system that employs a single-rod actuator, but the same approach can be taken for sizing systems with double-rod actuators or rotary actuators. The DC steering pump is primarily sized to provide adequate flow rate to the steering actuator in order to meet the fastest specified duty cycle, provided that it can operate within the working pressure and speed ranges. In the case of a single-rod actuator, caution must be taken by considering the larger piston chamber to ensure adequate performance at worst-case scenario. The maximum actuator swept volume is attained during the cylinder extension phase, where the pump outlet flow is directed into the piston chamber. The piston side swept volume, V_{swept_Piston}, is the product of the actuator piston side area, A_p, and its total stroke, H, from end to end as given by Eq. (3).

$$V_{swept\_Piston} = H\ A_P. \tag{3}$$

Knowing the fastest required duty cycle or the minimum cycle time, Δt_{min}, in which the machine needs to articulate from lock-to-lock, the maximum flow rate, Q_{max}, that the pump must deliver is calculated via Eq. (4).

$$Q_{\max} = \frac{V_{swept\_Piston}}{\Delta t_{\min}}. \tag{4}$$

Finally, the pump displacement volume, V_d, is determined after assuming an appropriate minimum engine speed, n_{eng}, and a practical volumetric efficiency, η_{vol} as shown in Eq. (5).

$$V_d = \frac{Q_{\max}}{n_{eng}\ \eta_{vol}}. \tag{5}$$

It should be noted that a safety factor must be applied to the calculated pump displacement volume, thus it is recommended to select the next size up available when referencing pump manufacturers catalogues.

3.2.2 Pump Control System Sizing

The pump displacement adjustment mechanism, shown earlier in Figure 16, mainly consists of a swash plate, control pistons, centering springs, and a proportional control valve. One of the main requirements for the adjustment system is to have fast dynamics that meet the response specifications of the steering system. Previous research (Grabbel, 2003) has shown that the dynamics of the adjustment system are dominated by the hydraulic proportional control valve, given the high natural frequency of the other mechanical components. As a result, the proportional valve must first be designed or specified to have the appropriate bandwidth frequency. Another consideration is for the valve to have an adequate flow rate capacity in order to adjust the pump displacement from minimum to maximum setting within a specified minimum time. The maximum required flow rate by the valve, Q_{PCS_max}, is calculated by determining the control piston swept volume, V_{PCS_Piston}, and dividing it by the minimum required time, Δt_{PCS_min}, for adjusting the pump displacement from minimum to maximum setting as given by Eq. (6).

$$Q_{PCS\_\max} = \frac{V_{PCS\_Piston}}{\Delta t_{PCS\_\min}}. \tag{6}$$

3.2.3 Low Pressure Charge Pump Sizing

After determining the maximum required flow rate for actuating the pump adjustment system, the size of the charge pump, V_{CP}, could be determined after establishing practical values for the engine speed and the charge pump volumetric efficiency, η_{vol_CP}, per Eq. (7).

$$Q_{CP} = n_{eng} V_{CP} \eta_{vol\_CP}. \tag{7}$$

It is noted here that the engine speed must be set at or above a certain threshold to meet the flow requirement when demanding maximum performance from the steering system.

3.2.4 Sizing Case Study

A compact five-tons wheel loader is designated as a baseline machine to serve as a prototype test vehicle for conducting experimental testing to validate the analytical results in this work. The machine is retrofitted with a DC steering system, which is sized in accordance with the above procedures.

3.2.4.1 DC Steering Pump

The machine's steering system employs a single-rod actuator with 0.070m piston diameter, 0.032m rod diameter, and 0.262m end-to-end stroke. The piston side swept volume is calculated as 0.00101m^3. The maximum desired steering rate is to articulate the machine from lock-to-lock in 3.0s. This corresponds to a maximum flow rate of 20.17L/min. Assuming an engine speed of 2000rpm and a pump volumetric efficiency of 90% results in a pump size of 11.20cm^3/rev. The

selected variable displacement axial piston pump, which is also capable of motoring and over-center operation, has a displacement volume of 18cm^3/rev.

3.2.4.2 Proportional Control Valve

For selecting an appropriate proportional valve, the pump displacement adjustment system dimensions must be known. For the selected pump, the control pistons have 0.022m diameter and 0.054m stroke. Requiring the pump displacement to be adjusted from minimum (-100%) to maximum (+100%) displacement in 0.150s, results in a required flow rate of 8.21L/min. The selected proportional directional control valve has a flow rating of 20 L/min at a pressure differential of 35bar per metering edge.

The valve has a zero lap spool configuration, a frequency response of >100Hz at 5% spool stroke, and a step response of <16ms at 100% signal.

3.2.4.3 Charge Pump

The size of the charge pump must be small enough to result in minimal engine parasitic losses, and at the same time large enough to provide the maximum required flow rate to actuate the pump adjustment system. As a result, a compromise must be made to reach an optimal size that meets both conditions. To provide a flow rate of 8.2L/min with an assumed volumetric efficiency of 92% at 1800rpm engine speed, the charge pump (gear type) size is selected to be 5.0cm^3/rev.

CHAPTER 4. DYNAMIC MODELING AND SIMULATION

Prior to proceeding into the implementation phase, modeling of any new system must be performed in order to check the concept feasibility, identify problematic areas, and design proper control algorithms. In this chapter, a high fidelity dynamic model of a DC steering system is described. The setup is modeled after an articulated frame steering vehicle with a single-rod steering actuator, which replicates the prototype machine used for experimental testing and validation of this work. However, it is must be noted that the derived models can be adapted to encompass other configurations, layouts, and architectures without further required modifications.

The vehicle model is composed of two main blocks: an electro-hydraulics module and a mechanics module. Figure 17 shows a block diagram of the system dynamic model structure and setup. The hydraulics module delivers the required flow rate into the steering actuator inducing linear translational motion, which corresponds to vehicle articulation or rotational motion. The pressure levels in the actuator chambers are determined by the loads computed within the mechanics module, which are mainly due to the opposing lateral forces at the ground-tire interface. The electrohydraulic pump control system adjusts the pump displacement according to the desired steering wheel angle and rate in a

closed loop fashion. The next sections describe in detail the individual models of the subsystems and components.

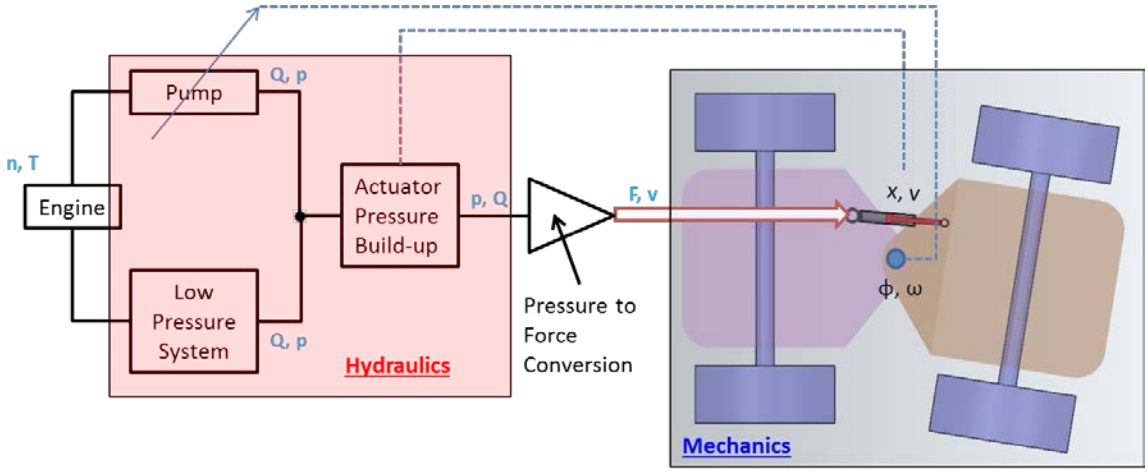

Figure 17: Block Diagram of DC Steering System Model.

4.1 Electro-hydraulic Subsystem Model

The electro-hydraulics module includes dynamic models of a variable axial piston pump/motor unit including nonlinear volumetric and torque losses, transmission line losses, an electrohydraulic pump control system, a low pressure source system, and a pressure build-up model that determines the pressure rise inside the actuator chambers.

4.1.1 Variable Displacement Pump/Motor Model

The variable displacement axial piston pump model is designed with careful consideration to volumetric and torque losses incurred throughout the entire pump operating region. First, the derived (actual) pump displacement volume is determined via the Toet Method from steady-state measurements conducted at constant speed, constant inlet pressure and temperature, and various load pressures. The derived displacement volume, V_d, is determined by fitting the

measurement data and extrapolating to zero pressure differential. V_d is a function of speed, pressure differential, and pump displacement per Eq. (8).

$$V_d = \frac{1}{n}.\frac{\sum_{j=1}^{k} Q_{ej}.\sum_{j=1}^{k}\Delta p_j^2 - \sum_{j=1}^{k}\Delta p_j.\sum_{j=1}^{k}\Delta p_j.Q_{ej}}{k.\sum_{j=1}^{k}\Delta p_j^2 - \left(\sum_{j=1}^{k}\Delta p_j\right)^2}. \tag{8}$$

where Q_e is the effective pump flow rate, n is the pump (engine) speed, and Δp is the pressure differential across the pump ports.

Steady-state measurements are then recorded at various speeds, displacements, and pressures at a constant inlet temperature. The measured data is fitted to a 3rd or 4th degree polynomial for generating the loss coefficients as functions of the operating conditions. Following are the governing equations that are used to generate the DC steering pump model, in *pumping* mode operation.

$$Q_e = \beta V_d\, n - Q_s. \tag{9}$$

where β is the normalized pump swash plate angle and Q_s is the volumetric loss flow rate given by Eq. (10)

$$Q_s\left(V_d, n, \Delta p\right)_{T=const.} = \sum_{i_1=0}^{I_1}\sum_{i_2=0}^{I_2}\sum_{i_3=0}^{I_3} K_Q\left(i_1, i_2, i_3\right) V_d^{i_1} n^{i_2} \Delta p^{i_3}. \tag{10}$$

The pump effective torque, T_e, is given by Eq. (11):

$$T_e = \beta V_d\, \Delta p + T_s. \tag{11}$$

where T_s is the torque loss given by Eq. (12).

$$T_s\left(V_d, n, \Delta p\right)_{T=cst} = \sum_{i_1=0}^{I_1}\sum_{i_2=0}^{I_2}\sum_{i_3=0}^{I_3} K_T\left(i_1, i_2, i_3\right) V_d^{i_1} n^{i_2} \Delta p^{i_3}. \tag{12}$$

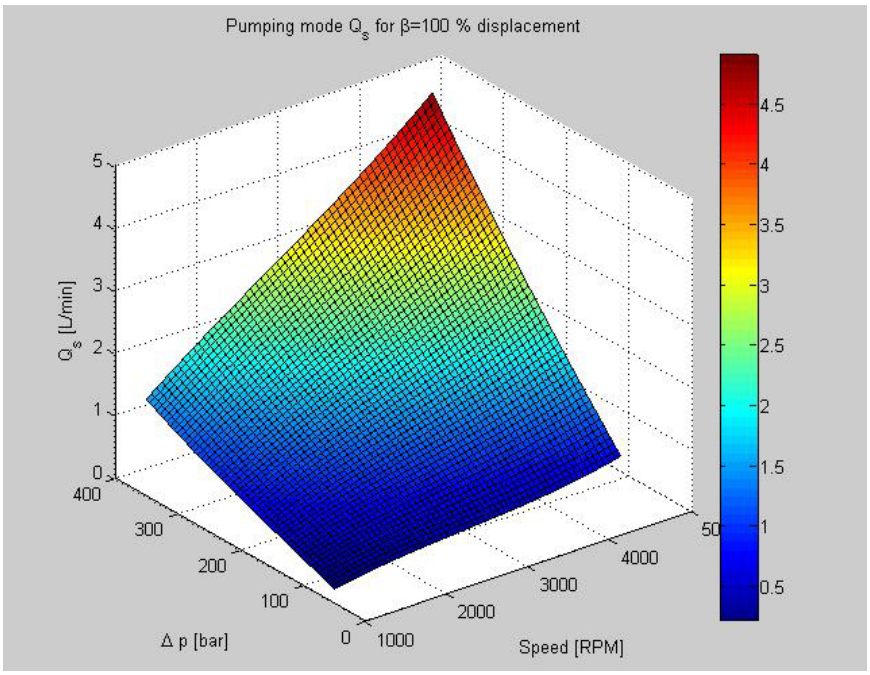

Figure 18: Sample Pump Flow Losses at Full Displacement.

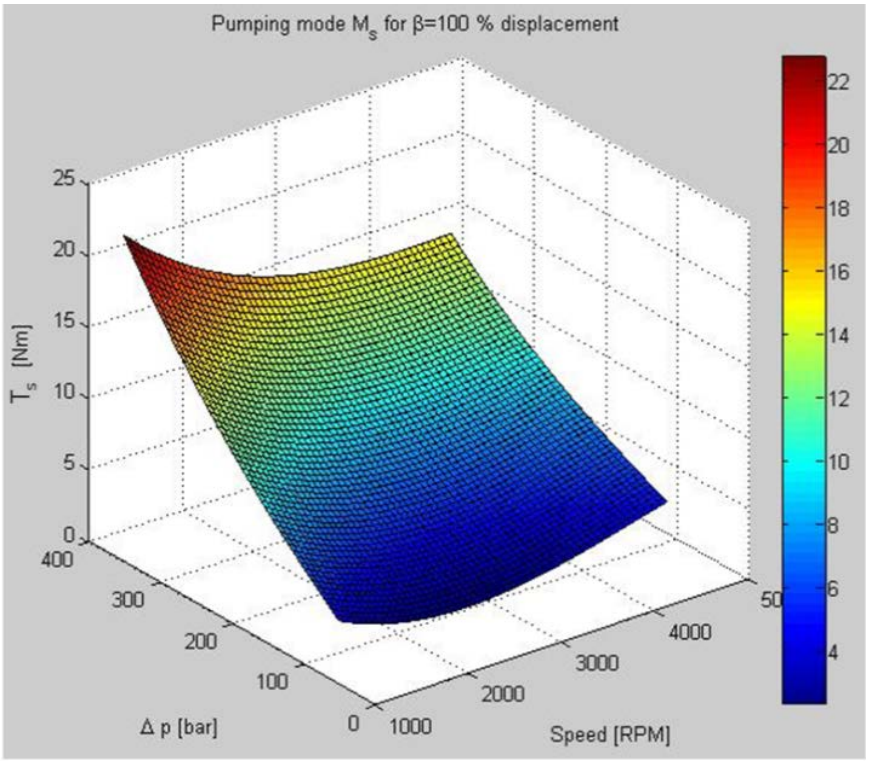

Figure 19: Sample Pump Torque Losses at Full Displacement.

4.1.2 Steering Actuator Pressure Build-up Equations

For calculating the rise in pressure inside the steering cylinder chamber as flow enters and leaves the control volume, pressure build-up is derived by combining the conservation of mass principle, compressible continuity equation, and the fluid bulk modulus equation. This leads to directly computing the pressure inside of a chamber by integrating the sum of flow rates entering and leaving the chamber, divided by the hydraulic capacitance of the control volume. As such, the pressure build-up inside the steering actuator piston chamber is given by Eq. (13).

$$p_A = \frac{1}{C_{HA}} \int \left(Q_A + A_A \dot{x} - Q_{Li} - Q_r \right) dt. \tag{13}$$

where p_A is the piston (A) side pressure, Q_A is the net flow entering / leaving the piston chamber, A_A is the piston side area, $\dot{x}$ is the actuator velocity, Q_{Li} is the internal leakage flow across the actuator chambers, and Q_r is the relief valve flow rate.

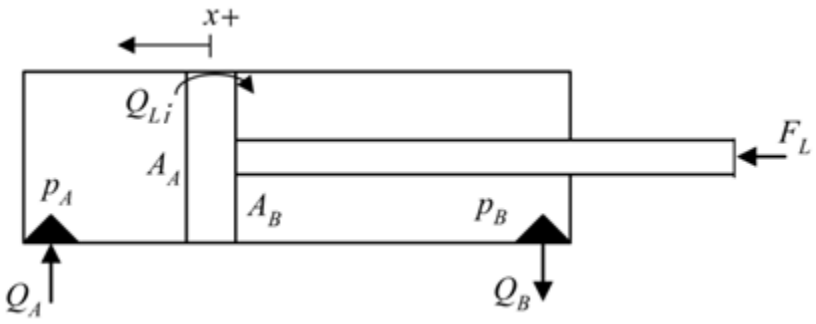

Figure 20: Illustration of Actuator Pressure Build-up.

It is noted that the zero-position is assumed to be at mid-stroke, and the actuator displacement and velocity are positive during compression as shown in Figure 20.

Hydraulic capacitance is calculated via Eq. (14)

$$C_{HA} = \frac{1}{K}\left[\left(\frac{H}{2} - x\right)A_A + V_{dead} + V_{LA}\right]. \tag{14}$$

where C_{HA} is control volume A hydraulic capacitance, K is the fluid bulk modulus, H is the total actuator stroke, x is the actuator position, V_{dead} is the dead volume inside the actuator, and V_{LA} is the transmission line A volume.

Similarly, the pressure in the rod chamber is determined via Eq. (15) and the corresponding hydraulic capacitance is given by Eq. (16).

$$p_B = \frac{1}{C_{HB}}\int\left(-Q_B - A_B\dot{x} + Q_{Li} - Q_r\right)dt. \tag{15}$$

where p_B is the rod (B) side pressure, Q_B is the net flow entering the rod chamber, and A_B is the rod side area.

$$C_{HB} = \frac{1}{K}\left\{\left(\frac{H}{2} + x\right)A_B + V_{dead} + V_{LB}\right\}. \tag{16}$$

where C_{HB} is control volume B hydraulic capacitance and V_{LB} is the transmission line B volume.

The actuator motion equation is given by

$$m_{eq}\ddot{x} = -A_A p_A + \alpha A_A p_B - F_R(\dot{x}) + F_L. \tag{17}$$

where m_{eq} is the equivalent mass coupled to the steering actuator, α is the single-rod actuator area ratio, F_R is the actuator friction force, and F_L is the actuator load force.

4.1.3 Actuator Friction Model

The sliding friction behavior between the actuator's rod and cylinder housing is modeled based on the Stribeck curve regime, which accounts for static friction, Coulomb friction, and viscous friction effects given by Eq. (18).

$$F_R(\dot{x}) = d_v\dot{x} + sign(\dot{x})\left(F_C + F_H e^{\frac{-|\dot{x}|}{\tau_H}}\right). \tag{18}$$

where F_R is the resultant friction force, d_v is the viscous damping coefficient, F_C is the Coulomb friction force, F_H is the static friction force, and τ_H is the static friction force time constant.

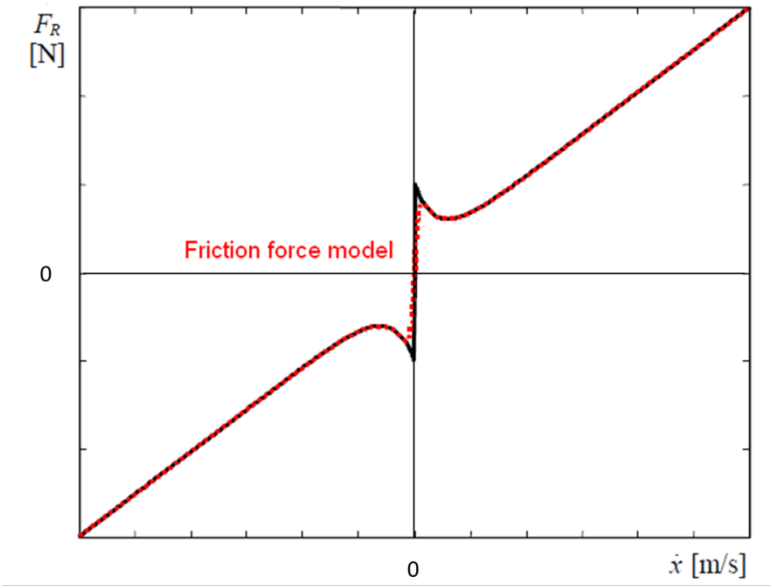

Figure 21: Characteristic Stribeck Friction Curve.

4.1.4 Transmission Line Losses

Transmission line losses are derived from the Navier-Stokes equations by balancing the pressure forces against the viscous forces. Given that the lines configuration (length and diameter) and fluid viscosity are virtually constant, the

pressure drop in the transmission lines, Δp_L, is determined by multiplying the effective flow rate by a constant gain given by Eq. (19).

$$\Delta p_L = \frac{8\mu l_L v}{R_L^{\,2}} = \left[\frac{8\mu l_L}{A_L . R_L^{\,2}}\right] Q_e. \tag{19}$$

where μ is the fluid dynamic viscosity, v is the fluid kinematic viscosity, l_L is the transmission line length, R_L is the transmission line radius, and A_L is the transmission line area.

4.1.5 Low Pressure System

The low pressure system consists of a fixed positive displacement charge pump of the gear type, a pressure relief valve, and two pilot-operated check valves (POCV) that are shown in Figure 22.

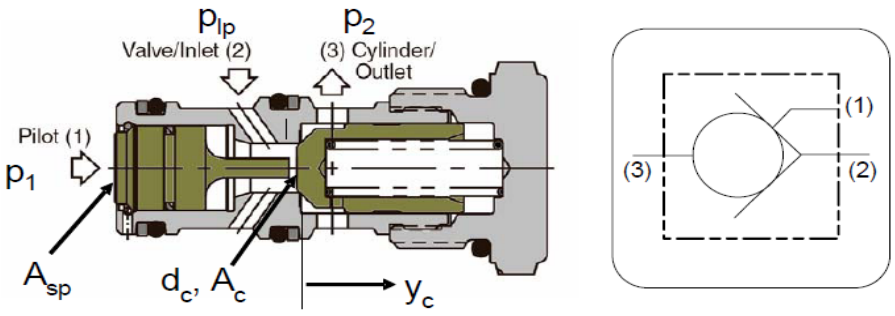

Figure 22: Pilot-Operated Check Valve.

The POCV is modeled using a force balance on the pilot spool, which determines both its displacement, y_c, as well as the mode of operation i.e. normal flow or reverse flow.

Normal Flow Direction:

$$y_c = \frac{1}{k_0}\left[A_c(p_{LP} - p_2) - F_{k0}\right]. \tag{20}$$

Reverse Flow Direction:

$$y_c = \frac{1}{k_0}\left[A_{sp}(p_1 - p_{LP}) + A_c(p_{LP} - p_2) - F_{k0} \right]. \tag{21}$$

The resulting POCV flow is given by Eq. (22).

$$Q_c = \alpha_D \sqrt{\pi A_c}\, 2 y_c sign(\Delta p) \sqrt{\frac{2}{\rho}|\Delta p|}. \tag{22}$$

where

$$\Delta p = p_{1/2} - p_{LP}. \tag{23}$$

where A_c is the cone orifice area, p_{LP} is the pressurized low pressure, p_1 is the pilot pressure, p_2 is the cylinder / outlet pressure, F_{K0} is the spring pre-load force, k_0 is the spring rate, A_{sp} is the spool area, and α_D is the discharge coefficient.

4.1.6 Pump Control System

The dynamics of the pump control system responsible for adjusting the swash plate angle are dominated by the proportional control valve dynamics, which are modeled as a linear second order transfer function from the commanded input voltage signal, u_{SV}, to the output spool position, y_{SV}, per Eq. (24).

$$\frac{Y_{SV}(s)}{U_{SV}(s)} = \frac{\omega_{SV}^2}{s^2 + 2\zeta_{SV}\omega_{SV}s + \omega_{SV}^2}. \tag{24}$$

where ω_{SV} is the proportional valve natural frequency and ζ_{SV} is its damping ratio.

4.2 Vehicle Dynamics Model

Making changes to the steering system of any moving vehicle requires a deep understanding of the vehicle dynamics aspect. The mechanics module primarily consists of a multi-DOF vehicle dynamics model based on Lagrange's mechanics.

The Lagrangian approach is adopted due to the complexity of forces and constraints associated with articulated multi-body vehicles, where the Newtonian approach is strenuous to apply given the vectorial nature and continuous variation of the forces and accelerations at hand.

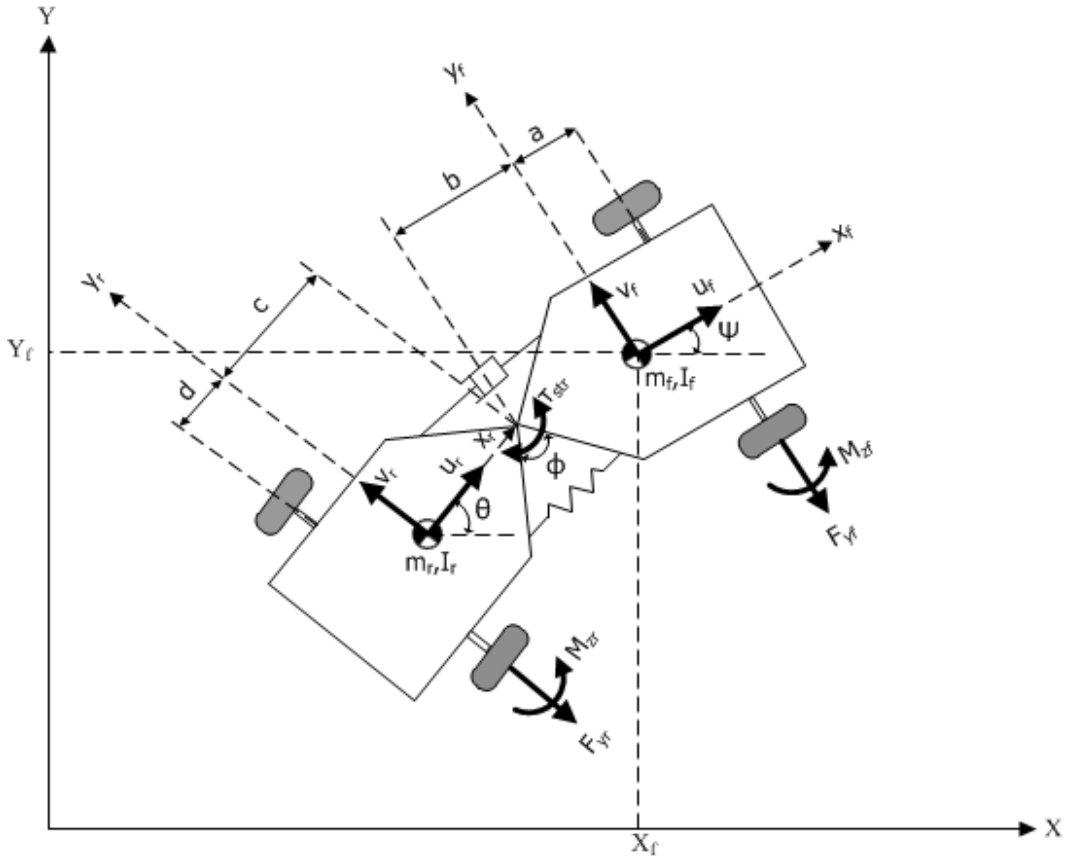

Figure 23: Articulated Vehicle Dynamics.

4.2.1 Lagrangian Mechanics

The standard form of the Lagrange equation is:

$$\frac{d}{dt}\left(\frac{\partial L}{\partial \dot{q}_i}\right)-\frac{\partial L}{\partial q_i}+\frac{\partial D}{\partial \dot{q}_i}=Q_i. \tag{25}$$

$$L=T-U. \tag{26}$$

where L is the Lagrangian function (defined as kinetic energy, T, minus potential energy, U), q is the set of generalized coordinates, D is the dissipative function, and Q_i is the set of generalized forces and moments. The kinetic energy includes the translational and rotational motions of the two constrained frames (front and rear) given by Eq. (27).

$$T = \frac{1}{2} m_f (\dot{X}_f^2 + \dot{Y}_f^2) + \frac{1}{2} I_f \dot{\psi}^2 + \frac{1}{2} m_r [(\dot{X}_f + b \sin\psi\dot{\psi} + c \sin\theta\dot{\theta})^2 \ldots + (\dot{Y}_f - b \cos\psi\dot{\psi} - c \cos\theta\dot{\theta})]^2 + \frac{1}{2} I_r \dot{\theta}^2. \tag{27}$$

When no steering input is present, that is, no flow to/from the actuator exists and ignoring leakage across the actuator sides, the hydraulic fluid inside the steering actuator creates the effect of a very stiff torsional spring at the articulation joint, whose stiffness, K_{aj}, is approximated via Eq. (28), which originates from the previously derived pressure build-up equation.

$$K_{aj} = \frac{K}{V_t} A_A^2 \left(1 + \alpha^2\right) \gamma r_j. \tag{28}$$

where V_t is the total volume of fluid under compression including the actuator chambers and transmission lines, γ is a conversion factor between the steering actuator linear motion and the vehicle rotational motion, and r_j is the normal distance between the articulation joint and the steering actuator force line of action. As for damping, the articulation joint friction along with the tires lateral damping play the role of a torsional damper present at the joint. As a result, the dissipative function and the potential energy can be expressed as functions of

the equivalent torsional spring and damping constants, and the articulation angle / rate given by Eq. (29) and Eq. (30).

$$U = \frac{1}{2} K_{aj} (\psi - \theta)^2. \tag{29}$$

$$D = \frac{1}{2} C_{aj} (\dot{\psi} - \dot{\theta})^2. \tag{30}$$

Generalized Coordinates

At a first glance, one logical choice for the set of generalized coordinates, q, is the global X and Y coordinates, along with ψ and θ, which are the angles that the front and rear frames make relative to the global X abscissa, respectively. Nonetheless, in order to allow for performing dynamic maneuvers with large deviations from the global axes such as steady-state cornering, a coordinate transformation to the local front frame longitudinal and lateral velocities, u_f and v_f respectively, is necessary per Eq. (31) and Eq. (32).

$$u_f = \dot{X}_f \cos\psi + \dot{Y}_f \sin\psi. \tag{31}$$

$$v_f = -\dot{X}_f \sin\psi + \dot{Y}_f \cos\psi. \tag{32}$$

The above coordinate transformation also results in reducing the order of the system. Another substitution that simplifies the system of equations and allows for explicitly stating the articulation angle, ϕ, a desired state variable from a controller design perspective, could be attained by applying Eq. (33).

$$\phi = \psi - \theta. \tag{33}$$

Consequently, the following set of state variables is selected:

$$\mathbf{q}(t) = \left(u_f, v_f, \dot{\psi}, \dot{\phi}\right)^T. \tag{34}$$

where $\dot{\psi}$ is the front yaw angle rate, and $\dot{\phi}$ is the articulation angle rate.

The partial derivatives of the kinetic energy with respect to the global position coordinates are now expressed in terms of the local velocities via the chain rule.

$$\frac{\partial T}{\partial \dot{X}_f} = \frac{\partial T}{\partial u_f} \cdot \cos\psi - \frac{\partial T}{\partial v_f} \cdot \sin\psi. \tag{35}$$

$$\frac{\partial T}{\partial \dot{Y}_f} = \frac{\partial T}{\partial u_f} \sin\psi + \frac{\partial T}{\partial v_f} \cdot \cos\psi. \tag{36}$$

Applying the Lagrangian equation and cancelling the zero terms, the equations of motion for the X_f and Y_f coordinates simplify to Eq. (37) and Eq. (38) respectively.

$$\frac{d}{dt}\left(\frac{\partial T}{\partial u_f}\cos\psi - \frac{\partial T}{\partial v_f}\sin\psi\right) = Q_{X_f}. \tag{37}$$

$$\frac{d}{dt}\left(\frac{\partial T}{\partial u_f}\sin\psi + \frac{\partial T}{\partial v_f}\cos\psi\right) = Q_{Y_f}. \tag{38}$$

The sine and cosine functions can be eliminated from the above equations by resorting to the following mathematical manipulation. First, expand Eq. (37) and multiply it by sin(ψ), second expand Eq. (38) and multiply it by cos(ψ), then subtract the former from the latter to obtain Eq. (39) for state variable, v_f.

$$\frac{d}{dt}\frac{\partial T}{\partial v_f} + \frac{\partial T}{\partial u_f}\dot{\psi} = Q_{v_f}. \tag{39}$$

Similarly, by expanding Eq. (37) and multiplying it by cos(ψ), expanding Eq. (38) and multiplying it by sin(ψ), then *adding* the two together yields Eq. (40) for state variable, u_f.

$$\frac{d}{dt}\frac{\partial T}{\partial u_f} - \frac{\partial T}{\partial v_f}\dot{\psi} = Q_{u_f}. \tag{40}$$

At this point, the kinetic energy expression can be formulated in terms of the front frame local velocities. The following transformations are applied to the rear frame local velocities.

$$u_r = \left(u_f \cos\phi - v_f \sin\phi\right) + b\sin\phi\dot{\psi}. \tag{41}$$

$$v_r = \left(u_f \sin\phi + v_f \cos\phi\right) - (c + b\cos\phi)\dot{\psi} + c\dot{\phi}. \tag{42}$$

Assuming small angle approximation for the articulation angle, ϕ, is rational especially when the vehicle is travelling at higher speeds near the straight ahead direction. It also serves the purpose of linearizing the equations, which is desired for later analysis and control of the system. Hence, Eq. (41) and Eq. (42) are written as Eq. (43) and Eq. (44) respectively.

$$u_r = u_f + v_f\phi. \tag{43}$$

$$v_r = -u_f\phi + v_f - \left(b + c\right)\dot{\psi} + c\dot{\phi}. \tag{44}$$

At last, the kinetic energy term can now be expressed in terms of the new set of state variables, u_f, v_f, ψ, and ϕ as shown in Eq. (45).

$$T = \frac{1}{2}m_f\left(u_f{}^2 + v_f{}^2\right) + \frac{1}{2}I_f\dot{\psi}^2 + \frac{1}{2}m_r[u_f{}^2 + v_f{}^2\phi^2 + 2u_f v_f\phi + u_f^2\phi^2 \ldots$$
$$+ v_f^2 + \left(b+c\right)^2\dot{\psi}^2 + c^2\dot{\phi}^2 - 2u_f v_f\phi + 2u_f\phi\left(b+c\right)\dot{\psi} - 2u_f c\phi\dot{\phi} \ldots \quad (45)$$
$$- 2v_f\left(b+c\right)\dot{\psi} - 2c\left(b+c\right)\dot{\phi}\dot{\psi} + 2v_f c\dot{\phi}] + \frac{1}{2}I_r\dot{\psi}^2 - I_r\dot{\psi}\dot{\phi} + \frac{1}{2}I_r\dot{\phi}^2.$$

4.2.2 Generalized Forces

From this point forward, the bicycle model is assumed and utilized for dynamic analysis of the vehicle. This model assumes that the lateral forces are the same at the left and right wheels and roll motion is negligible, which permits combining both lateral forces into one equivalent force acting at the same point, similar to the bicycle arrangement shown in Figure 24.

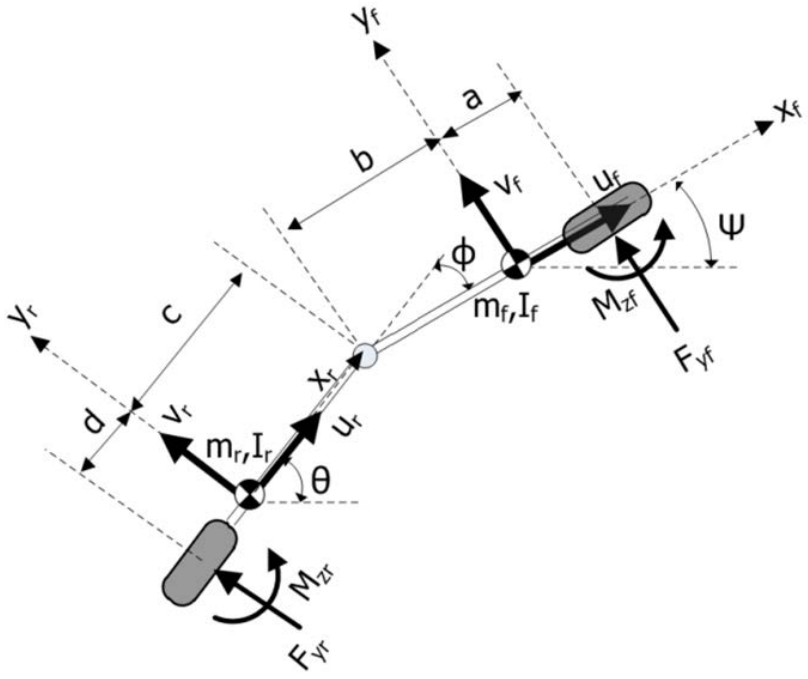

Figure 24: Bicycle Model of an Articulated Frame Steering Vehicle.

Using the virtual work principle, the right hand sides of the Lagrangian equations are resolved. Considering the external forces in Figure 24, the virtual work is given by Eq. (46).

$$\begin{aligned}\delta W = {} & F_{yf}\delta\left(y_f + a\sin\psi\right) + F_{yr}\delta\left[y_f - b\sin\psi - \left(c+d\right)\sin\theta\right]... \\ & + M_{zf}\delta\psi + M_{zr}\delta\theta.\end{aligned} \tag{46}$$

Substituting Eq. (33) into Eq. (46) and assuming small angle approximation, the virtual work can be expressed in terms of the selected state variables:

$$\begin{aligned}\delta W = {} & \delta_{yf}\left(F_{yf} + F_{yr}\right) + \delta\psi\left[aF_{yf} - \left(b+c+d\right)F_{yr} + M_{zf} + M_{zr}\right]... \\ & + \delta\phi\left[\left(c+d\right)F_{yr} - M_{zr}\right].\end{aligned} \tag{47}$$

Hence, the generalized forces for each of the state variables are given by Eq. (48), Eq. (49), and Eq. (50).

$$Q_{vf} = Q_{yf} = F_{yf} + F_{yr}. \tag{48}$$

$$Q_{\dot{\psi}} = aF_{yf} - \left(b+c+d\right)F_{yr} + M_{zf} + M_{zr}. \tag{49}$$

$$Q_{\dot{\phi}} = \left(c+d\right)F_{yr} - M_{zr}. \tag{50}$$

4.2.3 Tire Slip Angles, Lateral Forces, and Aligning Moments

For computing the forces at the tire-ground interface, it is necessary to determine the resulting tire slip angles first. The slip angle, α_s, is defined as the angle between the actual traveling direction of the tire and the direction of the tire centerline given by Eq. (51).

$$\alpha_s = \tan^{-1}\left(\frac{\mathrm{v}_{lateral}}{v_{longitudinal}}\right). \tag{51}$$

Using small angle approximation, the average slip angles of the front and rear tires are given by Eq. (52) and Eq. (53), respectively.

$$\alpha_{sf} = \left(\frac{v_f + a\dot{\psi}}{u_f} \right). \tag{52}$$

$$\alpha_{sr} = \left(\frac{v_f - (b+c+d)\dot{\psi} + (c+d)\dot{\phi}}{u_f} + \phi \right). \tag{53}$$

Numerous tire models have been proposed, and this area has been at the heart of several research projects and it will continue to be until a full understanding of the interaction between the tires and the ground is gained. Models such as the Metz, Fiala, Mobility Number, and Pacejka “Magic Formula” are all good candidates based on the conditions at hand relative to surface form, slip conditions, tire type, etc. However, the analysis in this work uses the linear tire model given its simplicity, linearity property, and validity for the maneuvers under consideration relative to vehicle speed, articulation angle, and tire slip angles. The linear tire model is given by Eq. (54) and Eq. (55).

$$F_{yf} = -N_f C_{\alpha f} \alpha_{sf}. \tag{54}$$

$$F_{yr} = -N_r C_{\alpha r} \alpha_{sr}. \tag{55}$$

where F_{yf} and F_{yr} are the front and rear tire lateral forces respectively, N_f and N_r are the front and rear axle vertical loads respectively, and $C_{\alpha f}$ and $C_{\alpha r}$ are the front and rear tires lateral force coefficients respectively.

Tire lateral forces tend to act behind the center of the tire contact patch, resulting in a self-aligning moment that acts as a balancing torque attempting to return the

tire to a zero slip condition. The moment arm that the lateral force is shifted by is known as the pneumatic trail.

$$M_{zf} = N_f C_{M\alpha f} \alpha_f = N_f C_{M\alpha f} \left(\frac{v_f + a\dot{\psi}}{u_f} \right). \tag{56}$$

$$M_{zr} = N_r C_{M\alpha r} \alpha_r = N_r C_{M\alpha r} \left(\frac{v_f - (b+c+d)\dot{\psi} + (c+d)\dot{\phi}}{u_f} + \phi \right). \tag{57}$$

where M_{zf} and M_{zr} are the front and rear tire aligning moments, respectively, and $C_{M\alpha f}$ and $C_{M\alpha r}$ are the front and rear tire aligning moment coefficients, respectively.

4.2.4 Axle Normal Loads

For accurate calculation of the tire lateral forces, the normal (vertical) tire loads must be first determined. Static equilibrium analysis of forces and moments leads to the expression of the front and rear axle normal forces in terms of the vehicle parameters defined in Figure 24.

$$N_f = \frac{m_r g d + m_f g (b+c+d)}{a+b+c+d}. \tag{58}$$

$$N_r = \frac{m_f g a + m_r g (a+b+c)}{a+b+c+d}. \tag{59}$$

4.2.5 Equations of Motion

Following the exercise of expressing the individual terms of the Lagrangian equation in terms of the state variables, this section highlights the steps for retrieving the equations of motion for each of the state variables.

State variable, v_f:

The reduced Lagrangian equation for coordinate, v_f, is given by Eq. (39). Taking time derivatives and partial derivatives on the left hand side leads to Eq. (60).

$$\begin{aligned}\frac{d}{dt}\frac{\partial T}{\partial v_f}+\frac{\partial T}{\partial u_f}\dot{\psi} &= \left(m_f+m_r\right)\dot{v}_f+\left(m_f+m_r\right)\dot{\psi}u_f-bm_r\ddot{\psi}-cm_r\ddot{\psi}+cm_r\ddot{\phi}\ldots \\ &+\left(m_f+m_r\right)\psi v_f\dot{\psi}+\left(m_f+m_r\right)\psi^2u_f\dot{\psi}-2b\psi\dot{\psi}^2-2c\psi\dot{\psi}\left(\dot{\psi}-\dot{\phi}\right).\end{aligned} \tag{60}$$

Ignoring nonlinear and second order terms in Eq. (60) and equating it to the generalized force, Q_{vf}, in Eq. (48) leads to Eq. (61), which is the equation of motion for state variable, v_f.

$$\begin{aligned}&\left(m_f+m_r\right)\dot{v}_f+\left(-bm_r-cm_r\right)\ddot{\psi}+\left(m_f+m_r\right)u_f\dot{\psi}+\left(cm_r\right)\ddot{\phi}=\left(\frac{-N_fC_{\alpha f}-N_rC_{\alpha r}}{u_f}\right)v_f\ldots \\ &-\left(\frac{N_rC_{\alpha r}\left(c+d\right)}{u_f}\right)\dot{\phi}-\left(N_rC_{\alpha r}\right)\phi+\left(\frac{-aN_fC_{\alpha f}-\left(b+c+d\right)N_rC_{\alpha r}}{u_f}-(m_f+m_r)u_f\right)\dot{\psi}.\end{aligned} \tag{61}$$

State variable, $\dot{\psi}$:

Taking the partial derivative of kinetic energy with respect to ψ results in Eq. (62).

$$\frac{\partial T}{\partial \psi}=\frac{\partial T}{\partial u_f}\cdot\frac{\partial u_f}{\partial \psi}+\frac{\partial T}{\partial v_f}\cdot\frac{\partial v_f}{\partial \psi}=\frac{\partial T}{\partial u_f}v_f-\frac{\partial T}{\partial v_f}u_f. \tag{62}$$

Hence, the reduced Lagrangian equation for variable, $\dot{\psi}$, is given by Eq. (63).

$$\frac{d}{dt}\frac{\partial T}{\partial \dot{\psi}}-v_f\frac{\partial T}{\partial u_f}+u_f\frac{\partial T}{\partial v_f}=Q_{\dot{\psi}}. \tag{63}$$

Applying the required substitutions, time derivatives, and partial derivatives, the equation of motion for variable $\dot{\psi}$ is obtained in Eq. (64).

$$\dot{v}_f\left[-m_r\left(b+c\right)\right]+\ddot{\psi}\left[I_f+I_r+m_r\left(b+c\right)^2\right]+\ddot{\phi}\left(-m_r bc-m_r c^2-I_r\right)-\dot{\psi}\left[m_r\left(b+c\right)u_f\right]=$$
$$v_f\left[\frac{-aN_fC_{\alpha f}+(b+c+d)N_rC_{\alpha r}+N_fC_{M\alpha f}+N_rC_{M\alpha r}}{u_f}\right]\ldots$$
$$+\dot{\psi}\left[\frac{\left(-a^2N_fC_{\alpha f}-(b+c+d)^2N_rC_{\alpha r}+aN_fC_{M\alpha f}-(b+c+d)N_rC_{M\alpha r}\right)}{u_f}+m_r(b+c)u_f\right]\ldots \quad (64)$$
$$+\dot{\phi}\left[\frac{(b+c+d)(c+d)N_rC_{\alpha r}+(c+d)N_rC_{M\alpha r}}{u_f}\right]+\phi\left[(b+c+d)N_rC_{\alpha r}+N_rC_{M\alpha r}\right].$$

State variable, $\dot{\phi}$:

The Lagrangian equation for state variable, $\dot{\phi}$, is shown in Eq. (65).

$$\frac{d}{dt}\frac{\partial T}{\partial\dot{\phi}}+\frac{\partial V}{\partial\phi}+\frac{\partial R}{\partial\dot{\phi}}=Q_{\dot{\phi}}. \quad (65)$$

The equation of motion for variable, $\dot{\phi}$, yields

$$\dot{v}_f(m_rc)+\ddot{\psi}\left(-m_rc^2-m_rbc-I_r\right)+\ddot{\phi}\left(m_rc^2+I_r\right) \;=$$
$$v_f\left[\frac{-\left(c+d\right)N_rC_{\alpha r}-N_rC_{M\alpha r}}{u_f}\right]+\dot{\psi}\left[\frac{\left(c+d\right)\left(b+c+d\right)N_rC_{\alpha r}+N_rC_{M\alpha r}\left(b+c+d\right)}{u_f}\right]\ldots \quad (66)$$
$$+\dot{\phi}\left[\frac{-\left(c+d\right)^2N_rC_{\alpha r}-N_rC_{Mr}\left(c+d\right)}{u_f}-m_rcu_f\dot{\phi}-C_a\right]+\phi\left[-N_rC_{\alpha r}-N_rC_{M\alpha r}\right].$$

4.2.6 System of Linear Equations of Motion

After individually deriving the equations of motion for each state variable, the equations could be assembled together as a system of first order ordinary differential equations, which can be solved using linear algebra principles. And since the end goal behind deriving a linear system of equations is to design control algorithms based on modern linear control theory, the equations are expressed with the derivatives of the state variables on the left hand side, and

the state variables themselves on the right hand side. This format, shown in Eq. (67), is in accordance with state-space formulation.

$$\begin{pmatrix} M_{11} & M_{12} & M_{13} & M_{14} \\ M_{21} & M_{22} & M_{23} & M_{24} \\ M_{31} & M_{32} & M_{33} & M_{34} \\ M_{41} & M_{42} & M_{43} & M_{44} \end{pmatrix} \begin{pmatrix} \dot{v}_f \\ \ddot{\psi} \\ \ddot{\phi} \\ \dot{\phi} \end{pmatrix} = \begin{pmatrix} C_{11} & C_{12} & C_{13} & C_{14} \\ C_{21} & C_{22} & C_{23} & C_{24} \\ C_{31} & C_{32} & C_{33} & C_{34} \\ C_{41} & C_{42} & C_{43} & C_{44} \end{pmatrix} \begin{pmatrix} v_f \\ \dot{\psi} \\ \dot{\phi} \\ \phi \end{pmatrix}. \tag{67}$$

where the elements of matrices M and C are given in Appendix A.

4.2.7 Validation of the Linear Dynamics Model

In deriving the linear dynamics model, multiple assumptions and simplifications are made. Nonlinear and higher order terms involving small quantities are ignored, roll and pitch motions are assumed negligible, lateral and yaw motions are neglected, longitudinal velocity of the front frame is assumed constant, and the tire cornering force is assumed proportional to the lateral slip angle. In order to confirm the validity and accuracy of the linear model, a multi-body nonlinear model is generated in MSC Adams software. Both linear and nonlinear numeric models are based on the parameters of the baseline vehicle, some of which are known and others are estimated.

Table 1: Baseline Vehicle Parameters.

Parameter	**Description**	**Value**	**Unit**
m	Vehicle Mass	4350	kg
m_f	Front Frame Mass	1653	kg
m_r	Rear Frame Mass	2697	kg

Table 1 Continued: Baseline Vehicle Parameters.

I_f	Front Frame Moment of Inertia	1500	kg.m^2
I_r	Rear Frame Moment of Inertia	2500	kg.m^2
wb	Vehicle Wheelbase	2.12	m
a	Distance From Front Frame CG to Front Axle	0	m
b	Distance From Front CG to Articulation Joint	1.06	m
c	Distance From Rear CG to Articulation Joint	1.06	m
d	Distance From Rear Frame CG to Front Axle	0	m
r_j	Normal Distance Between the Articulation Joint and the Steering Actuator Force Line of Action	0.2	m

Writing the system of equations in Eq. (67) in the standard format, $\dot{X} = [M^{-1}C]X$, and analyzing the eigenvalues of the resulting matrix indicates that the system is stable at all practical vehicle speeds given that all system poles are in the left-hand plane. The vehicle becomes unstable at irrationally high speeds exceeding 77 m/s (277 km/h) as shown in Figure 25. However, it is noted that not all vehicle parameters are exactly known, and as such some parameters are estimated or assumed. Previous research (Azad, 2006) showed that vehicle stability is sensitive to the following parameters: vehicle speed, locations of the front and rear frames centers of mass relative to their axles, front and rear frames masses and moments of inertia, surface condition, among others.

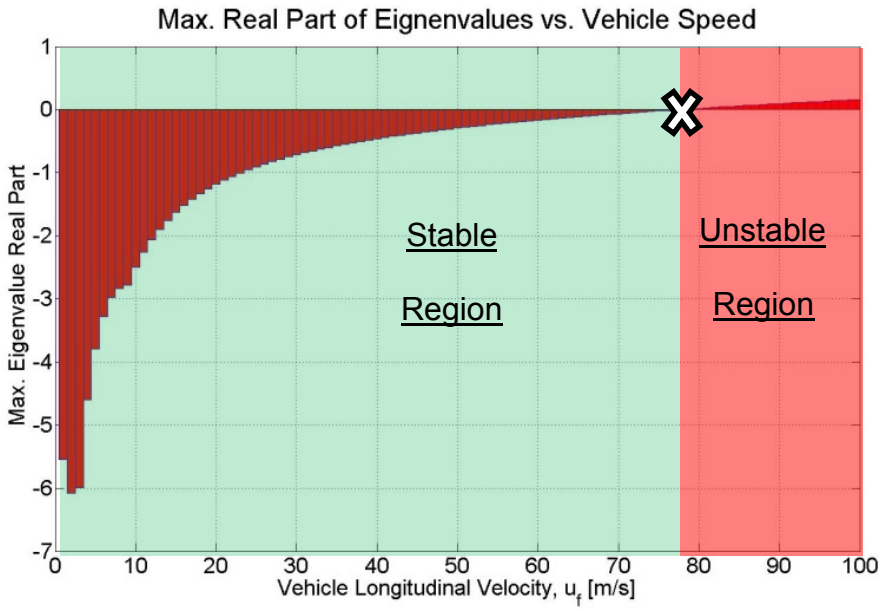

Figure 25: Dynamic System Stability Analysis.

The above results are compared with those obtained by MSC Adams software. The Adams model topology comprises two rigid bodies connected at the articulation (revolute) joint. A torsional spring with equivalent stiffness to the hydraulic fluid compressibility is added at the joint. Due to the combination of air entrapment, leakage, and flexibility of hydraulic hoses, the effective torsional stiffness may be reduced by a factor of up to 100 as found by (Horton & Crolla, 1986). A torsional damper with an equivalent damping coefficient to the articulation joint friction and the tires lateral damping is also added at the joint. It is noted here that this latter parameter is estimated based on literature review (Azad, 2006) due to the lack of specifications on the baseline machine. The rigid body masses and dimensions are set to reflect those of the baseline vehicle. The PAC 2002 Magic-Formula tire model is selected from the tire library, which is suitable for the considered maneuvers involving steady-state cornering and

single-lane change. Figure 26 shows the generated MSC Adams model that is used during the simulation run.

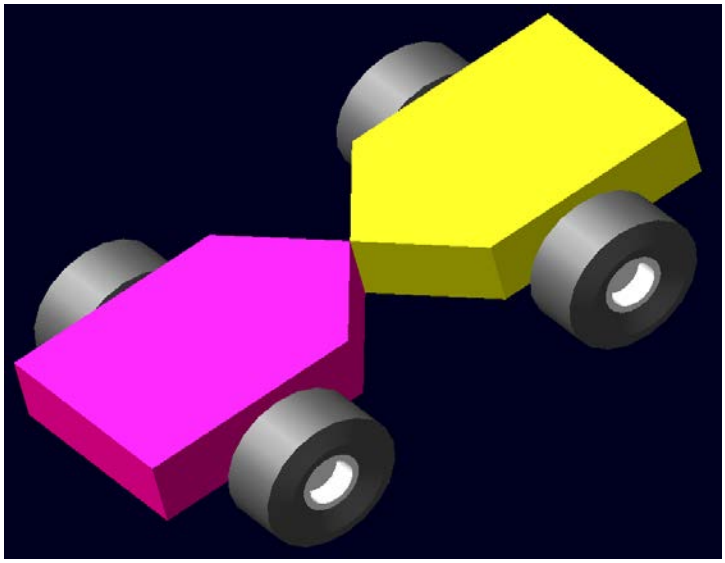

Figure 26: Adams Model of an Articulated Vehicle.

To validate the stability analysis predicted by the linear model, both models (linear and Adams) are setup to run simultaneously and simulate a situation where the vehicle initially starts in a perturbed position away from the origin, which allows for examining whether, and how fast, equilibrium is regained. Figure 27 shows the simulation results of a maneuver with a constant vehicle speed of 20 km/h (5.5 m/s) and an initial perturbation angle of 5 degrees. As seen, both models predict that stability is regained in approximately 0.5s, which confirms the eigenvalue analysis and validates the linear model derivation and linearization assumptions. The difference observed between the two curves is mostly due to the fact that the Adams model includes a highly fidelity tire model, which results in additional stiffness and damping due to the tire dynamics leading to lower vibration magnitude and shorter vibration period (higher frequency).

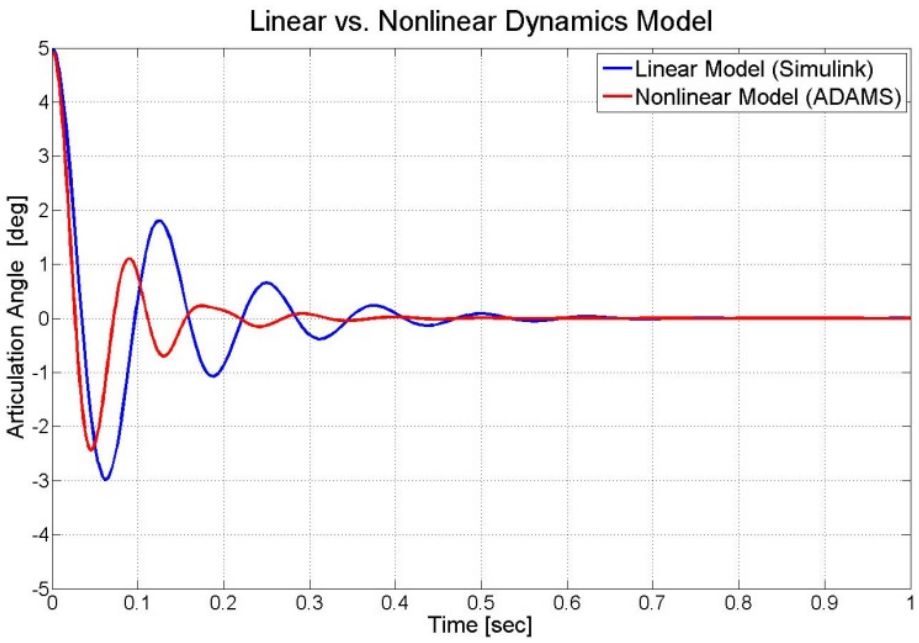

Figure 27: Vehicle Stability Analysis Comparison.

4.3 Linear Hydraulics Model

The hydraulics model derived in section 4.1 includes several nonlinearities such as pump losses (3-dimensional), actuator friction (discontinuity), valve flow gains (quadratic), and multiple saturations. Since the purpose is to derive a linear *system* model, which includes both the hydraulic and the vehicle dynamics, it is necessary to obtain a linear hydraulics model. The latter is ultimately derived based on the governing equations, assumptions, and linearizations in the following sections. Given the POCV four quadrants of operation, two separate linear models are developed. The four quadrants of operation include both pumping/motoring modes and positive/negative pressure differentials across the actuator sides. A rate limited logic switch is implemented to handle the switching between the models based on pressure differential.

Positive Δp:

In this mode the actuator's piston side is at high pressure and no flow is present across its POCV, whereas the rod side is at low pressure and is connected to the low pressure system via its own POCV. Normal and reverse flow is determined as described in section 4.1.5 based on a dynamic force balance on the spool. The flow gain, C_{LP}, is linearized against the POCV pressure differential. The flow rates into chambers A and B are given in Eq. (68) and Eq. (69) respectively.

$$Q_A = Q_1 = \beta Q_e. \tag{68}$$

$$Q_B = Q_2 + Q_{LP2} = Q_2 + C_{LP}\left(p_B - p_{LP}\right). \tag{69}$$

Q_e is the effective pump flow rate given by

$$Q_e = n\ V_d\ \eta_{vol}. \tag{70}$$

where η_{vol} is assumed to be constant for linearization purposes.

Another simplification is to assume that the hydraulic capacitances of both actuator chambers are constant, that is *time-invariant* from a control engineering standpoint, and equal to C_H when the actuator is in the middle position given by Eq. (71).

$$\mathrm{C}_H = \frac{1}{K}\left(A_A \frac{H}{2} + V_{dead} + V_{LA}\right). \tag{71}$$

The pressure build-up equations are then written as:

$$\dot{p}_A = \frac{1}{C_H}\left(\beta Q_e + A_A \dot{x} - K_{Li} p_A + K_{Li} p_B\right). \tag{72}$$

$$\dot{p}_B = \frac{1}{C_H}\left(-\beta Q_e - \alpha A_A \dot{x} + K_{Li} p_A - \left(C_{LP} + K_{Li}\right) p_B + C_{LP} p_{LP}\right). \tag{73}$$

The steering actuator force, F_L, is determined by applying dynamic equilibrium on the actuator rod:

$$F_L = -A_A p_A + \alpha A_A p_B - C_d \dot{x} - m_{eq} \ddot{x}. \tag{74}$$

where C_d is the viscous friction coefficient, and m_{eq} is the equivalent mass coupled to the steering actuator. As a result, pressures A and B can now be expressed in state-space format given by Eq. (75).

$$\begin{pmatrix} \dot{p}_A \\ \dot{p}_B \end{pmatrix} = \begin{pmatrix} -\frac{K_{Li}}{C_H} & \frac{K_{Li}}{C_H} \\ \frac{K_{Li}}{C_H} & -\frac{C_{LP} + K_{Li}}{C_H} \end{pmatrix} \begin{pmatrix} p_A \\ p_B \end{pmatrix} + \begin{pmatrix} \frac{A_A}{C_H} & 0 & \frac{Q_e}{C_H} & 0 \\ \frac{-\alpha A_A}{C_H} & 0 & \frac{-Q_e}{C_H} & \frac{C_{LP}}{C_H} \end{pmatrix} \begin{pmatrix} \dot{x} \\ \ddot{x} \\ \beta \\ p_{LP} \end{pmatrix}. \tag{75}$$

The output equation, which includes the actuator force only, is augmented to incorporate the actuator pressures for later validation purposes against the nonlinear hydraulic model.

$$\begin{pmatrix} F_L \\ p_A \\ p_B \end{pmatrix} = \begin{pmatrix} -A_A & +\alpha A_A \\ 1 & 0 \\ 0 & 1 \end{pmatrix} \begin{pmatrix} p_A \\ p_B \end{pmatrix} - \begin{pmatrix} c_d & m_{eq} & 0 & 0 \\ 0 & 0 & 0 & 0 \\ 0 & 0 & 0 & 0 \end{pmatrix} \begin{pmatrix} \dot{x} \\ \ddot{x} \\ \beta \\ p_{LP} \end{pmatrix}. \tag{76}$$

Negative Δp:

The linear system of the negative pressure differential state is obtained in a similar fashion like the positive pressure differential counterpart, with the main difference being that low pressure is on the piston side, A, which is connected to the low pressure system via its own POCV as observed in Eq. (77).

$$\begin{pmatrix} \dot{p}_A \\ \dot{p}_B \end{pmatrix} = \begin{pmatrix} -\frac{C_{LP}+K_{Li}}{C_H} & \frac{K_{Li}}{C_H} \\ \frac{K_{Li}}{C_H} & -\frac{K_{Li}}{C_H} \end{pmatrix} \begin{pmatrix} P_A \\ P_B \end{pmatrix} + \begin{pmatrix} \frac{A_A}{C_H} & 0 & \frac{Q_e}{C_H} & \frac{C_{LP}}{C_H} \\ \frac{-\alpha A_A}{C_H} & 0 & \frac{-Q_e}{C_H} & 0 \end{pmatrix} \begin{pmatrix} \dot{x} \\ \ddot{x} \\ \beta \\ p_{LP} \end{pmatrix}. \quad (77)$$

The negative Δp output equation is the same as that of the positive Δp system given by Eq. (76).

4.3.1 Validation of the Linear Hydraulic Model

The linear model is validated against the high-fidelity nonlinear model, which in turn has been thoroughly developed and validated throughout multiple research projects involving pump displacement controlled actuation (Rahmfeld, 2002), (Rahmfeld & Ivantysynova, 2004), (Rahmfeld & Ivantysynova, 1998), (Williamson, Zimmerman, & Ivantysynova, 2008), and (Williamson & Ivantysynova, 2010). To eliminate complexity and compounding error, the linear hydraulics model is coupled to a simple 1-DOF mechanics model simulating an articulated frame steering vehicle with a free-to-rotate front frame and a fixed rear frame. The sole purpose of the mechanics model is to relay the resultant actuator velocity and acceleration to the pressure build-up equations and the actuator force (output) equation. A static maneuver consisting of articulating the vehicle from the zero-position to +25° (left turn), then turning back to -25° (right turn) is devised, as shown in Figure 28.

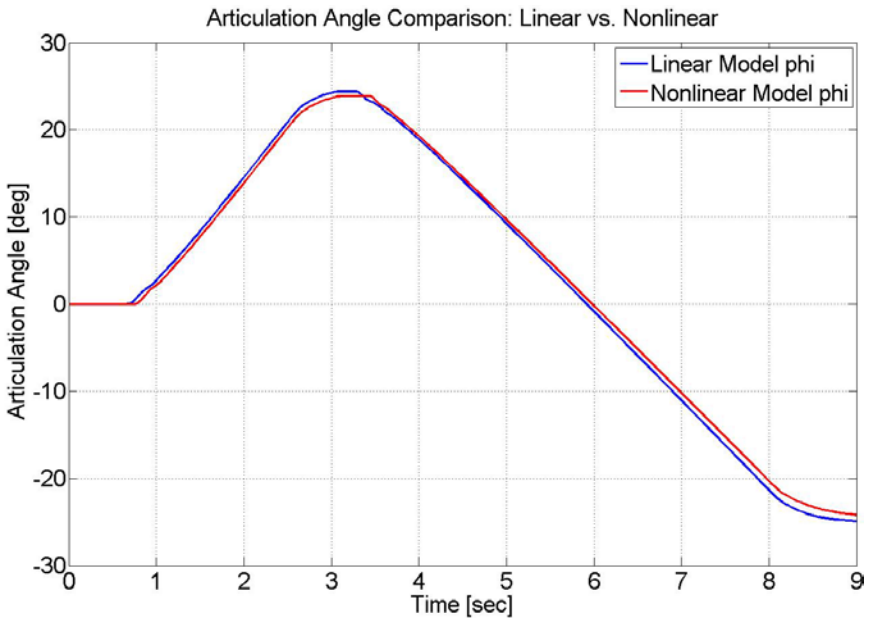

Figure 28: Linear vs. Nonlinear Vehicle Articulation Angles.

Using the sign convention of a left turn as positive, and that the steering actuator is mounted with its piston side (A) towards the rear frame, the following results, which collectively prove the validity of the linear model, are obtained.

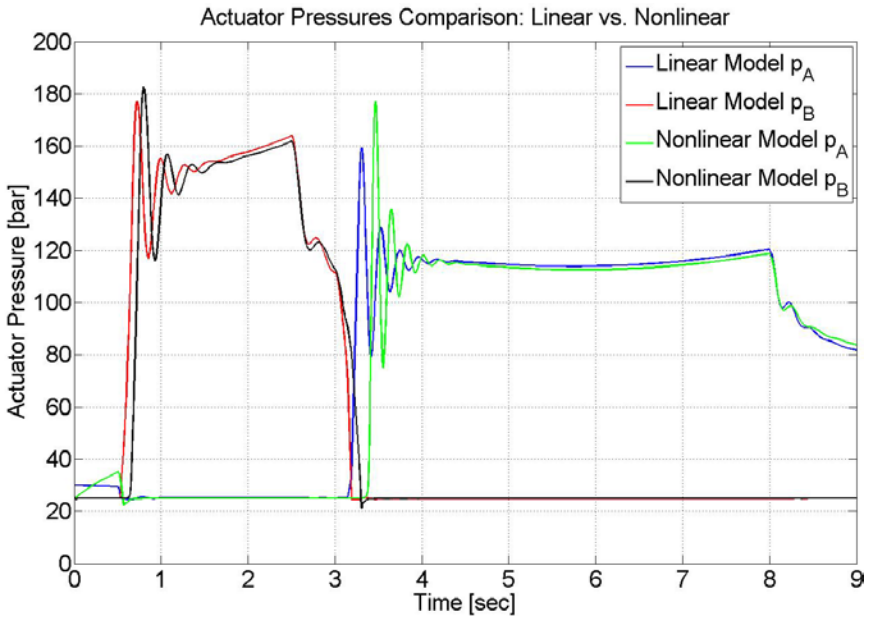

Figure 29: Linear vs. Nonlinear Actuator Pressures.

Figure 29 serves multiple validation purposes for both models. First, the pressure rise in the actuator chambers agrees with the desired articulation direction in the sense that turning left requires high pressure on side B, and vice versa. Second, both low pressure system models kept the low pressure side at the low pressure setting of 25bar. Third, the pressure differential magnitude generated across the actuator sides corresponds to the desired torque required for articulation, given the axle loads and the assumed tire-ground friction coefficient.

4.4 Linear System Model

The purpose behind deriving a linearized *system* model is to design advanced control algorithms based on modern control theory, thus it is essential to formulate the problem in time-based state-space format, preferably as a linear time-invariant (LTI) system.

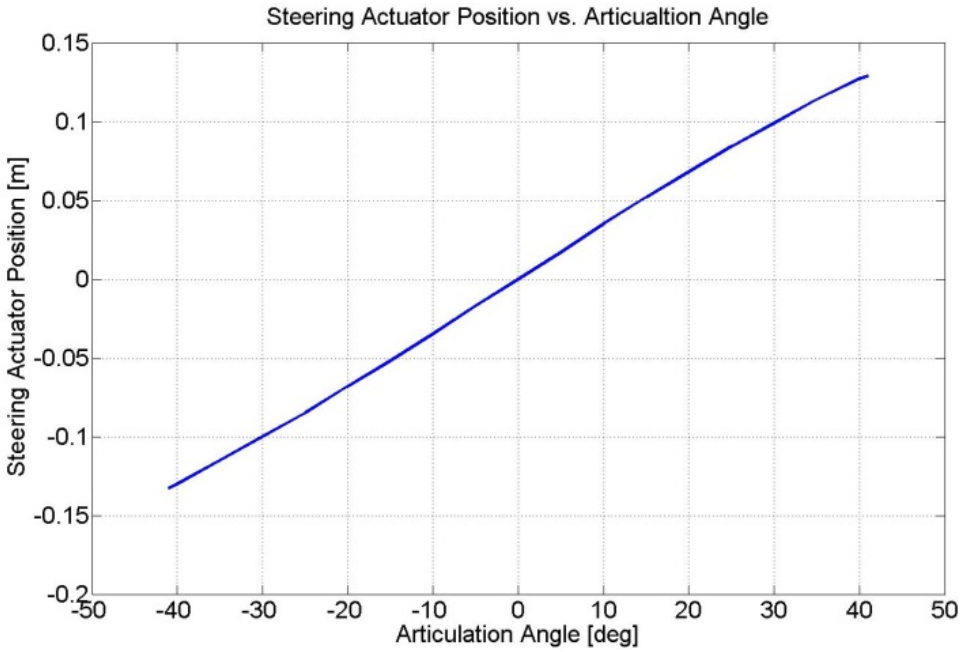

Figure 30: Actuator Displacement vs. Articulation Angle.

The translational motion of the steering actuator exhibits a virtually linear relationship relative to the vehicle steering angle in the entire articulation range of -40° to +40°, as shown in Figure 30, which is another enabler for linearizing the nonlinear plant.

Having separately derived and validated the linear *hydraulics* and *dynamics* models, the linear *system* model is generated by assimilating the two subsystems and coupling them at the steering actuator interface, where hydraulic pressure and flow are converted into mechanical force and motion. Two linear system models are generated for the two separate hydraulic models. The system model has six states corresponding to the four states of the vehicle dynamics model, $v_f, \dot{\psi}, \dot{\phi}, \phi$, and the two states of the hydraulic model, p_A and p_B.

Positive Δp System Matrices

$$\begin{pmatrix} M_{11} & M_{12} & M_{13} & M_{14} & 0 & 0 \\ M_{21} & M_{22} & M_{23} & M_{24} & 0 & 0 \\ M_{31} & M_{32} & M_{33} & M_{34} & 0 & 0 \\ M_{41} & M_{42} & M_{43} & M_{44} & 0 & 0 \\ 0 & 0 & 0 & 0 & 1 & 0 \\ 0 & 0 & 0 & 0 & 0 & 1 \end{pmatrix} \begin{pmatrix} \dot{v}_f \\ \ddot{\psi} \\ \ddot{\phi} \\ \dot{\phi} \\ \dot{p}_A \\ \dot{p}_B \end{pmatrix} =$$

$$\begin{pmatrix} C_{11} & C_{12} & C_{13} & C_{14} & 0 & 0 \\ C_{21} & C_{22} & C_{23} & C_{24} & 0 & 0 \\ C_{31} & C_{32} & C_{33} & S_{34} & -A_A r_j & \alpha A_A r_j \\ C_{41} & C_{42} & C_{43} & C_{44} & 0 & 0 \\ 0 & 0 & \frac{\gamma A_A}{C_H} & 0 & -\frac{K_{L_i}}{C_H} & \frac{K_{L_i}}{C_H} \\ 0 & 0 & -\frac{\gamma \alpha A_A}{C_H} & 0 & \frac{K_{L_i}}{C_H} & -\frac{C_{LP}+K_{L_i}}{C_H} \end{pmatrix} \begin{pmatrix} v_f \\ \dot{\psi} \\ \dot{\phi} \\ \phi \\ p_A \\ p_B \end{pmatrix} + \begin{pmatrix} 0 \\ 0 \\ 0 \\ 0 \\ \frac{Q_e}{C_H} \\ -\frac{Q_e}{C_H} \end{pmatrix} \beta + \begin{pmatrix} 0 \\ 0 \\ 0 \\ 0 \\ 0 \\ \frac{C_{LP}}{C_H} \end{pmatrix} p_{LP}. \quad (78)$$

where elements M_{ij} and C_{ij} are given by Eq. (67), and element S_{34} is the same as element C_{34} but without including the equivalent torsional stiffness, K_{aj}, to model the system with a steering input.

$$S_{34} = -N_r C_{\alpha r} - N_r C_{M\alpha r}. \tag{79}$$

Careful examination of Eq. (78) reveals how the steering force, via pressures p_A and p_B, gets translated from the hydraulics subsystem to the dynamics subsystem at the state variable corresponding to the articulation rate (row 3, columns 5 and 6). This is coherent with the fact that the applied steering torque induces rotational motion at the articulation joint. On the other hand, the dynamic subsystem motion (actuator velocity) is fed back to the hydraulic subsystem again via the state variable corresponding to articulation rate (column 3, rows 5 and 6) to influence the pressure build-up equation.

Negative Δp System Matrices

$$\begin{pmatrix} M_{11} & M_{12} & M_{13} & M_{14} & 0 & 0 \\ M_{21} & M_{22} & M_{23} & M_{24} & 0 & 0 \\ M_{31} & M_{32} & M_{33} & M_{34} & 0 & 0 \\ M_{41} & M_{42} & M_{43} & M_{44} & 0 & 0 \\ 0 & 0 & 0 & 0 & 1 & 0 \\ 0 & 0 & 0 & 0 & 0 & 1 \end{pmatrix} \begin{pmatrix} \dot{v}_f \\ \ddot{\psi} \\ \ddot{\phi} \\ \dot{\phi} \\ \dot{p}_A \\ \dot{p}_B \end{pmatrix} =$$

$$\begin{pmatrix} C_{11} & C_{12} & C_{13} & C_{14} & 0 & 0 \\ C_{21} & C_{22} & C_{23} & C_{24} & 0 & 0 \\ C_{31} & C_{32} & C_{33} & S_{34} & -A_A r_j & \alpha A_A r_j \\ C_{41} & C_{42} & C_{43} & C_{44} & 0 & 0 \\ 0 & 0 & \dfrac{\gamma A_A}{C_H} & 0 & -\dfrac{C_{LP}+K_{L_i}}{C_H} & \dfrac{K_{L_i}}{C_H} \\ 0 & 0 & -\dfrac{\gamma\alpha A_A}{C_H} & 0 & \dfrac{K_{L_i}}{C_H} & -\dfrac{K_{L_i}}{C_H} \end{pmatrix} \begin{pmatrix} v_f \\ \psi \\ \dot{\phi} \\ \phi \\ p_A \\ p_B \end{pmatrix} + \begin{pmatrix} 0 \\ 0 \\ 0 \\ 0 \\ \dfrac{Q_e}{C_H} \\ -\dfrac{Q_e}{C_H} \end{pmatrix} \beta + \begin{pmatrix} 0 \\ 0 \\ 0 \\ 0 \\ \dfrac{C_{LP}}{C_H} \\ 0 \end{pmatrix} p_{LP}. \tag{80}$$

For completeness, the system matrices corresponding to negative pressure differential are provided in Eq. (80).

4.4.1 Validation of the Linear System Model

As a final validation step, a high-fidelity nonlinear system model is generated by coupling the nonlinear hydraulics model with the nonlinear dynamics model as shown in Figure 31. To allow the two subsystems to interact, the Adams plant model is exported to input an actuator steering force and to output the articulation angle and rate. The coupled model is compared against the linear system by running a co-simulation in MATLAB Simulink® environment.

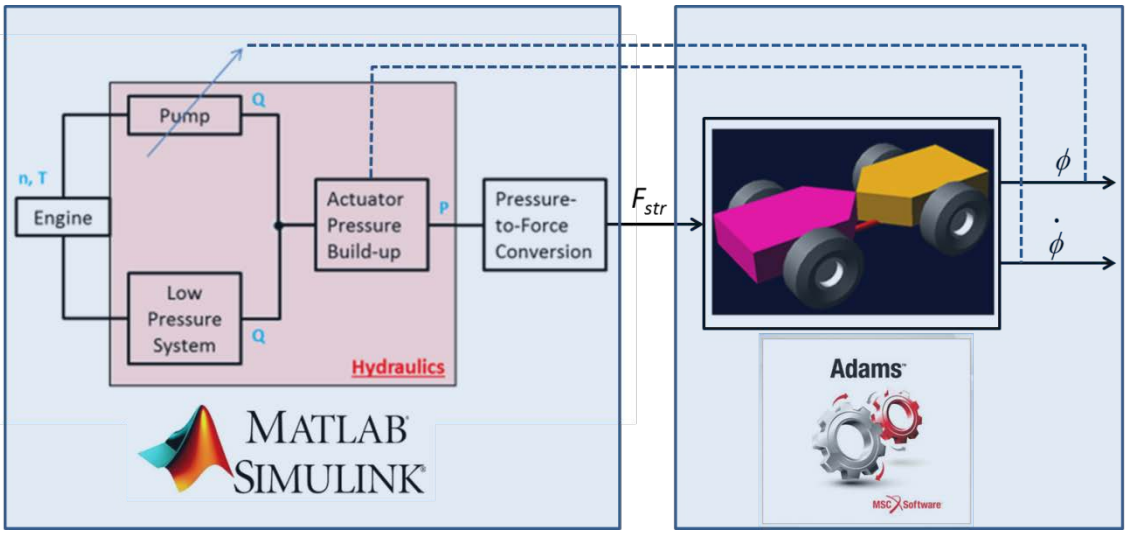

Figure 31: High Fidelity Nonlinear System Model with a Coupled MSC Adams Model in MATLAB Simulink® Environment.

In order for the Adams model to accept steering force as an input from the hydraulics model, the actuator is modeled as a linear spring and damper element joining the two frames as shown in Figure 32.

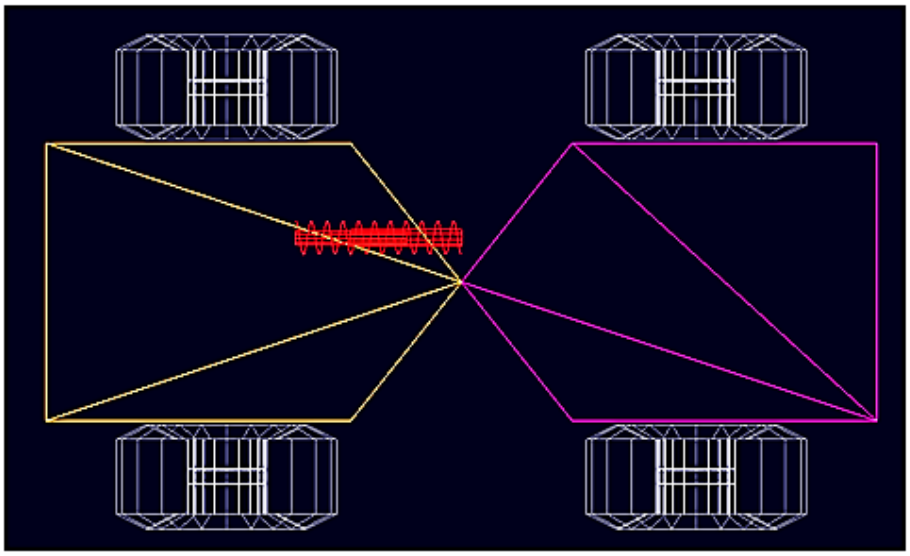

Figure 32: Adams Model Linear Actuator Setup.

On the other hand, the linear system model is setup to input pump flow for a given pump displacement, β, and outputs the state vector including the steering angle and rate as shown in Figure 33.

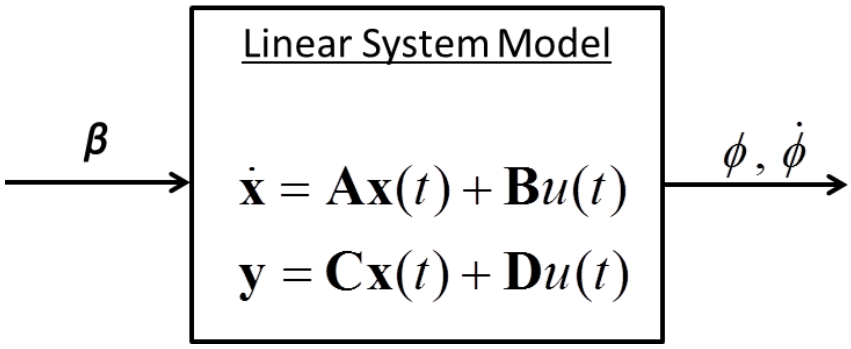

Figure 33: Linear System State-Space Model.

For validation purposes, the following maneuver is executed on both system models using a simple proportional controller for closed-loop position control. The vehicle speed is set to 5.5 m/s (20 km/h) and the articulation angle is ramped from 0° to +9° (left turn) in 3 seconds and held constant for the remaining

simulation time. The intent of this maneuver is to compare the resultant steering angles, tire slip angles, and tire lateral forces of the linear and nonlinear models while turning and at steady-state cornering. The overall results are satisfactory and provide confidence in the modeling approach. As seen in Figure 34, both models reached the commanded position and effectively held it. The time it took the vehicle to fully reach steady-state cornering is around 6 seconds into the simulation time.

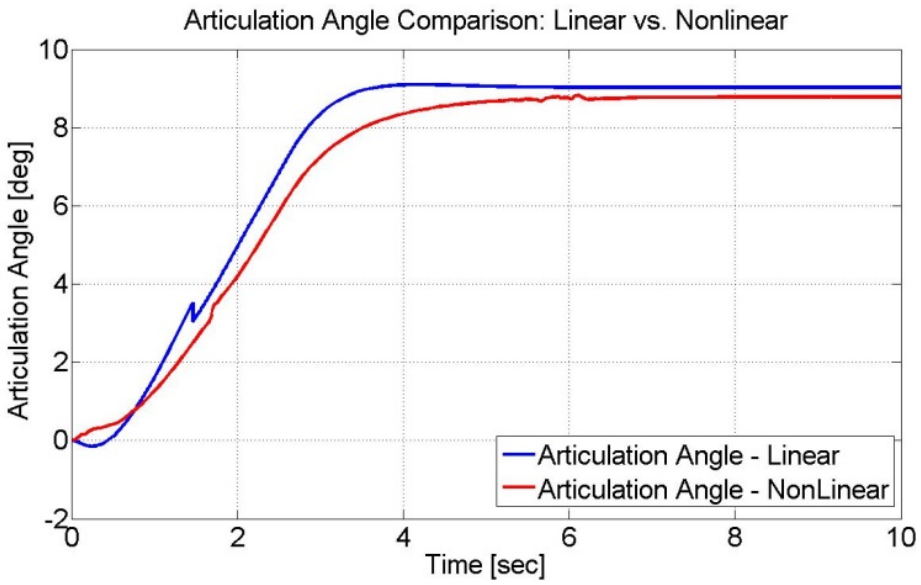

Figure 34: System Models Comparison – Articulation Angle.

Figure 35 shows excellent tracking between the two models relative to tire slip angles. It is noted that for accurate comparison, the individual tire slip angles calculated by MSC Adams software are added together at each axle, and then compared with the linear *bicycle* model, which lumps the two axle tires together. At steady-state conditions the tire slip angles are virtually equal, except for a

small steady-state error, which is mainly due to having a proportional controller only with no integral action to drive the steady-state error to zero.

These results are extremely valuable as they go to show the accuracy, validity, and efficacy of the simplified linear system model, which is simply a set of linear equations that can be numerically solved with ease, versus the nonlinear co-simulation multi-body models that are much more computationally expensive.

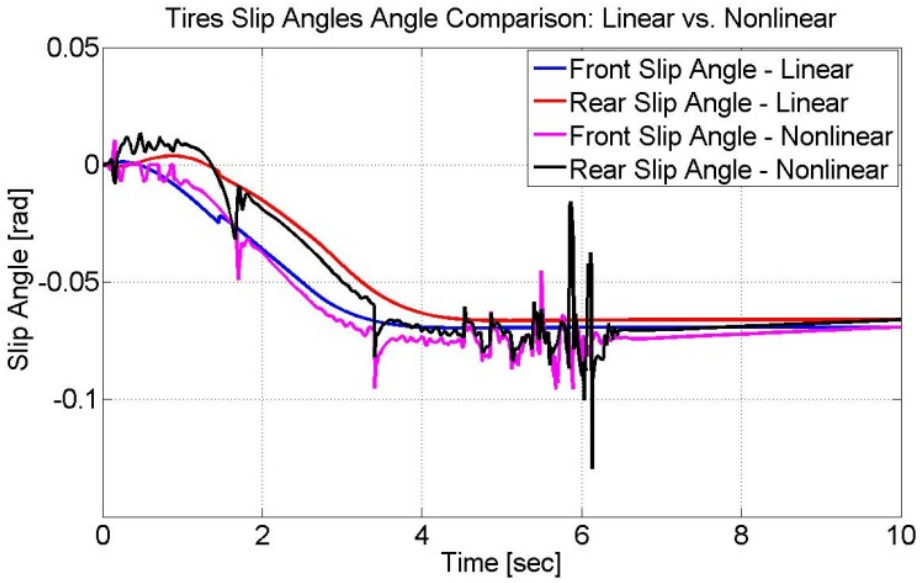

Figure 35: System Models Comparison – Tire Slip Angles.

Figure 36 shows the resulting tire lateral forces as computed by the two models. Again, satisfactory tracking and correspondence between the models are realized demonstrating the validity of the analysis approach as well as the precision of the estimated vehicle parameters.

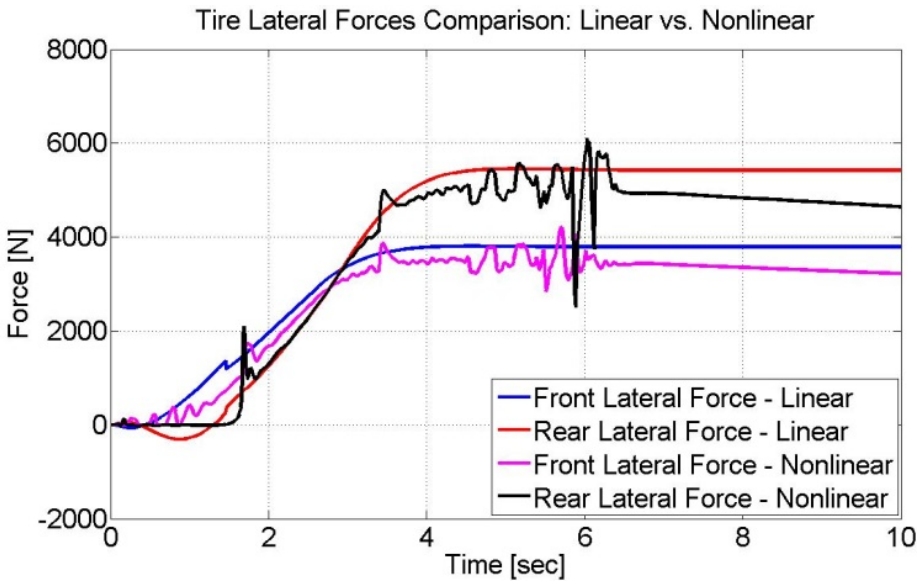

Figure 36: System Models Comparison – Tire Lateral Forces.

4.5 Chapter Summary

- Several dynamic models are derived and validated with the end purpose of having a linear system model that can be used as a LTI plant for controller design in mind.
- Linear and nonlinear models are generated and validated for each of the two subsystems: hydraulics and mechanics.
- The individual models are coupled together to form linear and nonlinear system models, which are then in turn validated.
- The above results demonstrate the effectiveness of the derived linear system relative to its validity, accuracy, and low computation cost.
- The obtained linear system model paves the way in front of generating suitable control algorithms based on modern control theory, including

model based designs given the low computational cost requirements that the derived linear model demands.

CHAPTER 5. CONTROLLER SYNTHESIS AND DESIGN

Two control strategies are considered in this chapter: a linear controller and a nonlinear (adaptive) controller. The linear controller is designed based on the previously derived linearized plant model using feedforward and full state feedback control via state error estimation. The feedforward portion inverts the nominal plant model dynamics, and the feedback loop operates on the state errors between the ideal model and the actual model due to modeling imperfections and deviations from the nominal case. On the other hand, the adaptive controller is designed to cope with parametric uncertainties and unmodeled nonlinearities by utilizing a self-tuning regulator algorithm, which continually adjusts the controller parameters as the actual plant parameter estimates are compared (online) against those of a specified reference model.

5.1 Linear Controller Design

A control strategy that yields optimal performance relative to dynamic response, trajectory tracking, accuracy, and non-synthetic operator feel is one that employs feedforward and feedback control. The block diagram of the devised controller structure is shown in Figure 37.

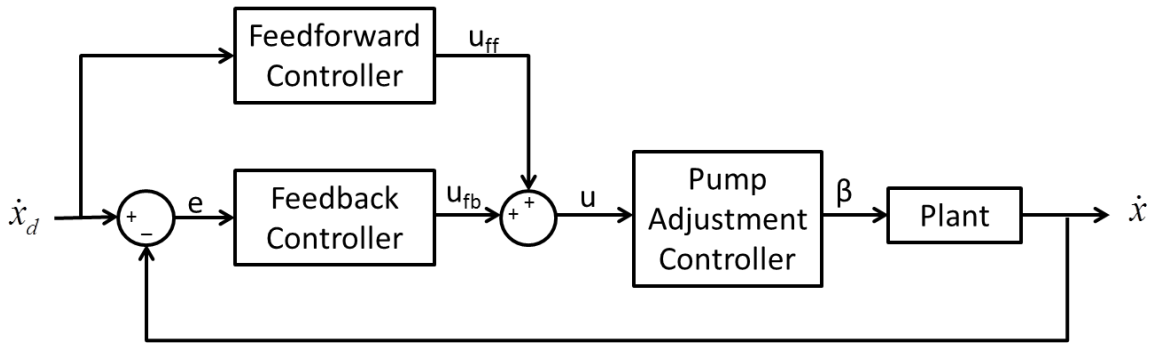

Figure 37: Controller Block Diagram.

In the previous chapter, a linear system model was obtained by first developing a nonlinear model and then constructing a linear approximation within a certain operating range. The derived linear time invariant (LTI) plant model facilitates the effort of designing a controller based on modern linear control theory. The motivation behind approximating a nonlinear system by a linear model is that "*the science and art of linear control is vastly more complete and simpler than they are for the nonlinear case*" according to (Goodwin, Graebe, & Salgado, 2000). For simplification, the system in Eq. (78) is written in the compact state-space format shown in Eq. (81) and Eq. (82).

$$\dot{x}(t) = \mathbf{A}X(t) + \mathbf{B}u(t). \tag{81}$$

$$y(t) = \mathbf{C}X(t) + \mathbf{D}u(t). \tag{82}$$

where $X \in R^n$ is the state vector, $u \in R^m$ is the control (input) signal, $y \in R^p$ is the output, and ***A, B, C*** and ***D*** are matrices of appropriate dimensions. This formulation lends itself to applying linear control theory relative to the notions of controllability and output controllability to be discussed in the upcoming sections.

5.1.1 Controllability

"*The issue of controllability is concerned with, whether or not, a given initial state x_0 can be steered to the origin in finite time using the input u(t)*" according to (Goodwin, Graebe, & Salgado, 2000). In other words, controllability implies that the input signal is capable of affecting a state and driving it to another desired state in a finite time. The derived linear system in Eq. (78) is setup to have a single input, which is the pump displacement as determined by the swash plate angle. Therefore, it is logical to anticipate that not all of the states are controllable from this single input, such as the vehicle velocity, and yaw angle rate. A check of the controllability matrix given in Eq. (83) can confirm this postulation, if the matrix is found to be rank deficient. If more inputs are incorporated into the model, such as engine throttle and brake torque, then all system states can be controllable. However, controlling the engine and the braking system is not part of this research work, and hence only the steering system input is considered.

$$W_C = [B \mid AB \mid A^2B \mid A^3B \mid A^4B \mid A^5B]. \tag{83}$$

To determine the rank of the controllability matrix numerically, the system matrices are populated with the baseline vehicle parameters, which reveal that the controllability matrix is in fact rank deficient.

5.1.2 Output Controllability

Another key check into the system properties is to determine its output controllability, which states that a system is output controllable if there exists an input, *u*, that will transfer the output, *y*, from any initial value to a final value in a finite time. Given the single input and single output of the steering system, it is

possible to confirm that the selected input can in fact control the selected output. Numerically checking the output controllability matrix, given by Eq. (84), of the baseline vehicle steering system results in a full matrix rank, which reveals that the system is indeed output controllable, as anticipated.

$$W_{OC} = [CB \mid CAB \mid CA^2B \mid CA^3B \mid CA^4B \mid CA^5B]. \tag{84}$$

5.1.3 Stability Analysis

Analyzing the stability of the articulated vehicle under consideration is of utmost importance given that a new steering system is included. With state-space format, stability analysis is performed by evaluating the eigenvalues of the state matrix, $\boldsymbol{A}$. This allows for determining the stability threshold of any given articulated vehicle as a function of vehicle forward speed, articulation angle, loading conditions, frames center of mass location relative to the axles, surface condition, and such. Such a setup presents a valuable tool for the design of articulated frame steering vehicles from a vehicle dynamics standpoint.

5.1.4 Reduced System Analysis

Since the focus of this research is the steering system of the vehicle (not the powertrain or braking systems) and given the results of the controllability study, it is analytical to reduce the vehicle down to an equivalent representative system, which results in minimal loss of fidelity and is completely controllable from the steering input alone. This is also beneficial for later investigation that will focus on the role of the new steering system in active safety, whereby the steering system intervention is the only control element independent of other active safety strategies such as engine torque vectoring or differential braking. Nonetheless,

the complete system is still required for research involving vehicle stability control and sensor fusion analysis, which are presented in subsequent chapters.

To condense the *vehicle* system down to a reduced equivalent *actuator* system, the front and rear frames are each represented by equivalent masses attached to the actuator rod and piston respectively, as shown in Figure 38.

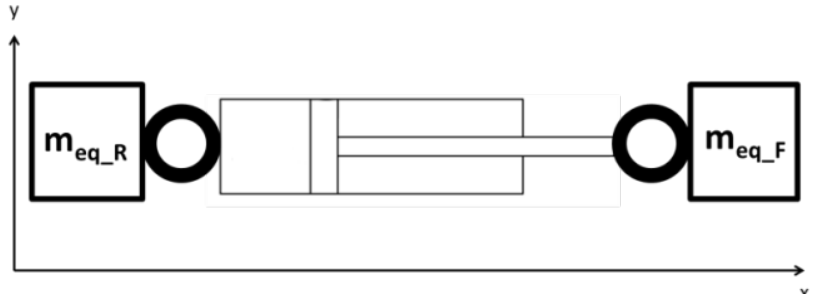

Figure 38: Reduced Steering Actuator System.

To determine the equivalent masses, dynamic equilibrium is applied where the steering actuator force, F_{str}, multiplied by its moment arm, r_j, balances the *inertial* load of the frames as illustrated by Figure 39.

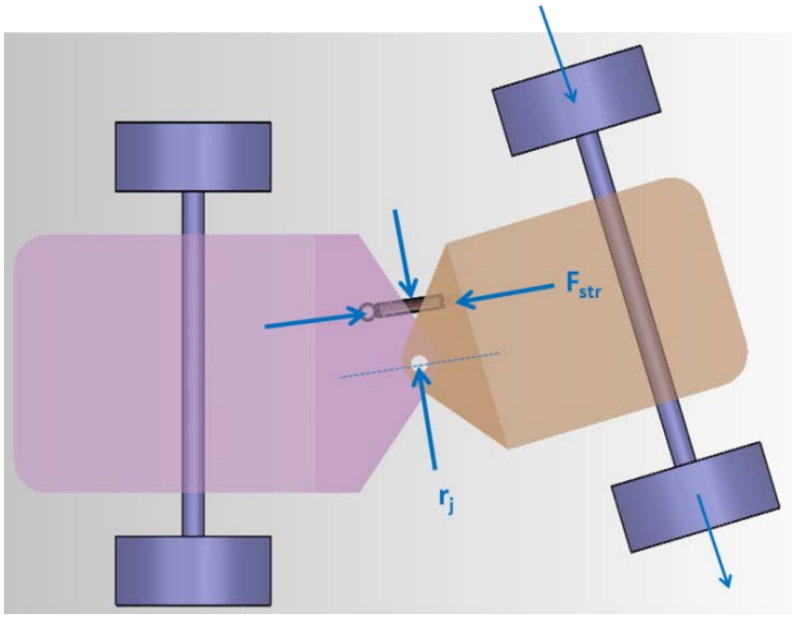

Figure 39: Calculation of Equivalent Masses.

The calculation of the equivalent front frame mass is given by Eq. (85), Eq. (86), and Eq. (87). The rear frame equivalent mass is calculated in a similar manner.

$$F_{str}\, r_j = I_f \ddot{\phi}. \tag{85}$$

$$F_{str} = m_{eq} \ddot{x}. \tag{86}$$

$$m_{eq\_F} = I_f \frac{\ddot{\phi}}{\ddot{x}} \frac{1}{r_j}. \tag{87}$$

The total equivalent mass, m_{eq}, is then given by

$$m_{eq} = \frac{m_{eq\_F}\, m_{eq\_R}}{m_{eq\_F} + m_{eq\_R}}. \tag{88}$$

The system equations of motion reduce down to the governing equations of the pressure rise inside the steering actuator chambers and the actuator dynamics given by Eq. (89).

$$\begin{pmatrix} \dot{x} \\ \ddot{x} \\ \dot{p}_A \\ \dot{p}_B \end{pmatrix} = \begin{pmatrix} 0 & 1 & 0 & 0 \\ 0 & \frac{-c_{eq}}{m_{eq}} & \frac{-A_A}{m_{eq}} & \frac{\alpha A_A}{m_{eq}} \\ 0 & \frac{A_A}{C_H} & \frac{-K_{Li}}{C_H} & \frac{K_{Li}}{C_H} \\ 0 & \frac{-\alpha A_A}{C_H} & \frac{K_{Li}}{C_H} & -\frac{C_{LP}+K_{Li}}{C_H} \end{pmatrix} \begin{pmatrix} x \\ \dot{x} \\ p_A \\ p_B \end{pmatrix} + \begin{pmatrix} 0 \\ 0 \\ \frac{Q_e}{C_H} \\ \frac{-Q_e}{C_H} \end{pmatrix} \beta + \begin{pmatrix} 0 \\ \frac{F_{LF}}{m_{eq\_F}} + \frac{F_{LR}}{m_{eq\_R}} \\ 0 \\ \frac{C_{LP} p_{LP}}{C_H} \end{pmatrix} \cdot \tag{89}$$

The equivalent system, shown in Figure 40, is now setup to mimic the real system in the sense that different forces can be applied to the rod side (attached to front frame) and the piston side (attached to rear frame) of the steering actuator. In actuality both frames rotate relative to the articulation joint and each corresponds to its own axle load.

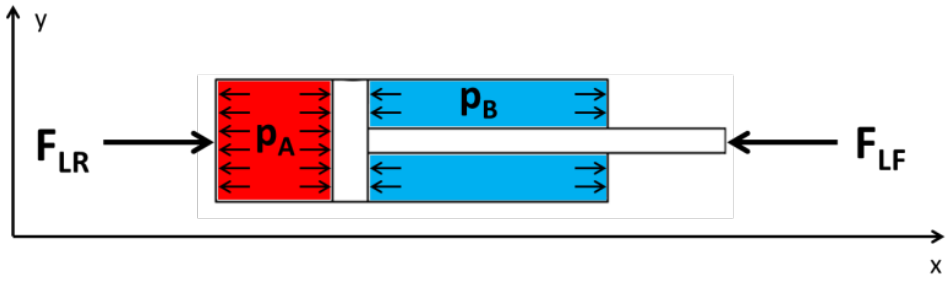

Figure 40: Equivalent Actuator Motion.

5.1.5 Feedforward Controller

The feedforward controller is model-based and its transfer function is determined based on the inverse of the plant transfer function to achieve 'perfect' tracking in the absence of model uncertainties and external/internal disturbances. As shown in Figure 41, perfect command tracking (x=x_d) is achieved when $G_{FF}(s) = G_P(s)^{-1}$.

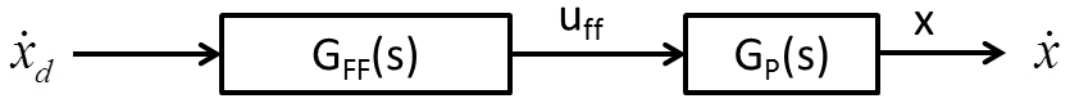

Figure 41: Feedforward Controller Design.

To properly derive the feedforward controller transfer function, it is essential to have an accurate *invertible* plant model. The corresponding transfer function of the system state-space model given by Eq. (89) is attained via Eq. (90).

$$G_P(s) = C(sI - A)^{-1}B + D. \tag{90}$$

The resultant transfer function is proper and takes the form given in Eq. (91).

$$G_P(s) = \frac{\dot{x}(s)}{\beta(s)} = \frac{-\frac{A_A}{m_{eq}}\left(\frac{Q_e(1+\alpha)}{C_H}\right)}{s^2 + \frac{c_{eq}}{m_{eq}}s + \frac{A_A{}^2}{m_{eq}}\left(\frac{1+\alpha^2}{C_H}\right)}. \quad (91)$$

The transfer function for the feedforward controller is the inverse of $G_P(s)$. However, when inversion is applied the resulting transfer function is improper, that is the numerator possesses a higher order than the denominator. To get around this restriction, the following mathematical manipulation is employed. Additional terms that only have effects at high frequencies larger than a certain cutoff frequency, ω_{ff}, are added to the denominator in order to render the transfer function bi-proper as given by Eq. (92).

$$G_{FF}(s) = \frac{s^2 + a_{ff}s + b_{ff}}{c_{ff}} \approx \frac{s^2 + a_{ff}s + b_{ff}}{c_{ff}\left(\frac{s}{\omega_{ff}} + 1\right)^2}. \quad (92)$$

5.1.6 Feedback Controller

Feedforward controllers can theoretically result in ideal tracking, if and only if the derived plant model is an exact replica of the real physical system in the absence of disturbances. However, this is never the case as all models have uncertainties no matter how high their fidelity is. In addition, physical systems are susceptible to both external and internal disturbances; and that is where the need for feedback arises in order to increase the robustness of the controller in the face of such uncertainties.

The feedback controller is designed based on full state feedback that operates on the *error* vector between the desired states and the actual (measured) states. Hence, a state feedback controller that acts as a regulator driving the state errors to zero is the preferred candidate of choice. Given that it is desired to not measure all the system states due to cost and maintenance reasons, and that the actuator displacement is the only state to be measured, the need for estimating the remaining states also arises. Hence, a control strategy that is based on output feedback in conjunction with state estimation is implemented. A state space formulation is derived for the deviation (error) system by calculating the error between an ideal system and the actual system. The ideal system is given by Eq. (93) and it represents a system with perfect command tracking.

$$\begin{aligned} \dot{\overline{x}} &= A\overline{x} + B\overline{u} \\ \overline{y} &= C\,\overline{x} = x_d . \end{aligned} \tag{93}$$

Defining the state error, input error, and output error respectively per Eq. (94)

$$\begin{aligned} \tilde{x} &= x - \overline{x} \\ \tilde{u} &= u - \overline{u} \\ \tilde{y} &= y - \overline{y}. \end{aligned} \tag{94}$$

results in the deviation system given by Eq. (95)

$$\begin{aligned} \dot{\tilde{x}} &= A\tilde{x} + B\tilde{u} \\ \tilde{y} &= C\tilde{x} = -e. \end{aligned} \tag{95}$$

Checking the observability matrix of the deviation system indicates that the system is completely state observable based on the selected measured output (position error), and therefore estimating the entire state error vector is possible.

The next task is to determine an observer feedback gain vector that accurately estimates the states, in a 'timely' manner. Pole-placement is the method of choice given the knowledge about the open-loop characteristic equation and the desired closed-loop performance relative to error convergence rate. The desired performance specifications are based on a second-order system with a certain percent overshoot (*%OS*) and rise time (t_r). The resultant damping ratio, ζ, and natural frequency, ω_n, are calculated via Eq. (96) and (97) respectively.

$$\zeta = \sqrt{\frac{\log^2\left(\frac{\%OS}{100}\right)}{\pi^2 + \log^2\left(\frac{\%OS}{100}\right)}}. \tag{96}$$

$$\omega_n = \frac{\left(\frac{\pi - \cos^{-1}(\zeta)}{t_r}\right)}{\sqrt{1+\zeta^2}}. \tag{97}$$

The desired closed-loop pole locations are then determined based on the computed damping ratio and natural frequency per Eq. (98).

$$p_{1,2} = -\zeta\omega_n \pm \omega_n\sqrt{1-\zeta^2}. \tag{98}$$

To arrive at a third order system, an additional pole is placed at five times the magnitude of the poles' real part in the left hand plane. The state error estimate is given by Eq. (99), in which *J* is the observer gain matrix.

$$\dot{\hat{x}} = A\hat{x} + B\tilde{u} + J(\tilde{y} - C\hat{x}). \tag{99}$$

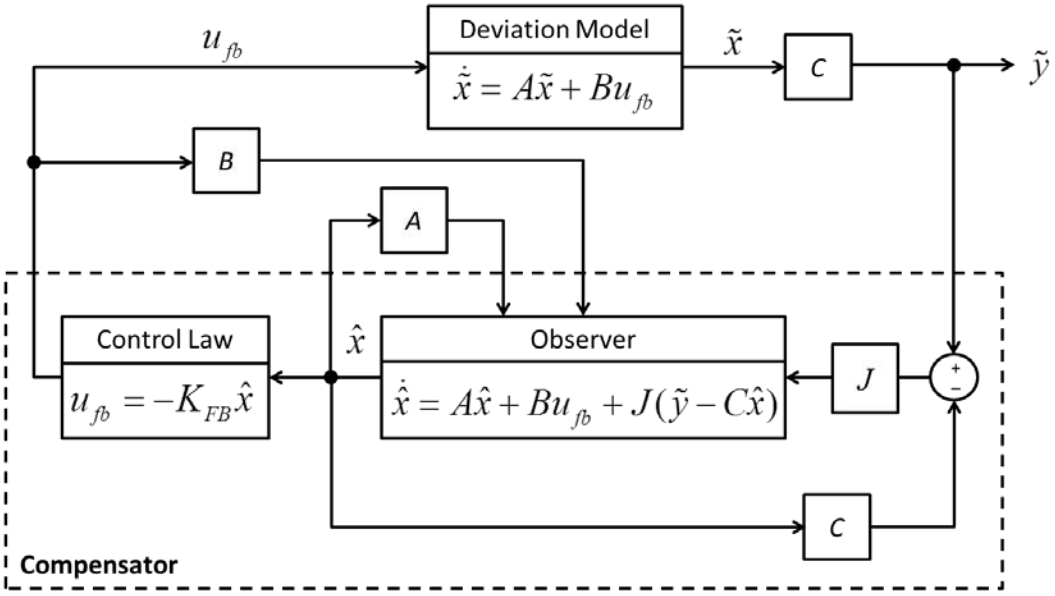

Figure 42: Feedback Controller Design.

A full-state feedback controller operating on the state error estimates is designed, in which the feedback gain matrix is computed via pole-placement in a similar manner as described above. The feedback term is given by Eq. (100).

$$\tilde{u} = u_{fb} = -K_{FB}\,\hat{x}. \tag{100}$$

where K_{FB} is the feedback gain matrix.

5.1.7 Controller Design Validation

To test the performance of the designed controller, two events are devised and simulated using the linear MATLAB model from which the controller is sythesized: 1) a sine wave command; 2) a ramp-up, hold, ramp-down command. The two events combined serve multiple validation purposes. First, they validate the proposed feedforward plus feedback controller architecture. Second, they confirm the computed plant parameters, which incorporate the baseline machine parameters such as equivalent masses and loads in the loaded and unloaded

cases. And third, they validate the analysis involving open-loop and closed-loop pole locations, state feedback gain matrix, K_{FB}, and observer gain matrix, J. Generally, the controller performance is satisfactory relative to tracking a varying command, rejecting disturbances, and holding a desired position. Naturally, the simulated events can be translated into commanded steering wheel angle/rate and a resultant vehicle steering angle/rate, given the established relationship between the two systems.

Figure 43 shows excellent tracking performance by the controller when tracking a sine wave input to the actuator position. Minimal lag can be discerned between the desired and actual position, however this cannot be felt by the operator and is therefore deemed unobjectionable.

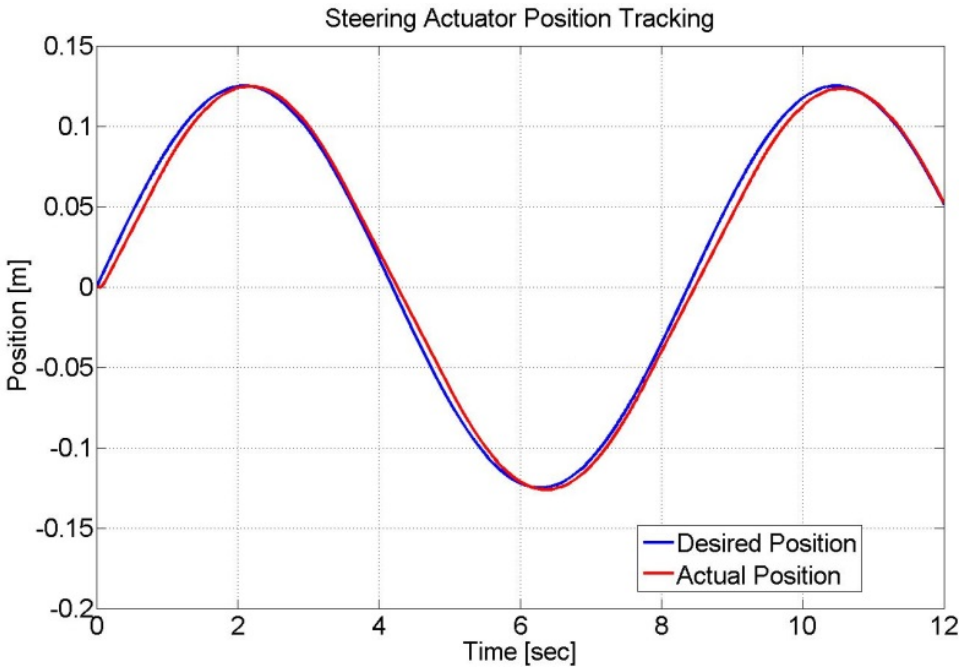

Figure 43: Actuator Position Tracking – Sine Wave.

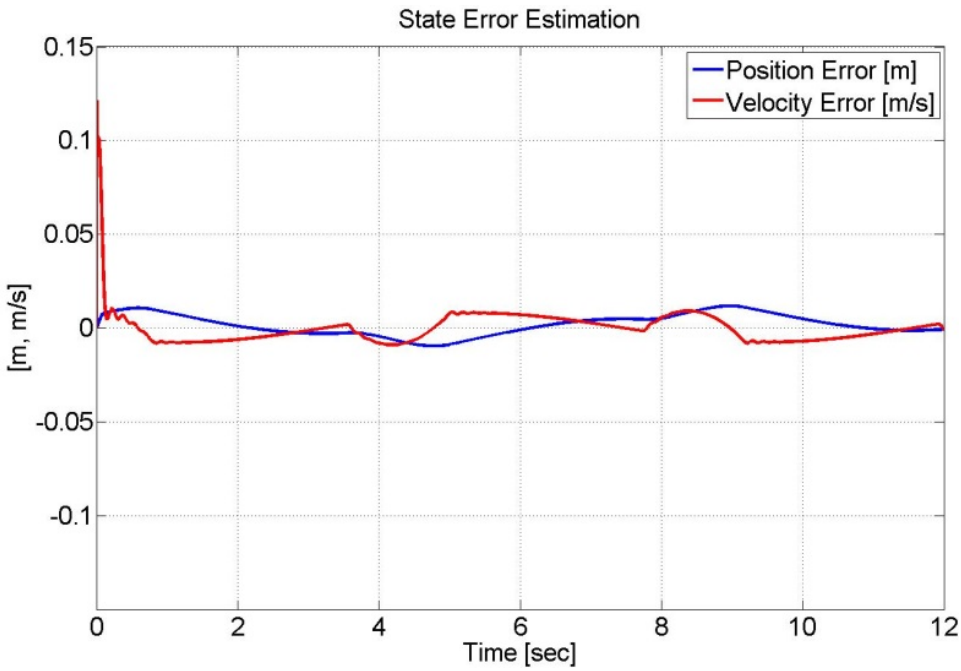

Figure 44: Actuator Position and Velocity Error Estimates – Sine Wave.

Figure 44 illustrates the fast convergence of the state estimates by the designed state observer, where the errors in the actuator position and velocity almost instantaneously converge to zero and are then regulated near zero throughout the entire event. This validates the placement of the observer poles in the sense that its estimates are accurate, exhibit fast convergence, and do not result in unrealistic control effort nor actuator saturation issues.

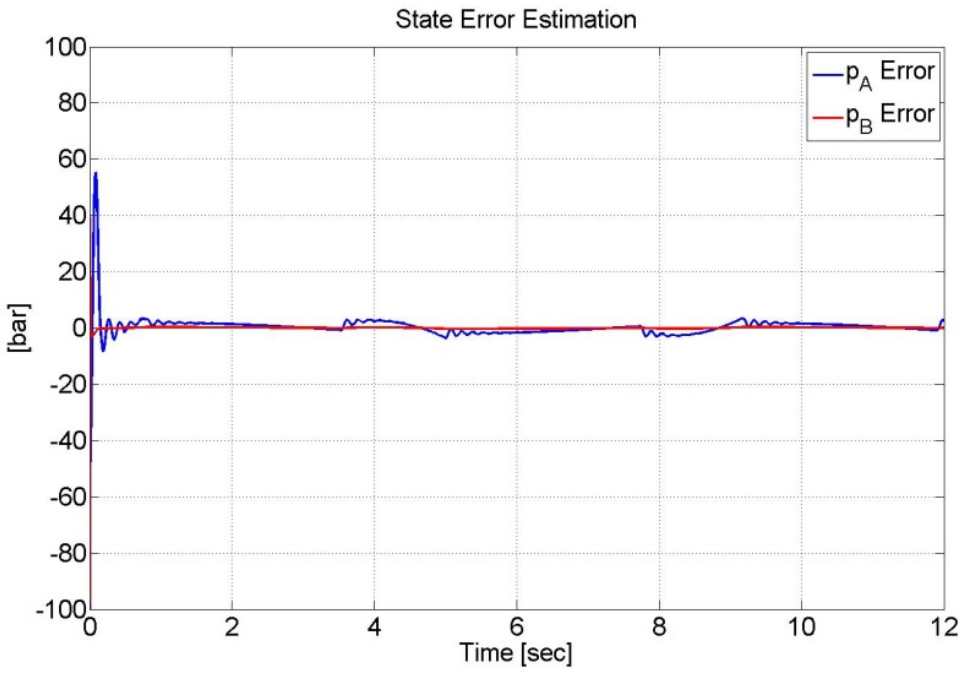

Figure 45: Actuator Pressures Error Estimates – Sine Wave.

Figure 45 shows that the error estimates of the pressures inside the actuator chambers stay near zero, indicating a fast convergence to the actual pressure states without having to physically sense them and the errors are successfully regulated near zero throughout the entire simulation.

The above results validate the exercise of converting a tracking problem into a regulation problem that regulates the state errors instead of the states themselves. The next two plots in Figure 46 and Figure 47 show the controller performance during a ramp-up, hold, and ramp-down event with a special focus on the hold phase for the evaluation of the steady-state tracking error.

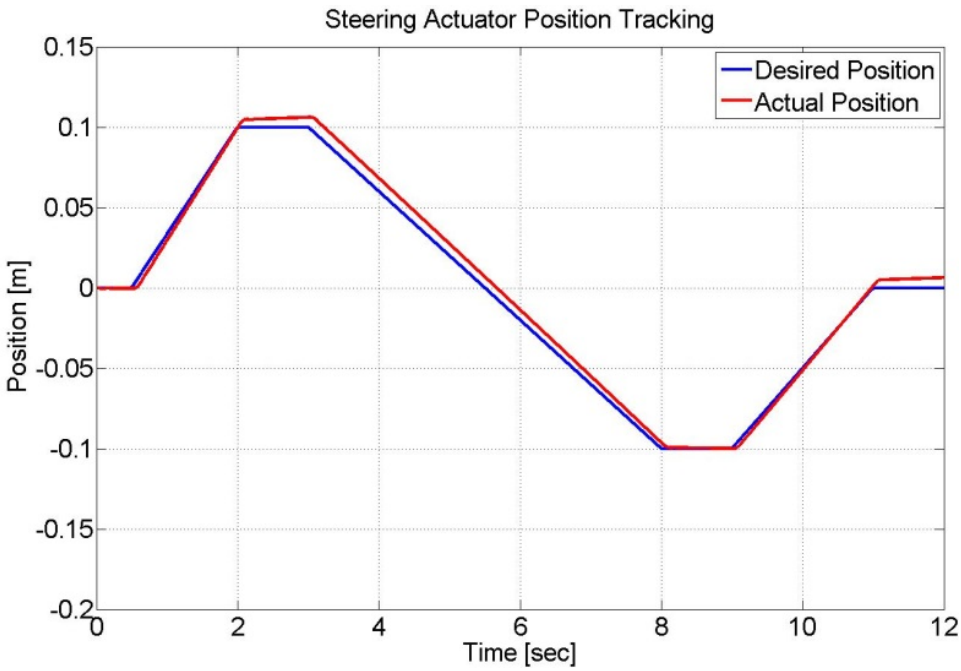

Figure 46: Actuator Position Tracking – Ramp & Hold.

Figure 46 shows the tracking performance for a ramp and hold event. Similar to the sine wave command, adequate tracking is achieved overall. The steady-state error observed during the hold phase can be reduced by incorporating integral action into the error state feedback controller, which can be simply realized by augmenting the state space with an additional error term as a new state, if the error is deemed unacceptable.

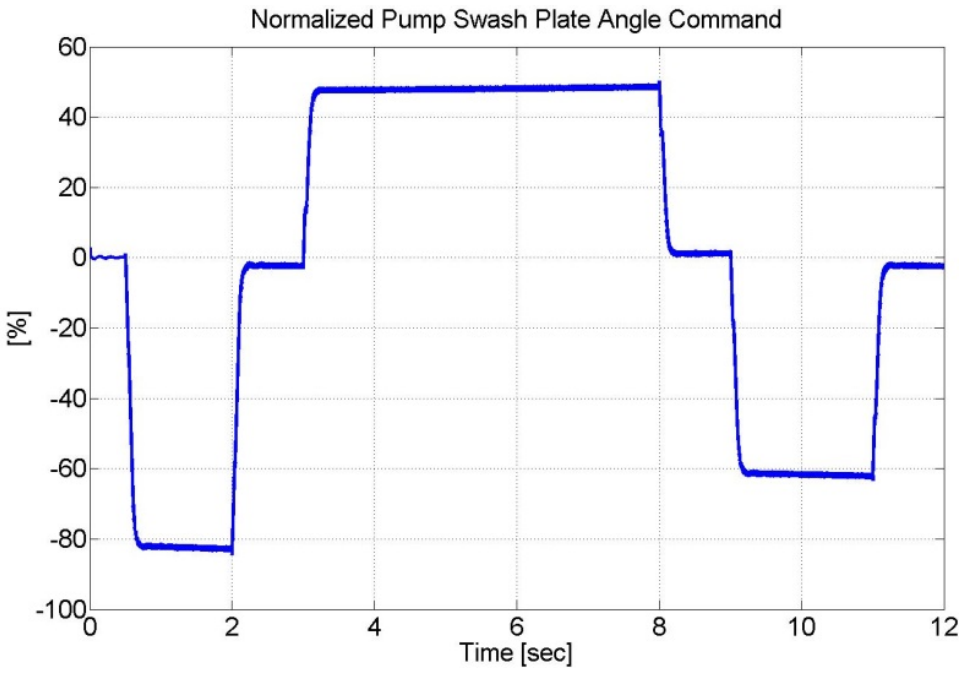

Figure 47: Instantaneous Pump Displacement – Ramp & Hold.

Figure 47 shows the instantaneous pump displacement during the ramp and hold event, with two main observations. First, the displacement during the hold phases requires more aggressive adjustment to minimize the steady-state error as stated above. Second, different pump displacements are required to move the actuator (articulate the machine) in opposite directions given the single-rod steering actuator area ratio.

Experimentally, the controller is implemented on the prototype test vehicle and a steering cycle is executed while articulating the machine in both turning directions. The normalized steering wheel angle rate is plotted against the normalized articulation angle rate in Figure 48. As seen, excellent tracking performance is realized by the controller with minimal delay, overshoot, and undershoot observed in both turning directions. It is noted that all of the

experimental results that are presented later in Chapter 7 are obtained with the linear controller in action.

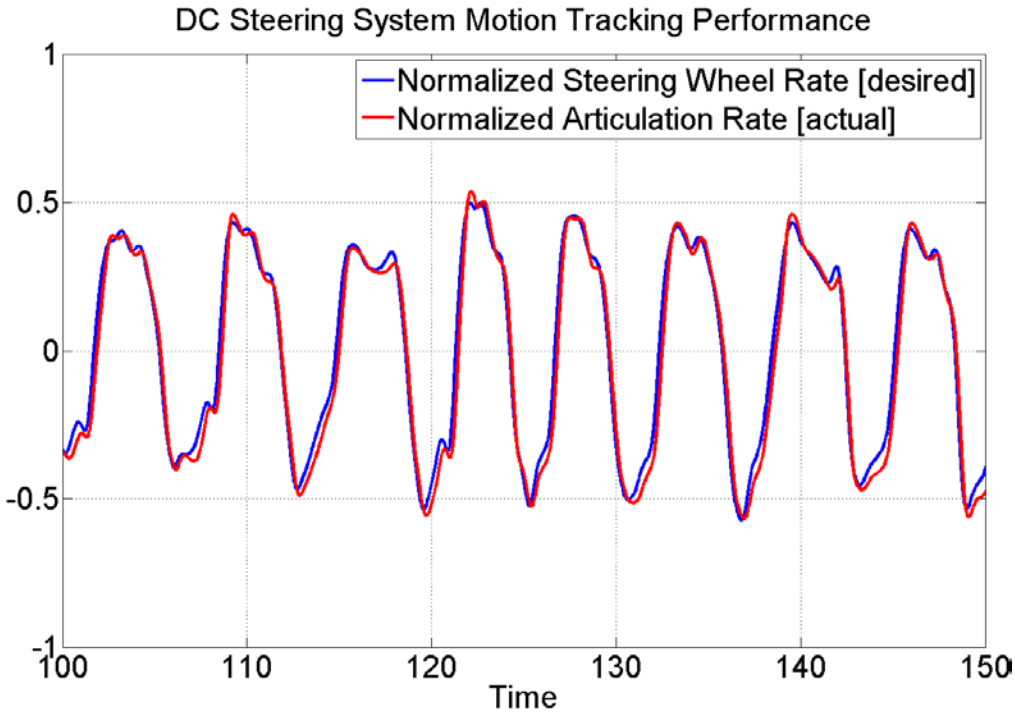

Figure 48: Linear Controller Tracking Performance – Experimental Results

5.2 Adaptive Nonlinear Controller

In the previous section, linearization techniques are applied to the system dynamic model and a linear controller to achieve motion control of the steering actuator is devised. However, to better deal with parametric uncertainties (e.g. load inertia, fluid bulk modulus) and uncertain nonlinearities associated with hydraulic systems (e.g. actuator seal friction and leakage, external disturbances), a nonlinear controller is explored. The work in this section investigates an indirect adaptive velocity controller in the form of a self-tuning regulator (STR) based on the Minimum-Degree Pole Placement (MDPP) approach, which updates the

controller parameters based on real-time estimates of the plant parameters provided by an online estimator realized via Kacsmarz's projection algorithm. This approach is adopted because it provides insight into the uncertain system parameters, which is desired for further research that requires particular knowledge of the plant parameters. Moreover, the designed indirect self-tuning regulator is not as computationally expensive as other adaptive algorithms, which demand faster processing speeds when deployed into a digital microprocessor. Furthermore, this adaptive control law allows for pole placement without the high gains associated with robust control algorithms. Lastly, the designed adaptive controller is capable of realizing both fine command tracking performance and efficient parameter estimation.

Various adaptive control schemes for manipulating hydraulic actuators have been proposed. Earlier research focused primarily on linear control theory. A robust adaptive controller applied to hydraulic servo systems for noncircular machining was proposed in (Tsao & Tomizuka, 1994). Another robust adaptive control scheme was devised in (Plummer & Vaughan, 1996) for the control of hydraulic servo-systems. An adaptive high bandwidth control of a hydraulic actuator was developed in (Bobrow & Lum, 1996). Feedback linearization techniques were employed in (Vossoughi & Donath, 1995) for controlling the motion of electrohydraulic systems. Adaptive sliding mode control was utilized in (Bonchis, Corke, Rye, & Ha, 2001), (Hisseine, 2005), (Li & Khajepour, 2005), and (Liu & Handroos, 1999). Adaptive robust control (ARC) based on backstepping techniques was followed in (Yao, Chiu, & Reedy, 1997) to realize motion control

of a double-rod actuator and later in (Yao, Bu, Reedy, & Chiu, 2000) to control a single-rod actuator.

Velocity control is the preferred scheme for controlling the motion of mobile machinery actuators since hydraulic control valves as well as servo-pumps supply a flow rate that corresponds to a velocity. The controller works in a feedforward fashion between the input and output. In the steering case, feedforward control reduces the effect of input disturbances (e.g. hand wheel perturbations) and results in a non-synthetic steering feel that emulates conventional feel. A logic switch is employed to transition into position control mode when no steering input is detected to hold a position. The feedforward control structure is shown in Figure 49.

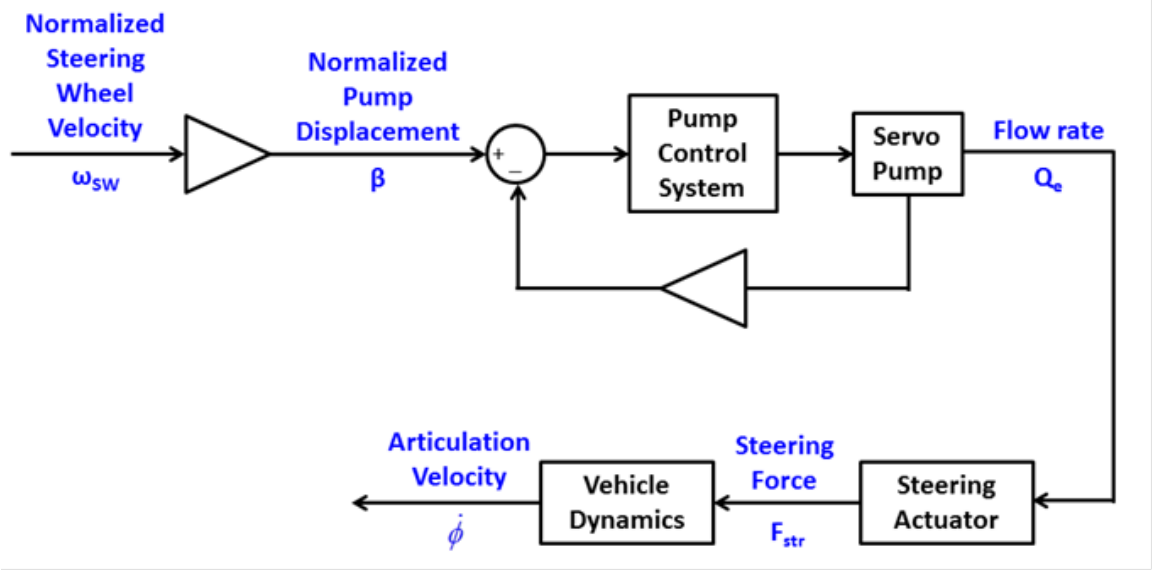

Figure 49: Feedforward Velocity Control.

In closed-loop control mode, a cascaded control structure is utilized given that the inner loop (pump control system) dynamics (>100Hz) are an order of magnitude faster than the outer loop (steered system) dynamics (<10Hz).

5.2.1 Plant Model Derivation

The equation of motion for the steering actuator is given by

$$m_{eq}\ddot{x} = -p_A A_A + \alpha p_B A_A - c_{eq}\dot{x} + F_L. \tag{101}$$

Rewriting the motion equation by substituting the actuator pressure build-up equations results in Eq. (102).

$$\begin{aligned} m_{eq}\ddot{x} + c_{eq}\dot{x} = {} & \frac{1}{s}\frac{-A_A}{C_H}\left(\beta Q_e + A_A\dot{x} - p_A K_{Li} + p_B K_{Li}\right)\ldots \\ & + \frac{1}{s}\frac{\alpha A_A}{C_H}\left(-\alpha\beta Q_e - \alpha A_A\dot{x} + p_A K_{Li} - p_B K_{Li}\right)\ldots \\ & + F_L. \end{aligned} \tag{102}$$

where *s* is the Laplace operator.

Consequently, the steering actuator velocity is given by

$$\dot{x} = \frac{-\frac{A_A}{m_{eq}}\left(\frac{1+\alpha^2}{C_H}\right)\beta Q_e + sF_L}{s^2 + \frac{c_{eq}}{m_{eq}}s + \frac{A_A^2}{m_{eq}}\left(\frac{1+\alpha^2}{C_H}\right)}. \tag{103}$$

A closer examination of Eq. (103) reveals the influence of each of the pump displacement, β, and the load force, F_L, on the actuator motion. The two components are split into Eq. (104) and Eq. (105)respectively.

$$\frac{\dot{x}}{\beta} = \frac{-\frac{A_A}{m_{eq}}\left(\frac{1+\alpha^2}{C_H}\right)Q_e}{s^2 + \frac{c_{eq}}{m_{eq}}s + \frac{A_A^2}{m_{eq}}\left(\frac{1+\alpha^2}{C_H}\right)}. \tag{104}$$

Eq. (104) represents a transfer function with the actuator velocity as an output, and the commanded pump displacement as an input.

$$\frac{\dot{x}}{F_L} = \frac{s}{s^2 + \frac{c_{eq}}{m_{eq}}s + \frac{A_A^2}{m_{eq}}\left(\frac{1+\alpha^2}{C_H}\right)}. \tag{105}$$

The transfer function in Eq. (105) represents the dynamic compliance of the system, which establishes the relationship between the applied load force and the corresponding actuator motion. Given the large stiffness of the hydraulic fluid, the dynamic compliance component can be ignored for actuator motion control, and only the transfer function in Eq. (104) is considered for motion control (Merritt, 1967).

For a negative pressure differential across the actuator chambers, a similar derivation is followed and the resulting transfer is given by

$$\frac{\dot{x}}{\beta} = \frac{-\frac{A_A}{\alpha\, m_{eq}}\left(\frac{1+\alpha^2}{C_H}\right)Q_e}{s^2 + \frac{c_{eq}}{m_{eq}}s + \frac{A_A^2}{m_{eq}}\left(\frac{1+\alpha^2}{C_H}\right)}. \tag{106}$$

which reveals that both systems have the same damping ratio, natural frequency, and poles with the only difference being that the DC gain of the negative pressure differential system is a (1/α) factor of the positive pressure differential

system. The resulting hydraulic natural frequency, ω_{n_Act}, and damping ratio, ζ_{Act}, are given by Eq. (107) and Eq. (108) respectively.

$$\omega_{n\_Act} = A_A \sqrt{\frac{1+\alpha^2}{m_{eq} C_H}}. \tag{107}$$

$$\zeta_{Act} = \frac{c_{eq}}{2\omega_n m_{eq}}. \tag{108}$$

The damping coefficient, c_{eq}, of the equivalent system includes the articulation joint friction and the tires lateral damping in addition to the actuator friction forces. Subsequently, the reduced system transfer function for a positive actuator Δp using the derived equivalent mass, m_{eq}, and equivalent damping, c_{eq}, terms is given by

$$\frac{\dot{x}(s)}{\beta(s)} = \frac{-\frac{A_A}{m_{eq}}\left(\frac{1+\alpha^2}{C_H}\right) Q_e}{s^2 + \frac{c_{eq}}{m_{eq}} s + \frac{A_A{}^2}{m_{eq}}\left(\frac{1+\alpha^2}{C_H}\right)}. \tag{109}$$

5.2.2 Adaptive Control Law

The adaptive control law adopted in this work is an indirect self-tuning regulator (STR) that uses the Minimum-Degree Pole Placement (MDPP) method for controller design, combined with a real-time estimator based on a modified Kacsmarz's projection algorithm for estimating the plant uncertain parameters. The design makes use of the *certainty equivalency principle*, which assumes that the parameter estimates are true in the design of the controller. The selected approach is *indirect* because the controller parameters are indirectly updated

based on the estimated plant parameters. The MDPP method forms the required map between the plant parameters and the controller parameters. A block diagram of the adaptive control structure is given in Figure 50 below.

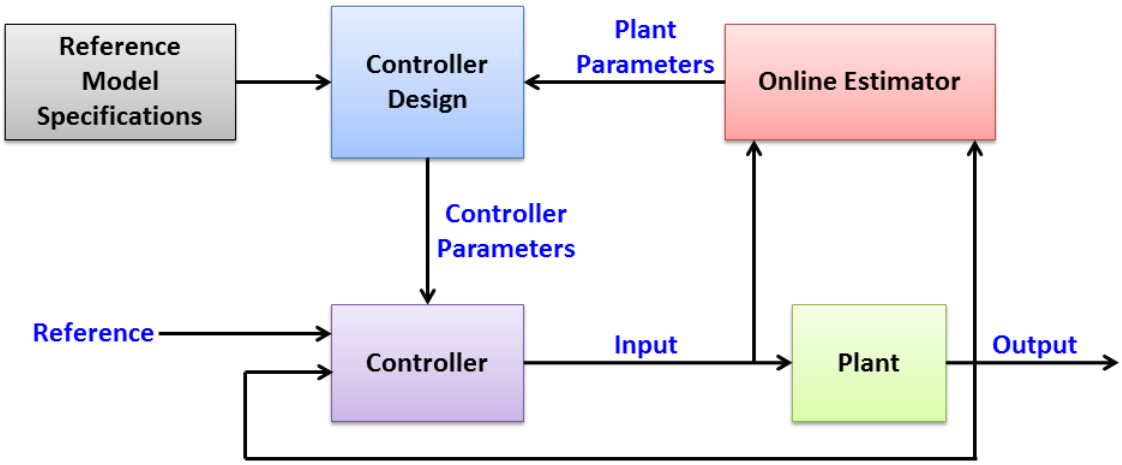

Figure 50: Indirect Adaptive Control Structure.

For designing the adaptive control law, the derived transfer function in Eq. (109) undergoes two modifications. The output is first averaged to account for the area difference between the two actuator sides, and is then normalized by considering the maximum actuator velocity to only propagate normalized signals throughout the system. The resulting transfer function, $G_p(s)$, for the single-input single-output (SISO) system is given by

$$G_P(s)=\frac{Y(s)}{U(s)}=\frac{-\frac{\alpha+1}{2\alpha}\frac{1}{\dot{x}_{\max}}\frac{A_A}{m_{eq}}\left(\frac{1+\alpha^2}{C_H}\right)Q_e}{s^2+\frac{c_{eq}}{m_{eq}}s+\frac{A_A^{\,2}}{m_{eq}}\left(\frac{1+\alpha^2}{C_H}\right)}=\frac{B_{AC}(s)}{A_{AC}(s)}. \tag{110}$$

Polynomials A_{AC} and B_{AC} in Eq. (110) are relatively prime as they have no roots in common and their roots are not within close vicinity, which makes the proposed control design valid. The control law is given by

$$R_{AC}u(t) = T_{AC}u_c(t) - S_{AC}y(t). \tag{111}$$

where R_{AC}, S_{AC}, and T_{AC} are polynomials and u_c is the control input signal to the controller.

Since the adaptive controller is deployed onto a digital microprocessor, a discrete time system is obtained via pulse transfer function with a sampling time, T_s, of 0.005s corresponding to a controller frequency of 200Hz.

$$G_p(z) = \frac{b_1 z + b_0}{z^2 + a_1 z + a_0} = \frac{B_{AC}(z)}{A_{AC}(z)}. \tag{112}$$

The discrete system is minimum phase with stable and well damped zeroes, which allows for simplifying the control design procedure of model-following by cancelling the plant zero. The desired performance specifications are stipulated via a reference model with specified natural frequency, ω_m, and damping ratio, ζ_m, which were set to 44rad/s (7Hz) and 0.7 respectively.

$$G_m(s) = \frac{\omega_m^2}{s^2 + 2\zeta_m\omega_m s + \omega_m^2} = \frac{B_m(s)}{A_m(s)}. \tag{113}$$

The pulse transfer function for the reference model, with zero cancelling, is given by

$$G_m(z) = \frac{b_{m1} z}{z^2 + a_{m1} z + a_{m0}} = \frac{B_m(z)}{A_m(z)}. \tag{114}$$

where b_{m1} is chosen to yield unity static gain. The reference model has the same pole excess as the plant model and the plant zero is stable and well-damped, thus it satisfies the following compatibility conditions:

$$\deg A_m = \deg A_{AC}. \tag{115}$$

$$\deg B_m = \deg B_{AC}. \tag{116}$$

Polynomial B is factored into a monic polynomial, B^+, and a complement, B^-, given by

$$B_{AC}(z) = B^+(z)\,B^-(z) = \left(z + \frac{b_0}{b_1}\right) b_1. \tag{117}$$

Polynomial A_o satisfies another compatibility condition:

$$\deg A_o = \deg A_{AC} - \deg B^+ - 1. \tag{118}$$

which results in A_o having a zero degree. For this work, A_o is set to 1.

$$A_o(z) = 1. \tag{119}$$

The last of the compatibility conditions is given by

$$B_m(z) = B^-(z) B'_m(z). \tag{120}$$

which results in

$$B'_m(z) = \frac{B_m(z)}{B^-(z)} = \frac{b_{m1}}{b_1} z. \tag{121}$$

Owing to the fact that the process model is of second order, polynomials R and S are of first order.

Solving the Diophantine equation:

$$A_{AC} R' + B^- S_{AC} = A_o A_m = A_c. \tag{122}$$

with the condition that

$$\deg S_{AC} < \deg A_{AC}. \tag{123}$$

leads to R′ being of zero degree and monic, therefore

$$R' = 1. \tag{124}$$

Polynomial *R* is constructed as

$$R_{AC}(z) = R'(z)B^{+}(z) = z + \frac{b_0}{b_1}. \tag{125}$$

Polynomial *S* takes the form

$$S_{AC}(z) = s_0 z + s_1. \tag{126}$$

The solution of the Diophantine equation leads to computing coefficients s_0 and s_1 given by

$$s_0 = \frac{a_{m1} - a_1}{b_1}. \tag{127}$$

$$s_1 = \frac{a_{m0} - a_0}{b_1}. \tag{128}$$

Notice that the closed loop characteristic polynomial, A_c, in Eq. (122) only contains polynomials *S* and *R*. Hence another condition, which must hold to guarantee model following, is used to determine polynomial *T* and is given by

$$\frac{B_{AC}T_{AC}}{A_{AC}R_{AC} + B_{AC}S_{AC}} = \frac{B_{AC}T_{AC}}{A_c} = \frac{B_m}{A_m}. \tag{129}$$

Polynomial *T* is then determined from

$$T_{AC}(z) = A_o(z)B'_m(z) = \frac{b_{m1}}{b_1} z. \tag{130}$$

A closer look at the control law in Eq. (111) indicates that it possesses two degrees of freedom with a feedforward term (T_{AC}/R_{AC}) and a negative feedback term ($-S_{AC}/R_{AC}$) given by

$$u = \frac{T_{AC}(z)}{R_{AC}(z)} u_c - \frac{S_{AC}(z)}{R_{AC}(z)} y. \tag{131}$$

Finally, the following adaptive control law is attained:

$$u(t) = -\frac{b_0}{b_1} u(t-1) + \frac{b_{m1}}{b_1} u_c(t) - \frac{a_{m1} - a_1}{b_1} y(t) - \frac{a_{m0} - a_0}{b_1} y(t-1). \tag{132}$$

5.2.3 Plant Parameter Estimation

The plant parameters in Eq. (112) are functions of quantities that are uncertain, difficult to measure, or vary with time. Hence, the need for estimating the plant parameters arises, and for that purposes several estimation algorithms can be employed. In this work, a Kacsmarz's projection algorithm is utilized and is chosen over the more common recursive least squares (RLS) method due to its simpler design, lower computational effort, and improved robustness. RLS estimation requires the continuous update of both a parameters set as well as the covariance matrix of the parameters, which dominates the computing effort. In fact, a RLS algorithm was implemented and indeed resulted in poor performance and bogging down of the real-time controller.

The plant model in Eq. (112) is expressed as a difference equation given by

$$y(t) = -a_1 y(t-1) - a_0 y(t-2) + b_1 u(t-1) + b_0 u(t-2). \tag{133}$$

Letting the parameter vector, θ_{AC}, be

$$\theta_{AC} = \begin{pmatrix} a_1 & a_0 & b_1 & b_0 \end{pmatrix}^T . \tag{134}$$

and letting the regression vector, φ, be

$$\varphi^T(t) = \begin{pmatrix} -y(t-1) & -y(t-2) & u(t-1) & u(t-2) \end{pmatrix}. \tag{135}$$

the output can be written as

$$y(t) = \varphi^T(t)\theta_{AC}. \tag{136}$$

Kacsmarz's estimation algorithm is given by

$$\hat{\theta}(t) = \hat{\theta}(t-1) + \frac{\varphi(t)}{\varphi^T(t)\varphi(t)}\left(y(t) - \varphi^T(t)\hat{\theta}(t-1) \right). \tag{137}$$

However, since it is desirable to be able to change the step length of the parameter adjustment, a factor γ is introduced in the numerator. At the same time, to avoid potential issues with having a zero denominator when φ(t) = 0, a positive constant factor ξ is added to the denominator. Hence, the *modified* Kacsmarz's estimation algorithm is given by

$$\hat{\theta}(t) = \hat{\theta}(t-1) + \frac{\gamma_{AC}\varphi(t)}{\xi + \varphi^T(t)\varphi(t)}\left(y(t) - \varphi^T(t)\hat{\theta}(t-1) \right). \tag{138}$$

The tuning factors, γ and ξ, are subject to the following conditions as established in (Astrom & Wittenmark, 2008):

$$\gamma_{AC} \geq 0. \tag{139}$$

$$0 < \xi < 2. \tag{140}$$

Finally, the control law previously derived in Eq. (132) is now expressed in terms of the parameter estimates, designated by the caret (^) symbol, and the reference model coefficients given by

$$u(t) = -\frac{\hat{b}_0}{\hat{b}_1}u(t-1) + \frac{b_{m1}}{\hat{b}_1}u_c(t) - \frac{a_{m1}-\hat{a}_1}{\hat{b}_1}y(t) - \frac{a_{m0}-\hat{a}_0}{\hat{b}_1}y(t-1). \quad (141)$$

5.2.4 Simulation Results

To validate the design of the control law and the parameter estimation algorithm, numerical simulations are executed with the controller and estimator having the same sampling frequency of 200Hz. For the projection algorithm, γ was set to 0.001 and ξ was set to 0.1. The main parameters used during the simulation are given in Table 2, where the listed true values are the ones used previously.

Table 2: Simulation Parameters.

Parameter	Initial	True Value	Unit
K	1.500E+09	1.950E+09	Pa
n	2.723E+02	2.094E+02	rad/s
m_{eq}	2.344E+04	2.813E+04	kg
c_{eq}	2.393E+05	2.871E+05	kg/s
C_{HA}	3.316E-13	4.311E-13	m^5/N
C_{HB}	2.776E-13	3.609E-13	m^5/N
C_H	3.046E-13	3.960E-13	m^5/N
a_1	-1.868E+00	-1.898E+00	-
a_0	9.502E-01	9.502E-01	-
b_1	-3.754E-02	-1.856E-02	-
b_0	-3.691E-02	-1.824E-02	-

A sinusoid wave with a frequency of 1 rad/s and normalized amplitude of 0.6 was used. Simulation time was set to 50 seconds and a discrete solver with a fixed step of 0.005s was utilized.

Figure 51 shows the system output tracking performance where u_c is the commanded signal, y_m is the reference model output, and y is the actual plant output. The simulation results illustrate that the system exhibits asymptotic output tracking where initially during the first 15 s of the simulation time, the plant

output does not perfectly follow the commanded trajectory. For the first sinusoid peak, the tracking error is relatively large (18%), but then starts decaying over the next three peaks until it finally fluctuates within a relatively small band (61%) for the remainder of the event, as shown in Figure 52.

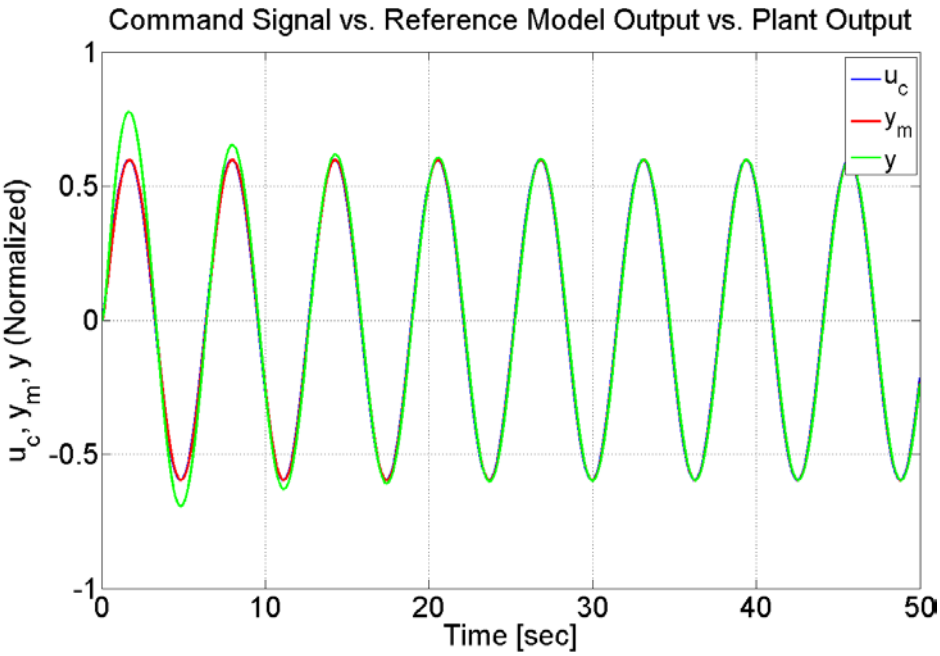

Figure 51: Output Tracking Performance.

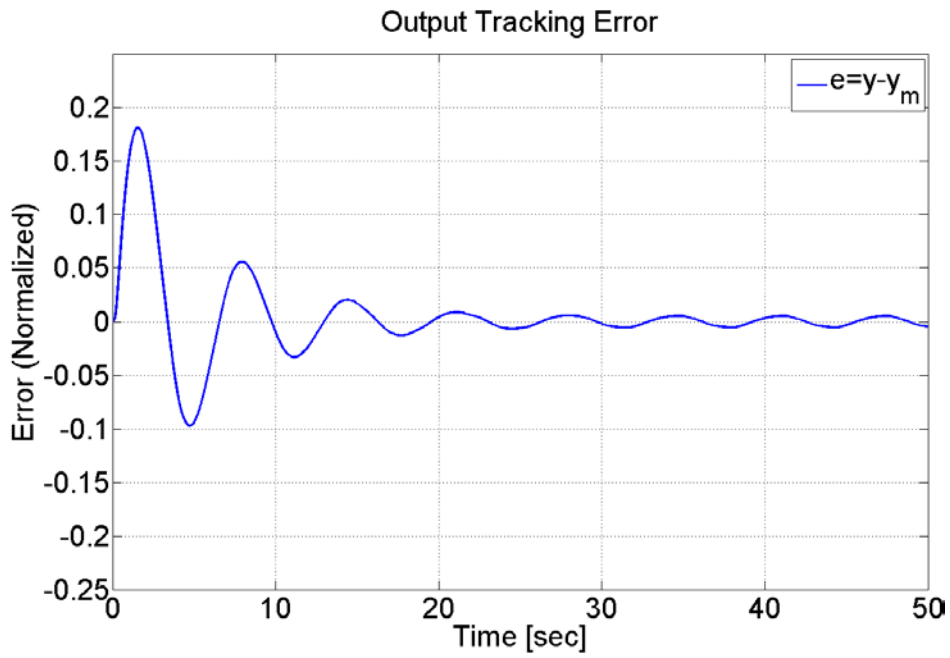

Figure 52: Output Tracking Error.

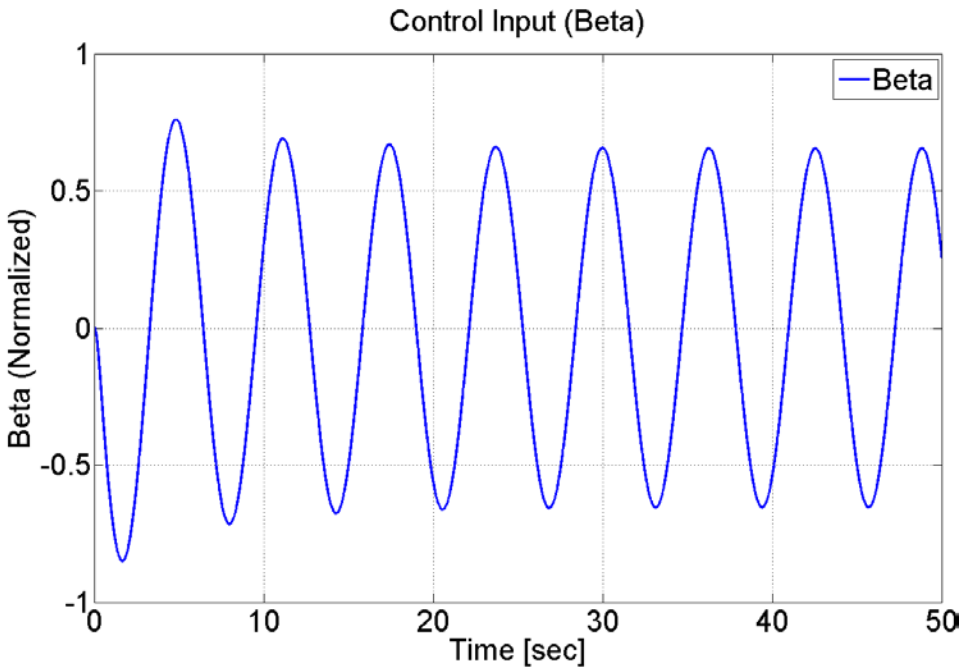

Figure 53: Control Input Signal.

Given that the initial parameter estimates are not exact, the control input signal (β), shown in Figure 53, overcompensates in the beginning until asymptotic

tracking is achieved. As for the plant parameter estimates, shown in Figure 54 through Figure 57, unsurprisingly they ultimately reach a steady-state level; however, they do not converge to their true values, which is consistent with adaptive control theory. A self-tuning regulator can guarantee zero tracking error asymptotically, but it does not guarantee that the adaptive estimates of the parameters will converge to their true values. This is a characteristic feature of all adaptive systems, in which the input signal must satisfy certain persistent excitation (PE) conditions for the convergence of parameter estimates to their true values. The simulated sinusoid does not qualify as a PE signal to estimate the considered four plant parameters; in fact, a sinusoid is a second order persistently exciting signal that can estimate two parameters at the most (Astrom & Wittenmark, 2008).

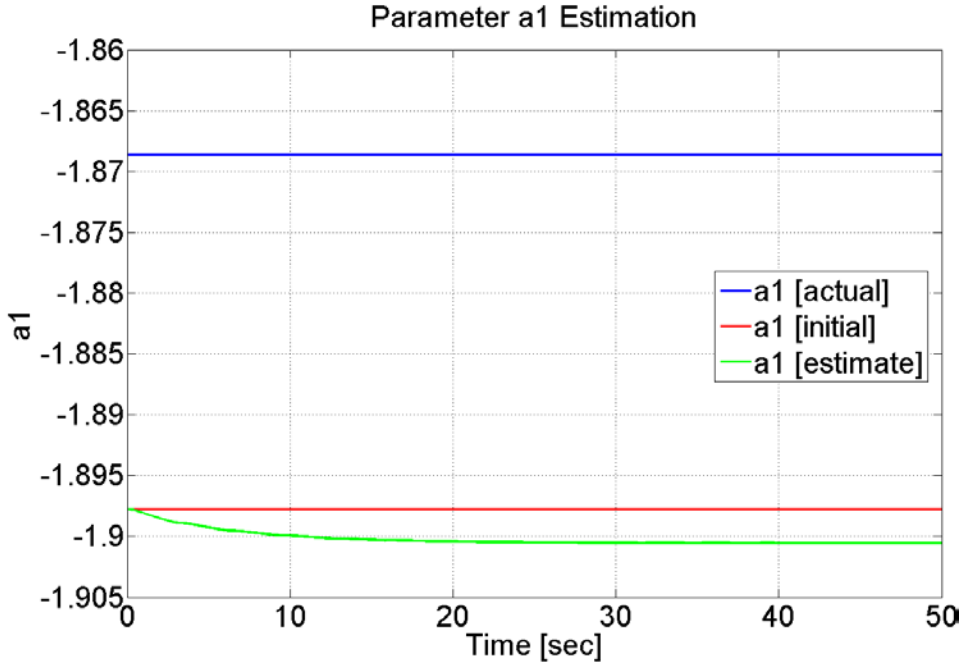

Figure 54: Parameter a_1 Estimate.

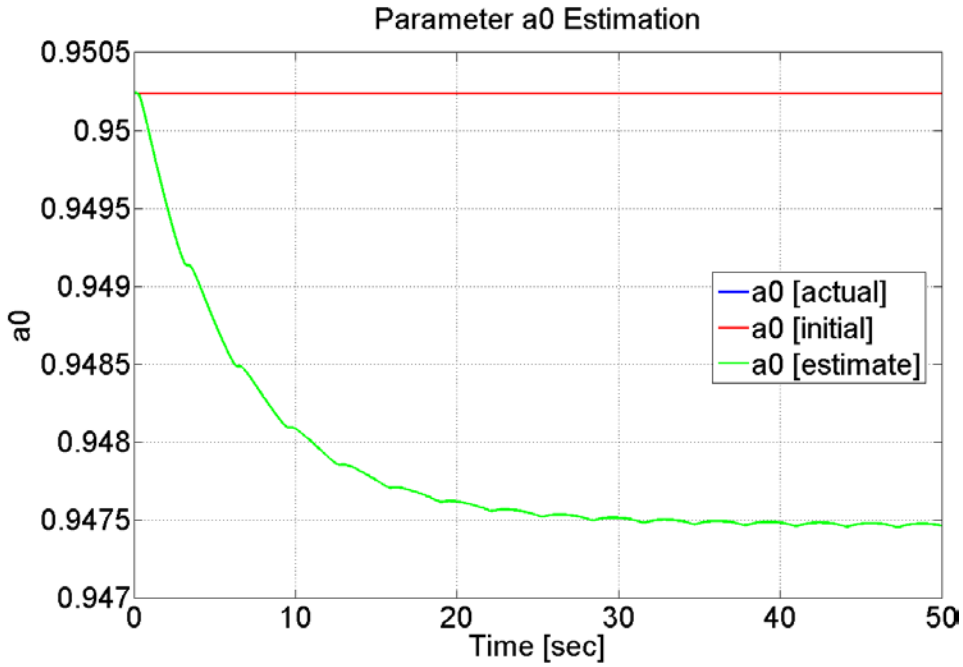

Figure 55: Parameter a_0 Estimate.

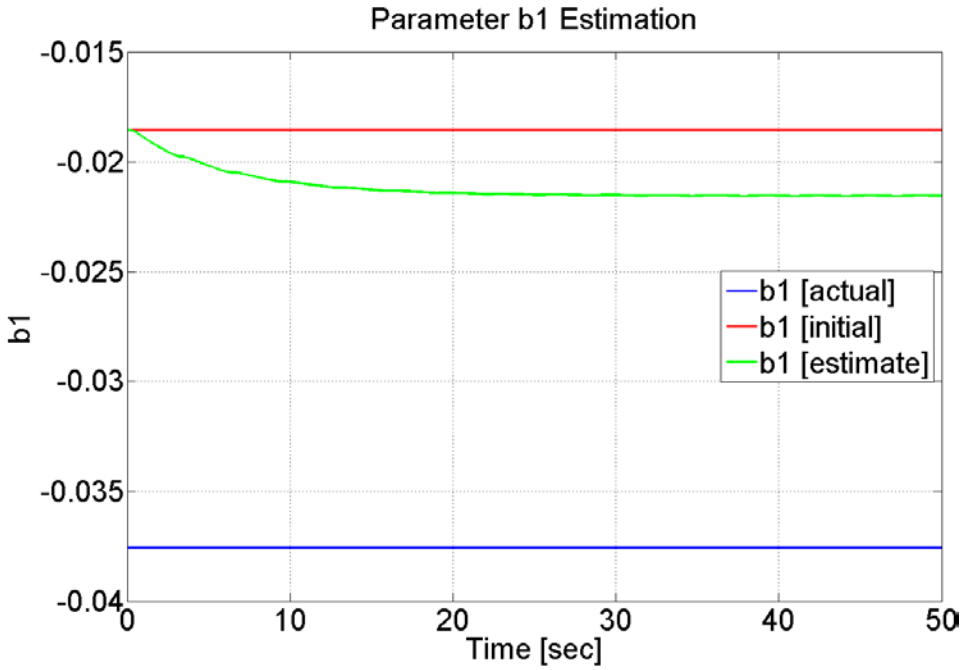

Figure 56: Parameter b_1 Estimate.

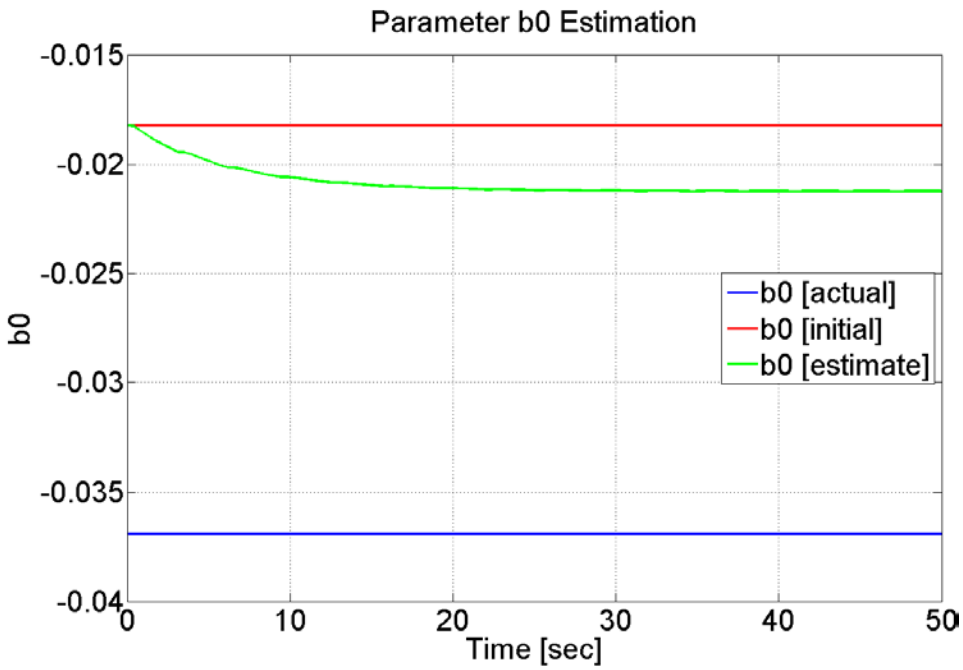

Figure 57: Parameter b_0 Estimate.

5.2.5 Experimental Results

To test the performance of the adaptive controller and parameter estimator in real-time, a model was compiled and deployed into the electronic control unit of the designated prototype test vehicle (compact wheel loader). Appropriate sensors, signal conditioning modules, and data acquisition system were installed. To validate the adaptability of the controller to varying conditions, two steering maneuvers were simulated successively. The first cycle was performed with an empty bucket, and the second cycle included loading the bucket with a dummy concrete load of 790kg shown in Figure 58.

Figure 58: Dummy Concrete Load in the Loader's Bucket.

The steering maneuver consisted of persistent articulation from one side to another for 100 seconds at approximately 0.5 normalized actuator velocity. The same adaptation factors were utilized in both cycles. The dummy load addition simulates the continually varying load inertia that the machine faces in typical operation, and can also simulate varying surface conditions that the machine operates on (e.g. asphalt, concrete, snow), which also result in varying actuator effort.

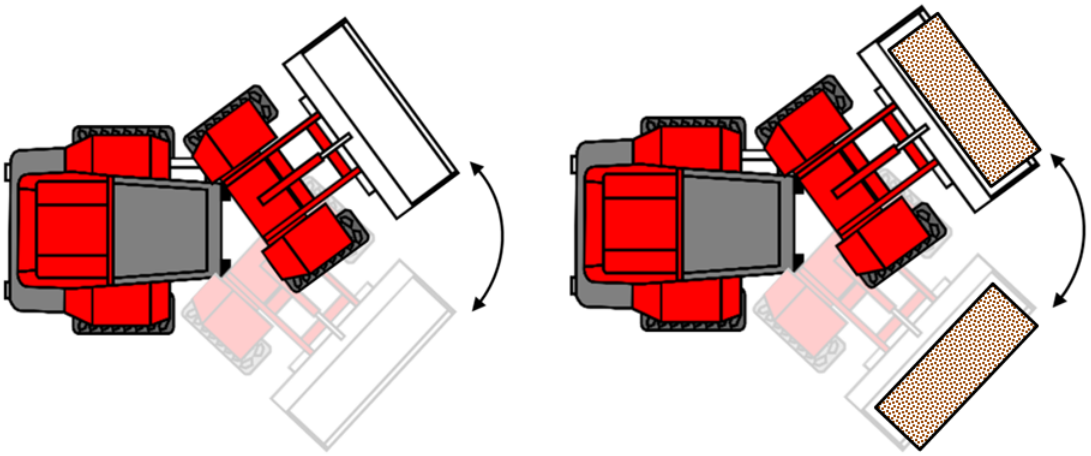

Figure 59: Steering Maneuver – Top View.

Figure 60 and Figure 61 show the measured results acquired on the machine. Three plots are included in each figure: the normalized steering wheel velocity, the normalized pump displacement or swash plate angle, and the normalized articulation velocity which corresponds to the steering actuator velocity.

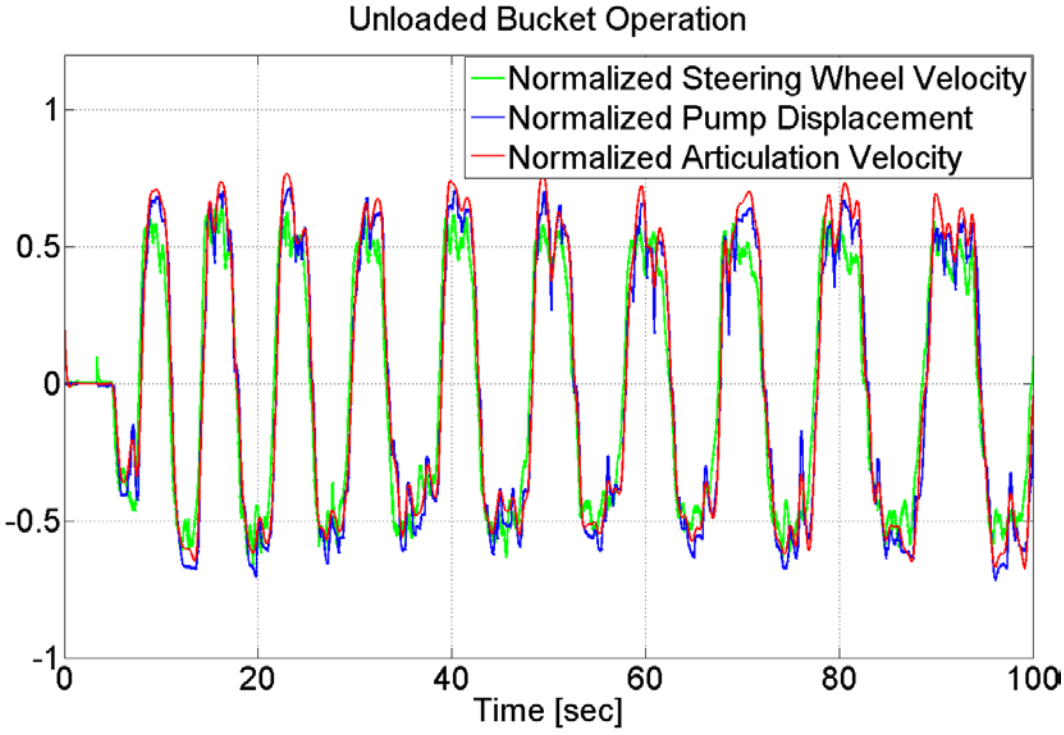

Figure 60: Unloaded Bucket Operation.

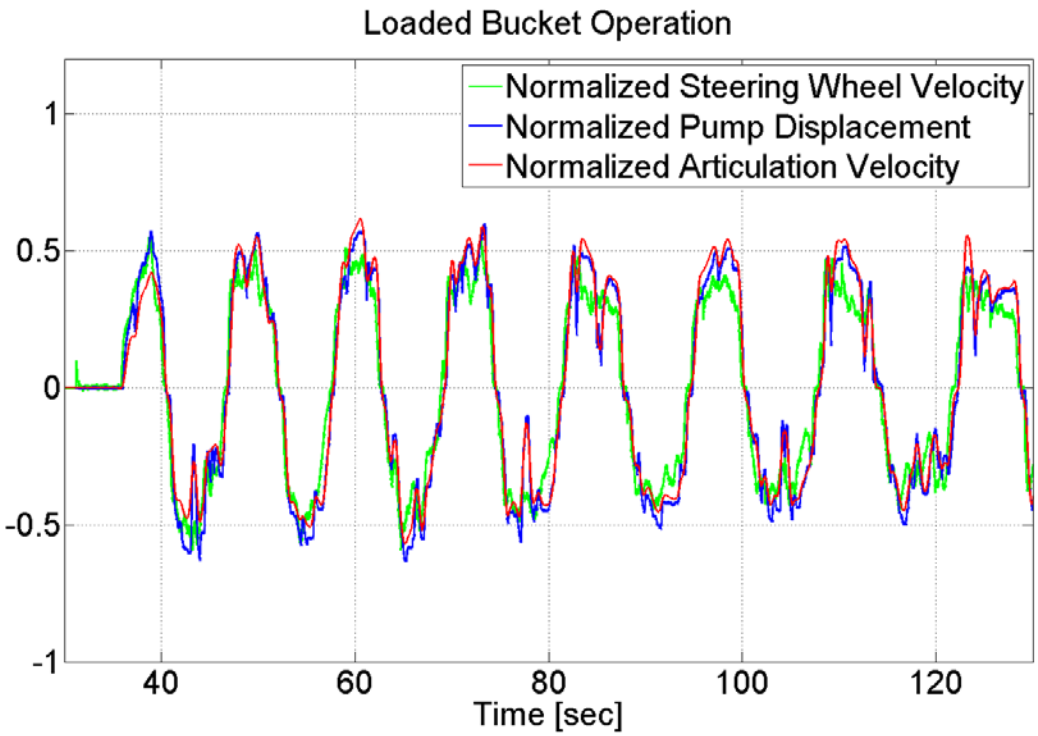

Figure 61: Loaded Bucket Operation.

Experimentally, the adaptive controller exhibits effective performance in the loaded and unloaded cases. Examining the performance plots reveals that the initial parameters are closer to the unloaded bucket case, as the normalized articulation velocity (output) tracks the normalized pump displacement (input) almost from the onset. On the other hand, with a loaded bucket the output does not track the input in the first steering cycle and the controller takes approximately 20 seconds before asymptotic tracking is achieved. Notice that the event time starts at 30 seconds, the time at which the adaptive controller is activated after the bucket is loaded. A final remark is made here concerning signal noise that stems from the utilized sensor and the devised algorithm to

attain steering wheel velocity from a position sensor, which requires differentiation, initialization, and revolution counting. This necessitates the implementation of a digital filter to smooth out the input signal. Also, the control input signal can have unrealizable transients at certain times, which are eliminated via a properly designed filter that introduces a minor delay, which resolves the issue and regulates the control signal. The above practical implementation issues are highlighted in (Astrom & Wittenmark, 2008) and signal filtration is in fact recommended as a remedial action.

5.3 Chapter Summary

- The complete system model is analyzed for controllability and output controllability to determine the system characteristics and what can and cannot be achieved from a control engineering standpoint.
- The system is found to be not completely state controllable based on a single steering input.
- With the selected single input and single output combination, the system is confirmed to be output controllable.
- A reduced model is derived and used for synthesizing a controller that combines feedforward and feedback control to achieve command tracking.
- The feedforward controller is based on a transfer function that represents the inverse of the previously derived plant transfer function.
- The feedback controller is based on full state feedback acting as a regulator on the state *errors*, which in turn are estimated by a state observer designed via pole placement technique.

- The controller design was validated in both simulation and experimentally, and yielded acceptable tracking performance, response, and control effort.
- An indirect adaptive velocity controller that allows for coping with parametric uncertainties and uncertain nonlinearities is designed.
- An indirect self-tuning regulator algorithm is selected for its low computational expense, suitability for the application on hand, and plant parameter estimation capability.
- The indirect self-tuning regulator combines the MDPP method for controller design with Kacsmarz's projection algorithm for estimating the plant uncertain parameters in real-time.
- The control design is validated in numerical simulations and experimentally on the prototype test vehicle.
- The controller was capable of adapting to varying inertia loads, demonstrating the efficacy of the adaptive scheme in the face of uncertainties.

Acknowledgement

The author would like to acknowledge the American Society of Mechanical Engineers (ASME) for providing the copyright permission to use the work presented in this chapter, which is in production by the *Journal of Dynamic Systems, Measurement, and Control*:

Daher, N. and Ivantysynova, M. 2014. An Indirect Adaptive Velocity Controller for a Novel Steer-by-Wire System. *ASME Journal of Dynamic Systems, Measurement, and Control*, Vol. 136, Issue 5, pp. 051012. http://dynamicsystems.asmedigitalcollection.asme.org/article.aspx?articleid=1849803

CHAPTER 6. INSTRUMENTATION AND EXPERIMENTAL SETUP

To validate the design, sizing, dynamic modeling, and controller design of the new DC steering system, a representative articulated frame steering vehicle in the form of a compact five-ton wheel loader, shown in Figure 62, is designated for that purpose. However, prior to the implementation of the new DC steering system, the stock machine with its hydrostatic steering system was baseline tested with the intent of capturing the benchmark fuel consumption, machine productivity, steering feel, and other relevant metrics. After baseline testing was completed, the machine was overhauled to retrofit the new DC steering system with its own pump, steering column assembly, sensors, controller and data acquisition system. Upon completion, the same baseline tests were repeated and the new performance results were analyzed and compared against the stock system showing considerable fuel savings, productivity gain, and overall fuel efficiency increase.

Figure 62: Baseline Test Vehicle – Compact Wheel Loader.

6.1 Instrumentation

Two instrumentation stages were performed: the first stage corresponds to the baseline machine, and the second stage corresponds to the overhauled prototype machine. In stage one, the baseline wheel loader was instrumented with an array of sensors, signal conditioning modules, and a data acquisition system in order to record relevant measurements for later comparison. The next sections describe the different instruments installed in stage one.

6.1.1 Articulation Angle Sensor

The *relative* angle between the front and rear frames is the articulation angle, and is measured via an angular magnetic sensor mounted at the articulation joint. The sensing element is affixed to the mounting bracket, which is attached to the rear frame, and the magnet is attached to the cap at the bottom of the hinge as shown in Figure 63.

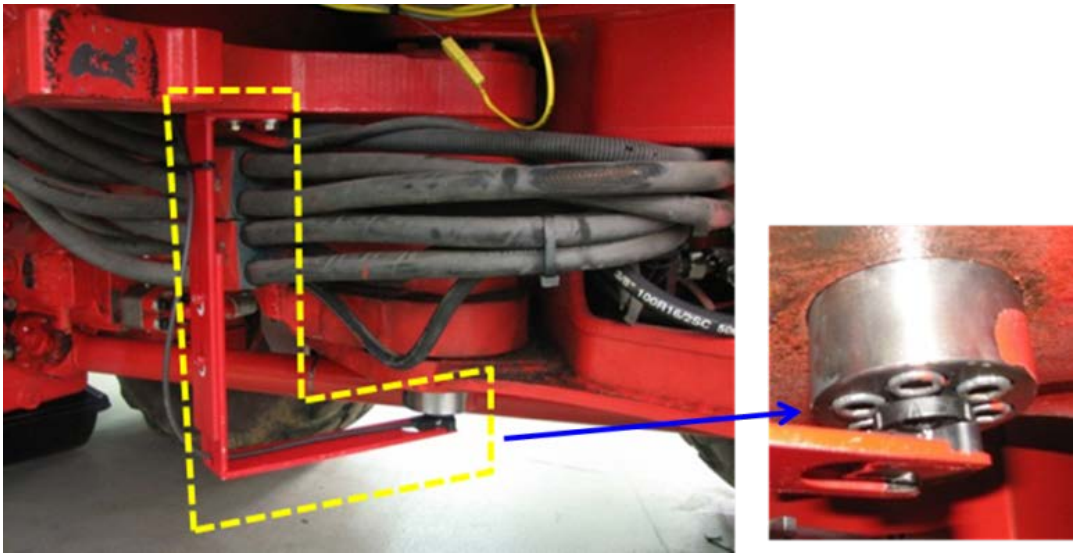

Figure 63: Articulation Angle Sensor.

The sensor's relevant specifications are listed in Table 3. The machine's articulation range is ±41° from lock-to-lock.

Table 3: Articulation Angle Sensor Specifications.

Sensor	**Articulation Angle**
Sensing Principle	Magnetic
Manufacturer	ASM
Part / Model Number	PRAS27
Input	18-36 VDC
Output	0.5-10 V
Range	0-105°
Resolution	0.03%
Repeatability	±0.03%
Linearity	±0.5%

6.1.2 Vehicle Speed Sensor

Given that the vehicle speed is a critical signal for the implementation of variable-rate and variable-effort steering for the new DC steering system, the wheel loader is instrumented with a digital speed sensor that is not available in the stock machine. The selected sensor functions as a radar that transmits microwaves that bounce off the ground, which returns part of the wave's energy to the transmitter, thus allowing for measuring the machine's true ground speed, independent of wheel slip. This is basically the principle of radar Doppler shift effect given later in Eq. (142).

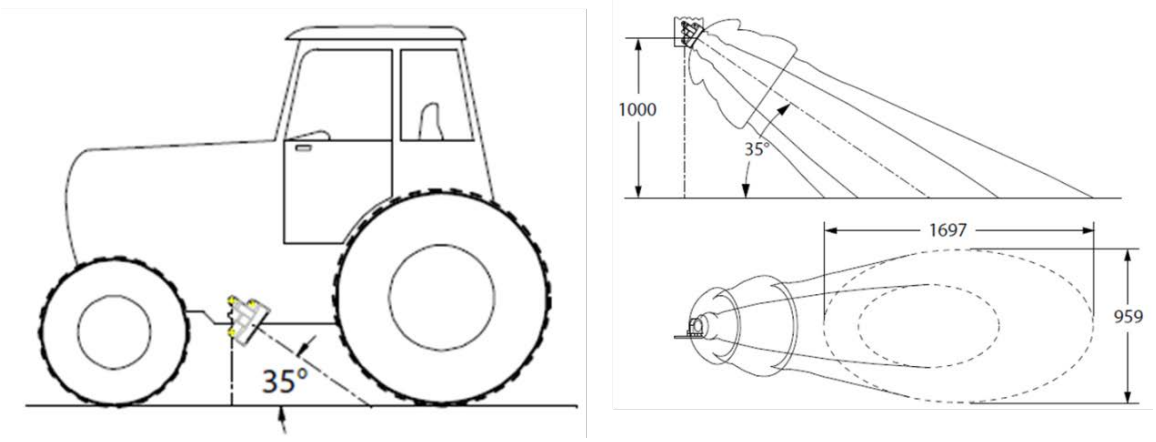

Figure 64: Recommended Installation Configuration and Doppler Signal Beam Line of Sight (Courtesy: Parker Hannifin).

This sensor is in fact used in various agricultural and forestry machinery that operate in comparable conditions (speed range, vibration, rough terrains) as the baseline wheel loader, which makes it suitable for this application.

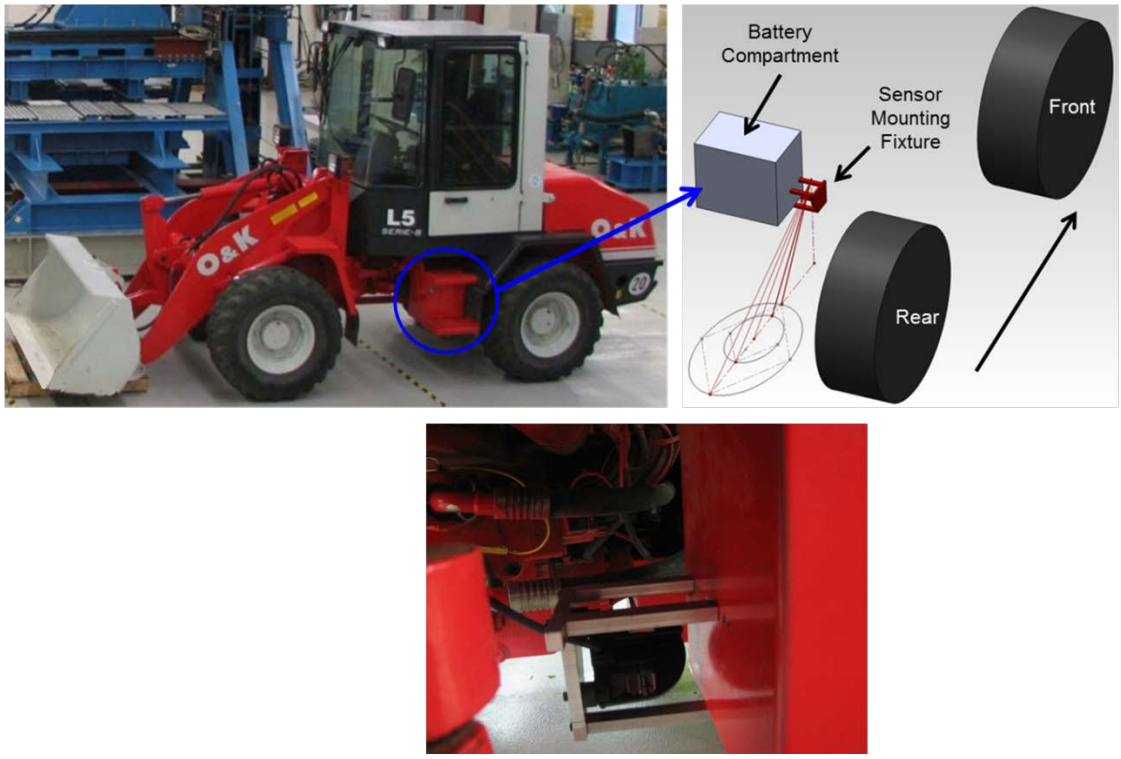

Figure 65: Vehicle Speed Sensor Installation.

The sensor's main specifications are given in Table 4.

Table 4: Vehicle Speed Sensor Specifications.

Sensor	**True Ground Speed**
Sensing Principle	RADAR
Manufacturer	Parker Hannifin
Part / Model Number	TGSS 740
Input	9-16 VDC
Output	58.9 Hz/mph (36.8 Hz/kph)
Range	0.3-44 mph (0.5-70 kph)
Accuracy	±1%: 2.0 to 44 mph (3.2 to 70 kph) ±3%: 0.2 to 2 mph (0.32 to 3.2 kph)

The sensor's output frequency is proportional to the speed of motion. With a selected transceiver frequency of 24.125GHz, the output frequency at 35° mounting angle is 58.9Hz/mph. The Doppler shift frequency is calculated as:

$$f_d = 2V\frac{f_0}{c}\cos(\Phi_s). \tag{142}$$

where f_d is the Doppler shift frequency (Hz), V is the velocity of the moving target (mph), f_o is the transceiver frequency (Hz), c is the celerity of light (671×10^6 mph), and Φ_s is the angle between the beam and path of target (°).

6.1.3 Yaw Angle Rate and Lateral Acceleration Sensor

Given the new DC steering system capability of providing active safety measures (e.g. yaw stability control), a yaw angle rate sensor is installed to measure the rate of rotation of the machine around the vertical axis. The selected yaw rate sensor also has a built-in accelerometer for measuring lateral acceleration. The yaw rate sensor is installed on the front frame near its center of gravity as shown in Figure 66.

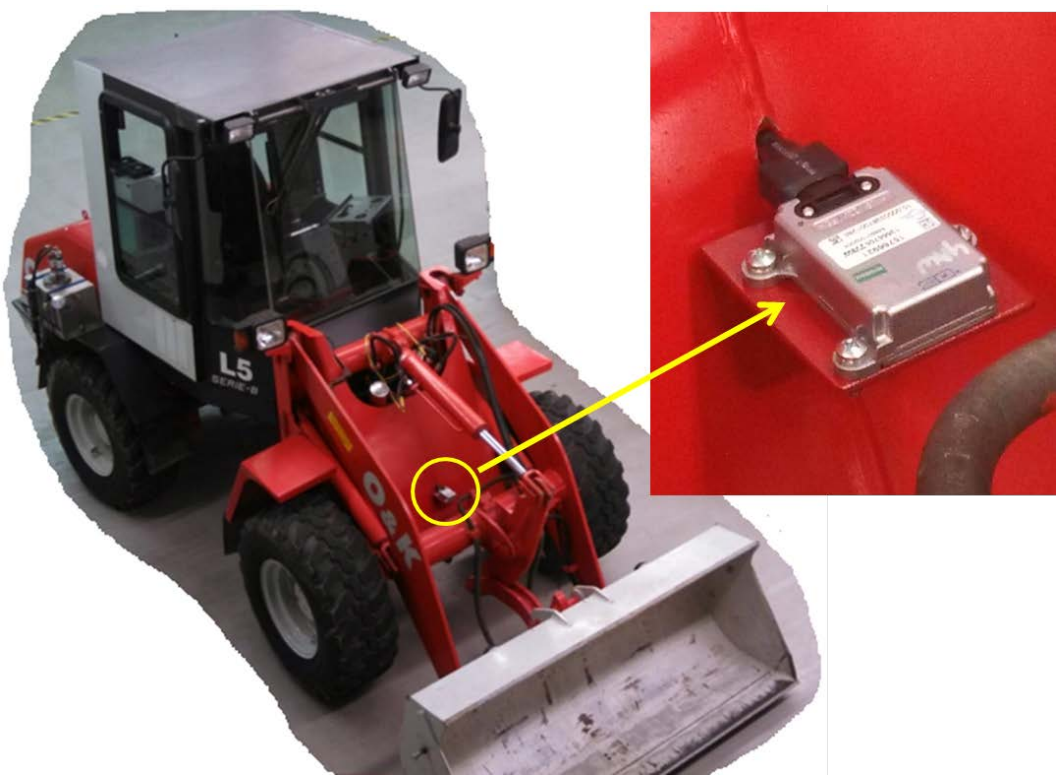

Figure 66: Yaw Angle Rate and Lateral Acceleration Sensor.

The key specifications of the yaw rate sensor are listed in Table 5 below.

Table 5: Yaw Rate Sensor Specifications.

Sensor	**Yaw Angle Rate**
Sensing Principle	Piezoelectric
Supplier	TRW Automotive
Sensitivity	26.27mV/°/s, ratiometric to supply voltage
Sensitivity Error	±3%
Linearity	±0.3% of full scale
Offset	2.5V±0.107V (± 4°/s)
Output Range	0.125-4.875 V

6.1.4 Steering Wheel Torque and Angle Sensors

To quantify the driver's steering input, the hand wheel must be equipped with both an angle sensor that measures rotational angle and speed, and a torque sensor that measures steering effort. The selected torque sensor uses a load cell that converts torque into an electrical signal by sensing the physical deformation, and therefore electrical resistance change, in a set of strain gauges. Given the low signal amplitude of strain gauges (milliamp range), a built-in amplifier is used to convert the output into a usable voltage range.

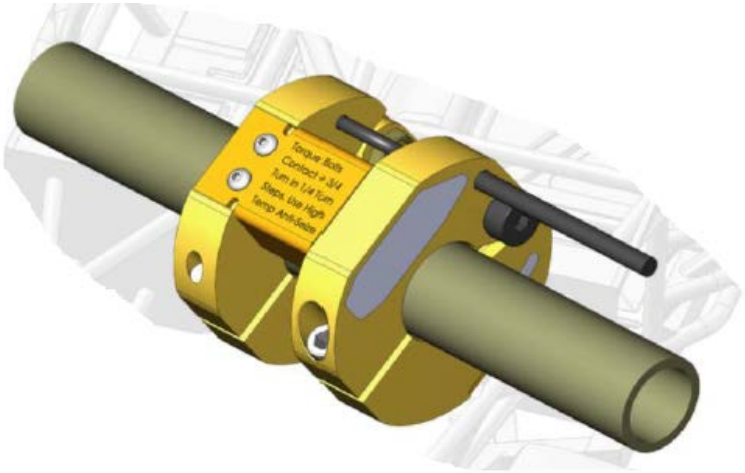

Figure 67: Steering Wheel Torque Sensor (Courtesy: Raetech Motorsports).

This type of sensor is used to accurately measure steering effort in various applications with an operating range of ±47Nm, which is suitable for the vehicle under consideration. The sensor's main specifications are listed in Table 6.

Table 6: Steering Wheel Torque Sensor Specifications.

Sensor	**Steering Wheel Torque**
Sensing Principle	Load Cell
Manufacturer	Raetech Motorsports
Part / Model Number	1169-01-06-404
Input	8-36 VDC
Output	0.1-4.9 V
Range	±35 ft-lb (± 47 Nm)
Static Error Band	±0.70%
Nonlinearity	±0.50%
Hysteresis	±0.50%

The sensor requires calibration with preset steering shaft configuration relative to its diameter, wall thickness, and material properties. This required the design and machining of a custom adapter, which is shown in Figure 68.

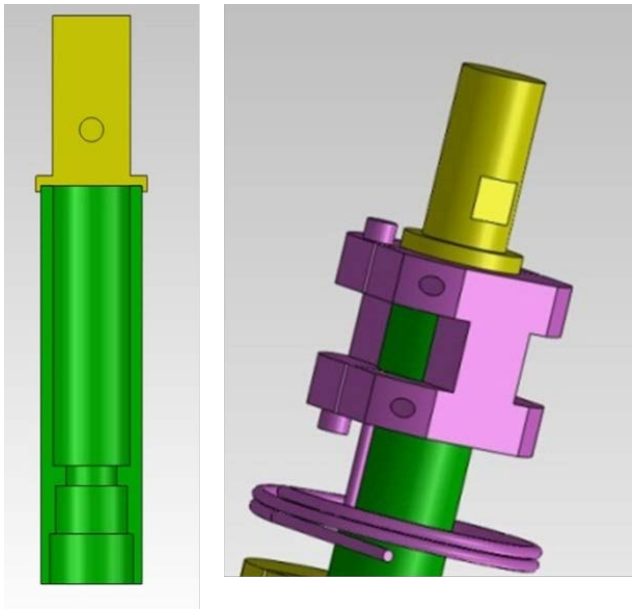

Figure 68: CAD Model of the Torque Sensor Adapter.

Prior to finalizing the adapter design, stress and deflection analysis is performed to verify that the designed adapter can endure the maximum applied steering loads, and to ensure that no additional deflection is introduced by the adapter.

Stress and Deflection Analysis

The baseline steering shaft is first analyzed for maximum torsional shear stress and twist angle, which are used as reference values for the design of the torque sensor adapter. The equations for calculating torsional shear stress and the resultant twist angle are given in Eq. (143) and Eq. (144) respectively.

$$\tau_{SW} = \frac{T_{SW}\, r_o}{J_P}. \tag{143}$$

where τ_{SW} is the torsional shear stress, T_{SW} is the steering wheel torque, r_o is the steering shaft outer radius, and J_p is the shaft's polar moment of inertia.

$$\varepsilon_{SW} = \frac{\tau_{SW} l}{G r_o}. \tag{144}$$

where ε_{SW} is the twist angle, l is the length of the considered cross-section, and G is the material's shear modulus.

For the baseline steering shaft, whose properties are given in

Table 7, the torsional shear stress at a maximum steering wheel torque of 47.45Nm is calculated to be 35.3 MPa, which is 9.1% of the material's yield strength. The resultant strain level is 0.441 millistrain corresponding to a twist angle of 0.092°. Since the selected torque sensor only accepts a shaft with a standard outer diameter of 25.40mm, these above results are used to design the

proper inner diameter of the adapter resulting in a wall thickness that yields similar stress levels and deflections.

Table 7: Baseline Steering Shaft Properties.

Material	1018 Steel	
Outer Radius, r_o	0.0110	m
Inner Radius, r_i	0.0085	m
Sensor Bolt-on Length, L	0.0400	m
Shear Modulus, G	8.00E+10	N/m^2
Yield Strength	3.86E+08	N/m^2
Polar Moment of Inertia, J_p	1.48E-08	m^4

Table 8 lists the properties of the designed steering torque adapter, which has a maximum torsional stress of 45.0MPa, a maximum strain of 0.563 millistrain, and a corresponding maximum twist angle of 0.102°.

Table 8: Steering Torque Adapter Properties.

Material	1018 Steel	
Outer Radius, r_o	0.0127	m
Inner Radius, r_i	0.0115	m
Sensor Bolt-on Length, L	0.0400	m
Shear Modulus, G	8.00E+10	N/m^2
Yield Strength	3.86E+08	N/m^2
Polar Moment of Inertia, J_p	1.34E-08	m^4

The steering wheel angle sensor is selected to be non-contact for durability and reliability purposes. The sensing element is affixed to the stationary steering

column housing and the magnet collar is attached to the torque sensor adapter, which rotates with the hand wheel.

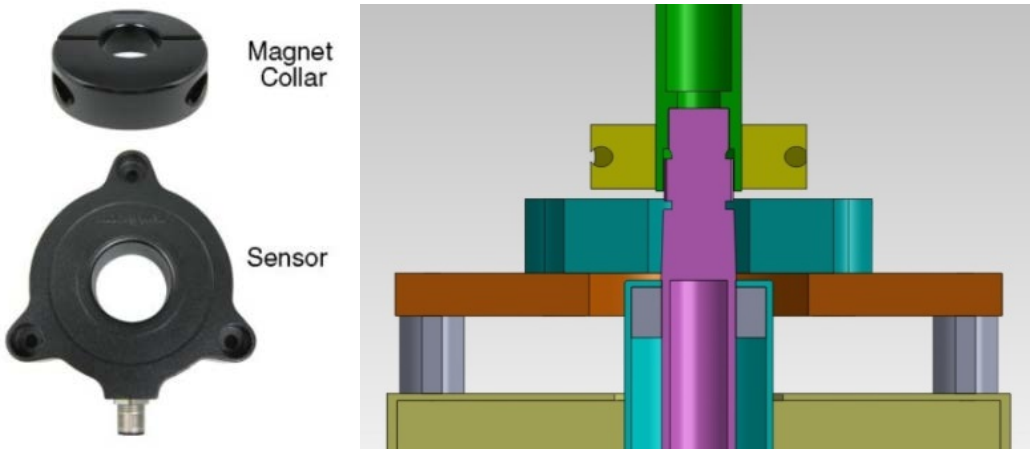

Figure 69: Steering Wheel Angle Sensor Illustration (Courtesy: Honeywell).

The main specifications of the steering wheel angle sensor are given in Table 9.

Table 9: Steering Wheel Angle Sensor Specifications.

Sensor	**Steering Wheel Angle**
Sensing Principle	Magnetic
Manufacturer	Honeywell
Part / Model Number	SMART
Input	12-30 VDC
Output	4-20 mA
Range	0-360°
Resolution	0.01°
Linearity	±0.03% @ 25°C
Offset	-0.044% (min) to 0.022% (max)
Accuracy	±0.069 %
Sensitivity	44.43-44.48 μA/°

The final design of the mounting fixtures and adapters used to install the steering wheel angle and torque sensors is shown in Figure 70.

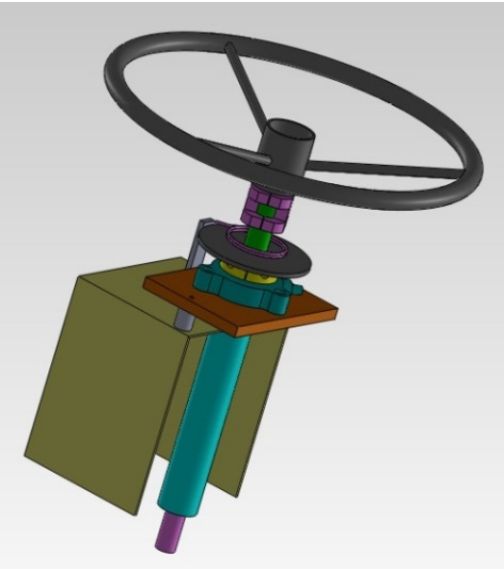

Figure 70: CAD Model of the Steering Wheel Angle and Torque Sensors Mounting Fixtures and Adapters.

Figure 71: Installation of the Steering Wheel Angle and Torque Sensors.

Multiple concepts were investigated as cable management solutions to extend and retract the torque sensor wiring harness as the hand wheel rotates. One solution is shown in the final implementation pictured in Figure 71. However, this solution only provides few steering turns at a time before the cable is fully

consumed and coiled inside the housing. Another solution, which allows for multiple steering wheel turns without rapidly consuming the torque sensor cable, is based on the pulley system shown in Figure 72. The system utilized four pulleys to achieve the desired reduction ratio to perform baseline testing without interruption to free up the torque sensor cable.

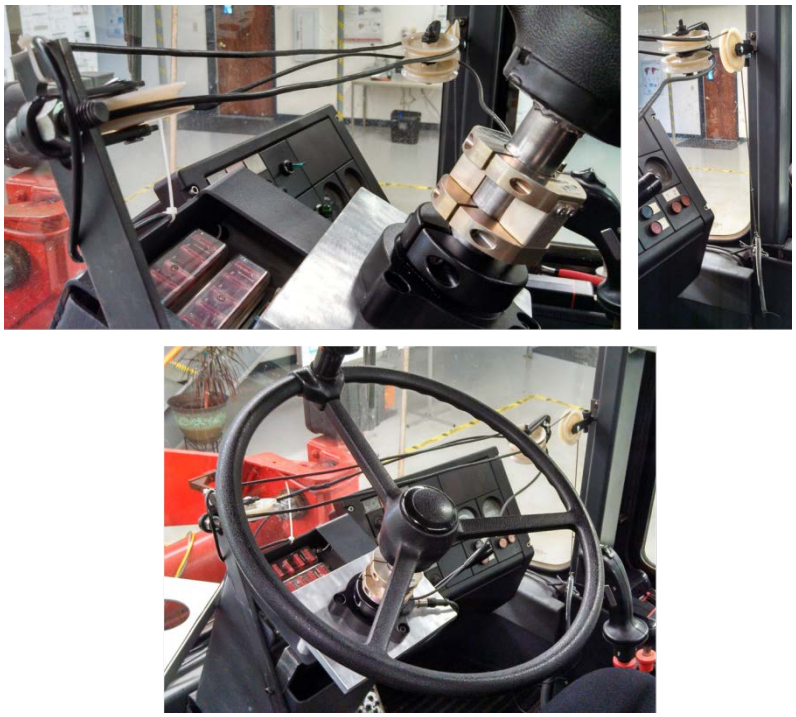

Figure 72: Pulley System for Torque Sensor Cable Management on Stock Machine.

6.1.5 Engine Speed and Throttle Sensors

In the hydrostatic- and the DC- steering systems, the steering pump runs at the same speed as the engine. To acquire the engine speed, two studs are added to the engine crankshaft pulley and a hall-effect sensor is installed to sense the magnetic field change as the ferrous studs pass by. The sensor outputs a frequency that is converted to analog voltage signal via a frequency-to-voltage

converter that employs electrical resistors and capacitors. In the absence of an accelerator pedal sensor, the engine throttle is measured via an angular sensor that measures the rotation of the throttle linkage at the engine housing.

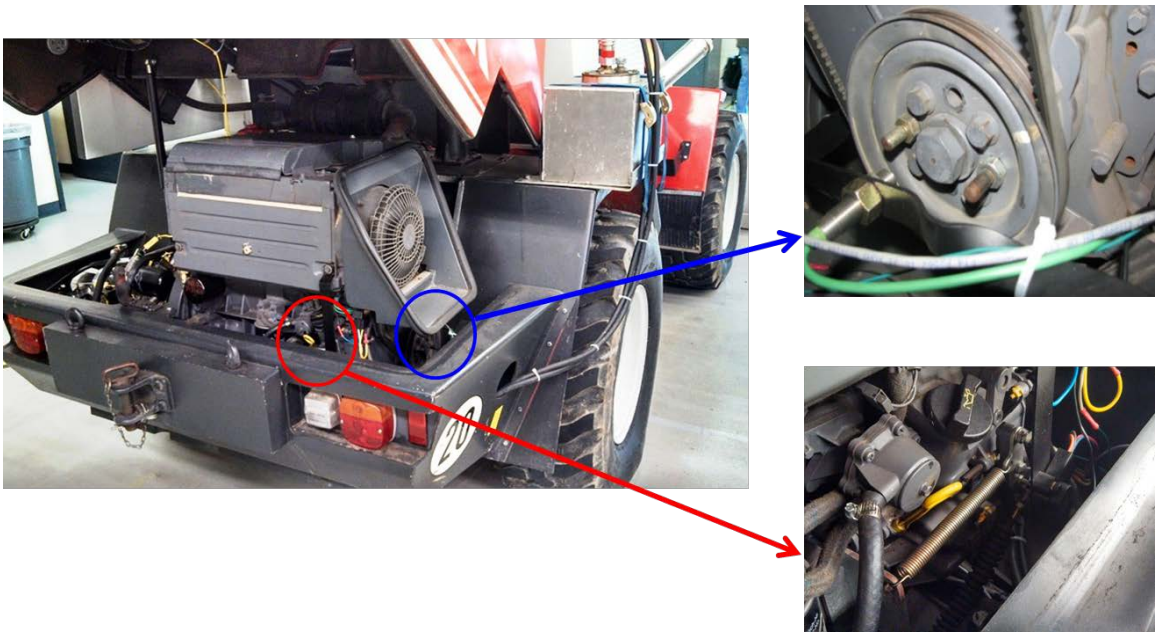

Figure 73: Engine Speed (Blue) and Throttle (Red) Sensors.

Table 10: Engine Speed Sensor Specifications.

Sensor	**Engine Speed**
Sensing Principle	Magnetic (Hall-effect)
Manufacturer	Honeywell
Part / Model Number	SNDJ-H3L-G02
Input	8-25 VDC
Output	Frequency (Square Wave) Output voltage HI: power supply voltage Output voltage LO: <0.5 Volt @ I = 25 mA
Range	0-15 kHz

Table 11: Engine Throttle Sensor Specifications.

Sensor	**Engine Throttle**
Sensing Principle	Potentiometer
Manufacturer	Parker Hannifin
Part / Model Number	RS70
Input	5.0 ±10% VDC
Output	0.5-4.5 V
Range	170°
Total Error (<=170°)	Max 3.0% FS
Hysteresis	1.0% when no shaft end float is allowed

6.1.6 Electronic Control Unit and Data Acquisition System

A National Instruments CompactRio real-time controller and data logger is specified for recording baseline measurements in addition to ultimately serving as a real-time controller for the new DC steering system.

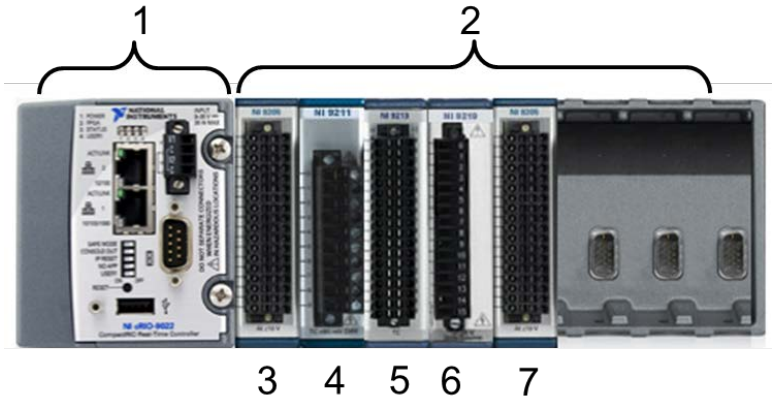

Figure 74: NI CompactRio Controller, Chassis, and Modules.

The image shown in Figure 74 specifies the components used for acquiring the baseline measurement data and are detailed below as numbered in the figure.

1. NI cRio-9024: Real-time Controller, 800 MHz, 512 MB DRAM, 4 GB Storage

2. NI cRio-9112: Chassis 8-Slot, Virtex-5 LX30 cRIO Reconfigurable Chassis
3. NI Module 9213: Thermocouple Input, +/- 80mV, 24-Bits, 16 channels
4. NI Module 9264: Analog Output, +/- 10V, 16-Bits, 16 channels
5. NI Module 9203: Analog Input (Current), ±20 mA, 16-Bits, 8 channels
6. NI Module 9205: Analog Input, +/- 10V, 16-Bits, 32 S.E. / 16 diff. channels
7. NI Module 9211: Thermocouple Input, +/- 80mV, 24-Bits, 4 channels

The real-time testing, simulation, and data acquisition software is based on National Instruments (NI) VeriStand 2011 version.

6.1.7 Electrical Wiring

Figure 75 shows the industrial enclosure that houses the controller, chassis, modules, sensor cables, and the remaining electronic components including frequency-to-voltage converters, wireless router, voltage converters, and terminal blocks that are used for providing the various voltage sources.

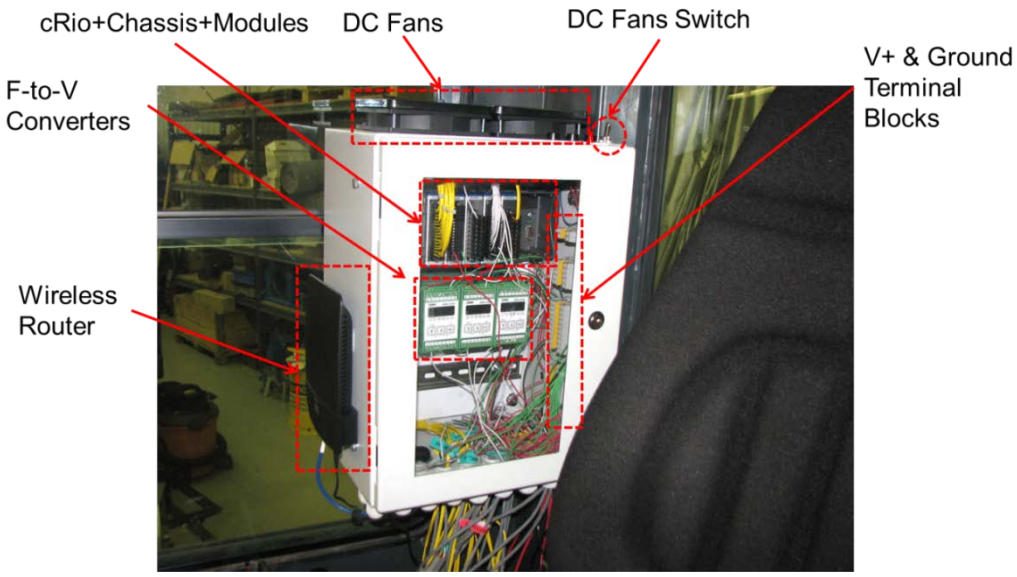

Figure 75: Fully Populated Industrial Enclosure.

Appendix B includes the overall wiring schematic of the data acquisition system utilized during baseline testing. The diagram shows two 12V batteries since the controller has its own dedicated battery, five data acquisition modules for handling various signal types, two direct current converters for providing 5V and 24V, an emergency stop switch that shuts off the engine in case of an emergency, and a series of relay switches that control the power-up and power-down routines.

Appendix C provides an enlarged view of the switches structure and logic, which control the sequence of events for *safely* powering the system up and down. The procedures for start-up, shut-down, and emergency shut-down are given in Appendix D.

6.1.8 Fuel Measurement System

For accurate measurement of fuel consumption during baseline testing, a secondary fuel tank was installed having a quick-disconnect design that allows for quickly switching back to the machine's primary fuel tank. The mass of the secondary tank (plus fuel) is measured pre- and post-testing via a digital scale with an accuracy of 1.0g. The devised system has excellent precision, simple design and manufacturing, and an economical cost.

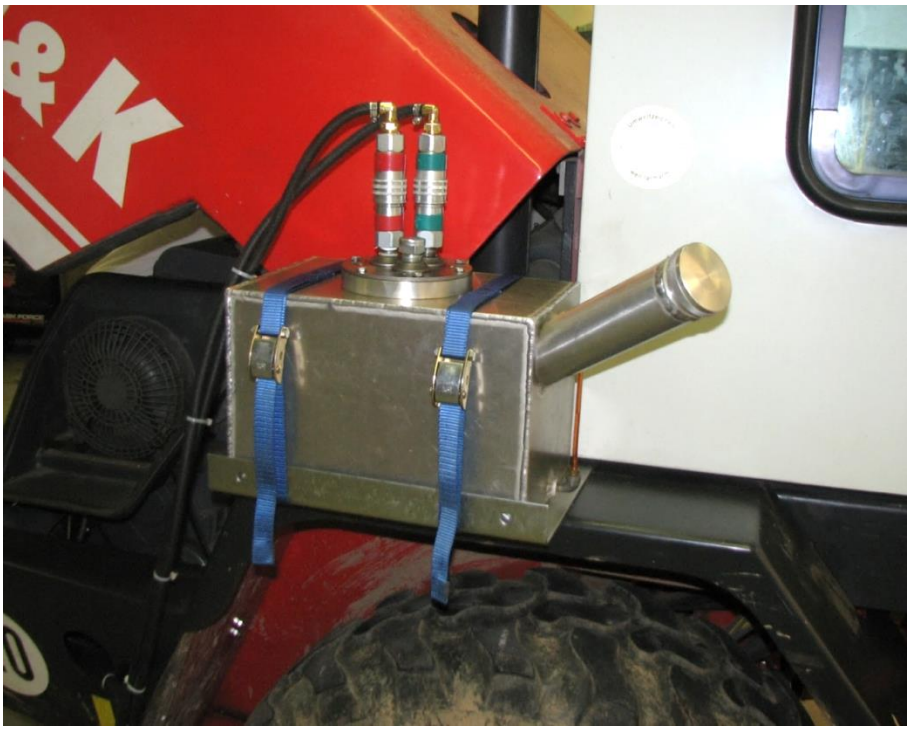

Figure 76: Secondary Fuel Tank.

6.2 Baseline testing

The short truck loading cycle is a standard cycle that is typically used in the mobile industry in order to characterize the entire machine performance with all functions operational. For instance, when the wheel loader executes the truck loading cycle, the working hydraulics (implement) functions as well as the hydrostatic transmission are active for a large portion of the cycle. This makes it really hard to pinpoint the contribution of the steering system alone, especially since the event includes limited steering maneuvers. This necessitated the need for devising a new cycle that can accurately assess the steering system's own contribution to the overall fuel consumption under specified conditions.

As such, a steering-only maneuver was devised where only the steering system is active during the cycle. The machine fully articulates from left to right while staying stationary in the longitudinal direction, and hence the transmission remains in neutral. The boom and bucket functions are maintained at predetermined settings requiring no hydraulic power supply. The axle loads are established with a fixed bucket load and specified surfaces. The engine throttle is held at its maximum level and the cycle duration is fixed.

Table 12: Steering-only Cycle Settings.

Articulation Angle	-41° to +41°
Bucket Load	790kg
Boom Angle	10%
Bucket Angle	40%
Engine Throttle	100%
Transmission Gear	Neutral
Ground Surface	Concrete and Grass
Cycle Duration	260s

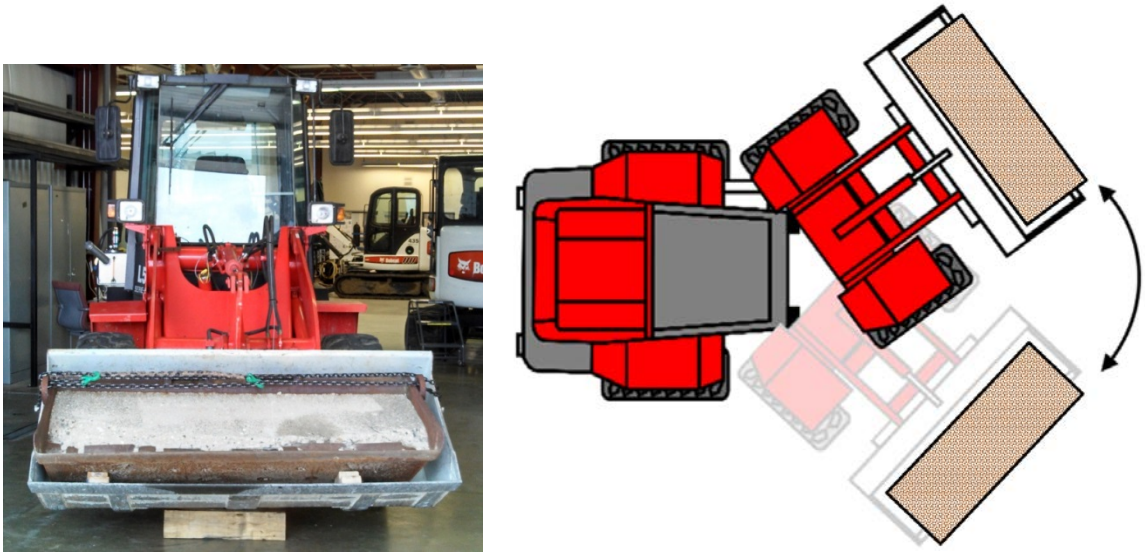

Figure 77: Baseline Testing of Wheel Loader – Steering-only Cycle.

6.3 DC Steering System Implementation

As seen in Figure 78, the new DC steering system requires the addition of two main components: a variable displacement pump and a tactile feedback device (TFD). From a top-level operation, the controller inputs the steering wheel angle and rate, vehicle speed, and vehicle articulation angle and then commands the appropriate pump displacement and steering wheel torque feedback level.

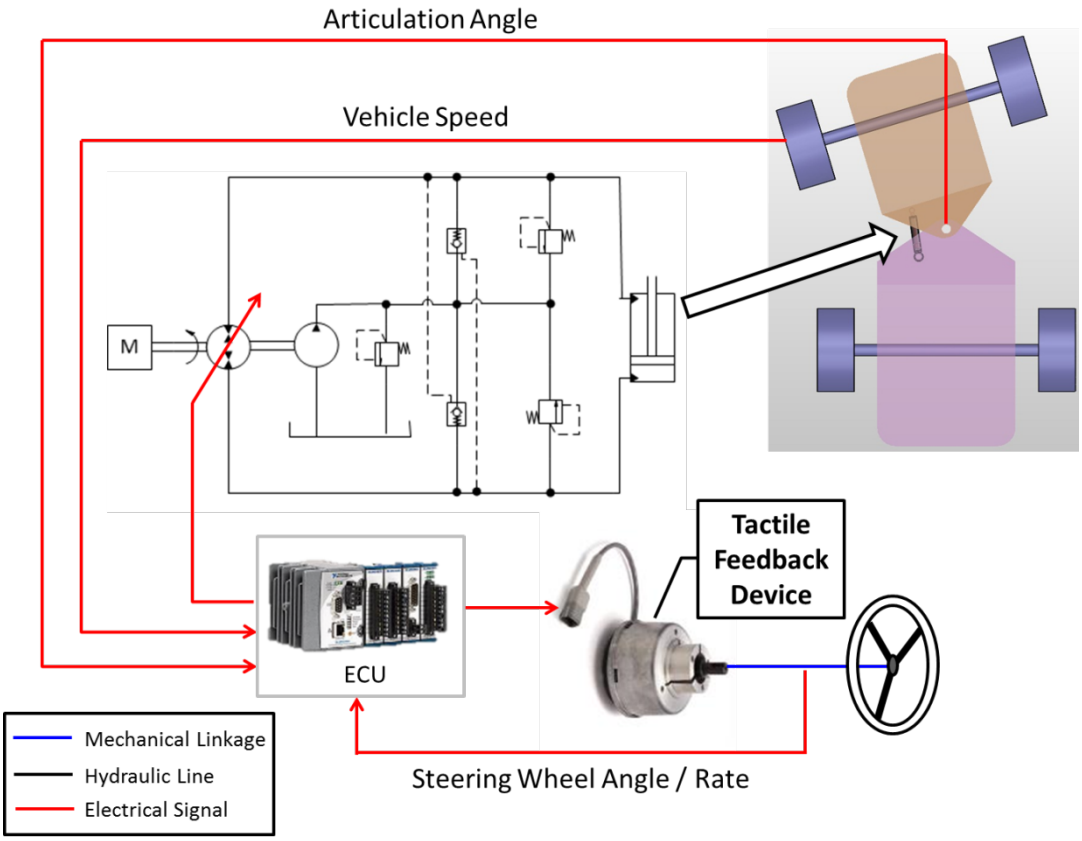

Figure 78: DC Steering System Diagram.

Before implementing the new DC steering system, the following hydrostatic steering system components are removed. The hydro-mechanical rotary valve unit is detached from the steering shaft, the priority-steer valve is removed, and the main supply pump is replaced with another, as will be explained later. The

new DC steering system requires the addition of a tactile feedback device, which is installed in the same location of the removed rotary valve at the bottom of the steering shaft. The new DC steering pump is installed in between the transmission pumps and the working hydraulics pump.

6.3.1 DC Steering Pump

Following the sizing procedures and results in section 3.2, an 18cm^3/rev variable displacement axial piston pump is selected. A 20L/min proportional directional control valve having an appropriate bandwidth frequency is used. The original main gear pump plus charge pump combination assembly is augmented with an additional 5cm^3/rev charge pump, dedicated for the DC steering system low pressure source. Figure 79 shows the schematic of the new hydraulic system of the prototype wheel loader including the DC steering pump and charge pump.

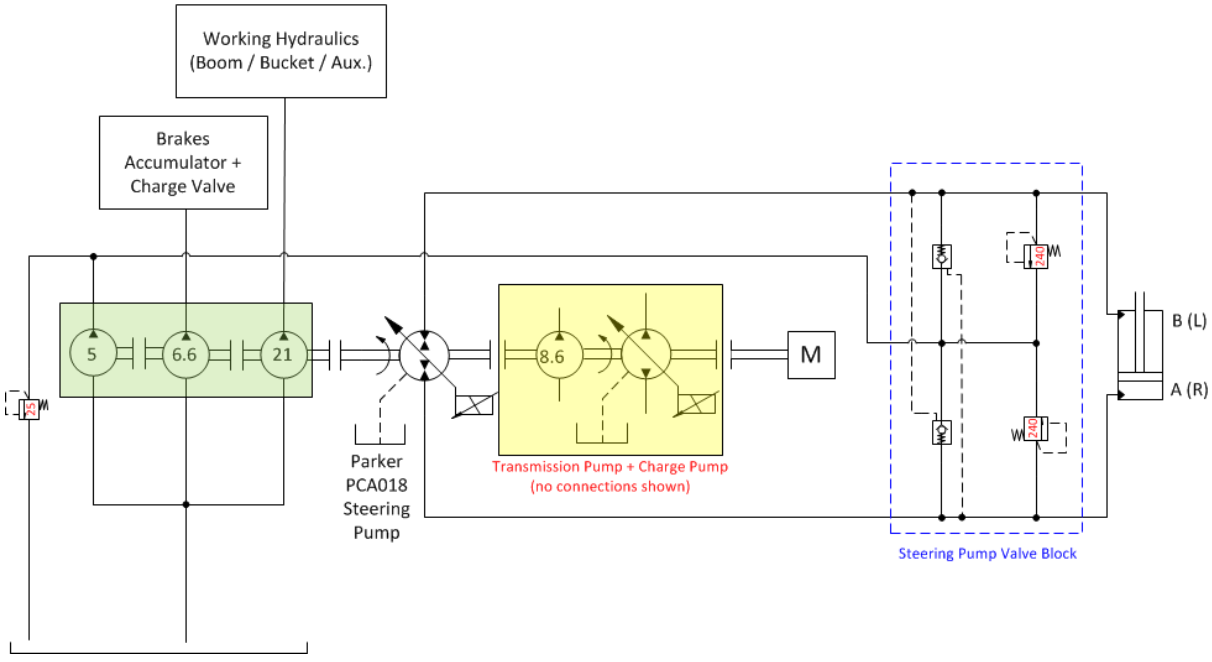

Figure 79: Wheel Loader New Hydraulic System Schematic.

Figure 80 shows the installation of the hydraulic components of the DC steering system: the through-shaft pump is enclosed in the red dashed rectangle, the proportional valve is enclosed in the green dashed rectangle, and the charge pump is enclosed in the blue dashed rectangle.

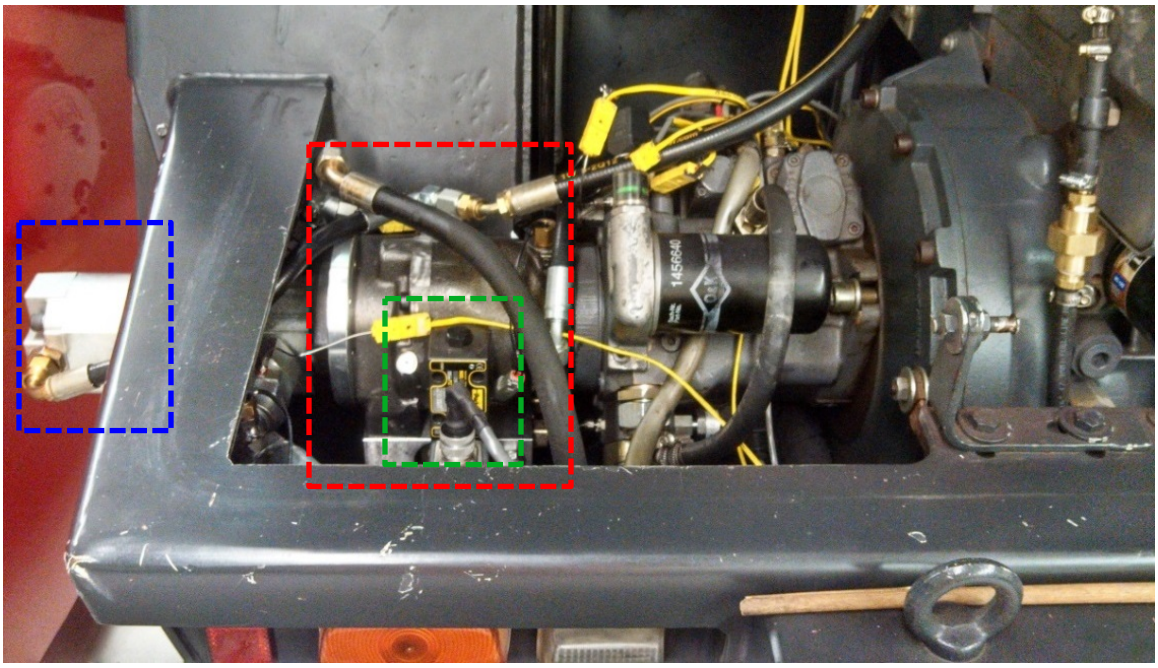

Figure 80: Installation of the DC Steering System Hydraulic Components.

6.3.2 Tactile Feedback Device

The DC steering system is a by-wire system that does not have a mechanical linkage between the operator and the steered components. Therefore, without any additional components the steering wheel can freewheel with minimal resistance and no positive stops. It is established that loss of steering wheel feedback is not acceptable to operators and can lead to hazardous outcomes. To overcome this challenge, the new DC steering system employs an electronic braking device that resists steering wheel motion providing the conventional

resistance that operators are used to. The selected tactile feedback device (TFD) employs a magneto-rheological (MR) brake that linearly outputs torque based on input current. The device has a built-in inductor that generates a magnetic field, which induces a magnetic flux that traverses the gap between the rotor and the stator. The gap is filled with magnetically responsive iron particles that align to form chains when exposed to a magnetic field. The relative motion between the rotor and stator develops a shear action between the magnetic particles. The result is a torque on the output shaft that is proportional to the input current. An additional feature of the selected TFD is that it has a built-in angle sensor with dual outputs for redundancy provisions.

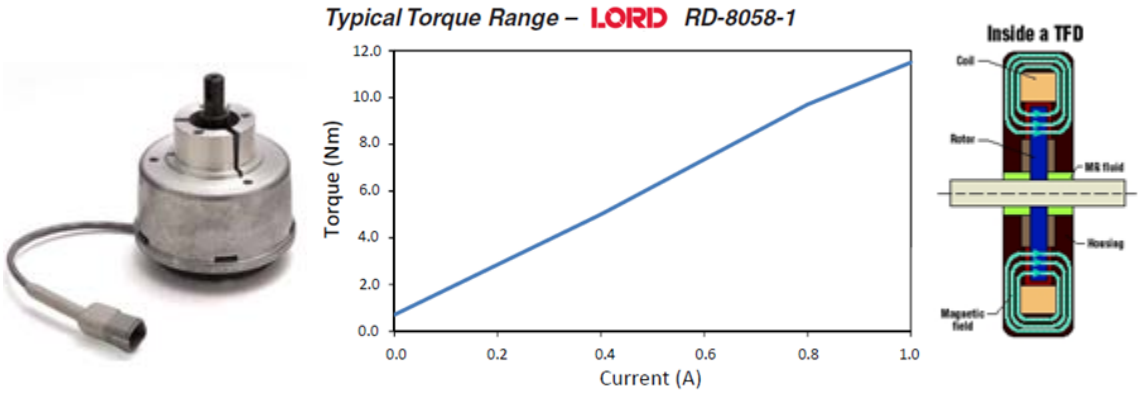

Figure 81: Tactile Feedback Device (Courtesy: LORD Corporation and Machine Design).

The selected TFD allows for realizing the following functions. The system can vary the level of force feedback based on vehicle speed as previously explained in section 3.1.2. The system is also capable of simulating travel limits when the maximum steering angle is reached, alerting the operator with multiple options such as a steering wheel pulse, gradual stiffening, and full lock at the stops. The

TFD also addresses the issue of the operator leading the machine by applying a faster hand wheel turning rate than it can realistically achieve, where the TFD increases stiffness as a function of rotary speed to limit the operator's turning pace. Last but not least, the TFD can vary force feedback based on load pressure and therefore simulate obstacles to alert the operator of such conditions. It is noteworthy to mention that a MR-fluid based device has a very favorable smooth torque output without the stick-slip or cogging behavior of competing technologies such as electric motors. At the same time, the MR brake has a smaller size and mass, leading to a higher bandwidth, and is extremely energy efficient given its low power consumption.

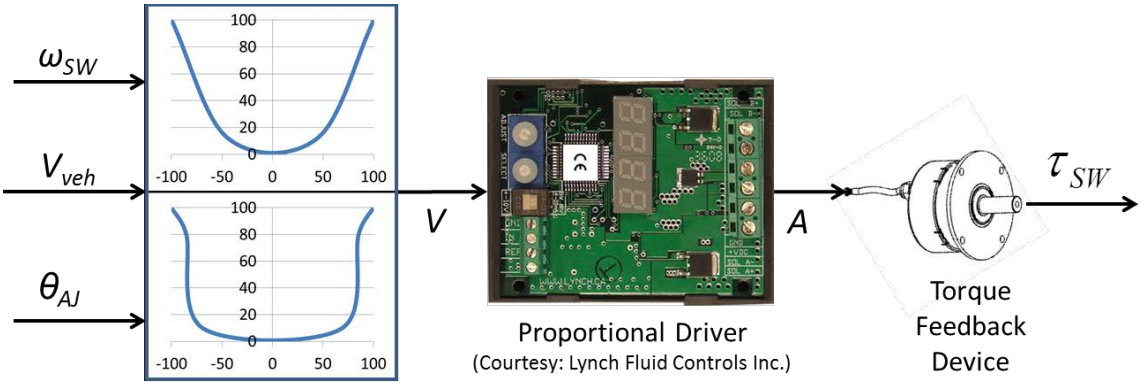

Figure 82: TFD Control Scheme.

Figure 82 shows a generic control scheme of the TFD taking in multiple inputs including, but not limited to, steering wheel rotational speed, ω_{SW}, vehicle speed, V_{veh}, and articulation joint angle, θ_{AJ}, and outputting an appropriate voltage that gets transformed by a proportional driver into current, which determines the TFD's output torque, τ_{SW}.

6.3.3 Steering Column Assembly

The stock steering column assembly consists of a steering shaft housed inside of a tubular structure, which is bolted onto the rotary proportional valve body. The steering shaft end has matching splines that insert into the rotary valve to provide synchronous rotational motion.

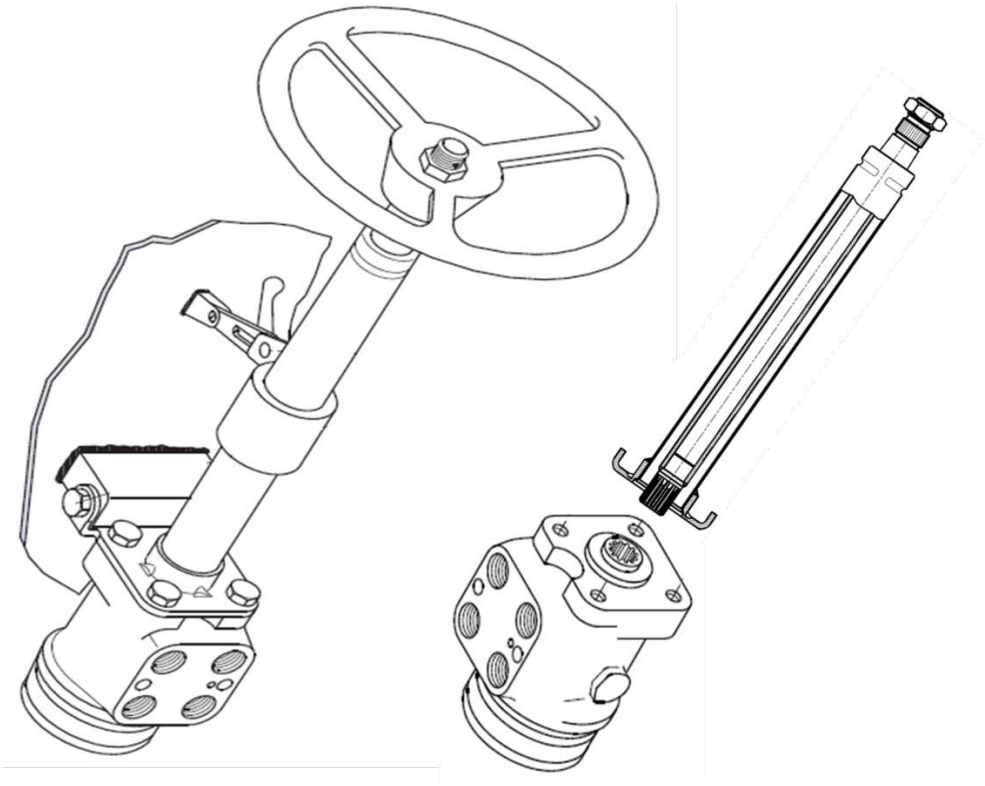

Figure 83: Stock Steering Column Assembly and Steering Valve (Courtesy: Danfoss Power Solutions).

On the other hand, the new DC steering column assembly consists of the steering wheel attached to the TFD via a steering shaft. For packaging purposes, the TFD is installed in place of the stock rotary proportional valve using the same mounting adapter and location. As seen in Figure 84, the new steering shaft has multiple sections that are custom designed and machined to house the torque

sensor (magenta), a slip ring (green) used as a cable management solution for the torque sensor allowing infinite rotations, and two adapters that attach the steering shaft to the TFD (gray) and the steering wheel (yellow). It is noted that for research purposes only, the steering shaft is instrumented with a torque sensor and a slip ring in order to allow for the development of TFD control algorithms. In series production, a torque sensor is not required.

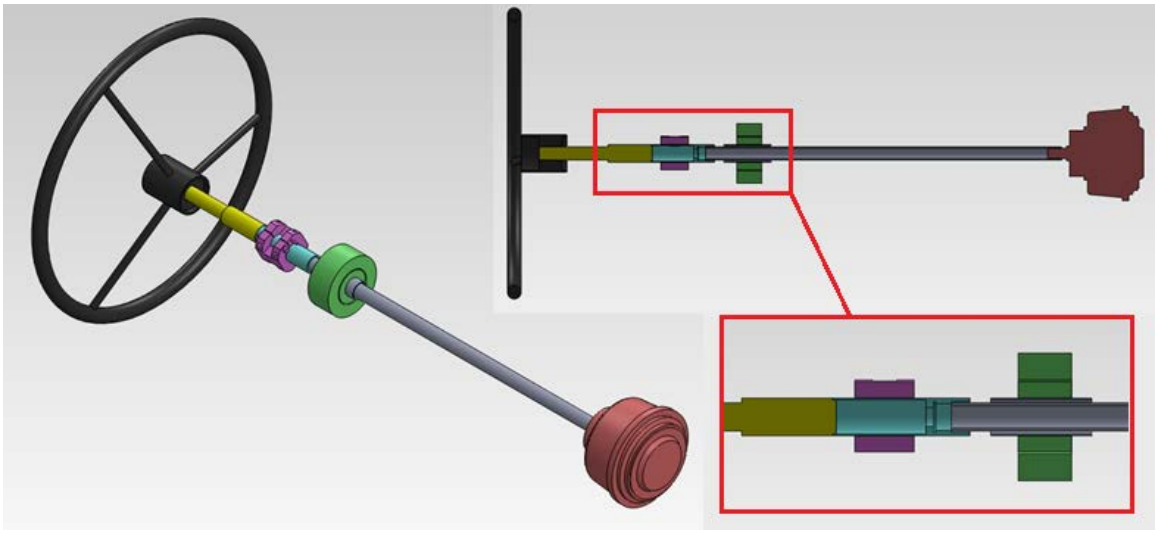

Figure 84: CAD Model of the New Steering Column Assembly.

The new steering column components that were installed on the prototype wheel loader are shown in Figure 85.

Figure 85: Components of the New Steering Column Assembly.

Figure 86: Integration of the New Steering Column Assembly.

Figure 86 shows the assembled steering column with the required parts only on the left; integration of the torque sensor, slip ring, and mounts in the middle; and the finished product as installed in the prototype wheel loader on the right.

6.3.4 Prototype DC Steering System Wiring Schematic

The baseline electrical system is modified to accommodate the addition of the following new components that are specific to the DC steering system:

- Pump adjustment system's proportional control valve
- Pump swash plate angle sensor
- Torque feedback device
- Proportional valve driver for controlling the TFD

The revised wiring schematic of the new DC steering system is shown in Appendix E.

6.4 Chapter Summary

- As a first step, the wheel loader is instrumented with an array of sensors, signal conditioning modules, and a data acquisition system to record the baseline testing results for later comparison against the new DC steering system.
- The machine is instrumented with an articulation angle sensor, a vehicle speed sensor, steering wheel torque and angle sensors, engine speed and throttle sensors, a real-time controller and data logger, and a fuel measurement system.
- Baseline testing is performed and data is recorded on a steering-only cycle that is devised to characterize the steering system alone without the other hydraulic systems (transmission and implements) being active.

- After baseline measurements are completed, the new DC steering system is implemented by installing a variable displacement pump, a tactile feedback device, and a custom designed steering column assembly.
- The electrical system is renovated to accommodate the electronics of the newly added components specific to the DC steering system.

CHAPTER 7. FUEL EFFICIENCY EXPERIMENTAL TESTING RESULTS

After the hardware implementation phase of the new DC steering system was completed, the linear controller designed in Section 5.1 was implemented, and the steering-only cycle was repeated under the same conditions that the stock machine was baseline tested at per Table 12. The fuel tank mass was measured pre- and post-test for calculating fuel consumption during each cycle. In order to also assess how efficiently the fuel is being used, another performance index that measures the amount of work done per fuel consumed is considered.

The cumulative steering work performed by the machine during a steering-only maneuver is computed based on the integration of the steering torque multiplied by the total rotation of the articulated frame over time, as shown in Eq. (145).

$$W_{str} = \int \tau_{str}\, \dot{\phi}\, dt. \tag{145}$$

where W_{str} is the cumulative steering work, τ_{str} is the steering torque, and $\dot{\phi}$ is the rotational speed of articulation.

The relative rotational speed of the two frames is determined by differentiating the measured steering angle signal and applying a properly designed second-order low-pass Butterworth filter. The steering torque is calculated based on measured pressure data and known machine kinematics as given in Eq. (146).

$$\tau_{str} = F_{str}\, r_j . \tag{146}$$

where F_{str} is the steering actuator hydraulic force, and r_j is the steering moment arm length which is the normal distance between the articulation joint and the actuator force line of action.

The actuator force is calculated based on the measured actuator piston pressure, p_A, and rod pressure, p_B, and their respective areas as given by Eq. (147).

$$F_{str} = A_A(p_A - \alpha p_B). \tag{147}$$

On the other hand, the moment arm length, r_j, is accurately calculated as a function of the articulation angle, ϕ, as shown in Figure 87. A trigonometric relationship is established between the two quantities based on the mounting geometry of the steering actuator. The plotted second-order polynomial represents a least-squares fit having a coefficient of determination, R^2, which is greater than 0.99 yielding adequate precision.

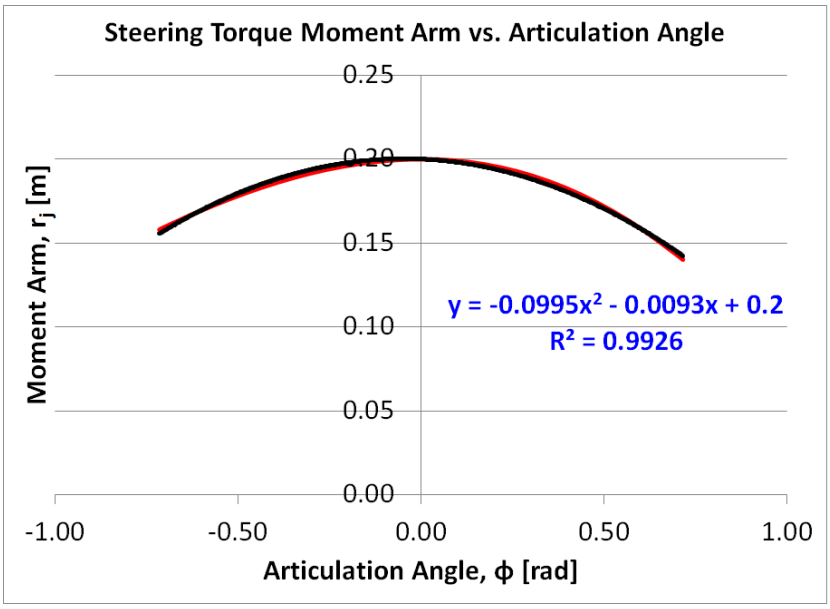

Figure 87: Relationship between Steering Angle and Moment Arm Length.

7.1 Baseline Measurements

The baseline machine was instrumented with pressure and speed sensors to examine the pressure drops across the hydrostatic steering system components, and to compute their individual power losses. Figure 88 is provided to identify the main components and the pressure sensors installed on the hydrostatic steering system. The enumerated hydraulic components (blue) are identified in Table 13.

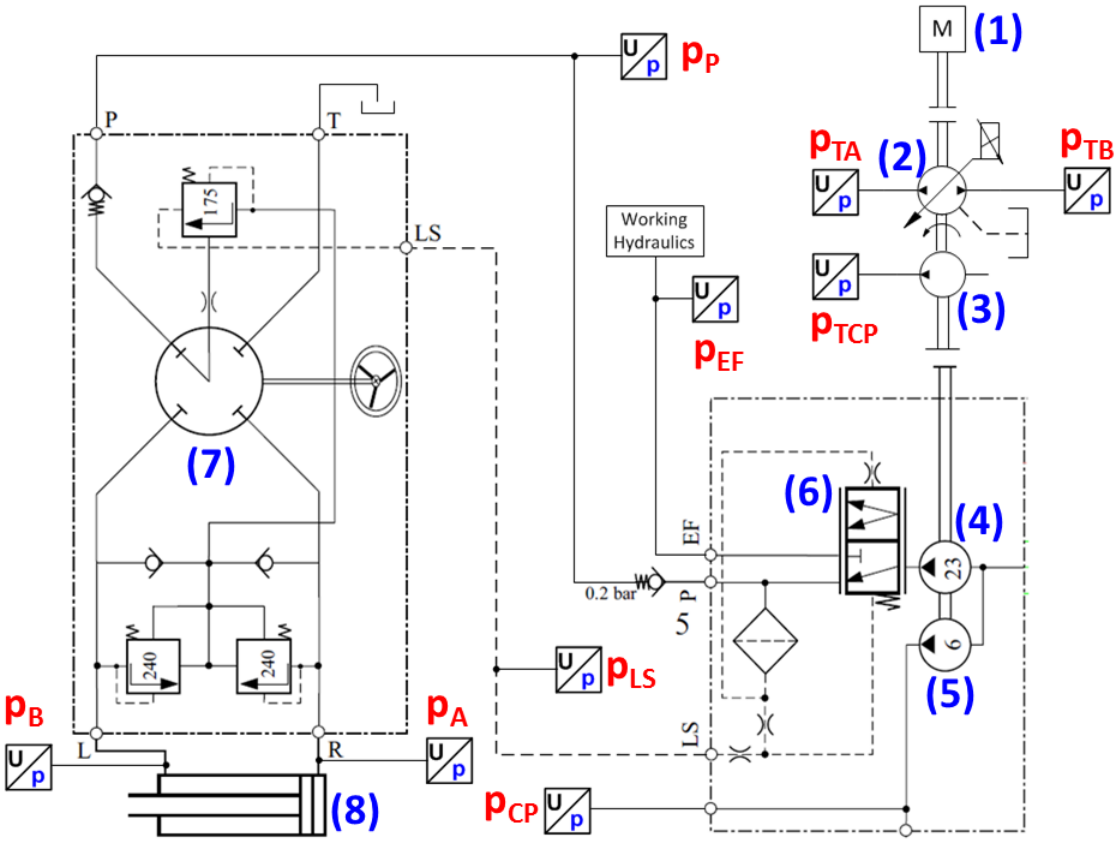

Figure 88: Hydrostatic Steering System Components and Sensors.

Table 13: Identification of Conventional Valve Controlled Steering System Components.

(1)	Engine
(2)	Transmission Pump

Table 13 Continued: Identification of Conventional Valve Controlled Steering System Components.

(3)	Transmission Charge
(4)	Main Pump
(5)	Charge Pump
(6)	Priority Valve
(7)	Steering Valve
(8)	Steering Actuator

The installed pressure sensors (red) are also highlighted on the schematic and are described in Table 14.

Table 14: Identification of Hydrostatic Steering System Pressure Sensors.

p_{TA}	Transmission Line A Pressure
p_{TB}	Transmission Line B Pressure
p_{TCP}	Transmission Charge Pump
p_{EF}	Working Hydraulics Pressure
p_p	Steering Valve Upstream
p_{LS}	Load-sensing Pressure
P_{CP}	Charge Pump Pressure
p_A	Steering Actuator Piston
p_B	Steering Actuator Rod

To determine the engine brake power, the engine speed and torque must be known. A speed sensor is installed to measure engine speed, and the engine load torque is determined by calculating the individual torques generated by each hydraulic pump. The torque, $T_{(\bullet)}$, of each pump is given by

$$T_{(\bullet)} = V_{d(\bullet)} \Delta p_{(\bullet)} \eta_{hm(\bullet)}. \tag{148}$$

where $V_{d(\bullet)}$ is the displacement volume, $\Delta p_{(\bullet)}$ is the pressure differential, and $\eta_{hm(\bullet)}$ is the hydro-mechanical efficiency of the respective pump. The net engine torque, $T_{eng,}$ is given by

$$T_{eng} = T_{TP} + T_{TCP} + T_{MP} + T_{CP}. \tag{149}$$

where T_{TP} is the transmission pump torque, T_{TCP} is the transmission charge pump torque, T_{MP} is the main pump torque, and T_{CP} is the main charge pump torque. The engine power, P_{eng}, is given by

$$P_{eng} = T_{\text{eng}} n. \tag{150}$$

where n is the pump (engine) speed. The main pump output power, P_{MP}, is given by

$$P_{MP} = \Delta p_{MP} Q_{MP}. \tag{151}$$

where Q_{MP} is the main pump flow rate given by

$$Q_{MP} = n V_{d,MP} \eta_{vol,MP}. \tag{152}$$

where $\eta_{vol,MP}$ is the main pump volumetric efficiency. Therefore, the power loss of the main pump, $P_{s,MP}$, is given by

$$P_{s,MP} = P_{eng} - P_{MP}. \tag{153}$$

After determining the engine brake power and the main pump output power, the power loss across the priority valve and the steering valve are determined. The power loss across the priority valve is determined by multiplying the pump flow rate and the pressure drop across the valve:

$$P_{s,priority} = \Delta p_{priority} Q_{MP}. \tag{154}$$

The pressure drop across the priority valve is determined from the pressure drop curves shown in Figure 89. The minimum curves apply when the pressure on the working hydraulics (p_{EF}) connection is higher than the control spring pressure. The curves for control spring pressure (10bar) apply when pressure on the EF connection is zero.

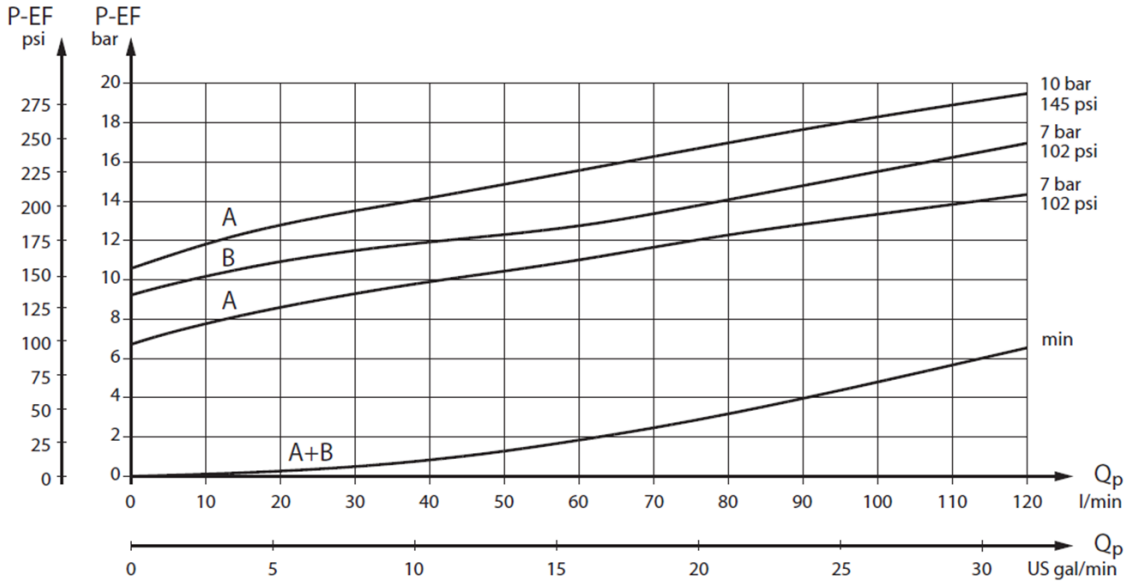

Figure 89: Priority Valve Pressure Drop Curves.

In the prototype test vehicle, the priority valve block is mounted directly on the main pump block, and as such the main pump's outlet pressure is not directly measured. The pressure drop across the priority valve along with the measured downstream pressure (p_P) are summed to determine the main pump outlet pressure.

The power loss across the steering valve is determined by subtracting the valve's output power from its input power (priority valve's output power). The steering valve power loss is given by

$$P_{s,str} = p_P Q_{MP} - \max(p_A, p_B)\dot{x}A_B \quad \ldots\ p_A < p_B, \tag{155}$$

$$P_{s,str} = p_P Q_{MP} - \max(p_A, p_B)\dot{x}A_A \quad \ldots\ p_A > p_B. \tag{156}$$

The actuator velocity is determined based on the kinematic relationship between the vehicle's articulation angle and the steering actuator position.

Finally, the actuator power loss is determined by subtracting its output power from its input power (the steering valve's output power). The actuator's output power, P_{act}, is given by

$$P_{act} = \left[p_A A_A - p_B (A_A - A_B)\right]\dot{x}. \tag{157}$$

The measured pressure signals are filtered to remove the sensors high frequency noise content, and the absolute values of the calculated power are taken to generate non-negative values.

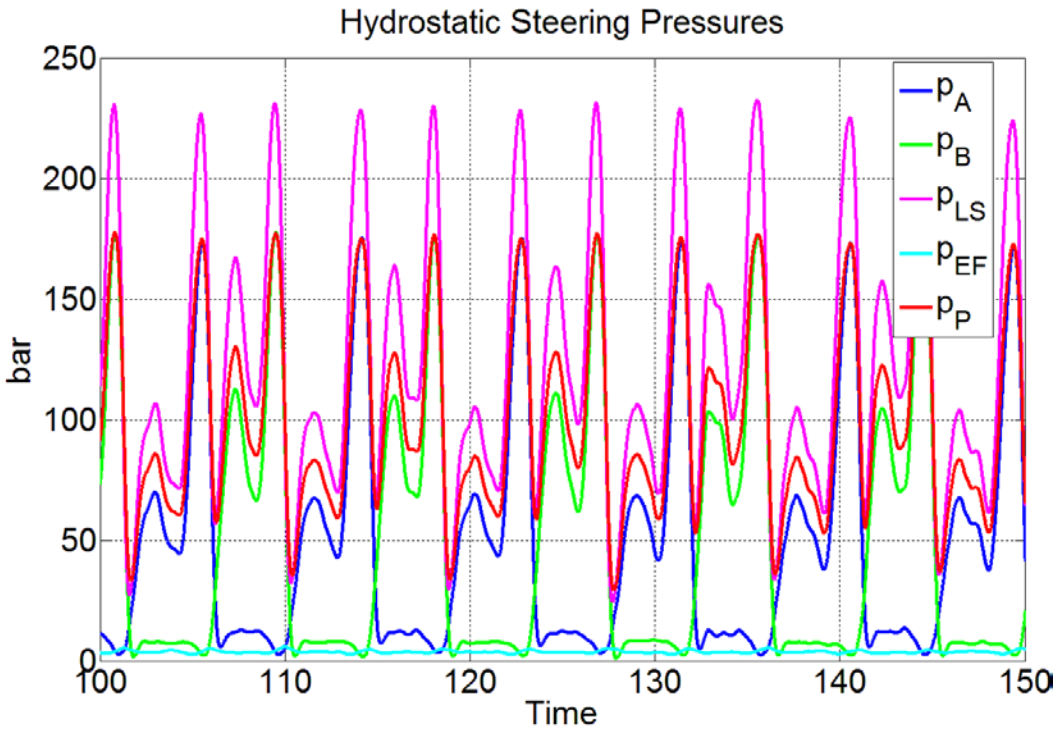

Figure 90: Hydrostatic Steering Pressures – 50s Window.

Figure 90 shows the conventional valve controlled steering system pressure signals acquired during the articulation maneuver, between 100-150 seconds of the total event time of 260 seconds. The load-sensing pressure (p_{LS}) is highest, followed by the pressure downstream of the priority valve (p_P) and then the actuator high pressure side. The working hydraulics pressure (p_{EF}) is near zero for the entire time since the implement functions are not operated. The actuator low pressure side ranges between 5-10bar depending on the active high pressure chamber and the actuator area ratio.

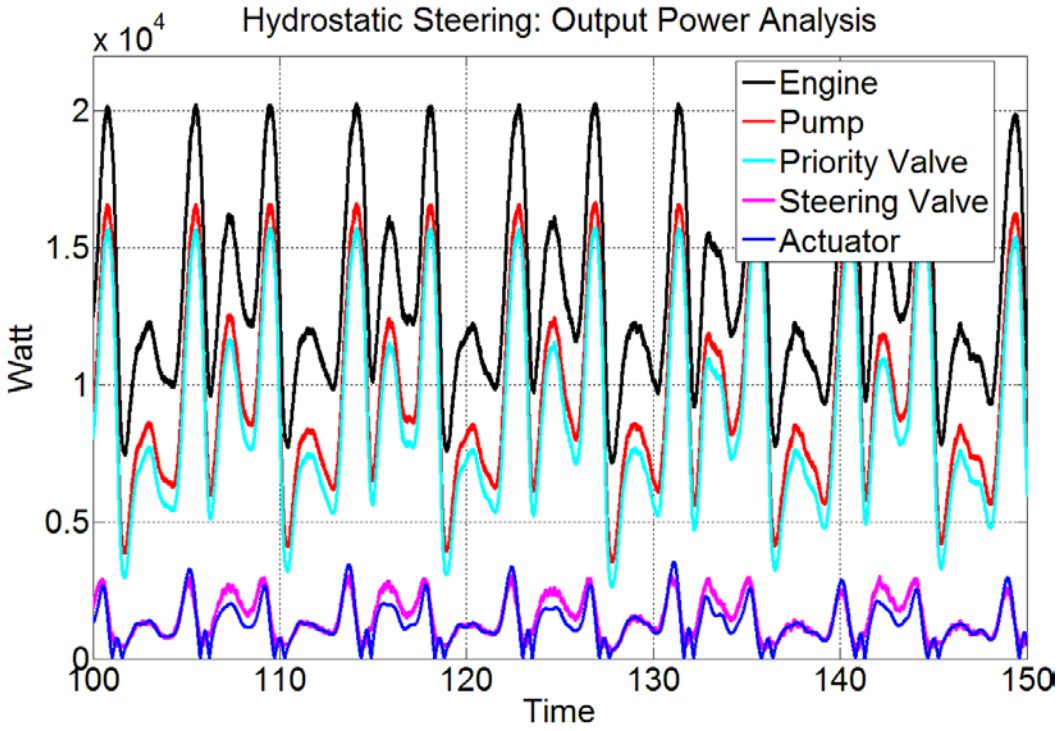

Figure 91: Hydrostatic Steering Output Power Analysis – 50s Window.

Figure 91 shows the computed output power of each of the system components starting from the engine and down to the steering actuator, between 100-150 seconds. The dominant power loss occurs between the priority valve output and

the steering valve output, which corresponds to the losses of the hydro-mechanical steering valve. Investigation into the energy efficiency of each of the components is summarized in Table 15. Energy is computed by integrating the individual powers over the entire event, and the efficiency percentage is computed by dividing the output energy by the input energy.

Table 15: Conventional Valve Controlled Steering System Components Efficiency.

Main Central	72.9%
Priority Valve	90.8%
Steering Valve	16.9%
Actuator	86.0%

Table 16 shows a summary of the measurement results that were acquired from the baseline machine with its stock hydrostatic steering system.

Table 16: Baseline Machine Testing Results – Steering-only Cycle.

Surface Type	**Event I.D.**	**Fuel Consumed [kg]**	**Total Steering Work Done by Machine [MJ]**	**Steering Work per Fuel Mass [MJ/kg]**
Grass	CW1	0.274	No data recorded	
	ND1	0.294	0.633	2.15
	CW2	0.354	0.635	1.79
	ND2	0.224	0.653	2.91
Concrete	ND	0.308	0.636	2.07
Average		0.291	0.639	2.232

7.2 DC Steering Measurements

After baseline testing to establish a benchmark was performed on the stock machine, the DC steering system was retrofitted on the prototype test vehicle. A variable displacement pump is installed between the transmission pumps and the working hydraulics pump, and a charge pump is added to supply low pressure to the DC steering system. The DC steering system schematic with its main components and pressure sensors are shown in Figure 92.

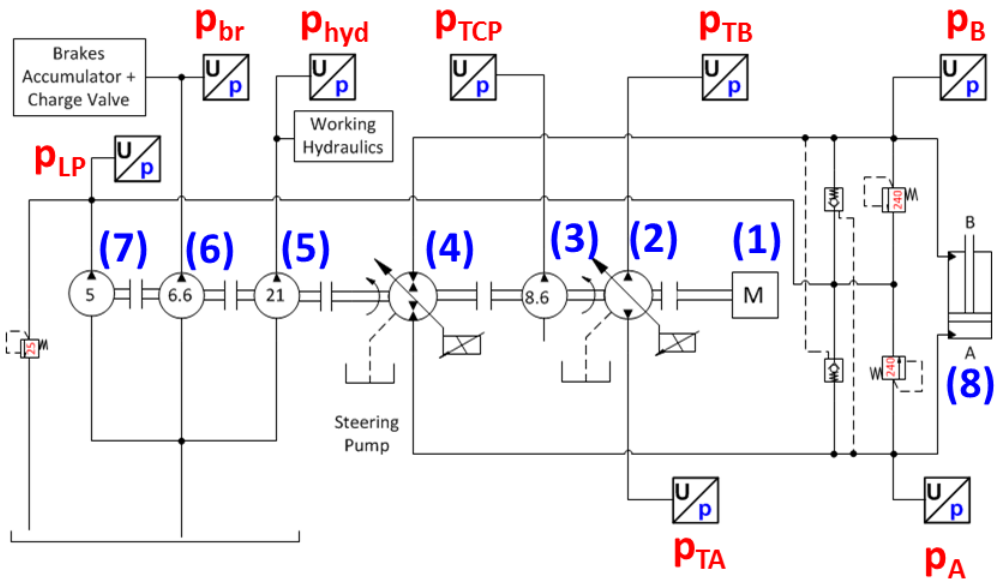

Figure 92: DC Steering System Components and Pressure Sensors.

The main system components (blue) are enumerated on the schematic and are listed in Table 17

Table 17: Identification of DC Steering System Components.

(1)	Engine
(2)	Transmission Pump
(3)	Transmission Charge Pump
(4)	DC Steering Pump

Table 17 Continued: Identification of DC Steering System Components.

(5)	Working Hydraulics Pump
(6)	Charge Pump
(7)	DC Steering Low Pressure Pump
(8)	Steering Actuator

The installed pressure sensors (red) are also indicated on the schematic and are listed in Table 18.

Table 18: Identification of DC Steering System Pressure Sensors.

p_{TA}	Transmission Line A Pressure
p_{TB}	Transmission Line B Pressure
p_{TCP}	Transmission Charge Pump
p_{A}	Steering Actuator Piston Pressure
p_{B}	Steering Actuator Rod Pressure
p_{hyd}	Working Hydraulics Pressure
p_{br}	Brakes Pressure
p_{LP}	Steering Low Pressure System

Figure 93 shows the DC steering system pressures during the articulation maneuver, between 100-150 seconds of the event. The same actuator pressure magnitudes are recorded as with the conventional valve controlled (hydrostatic) steering system, which confirms that identical operating conditions were indeed achieved relative to load magnitude and tire-ground interface conditions. It is noted that a slight pressure drop occurs across the transmission lines, but since its magnitude is small (<1bar) it is neglected in the energy analysis of the DC steering system.

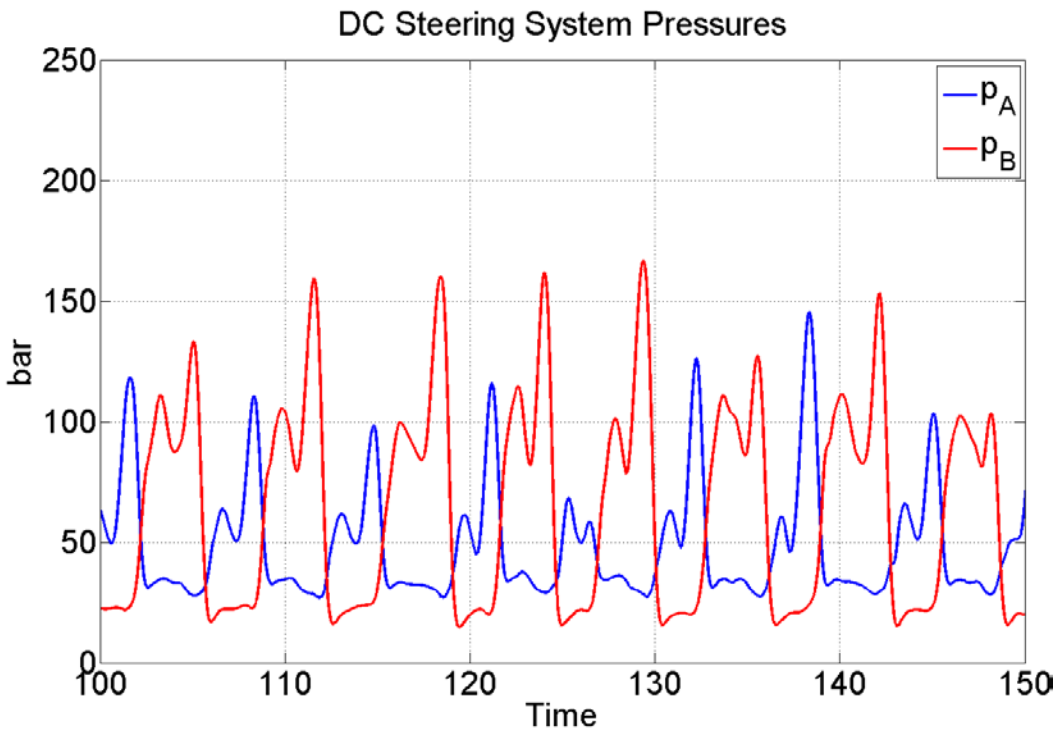

Figure 93: DC Steering Pressures – 50s Window.

Figure 94 shows the computed output power of the system's three main components: engine, pump, and steering actuator, between 100-150 seconds. Notice how with the DC steering system the engine operates around 5.5kilowatts on average, which is a significant reduction when compared with the 13.5kilowatts in the case of the hydrostatic steering system. This reduction translates into considerable fuel savings as will be shown later. The prevailing power loss occurs at the DC steering pump, which is the main loss contributor in the new pump controlled system.

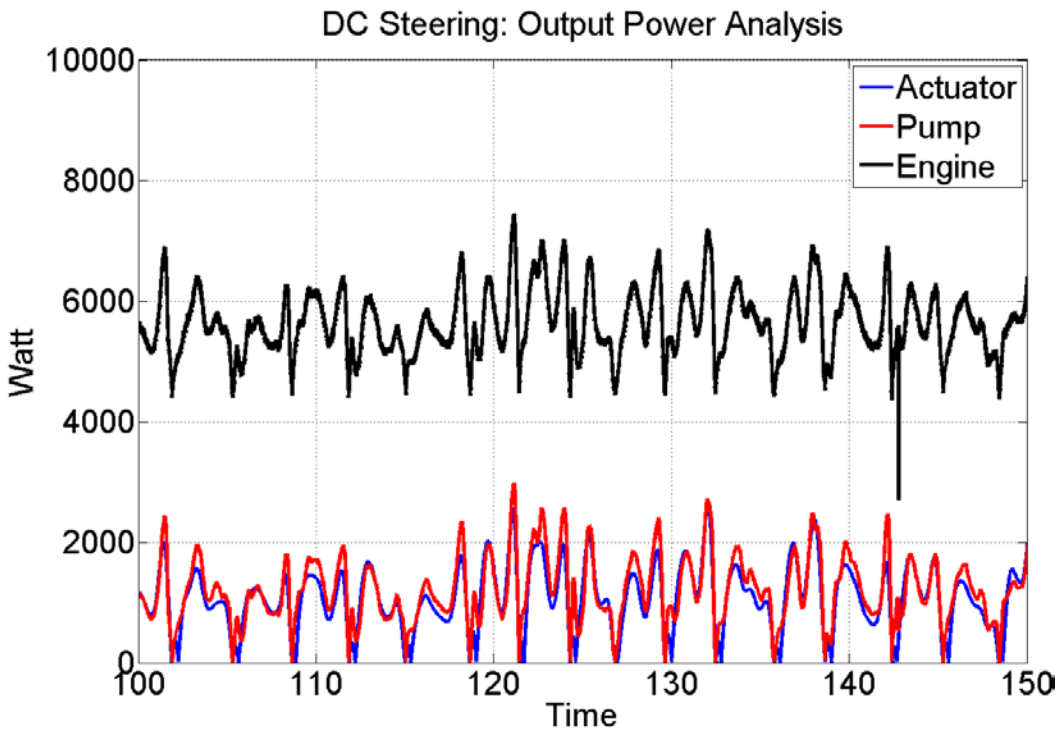

Figure 94: DC Steering Output Power Analysis – 50s Window.

A similar energy efficiency analysis is performed on the DC steering system components as with the conventional valve controlled steering system. The results are summarized in Table 19.

Table 19: DC Steering System Components Efficiency.

DC steering pump	22.8%
Actuator	89.0%

As the main contributor to power loss in the DC steering system, an investigation into the pump efficiency is provided. Hydraulic pump efficiency depends on many factors including the pump design (e.g. gear, gerotor, swash plate type axial piston, bent-axis axial piston, radial piston, to name a few), pressure level, operating speed, temperature, and stroke level in the case of variable

displacement pumps. Two power losses are typically considered in pumps: volumetric losses and torque losses. Complete analytical derivation of hydraulic pump losses is not possible at present. This is due to the complexities of compound physical phenomena involved in power loss. Therefore, empirical expressions are derived and used for computing pump losses, as presented in Section 4.1.1. The obtained results prompt further examination into the root cause behind the relatively low efficiency of the DC steering pump. The measured pump displacement and pressure differential across the DC steering pump ports, shown in Figure 95, reveal that the pump operates at an inopportune combination of these two influencing factors.

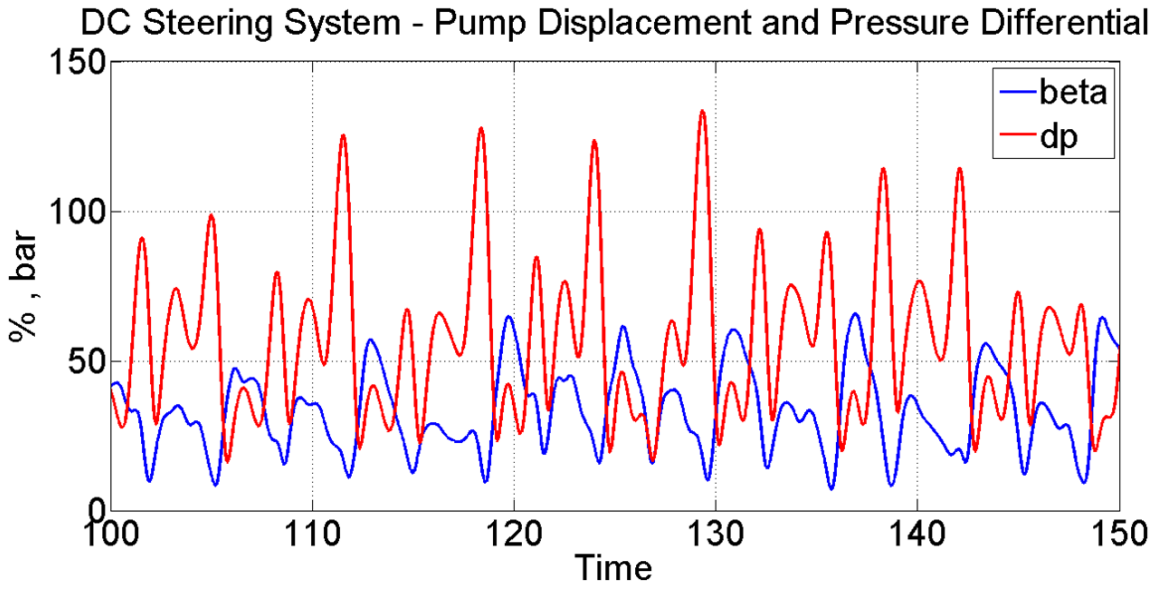

Figure 95: Instantaneous Pump Displacement and Pressure Differential across the DC Servo-pump.

The pump displacement (beta) is on average around 30%, which is considered a low displacement where output power is small compared to pump losses and therefore overall efficiency is low. The low pump displacement is mainly due to

the fact that the selected pump size is larger than the required size that was obtained in Section 3.2.4.1, which was necessary to meet the packaging, interface, and timing constraints of the project. Low pump displacements are also due to the high engine speed (full throttle) during the articulation event, which brings forward another energy saving strategy. For a DC system, engine power management is feasible and has been successfully implemented in (Williamson & Ivantysynova, 2010). The optimal control algorithm generally forces the engine to operate at lower speeds and the DC pump to operate at higher displacements, which are both in the right direction of decreasing energy dissipation.

Table 20 shows a summary of the measurement results that were acquired from the prototype machine after the installation of the new DC steering system.

Table 20: DC Steering Prototype Machine Testing Results – Steering-only.

Surface Type	Event I.D.	Fuel Consumed [kg]	Total Steering Work Done by Machine [MJ]	Steering Work per Fuel Mass [MJ/kg]
Grass	G1	0.256	0.818	3.20
	G2	0.234	0.777	3.32
	G3	0.310	0.832	2.68
Concrete	C1	0.268	0.775	2.89
	C2	0.188	0.704	3.74
	C3	0.236	0.797	3.38
Average		0.249	0.784	3.203

Table 21 provides a comparison between the average results of the two systems revealing a very favorable outcome for the new steering technology. The DC steering system resulted in decreasing the fuel consumption by 14.5%, which is a

significant difference when considering typical fuel saving measures. Furthermore, the machine was able to perform more steering work in the same amount of time, which translated into a machine productivity increase of 22.6%, all while consuming less fuel. This compounded effect can be quantified by introducing a fuel efficiency index, which reflects the amount of useful steering work that the machine performs per mass of fuel and hence how efficiently the fuel is used. With this designation, the new DC steering system resulted in a substantial fuel efficiency increase of 43.5%.

Table 21: Comparison between Hydrostatic and DC Steering Systems.

	Fuel Consumed [kg]	**Total Steering Work Done by Machine [MJ]**	**Steering Work per Fuel Mass [MJ/kg]**
Stock Hydrostatic Steering	0.291	0.639	2.232
New DC Steering System	0.249	0.784	3.203
Difference [%]	-14.5%	+22.6%	+43.5%

The above metrics portray different aspects of the systems and they complement one another for a global assessment of the two technologies. The energy losses associated with the components of the two steering systems are portrayed in Figure 96. The first stark observation is the relative size of the appropriately scaled pie charts. The DC steering system dissipates considerably less energy (1.52MJ) than the conventional valve controlled (hydrostatic) steering system (3.51MJ), a vast 2.3 times factor. In the hydrostatic steering system, the hydraulic control valve is responsible for 61% of the lost energy. In the case of the DC

steering system, the pump dominates the energy losses as it constitutes the main power loss source in the new system. The DC steering system efficiency can be improved by using the properly sized variable displacement axial piston pump and by implementing engine power management strategy, as explained above.

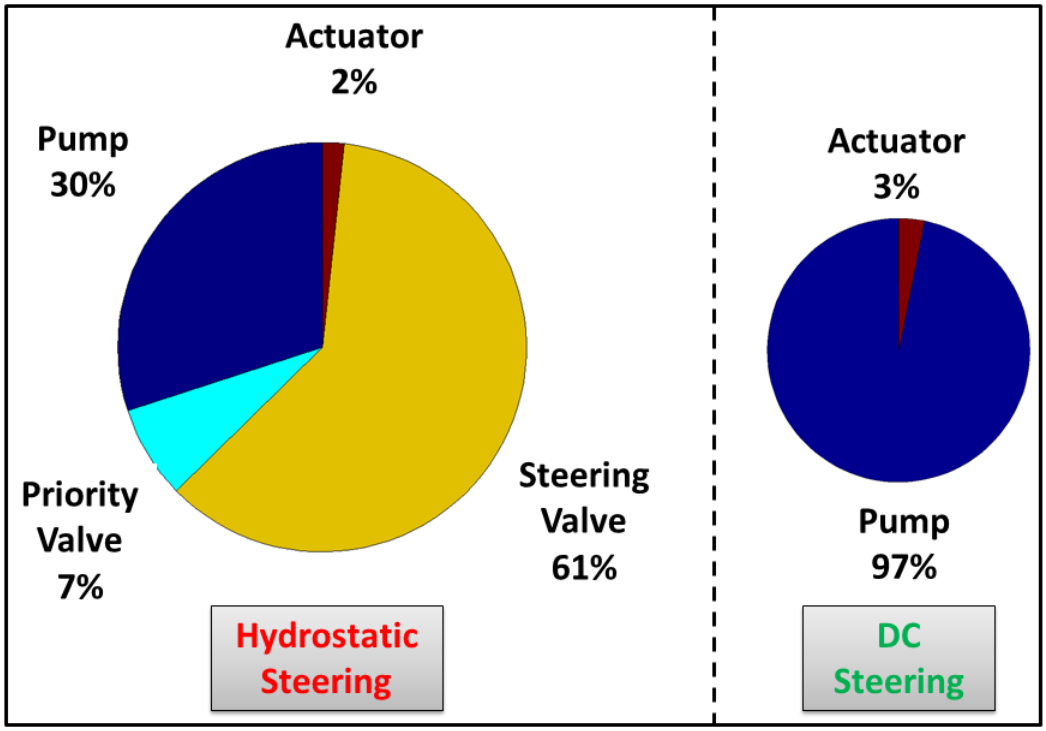

Figure 96: Energy Losses Comparison (Pie Charts are to Scale).

7.3 Chapter Summary

- Efficiency analysis of the two systems reveals that the conventional valve controlled (hydrostatic) steering system losses are dominated by throttling losses across the hydro-mechanical steering valve, which accounts for 61% of the total dissipated energy.

- The DC steering system losses are dominated by the variable displacement pump since the pump is the only control element between the power source and the consumer.
- For the same cycle, DC technology significantly reduces the steering system energy losses, which are cut down by a factor of 2.3 times over the conventional valve controlled steering.
- DC steering results in 14.5% fuel savings, 22.6% machine productivity gain, and a total of 43.5% fuel usage efficiency increase.

Acknowledgement

The author would like to acknowledge Elsevier for granting the rights to use the work presented in this chapter, which was published in the *Energy Conversion and Management* Journal:

Daher, N. and Ivantysynova, M. 2014. Energy Analysis of an Original Steering Technology that Saves Fuel and Boosts Efficiency. *Energy Conversion and Management*, Vol. 86, pp. 1059-1068

http://www.sciencedirect.com/science/article/pii/S0196890414005986

CHAPTER 8. YAW STABILITY CONTROL VIA ACTIVE STEERING

Stability control systems geared towards wheel-steered passenger vehicles and articulated heavy commercial vehicles have seen steady progress and have been under rigorous research and development for the past few decades. On the other hand, the off-highway machinery sector has lagged behind in this area and very few publications that deal with this topic are found in literature.

Early research into ground vehicle stability control systems originated in the automotive industry in the late 1980s and early 1990s, with the purpose of controlling yaw motion and lateral slippage at high speeds and on low friction surfaces. In the mid-1990s, a robust control strategy was introduced in (Ackermann, 1994) and (Ackermann, 1997) to prevent car skidding by separating the tasks of path following and disturbance attenuation, which was accomplished by deriving a decoupled yaw dynamics model from the lateral acceleration. A Vehicle Dynamics Control (VDC) system was developed in (Zheng, Tang, Han, & Zhang, 2006) for tracking desired vehicle behavior, by using a cascaded control structure consisting of a yaw moment major controller and a wheel slip minor controller. A linear quadratic regulator (LQR) was used for yaw moment control and sliding mode control (SMC) was employed for wheel slip control. Practical vehicle stability control schemes, as employed by major original equipment

manufacturers (OEM), were later consolidated in (Rajamani, 2005) with engine torque vectoring, differential braking, and active steering as the main strategies that can be employed separately or in an integrated fashion, as proposed in (He J. , 2005).

On the commercial vehicles side, multiple researchers have investigated the stability of articulated heavy vehicles (AHV), namely semi-trailer trucks, and proposed various control strategies to improve their maneuverability. Much of the work focused on improving the semi-trailer's ability to track the tractor's trajectory by controlling the articulation angle based on a derived reference model, as developed by various researchers in (Fancher, Winkler, Ervin, & Zhang, 1998), (Odhams, Roebuck, Jujnovich, & Cebon, 2011), (Chen & Shieh, 2011), and (Tabatabaei Oreh, Kazemi, & Shahram, 2013). A new concept was proposed in (Cheng, Roebuck, & Cebon, 2011) where a virtual driver model was utilized to minimize both the lateral acceleration of the trailer's center of gravity and the path-tracking deviation by employing optimal linear quadratic theory. Likewise, a LQR controller was proposed in (Palkovics & El-Gindy, 1996) for directional control of AHV at high speeds. The devised strategy required the minimization of critical vehicle state variables, which was adopted in (El-Gindy, Mrad, & Tong, 2001), (Hac, Fulk, & Chen, 2008), and (Zong, Zhu, Wang, & Liu, 2012).

Since the above control schemes result in improved stability but not enhanced maneuverability, a SMC strategy was devised in (Tabatabaei Oreh, Kazemi, & Azadi, 2014) to improve the robustness of the controller in the face of uncertainties and unmodeled dynamics. The researchers showed an improved

overall performance over the LQR controller, especially under severe driving conditions.

In this work, a yaw stability control system for articulated frame steering (AFS) vehicles is researched and implemented on the prototype test vehicle. A high-fidelity dynamics model is derived while keeping the vehicle's yaw rate decoupled from the lateral acceleration, in order to separate the primary path-following task (driver) from the secondary disturbance-attenuation task (controller). The control algorithm is then designed such that the two tasks do not hamper one another, and that the automatic controller is quickly activated for a short period of time to counteract instabilities, and then smoothly relinquishes control back to the human operator.

8.1 Desired Yaw Rate Model

To control the yaw dynamics of the AFS vehicle, a reference model is derived for use in the design of the control algorithm. The yaw rate response to a steering input by the driver is given by

$$\frac{\dot{\psi}_{des}}{\phi_{driver}} = \frac{u_f}{(1 + K_{us} u_f{}^2)(a+b+c+d)}. \tag{158}$$

where ψ_{des} is the desired yaw angle, ϕ_{driver} is the driver's articulation angle input, and K_{US} is the understeer gradient given by

$$K_{US} = \frac{(\frac{1}{C_{\alpha f}} + \frac{1}{C_{\alpha r}})(b+c)m_r + (m_f + m_r)(\frac{a}{C_{\alpha r}} - \frac{b+c+d}{C_{\alpha f}})}{(a+b+c+d)^2}. \tag{159}$$

as derived in (He, Khajepour, McPhee, & Wang, 2005).

Equation (158) results in a reasonably accurate estimation of the desired yaw rate in the case of high friction road surfaces. Since the attainable lateral acceleration cannot exceed the adhesion limits at maximum friction conditions, the following limitation is imposed on the desired yaw rate

$$\left|\dot{\psi}_{des}\right| \le \frac{\mu_f g}{u_f}. \tag{160}$$

where μ_f is the tire-ground friction coefficient and g is the gravity constant. However, in many cases the friction coefficient is unknown, and very hard to estimate, the lateral acceleration is used instead

$$\left|\dot{\psi}_{des}\right| \le \frac{a_y}{u_f}. \tag{161}$$

A suitable upper bound for the yaw rate is established in (Rajamani, 2005) and is given by

$$\dot{\psi}_{\max} = 0.85\frac{a_y}{u_f}. \tag{162}$$

The target yaw rate is then defined as:

$$\dot{\psi}_{target} = \begin{cases} \dot{\psi}_{des} & \ldots \quad \left|\dot{\psi}_{des}\right| \le \dot{\psi}_{\max} \\ \dot{\psi}_{\max} sgn(\dot{\psi}_{des}) & \ldots \quad \left|\dot{\psi}_{des}\right| > \dot{\psi}_{\max} \end{cases}. \tag{163}$$

In the presence of an input steering torque, the yaw rate dynamics are obtained via Eq. (164), which reveals how the steering system influences the yaw dynamics.

$$\ddot{\psi} = \frac{1}{I_f + I_r + m_r(b+c)^2}\{aF_{yf} - (b+c+d)F_{yr} - [m_r(b+c)]\dot{v}_f \ldots + m_r(b+c)u_f\dot{\psi} + [I_r + m_r c(b+c)]\ddot{\phi} + \tau_{str}\}. \quad (164)$$

where τ_{str} is the steering torque.

8.2 Yaw Stability Control Algorithm

The purpose of an active steering controller is to provide corrective action by adjusting the steering angle to follow the path as intended by the driver. Hence, the aggregate articulation angle is a combination of the driver input to follow a certain path and the automatic controller command to attenuate the disturbances, which is given by

$$\phi = \phi_{driver} + \phi_{SbW}. \quad (165)$$

where ϕ_{SbW} is the corrective articulation angle commanded by the stability control system.

In the new DC SbW system, the controller regulates the pump adjustment system to guarantee tracking between the desired and actual paths.

The desired articulation angle based on the driver's input is given by

$$\phi_{driver} = k_{FF}\theta_{SW}. \quad (166)$$

where k_{FF} is a feedforward gain and θ_{SW} is the steering wheel angle.

The corrective articulation angle of the SbW controller is given by

$$\phi_{SbW} = k_{FB}\int\left(-\dot{\psi} + \dot{\psi}_{target}\right)dt. \quad (167)$$

where k_{FB} is a feedback gain.

The control input to the pump adjustment system is then given by

$$\beta_{cmd} = k_p \left[k_{FF}\theta_{SW} + k_{FB} \int \left(-\dot{\psi} + \dot{\psi}_{target} \right) dt - \phi_{meas} \right]. \quad (168)$$

where k_p is a proportional feedback gain.

The control law in Eq. (168) is further amended to make real-time implementation practical. Specifically, the active steering system should quickly intervene when a disturbance is detected and stay active for a relatively short period of time (<1 second) and then relinquish control back to the operator, who does best at path following. At the same time, during steady-state operation, the active steering system should stay in standby mode and not interfere with the driver's input. To address the above issues, the standard integrator is replaced with a fading integrator whose transfer function is given by

$$G_{FI}(s) = \frac{s}{s^2 + \lambda s + 1}. \quad (169)$$

where λ is a tuning parameter of the integrator's fading period.

Another factor that must be considered is the transient response of the SbW system relative to the steering wheel input. To ensure that the vehicle yaw dynamics are softly excited for safety and comfort purposes, a pre-filter is devised to shape the transient response and is given by

$$F_p(s) = \frac{K(u_f)}{\tau_{PF} s + 1}. \quad (170)$$

where $K(u_f)$ is associated with the understeer gradient and τ_{PF} is a time constant.

Figure 97 shows a block diagram of the stability controller with the pre-filter and fading integrator implementations.

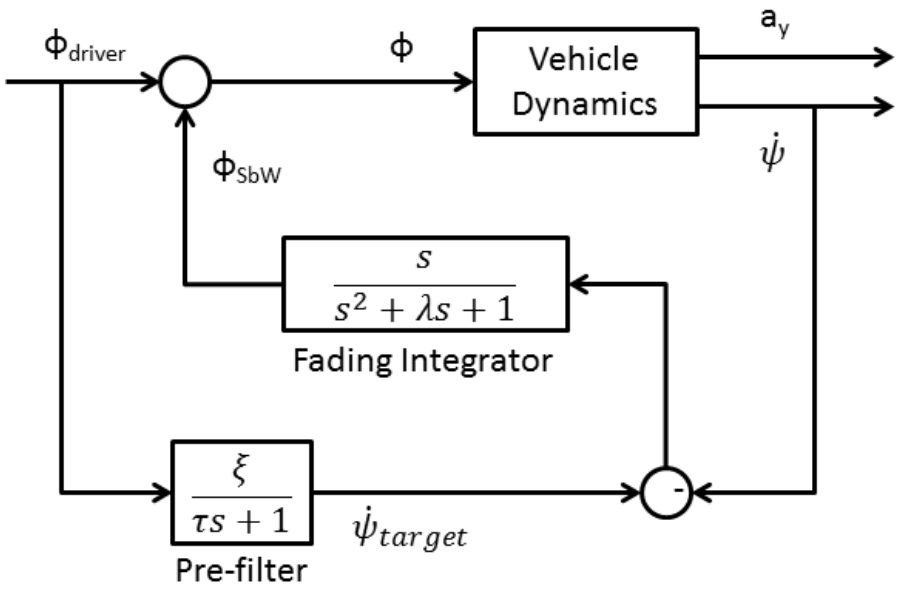

Figure 97: Controller Block Diagram.

8.3 Simulation Results

To test the validity of the derived system dynamical model and the design of the proposed control algorithm, a numerical simulation model is executed in MATALB Simulink® environment. A block diagram of the model is given in Figure 98. The operator commands a certain steering wheel angle, which is interpreted as a desired yaw angle rate based on the vehicle velocity. A target yaw rate is then determined based on the surface conditions and the maximum achievable yaw angle rate and lateral acceleration. The stability controller inputs the driver commanded articulation angle, vehicle velocity, target yaw rate, and the realized yaw rate and articulation angle as computed by the vehicle dynamics module, and commands the appropriate pump displacement accordingly.

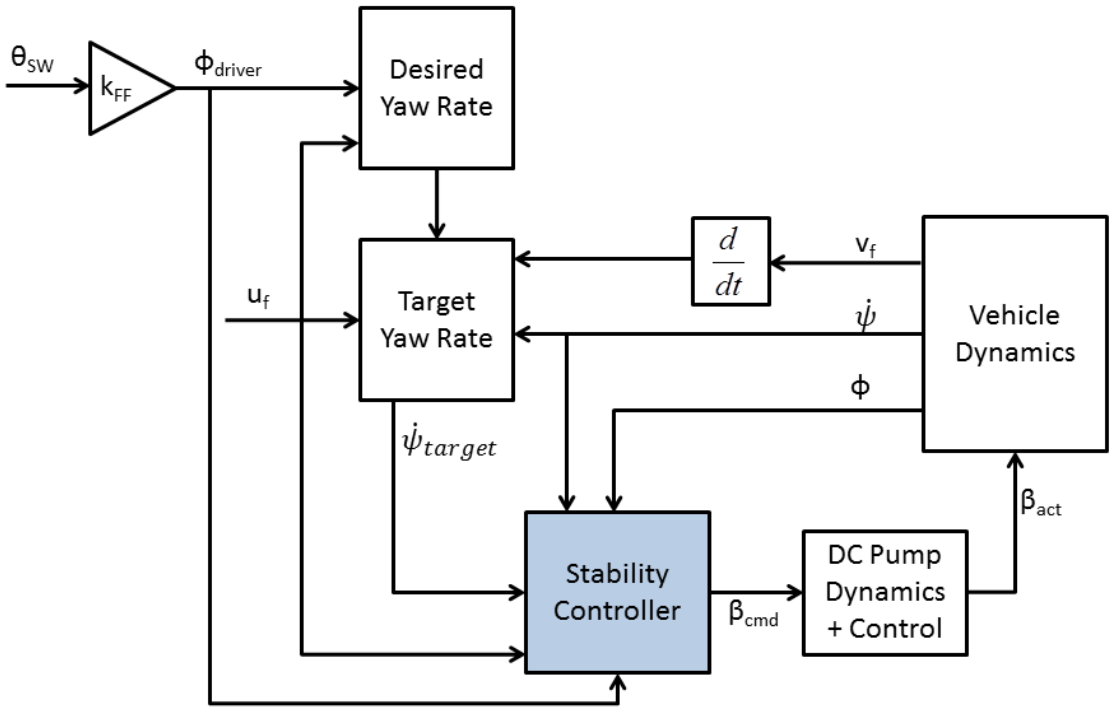

Figure 98: Simulation Model Block Diagram.

The simulation model is executed with the parameters of the prototype test vehicle (five-tons front wheel loader). Table 22 lists the key parameters used in the numerical simulations.

Table 22: Simulated Vehicle Parameters.

Parameter	Value	Unit
m_{veh}	4350	kg
m_f	1653	kg
m_r	2697	kg
a	0	m
b	1.06	m
c	1.06	m
d	0	m
C_{af} , C_{ar}	3.4	rad^{-1}
V_P	18	cm^3/rev
A_A	0.0038485	m^3
A_B	0.0030442	m^3
r_j	0.2	m
n	2500	rpm

A standard dynamic maneuver, J-Turn, is utilized to evaluate the effectiveness of the stability control algorithm. To induce lateral instability at low-to-moderate speeds that off-highway vehicles typically travel at, a low friction surface is modeled. As depicted in Figure 99, the purpose of the stability controller is to get the vehicle to follow the desired path by the operator, up to the allowable adhesion limits of the road surface. When the yaw stability control system is inactive, the vehicle starts skidding sideways and tracks a larger curvature path, or in some instances completely loses control and exhibits spinout.

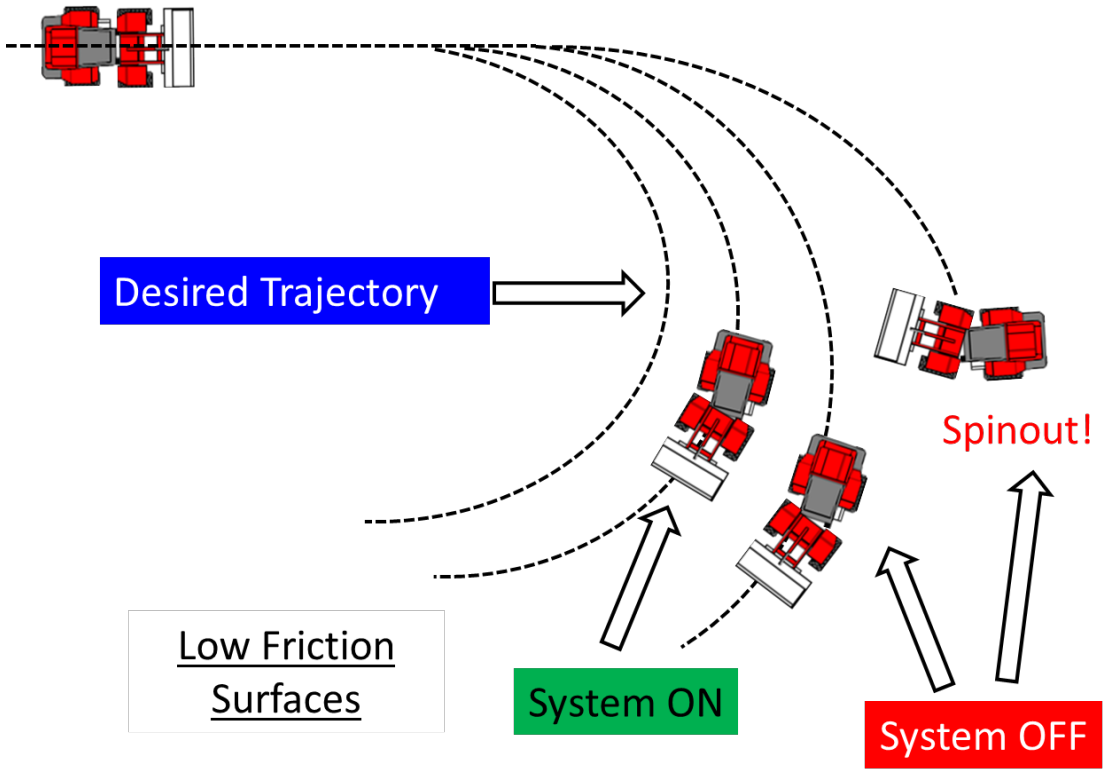

Figure 99: J-Turn Maneuver on Low Friction Surfaces.

To give both qualitative and quantitative assessment of the system's efficacy in attenuating lateral disturbances, a bird's-eye view of the vehicle undergoing the maneuver is provided. For that purpose, the global coordinates of the front and

rear frames are derived in Eq. (171) through Eq. (174). For reference, the front frame is plotted in blue and the rear frame is plotted in red, assuming a single-track bicycle model.

$$X_f = \int \left[u_f \cos(\psi) - v_f \sin(\psi) \right] dt. \tag{171}$$

$$Y_f = \int \left[u_f \sin(\psi) + v_f \cos(\psi) \right] dt. \tag{172}$$

$$X_r = X_f - b\cos(\psi) - c\cos(\theta). \tag{173}$$

$$Y_r = Y_f - b\sin(\psi) - c\sin(\theta). \tag{174}$$

where θ is the rear frame yaw angle given by

$$\theta = \psi - \phi. \tag{175}$$

A J-Turn is simulated with the vehicle traveling at 40 km/h on a snow covered surface (μ_f = 0.2), where the vehicle starts by travelling in a straight line and then a step steering input is applied and held. Figure 100 shows a top-view of the simulation results. As anticipated, the desired yaw rate motion curve is the smallest since it represents the yaw response on high friction surfaces. The target yaw rate motion curve is a bit larger as it takes into consideration the adhesion limits at the tire-ground interface based on the lateral acceleration. With the stability control system active, the vehicle attempts to track the target yaw rate path, and if the adhesion limit allows, to get as close as possible to the desired yaw rate path. However, when the system is turned off, the vehicle skids sideways and follows a larger curvature path.

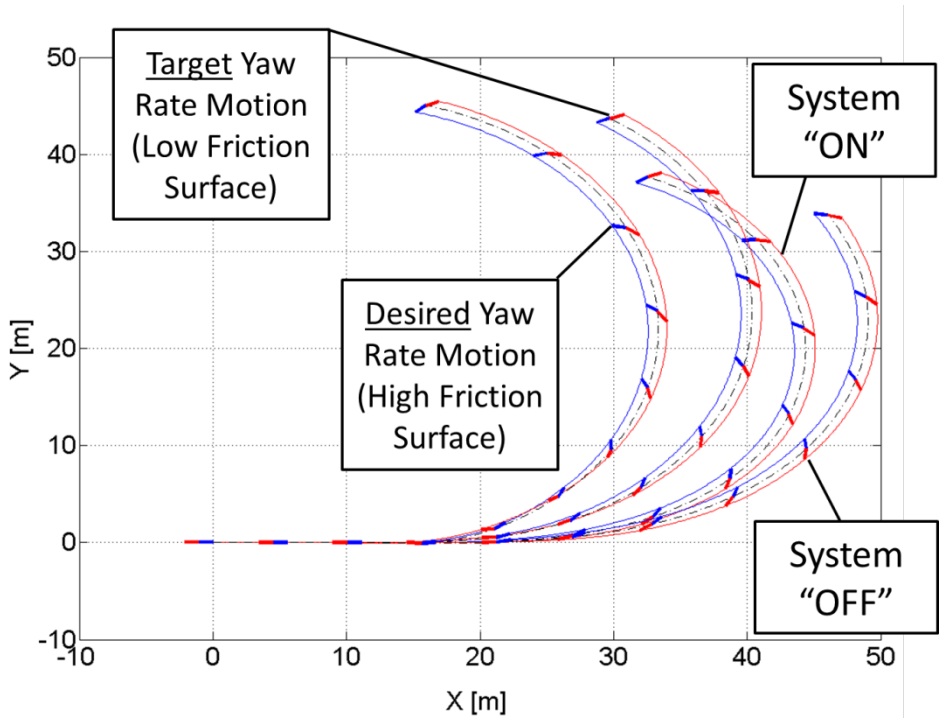

Figure 100: J-Turn Maneuver Simulation Results.

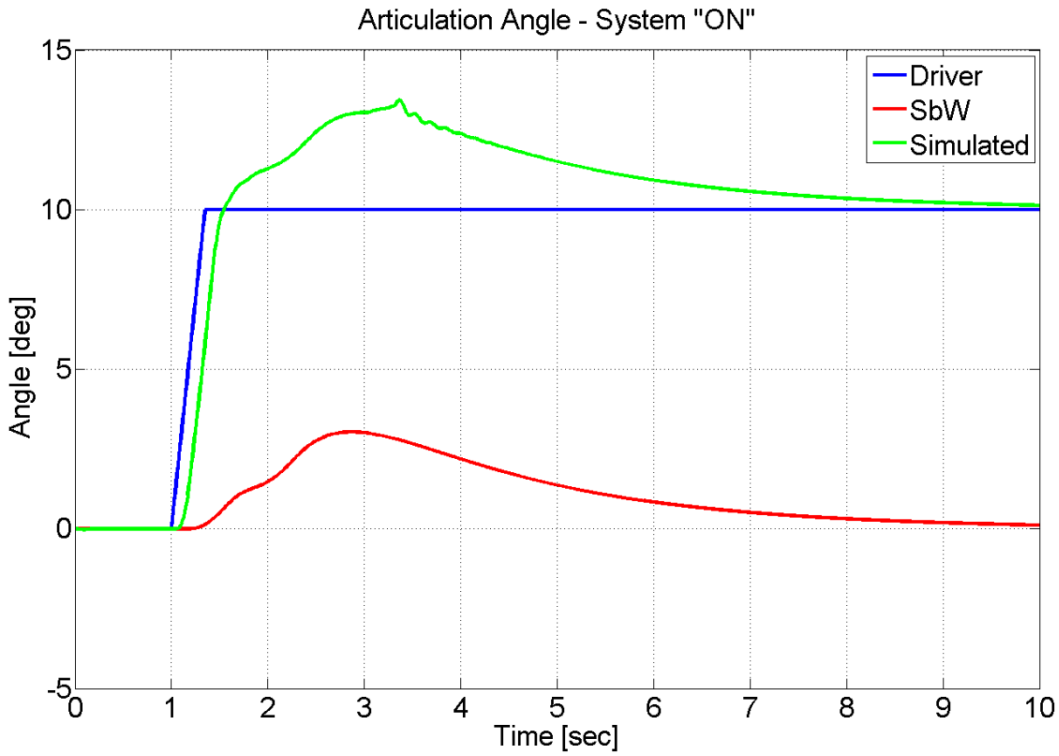

Figure 101: Articulation Angle Contributions.

Figure 101 shows the articulation angles as demanded by the driver and the SbW controller, which commands an additional corrective action to cause the vehicle to track the target yaw rate path.

8.4 Experimental Results

A suitable test track, shown in Figure 102, is selected to have the appropriate size and surface conditions that allow for conducting dynamic maneuvers at appropriate speeds in a controlled manner. The prototype test vehicle has a maximum speed of 20km/h since it is not meant to travel between working sites for transporting materials, which is not the case with most modern wheel loaders that must travel at higher speeds. Therefore, in order to induce lateral instabilities in the prototype vehicle, a low friction surface is required. The selected test track is paved with gravel, thus the road surface is composed of snow-covered gravel as shown in Figure 103.

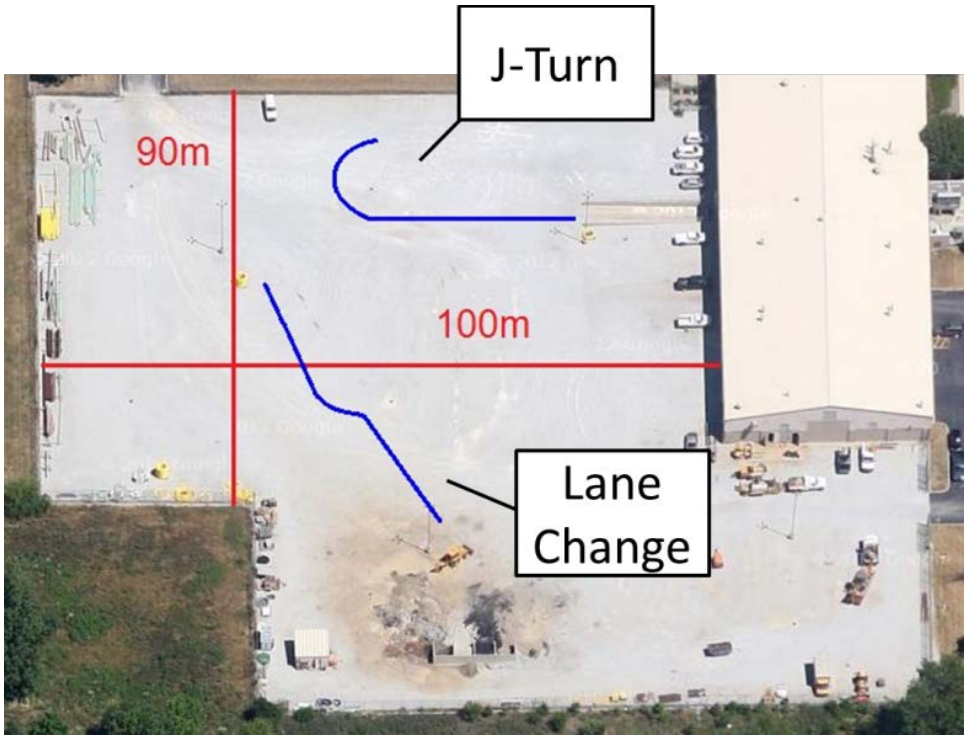

Figure 102: Track for Experimental Testing and Validation (top view).

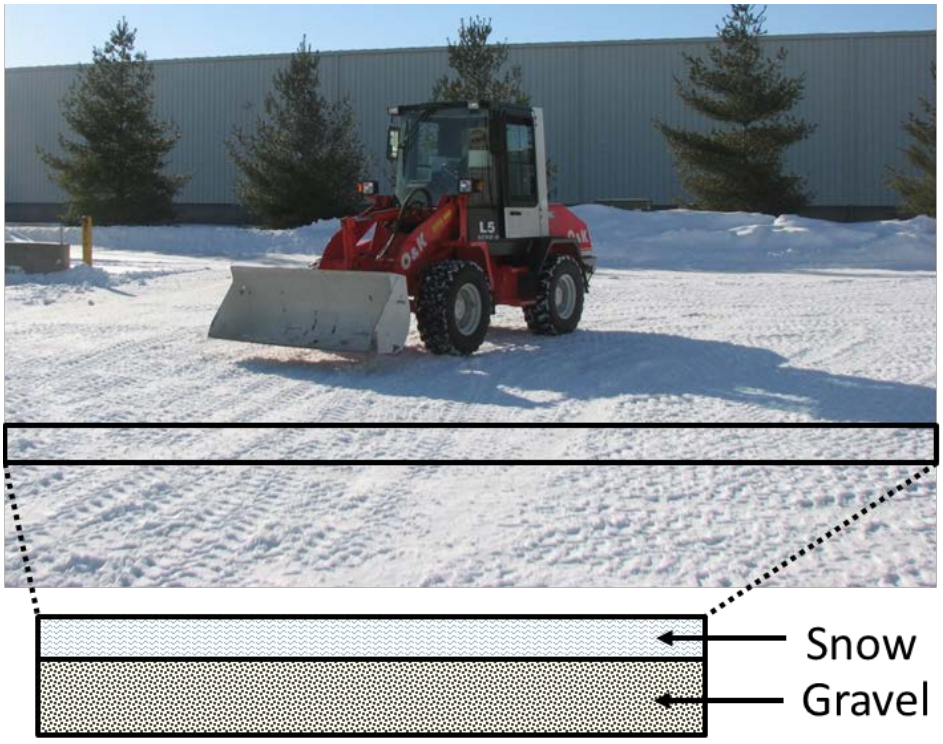

Figure 103: Low-friction Surface Composition.

Several J-Turn maneuvers are conducted at 20 km/h with the stability control system turned on and off. Figure 104 shows three representative plots for each scenario, and illustrates the improved performance when the stability controller is activated. When the system is turned off, the vehicle drifts sideways and departs from the intended path. With the system active, the vehicle is able to track a smaller radius turn, which is closer to the driver's intended path. From a characteristic standpoint, the intervention of the SbW is subtle to the driver, and the relinquishing of control back to the driver after intervention is seamless, which validates the design of the pre-filter and fading integrator described in Section 8.2.

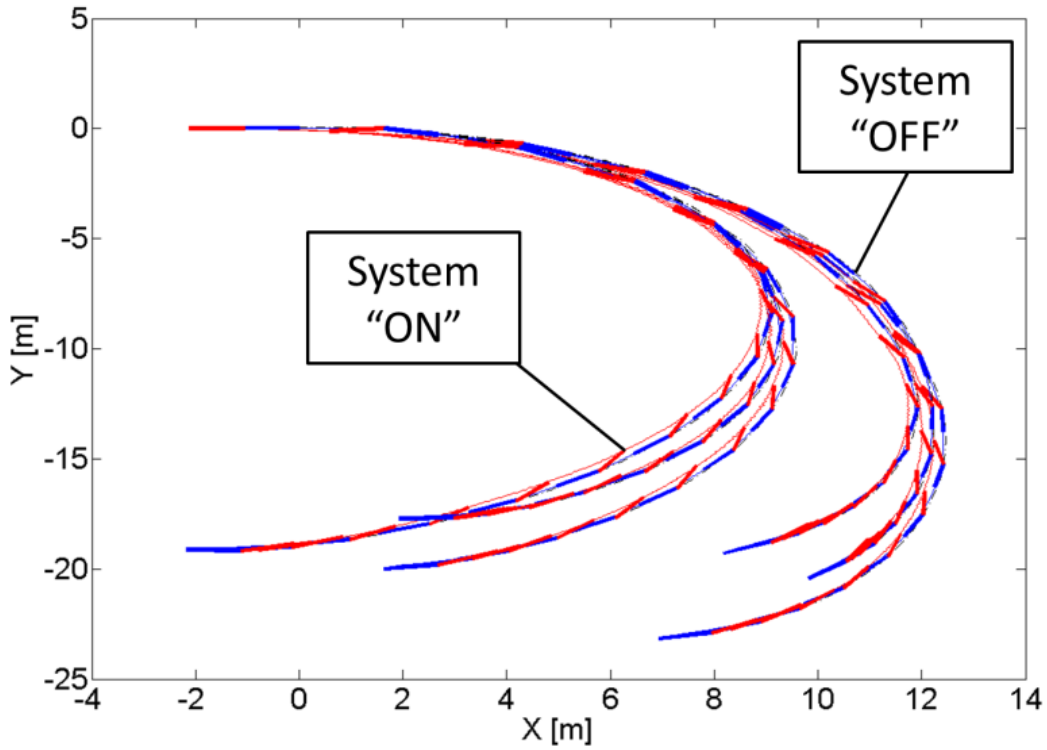

Figure 104: J-Turn Maneuver Experimental Results.

For further validation, another standard dynamic maneuver is conducted and the performance of the SbW controller is evaluated. A single lane change (SLC)

maneuver is executed by applying a sinusoidal input to the steering wheel, as depicted in Figure 105, while the vehicle travels at 20km/h.

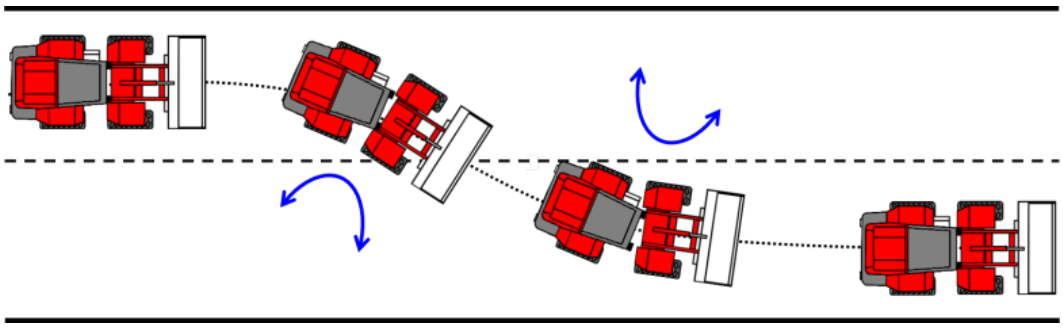

Figure 105: Single Lane Change Maneuver Depiction.

Even though wheel loaders do not necessarily drive on paved roads often, however this test demonstrates the SbW system's ability to track the driver's intended path with continuous input at the steering wheel. At the same time, it demonstrates the SbW system's ability to deliver constant and consistent performance as evident in Figure 106, where the vehicle changes lane and ends up in almost the same location repeatedly. On the other hand, when the system is deactivated, the driver has much more difficulty in guiding the vehicle to end up in the adjacent lane, and in certain instances the vehicle overshoots and crosses the lane borders due to skidding.

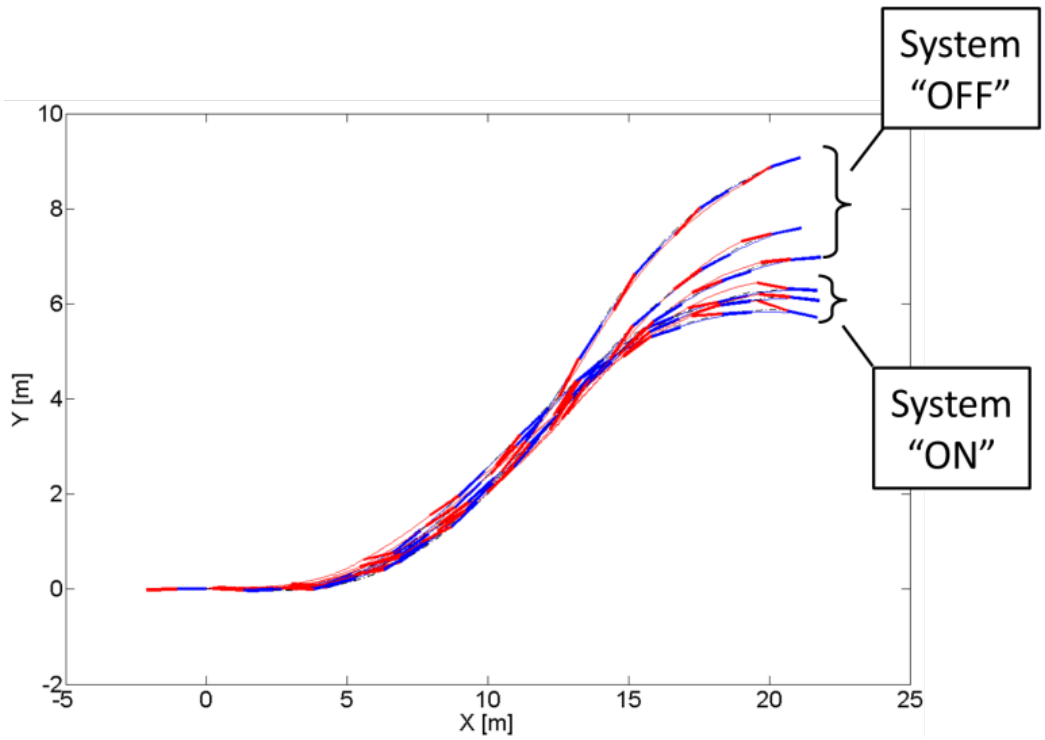

Figure 106: Single Lane Change Maneuver Experimental Results

8.5 Chapter Summary

- A high-fidelity vehicle dynamics model is derived while keeping the yaw rate decoupled from the lateral acceleration, in order to separate the primary path-following task (driver) from the secondary disturbance-attenuation task (controller).
- The control algorithm is designed to prevent the two tasks from hindering one another, to quickly activate the automatic controller for a short period of time to counteract instabilities, and to smoothly relinquish control back to the driver.
- Simulation and experimental testing results validate the dynamical model, the control algorithm design, and the new SbW system's effectiveness in

counteracting yaw instabilities on low-friction surfaces using standard vehicle dynamic maneuvers.

- The new DC SbW technology offers enhanced safety, in addition to its fuel efficiency increase benefits.

Acknowledgement

The author would like to acknowledge Elsevier for granting the rights to use the work presented in this chapter, which was submitted to the *Control Engineering Practice* Journal (Manuscript No. CONENGPRAC-D-14-00439) and is under review at the time of this dissertation's submittal.

CHAPTER 9. VIRTUAL YAW RATE SENSOR

The notion of observability reveals the ability, or lack thereof, to estimate certain states based on the commanded input, measured output, and an embedded mathematical model of the system. Given that in most real-world applications not all of the system states can be measured, for various considerations, the concept of virtual sensing gains favorability for its effectiveness and convenience in providing critical information that would otherwise be hard or costly to retrieve. In this work, a virtual sensor that estimates an articulated frame steering vehicle's front frame yaw angle rate is investigated. For the DC SbW system, the yaw rate is a critical parameter that is required for the design of stability control algorithms that influence the vehicle yaw motion via active steering intervention. Figure 107 shows the block diagram of the designed observer structure. The observer inputs are the measured signals from the installed sensors, which in this case include the vehicle speed and articulation angle, and the control signal (pump displacement) as commanded by the controller. The signals are fed into the embedded reference model, which emulates the real system up to a certified fidelity, then based on a properly designed observer, the error between the actual measurement and its estimate decays to zero at a desired rate.

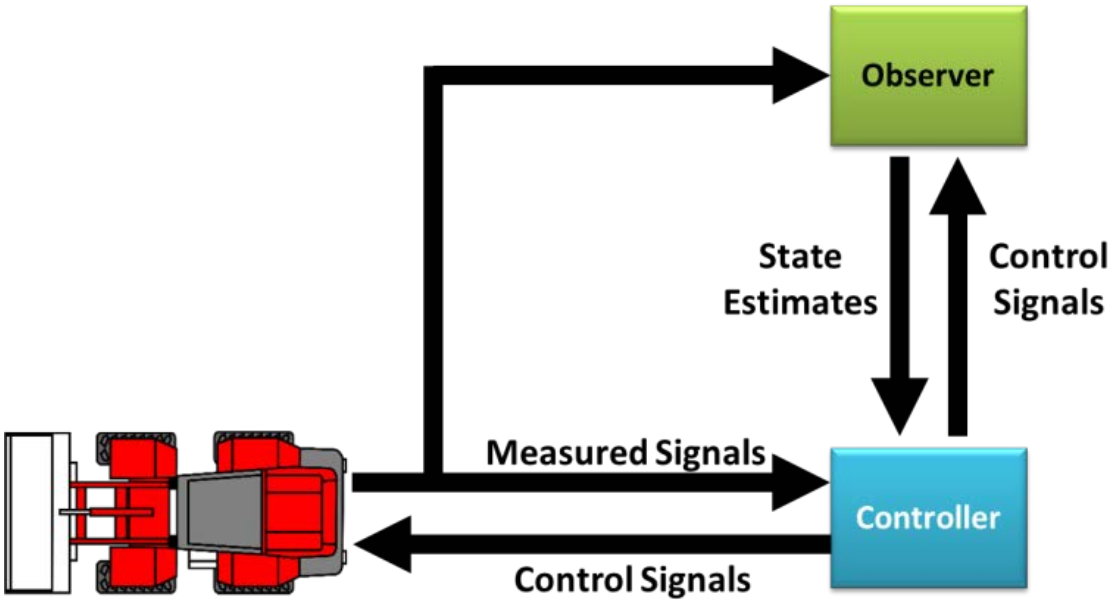

Figure 107: State Observer Block Diagram.

9.1 Observability

"*Observability is concerned with the issue of what can be said about the state given measurements of the plant output*" according to (Goodwin, Graebe, & Salgado, 2000). Given that in most real-world applications the number of measured outputs is less than the number of states, the notion of observability is of extreme importance in the sense that certain valuable states, which are not or cannot be measured, can still be estimated given the knowledge about other measured states (outputs) and control signal input(s).

$$\begin{pmatrix} M_{11} & M_{12} & M_{13} & M_{14} & 0 \\ M_{21} & M_{22} & M_{23} & M_{24} & 0 \\ M_{31} & M_{32} & M_{33} & M_{34} & 0 \\ M_{41} & M_{42} & M_{43} & M_{44} & 0 \\ 0 & 0 & 0 & 0 & 1 \end{pmatrix} \begin{pmatrix} \dot{v}_f \\ \ddot{\psi} \\ \ddot{\phi} \\ \dot{\phi} \\ \Delta\dot{p}' \end{pmatrix} = \begin{pmatrix} C_{11} & C_{12} & C_{13} & C_{14} & 0 \\ C_{21} & C_{22} & C_{23} & C_{24} & 0 \\ C_{31} & C_{32} & C_{33} & S_{34} & -A_A r_j \\ C_{41} & C_{42} & C_{43} & C_{44} & 0 \\ 0 & 0 & \dfrac{\gamma(1+\alpha^2)A_A}{C_H} & 0 & -\dfrac{(1+\alpha)K_{L_i}}{C_H} \end{pmatrix} \begin{pmatrix} v_f \\ \dot{\psi} \\ \dot{\phi} \\ \phi \\ \Delta p' \end{pmatrix} \ldots$$
$$+ \begin{pmatrix} 0 \\ 0 \\ 0 \\ 0 \\ \dfrac{(1+\alpha^2)Q_e}{C_H} \end{pmatrix} (\beta) + \begin{pmatrix} 0 \\ 0 \\ 0 \\ 0 \\ \dfrac{(1-\alpha^2)K_{L_i}}{C_H} \end{pmatrix} (p_{LP}). \tag{176}$$

Equation (176) is written more compactly in the state-space format in Eq. (177).

$$\dot{X}_{sys}(t) = A_{sys} X_{sys}(t) + B_{sys} u_{sys}(t) + F_{sys}. \tag{177}$$

$$y_{sys} = C_{sys} X_{sys}(t) + D_{sys} u_{sys}(t). \tag{178}$$

where $X_{sys} \in R^5$ is the system state vector, $u_{sys} \in R^1$ is the control signal, $y_{sys} \in R^1$ is the output, and A_{sys}, B_{sys}, C_{sys}, D_{sys} and F_{sys} are matrices of appropriate dimensions. It is noted here that the only desired output to be physically measured is the articulation angle between the vehicle's two frames, which is the fourth state in the system's state-space as shown in Eq. (179).

$$C_{sys} = \begin{bmatrix} 0 & 0 & 0 & 1 & 0 \end{bmatrix}. \tag{179}$$

Accordingly, the complete plant model is now represented by a linear-time-invariant (LTI) single-input single-output (SISO) system, where the single-input to the system is the desired pump swash plate angle, β, and the single-output is the vehicle articulation angle, ϕ, as displayed in Figure 108. This formulation lends

itself to applying modern estimation techniques, which is the subject of the next section.

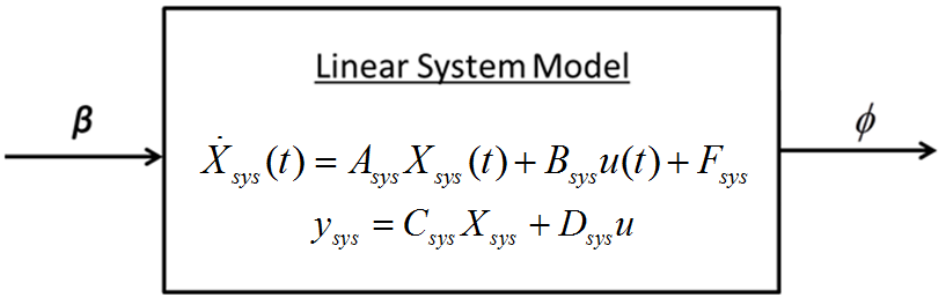

Figure 108: SISO LTI System State Space.

The observability of the linear system is checked by determining the rank of the observability matrix, $\boldsymbol{W_O}$, given in Eq. (180), which is equivalent to the number of observable states based on the specified input(s) and output(s).

$$\mathbf{W_O} = \left(C_{sys} \mid C_{sys}A_{sys} \mid C_{sys}A_{sys}^{\ 2} \mid C_{sys}A_{sys}^{\ 3} \mid C_{sys}A_{sys}^{\ 4} \mid C_{sys}A_{sys}^{\ 5}\right)^T. \qquad (180)$$

The observability matrix is found to have a full rank and the vehicle system is indeed completely state observable, which allows for proceeding to the observer design.

9.2 Observer Design via Pole Placement

The standard form of a Luenberger observer is given in Eq. (181).

$$\dot{\hat{X}}_{sys}(t) = A_{sys}\hat{X}_{sys}(t) + B_{sys}u_{sys}(t) + J_{PP}[y_{sys}(t) - C_{sys}\hat{X}_{sys}(t)]. \qquad (181)$$

where $\hat{X}_{sys}(t)$ is the state estimates vector and $\boldsymbol{J_{PP}}$ is the observer gain matrix.

The observer gain multiplies the estimate error, which represents the feedback error between the actual observation and the reference model output. The desired dynamic performance specifications of the observer are based on a

designated second-order system having specified percent overshoot (*%OS*) and rise time (t_r). The resultant damping ratio, ζ, and natural frequency, ω_n, are calculated in (182) and (183) respectively.

$$\zeta = \sqrt{\frac{\log^2\left(\frac{\%OS}{100}\right)}{\pi^2 + \log^2\left(\frac{\%OS}{100}\right)}}. \tag{182}$$

$$\omega_n = \frac{\left(\frac{\pi - \cos^{-1}(\zeta)}{t_r}\right)}{\sqrt{1+\zeta^2}}. \tag{183}$$

The system closed-loop poles are computed in Eq. (184).

$$p_{1,2} = -\zeta\omega_n \pm \omega_n\sqrt{1-\zeta^2}. \tag{184}$$

The closed-loop characteristic equation yields the coefficients for calculating matrix, J_O, which is computed by subtracting the open-loop and closed-loop coefficients. Finally, the observer gain matrix of the original system is obtained by multiplying the transformation matrix, T_{SO}, and matrix J_O.

$$J = T_{SO}\, J_O. \tag{185}$$

The observer poles are placed at some multiple of the system closed-loop poles based on the desired estimation speed, convergence, and accuracy.

9.3 Linear Quadratic Estimator (LQE)

The pole placement technique followed in the previous section returns an observer that does not take into account measurement noise associated with practically all industrial sensors, and thus may not be robust in the face of

external and internal disturbances. As such, the system equations can be augmented to include noise effects as seen in Eq. (186) and Eq. (187).

$$\dot{X}_{sys}(t) = A_{sys}X_{sys}(t) + B_{sys}u_{sys}(t) + F_{sys} + G_{sys}w_{sys}(t). \tag{186}$$

$$y_{sys} = C_{sys}X_{sys} + D_{sys}u_{sys} + \nu(t). \tag{187}$$

where $w_{sys}(t)$ is the process disturbances and $v_{sys}(t)$ is the measurement noise. Both $w_{sys}(t)$ and $v_{sys}(t)$ are assumed to be Gaussian white noise with zero mean, and the two are not correlated with each other. The specified performance index is to minimize the sum of squares of the estimated error, which is achieved by the following optimal estimator:

$$\dot{\hat{X}}_{sys}(t) = A_{sys}\hat{X}_{sys}(t) + B_{sys}u_{sys}(t) + K_e[y_{sys}(t) - C_{sys}\hat{X}_{sys}(t)]. \tag{188}$$

where K_e is the optimal observer gain given in Eq. (189).

$$K_e = P_e C_{sys}^T V_{sys}^{-1}. \tag{189}$$

and P_e is the solution to the algebraic Riccati equation given in Eq. (190).

$$A_{sys}P_e + P_e A_{sys}^T + G_{sys}W_{sys}G_{sys}^T - P_e C^T V_{sys}^{-1} C_{sys} P_e = 0. \tag{190}$$

The optimal observer gain matrix, K_e, determines the proper weight balance of the disturbance matrices that yield optimum results relative to control energy and estimation error.

9.4 Simulation and Measurement Results

To permit executing numerical simulations and conducting measurements on the prototype test vehicle, a controller was first designed to meet specified performance criteria relative to command tracking, response, and stability.

To select a suitable observer, a comparison between the two observer designs is conducted. When the measurement signal contains little to no noise, both observers perform adequately and yield equivalent results. However, in the presence of sensor noise as is the case in actual measurements, the LQE observer, outperforms the pole-placement (PP) observer as seen in Figure 109, which compares optimally selected observer poles and matrices weights. The PP observer results in significantly noisier signal when compared with the relatively smooth output of the LQE observer. Therefore, the LQE design is selected for implementation on the test vehicle, and the results shown in the next section are those of the LQE observer compared with the actual yaw rate sensor output.

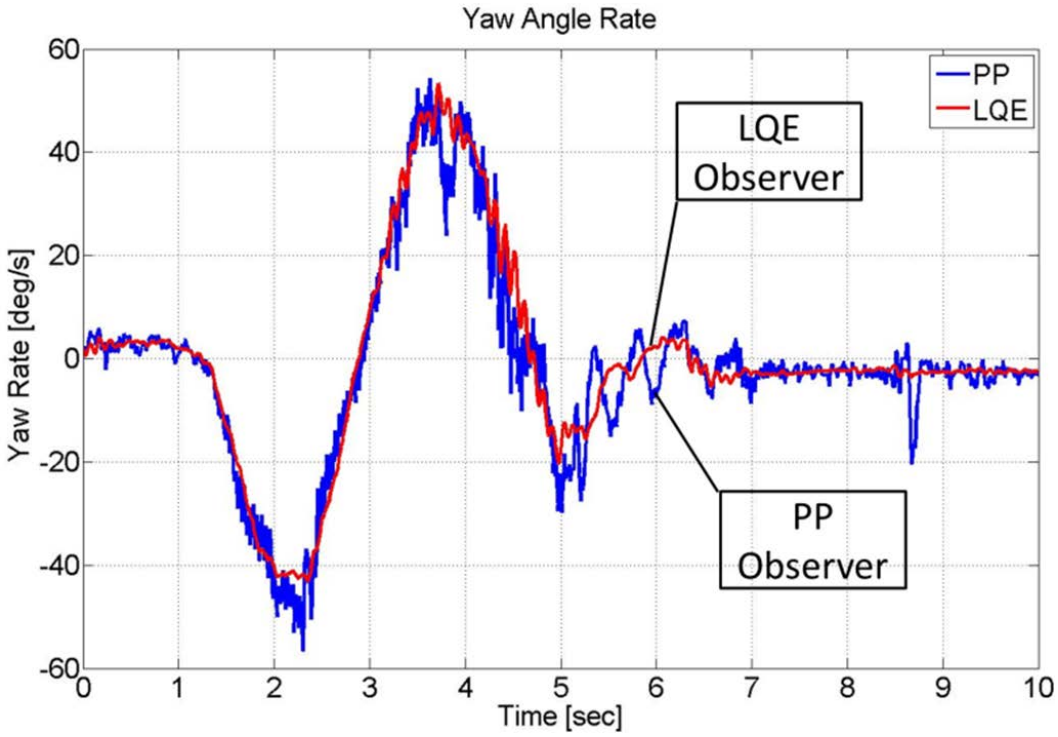

Figure 109: Observers Comparison.

Two types of maneuvers are devised, numerically simulated, and experimentally executed on the prototype test vehicle. In the first maneuver, the vehicle performs steady-state cornering (SS Cornering) at constant vehicle speed, engine speed, and articulation angle.

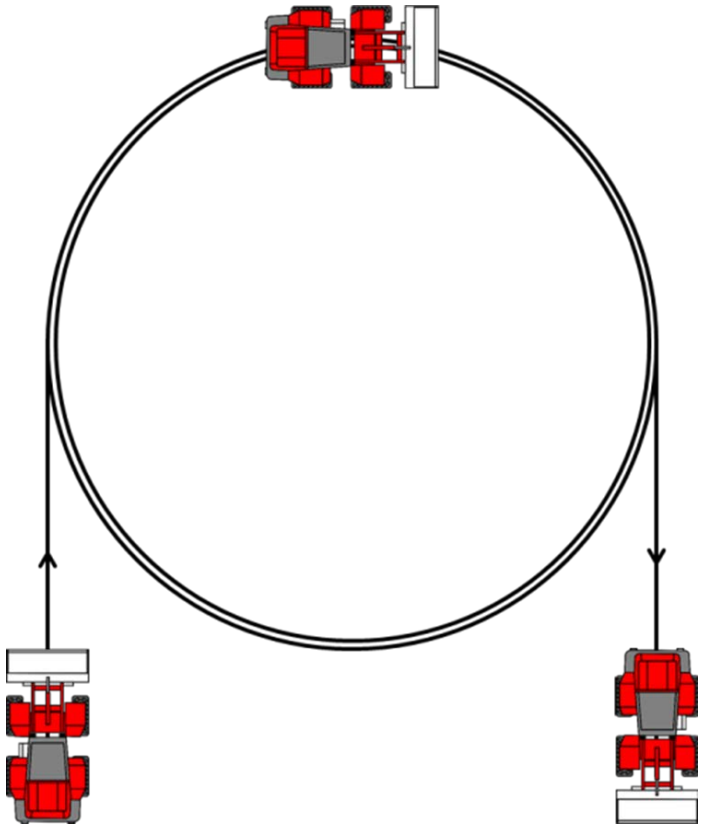

Figure 110: Steady-State Cornering Maneuver.

The second maneuver involves a single lane change (SLC) event that aims at testing the observer performance in dynamic situations where the articulation angle and correspondingly the yaw rate are both varied, at variable vehicle and engine (pump) speeds.

The virtual sensor performance is evaluated in the above maneuvers, SS Cornering and SLC, where the yaw angle rate and articulation angle are

estimated and compared against the measured signals. The next series of plots display the output of the LQE observer (“Estimate”), which evolves based on the acquired measurements, and the measured yaw rate signals (“Measured”). Before examining the plots, a few remarks are made. For the system model to handle making both left and right turns, a switching logic is devised to activate the proper system model based on the turning direction. The sampling and controller frequencies are set at 100Hz, which is suitable for the industrial controller installed in the prototype test vehicle. Lower frequencies are required given the cost burdens that are placed on real-time controllers of commercial off-highway machines, which limit the maximum speed of the selected digital microprocessor. To assess the impact of time delays that stem from discretization, the observer is validated from frequencies as high as 500Hz down to 100Hz without substantive loss of accuracy or conversion rate. This outcome is due to the fact that the estimation problem of the designed linear observer is solved in a much quicker fashion than more complex estimation algorithms such as nonlinear observers and online linearization schemes like the extended Kalman filter.

During steady-state cornering, the vehicle speed is maintained around 10km/h (2.78m/s), the pump speed is held constant at 1800rpm, and the articulation angle is held at -19° (clockwise).

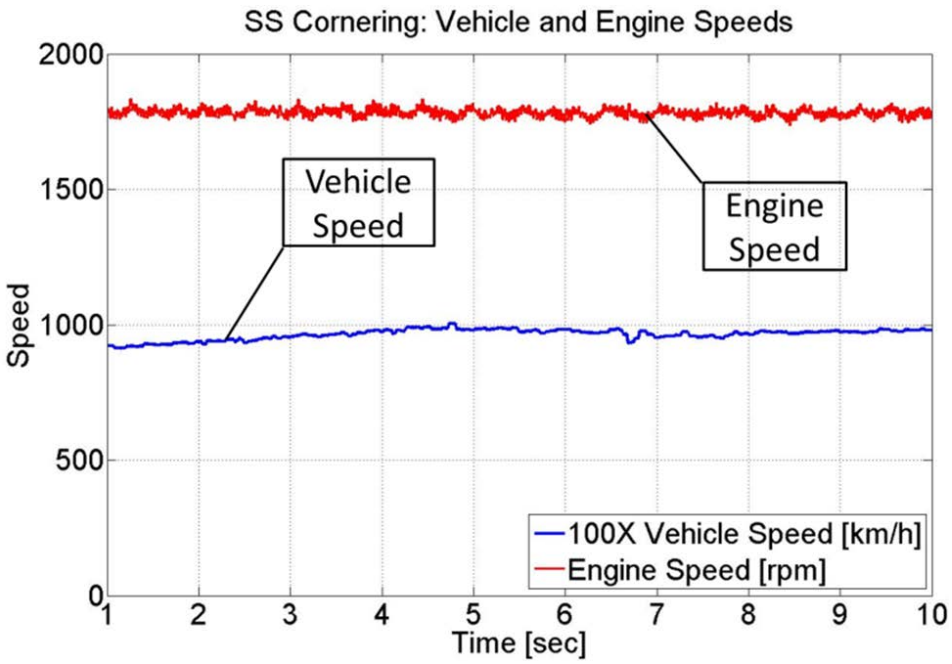

Figure 111: Vehicle and Engine Speeds – SS Cornering.

Figure 112 and Figure 113 show that the observer accurately estimates both the articulation angle and the yaw angle rate.

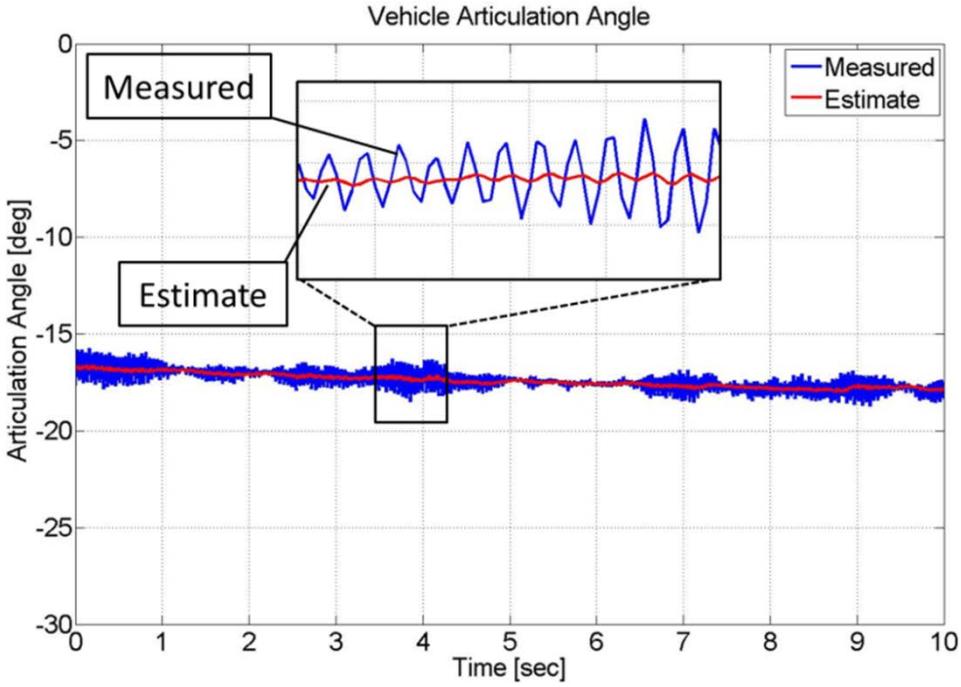

Figure 112: Articulation Angle – SS Cornering.

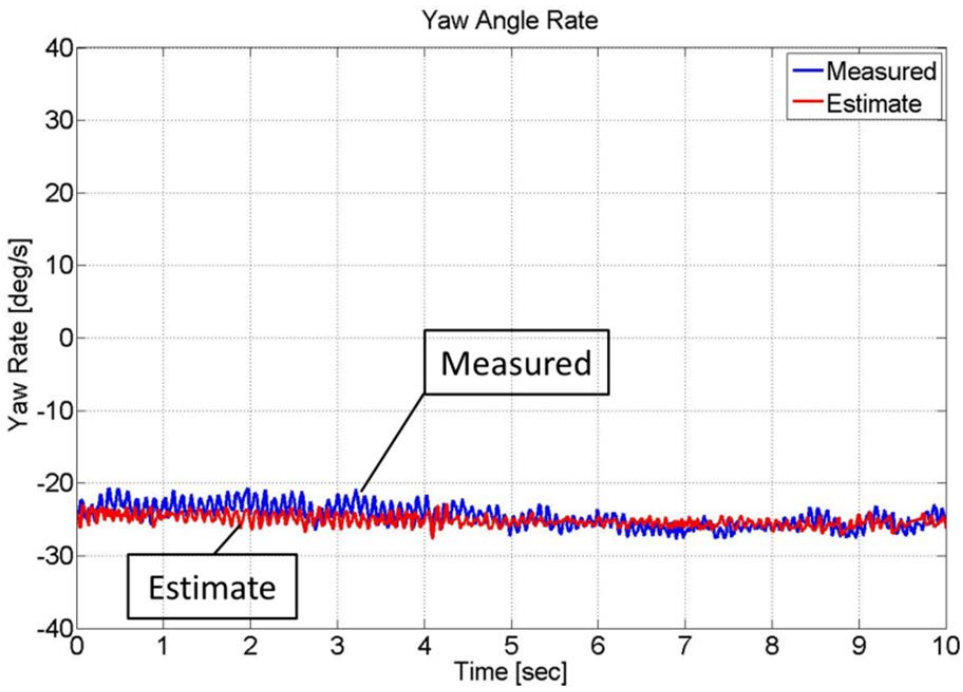

Figure 113: Yaw Angle Rate – SS Cornering.

To assess the dynamic performance of the observer, the results of the single lane change event must be examined. The engine and vehicle speeds are also varied to test the robustness of the estimation algorithm over a wide range of operation. The vehicle speed starts near its maximum of 20km/h and then ramps down to zero. Similarly, the engine (steering pump) speed is varied from minimum (idle) speed to maximum (wide open throttle) speed.

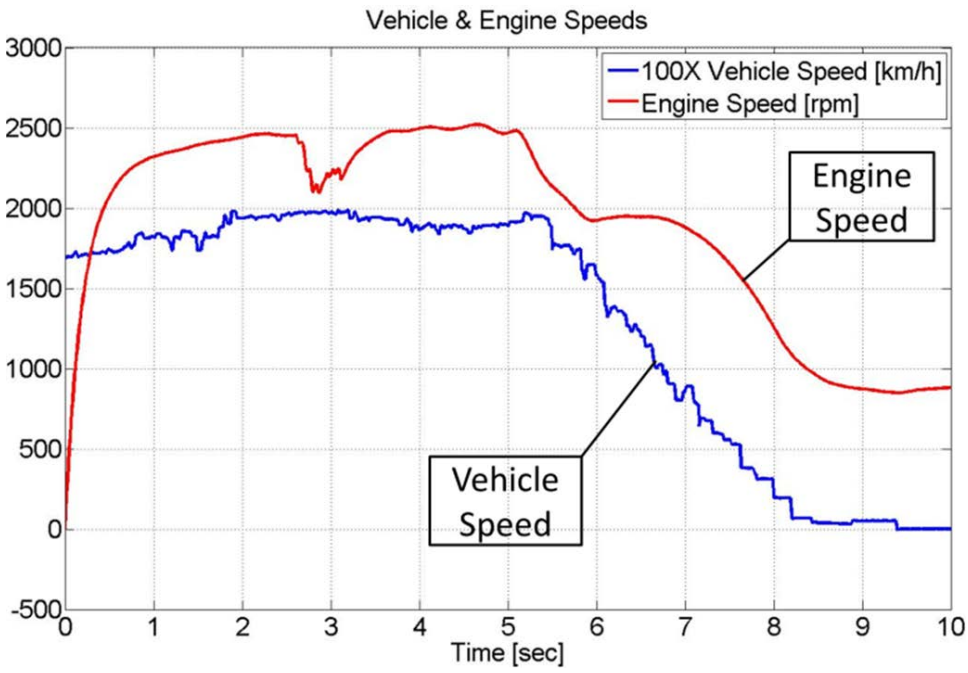

Figure 114: Vehicle and Engine Speeds – SLC

Figure 115 and Figure 116 illustrate that the observer outputs accurately track the measured signals even as the vehicle speed, engine speed, and articulation angle are significantly varied.

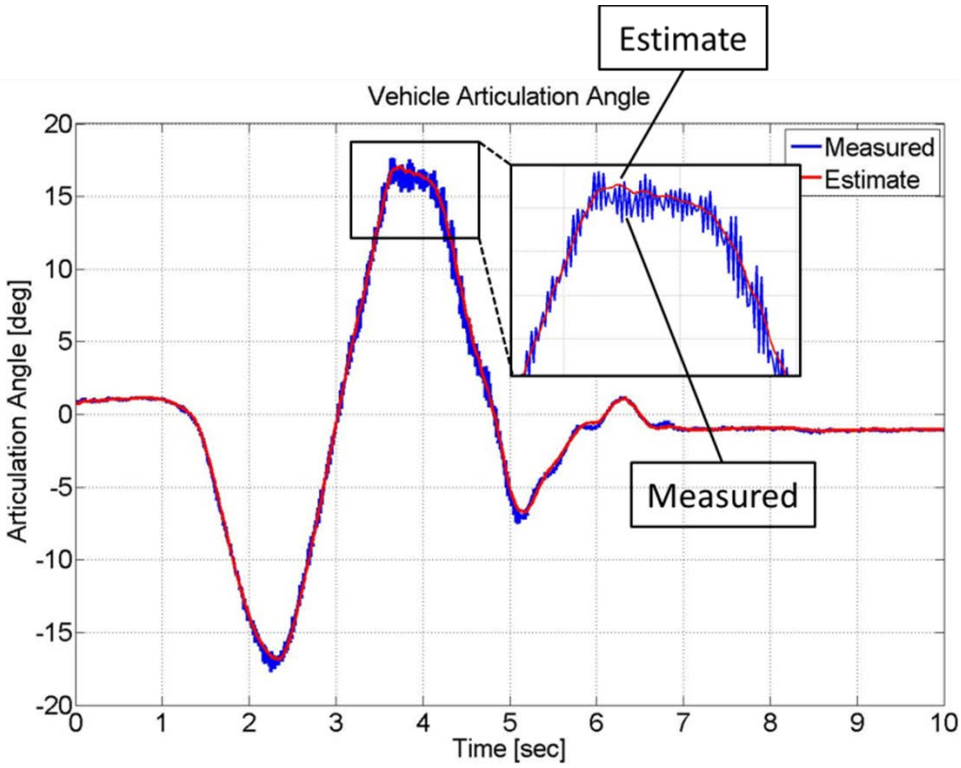

Figure 115: Articulation Angle – SLC.

Figure 115 also illustrates that the LQE observer output corresponding to the articulation angle is smoother than the actual sensor output with high frequency noise, which is consistent with the employed estimation theory.

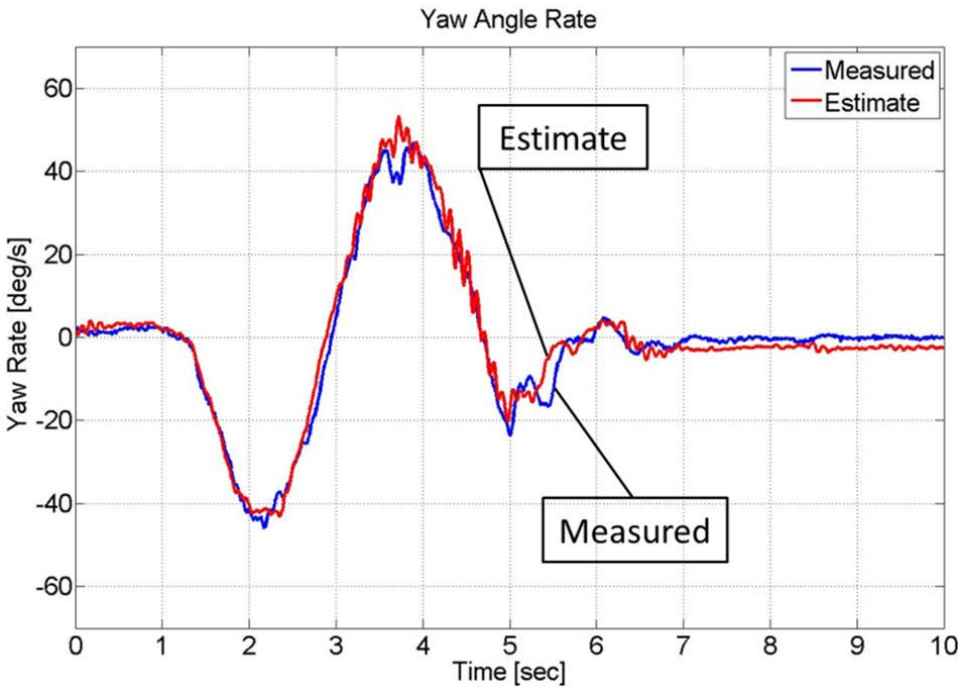

Figure 116: Yaw Angle Rate – SLC.

9.5 Robustness against Nonlinearities and Uncertainties

Besides variable operating conditions such as vehicle speed and engine speed, which were addressed in the previous section, there are several nonlinearities and uncertainties that can influence the observer performance. Nonlinearities such as the steering pump volumetric efficiency, the steering actuator and articulation joint friction forces, and the tire lateral forces are all linearized in the mathematical model. At the same time, uncertainties such as surface condition, fluid bulk modulus due to air entrapment, and vehicle parameters (moment of inertia, center of gravity location) can all have effects on the accuracy of the observer outputs. To test the robustness of the designed observer in the face of such factors, a SLC maneuver is conducted on a gravel surface that is covered with snow as shown in Figure 103.

Such a maneuver causes the vehicle to have large tire slip angles that exceed the linear range for computing lateral forces, and the deformable surface will inject a multitude of uncertainties that are not captured by the mathematical model.

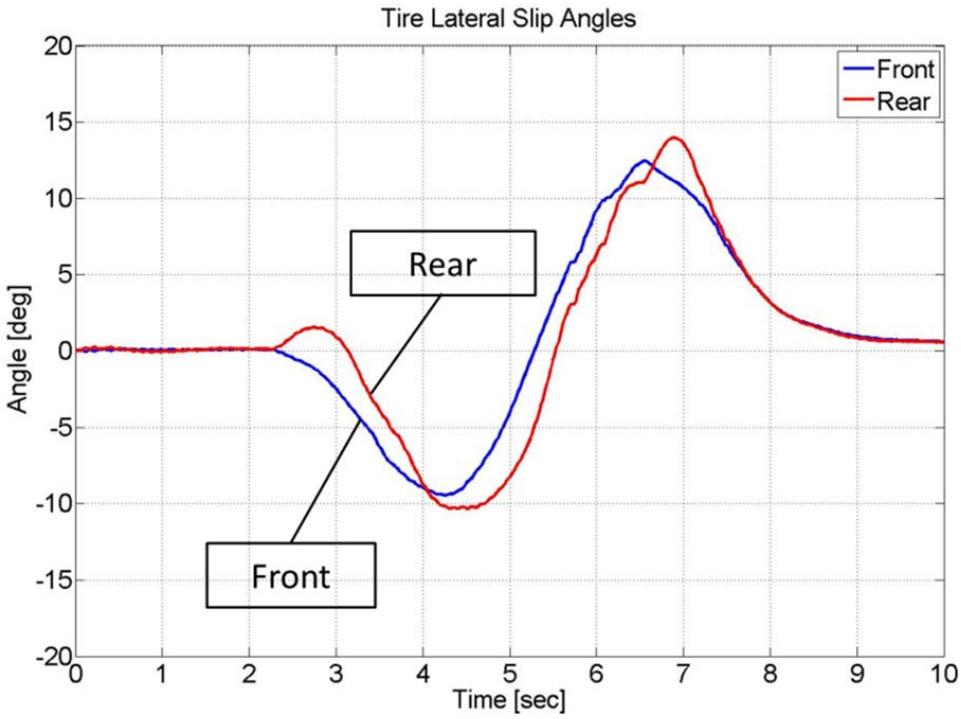

Figure 117: Tire Lateral Slip Angles – SLC on Snow.

Figure 117 shows the tires lateral slip angles as the vehicle conducts a SLC maneuver on the low-friction deformable surface, which fall in the nonlinear range of 10-15° and certainly exceed the typical linear range (<5°). The additional tire slip causes the front and rear frames to skid, and the tire lateral forces reach their saturation limits at the surface's coefficient of adhesion.

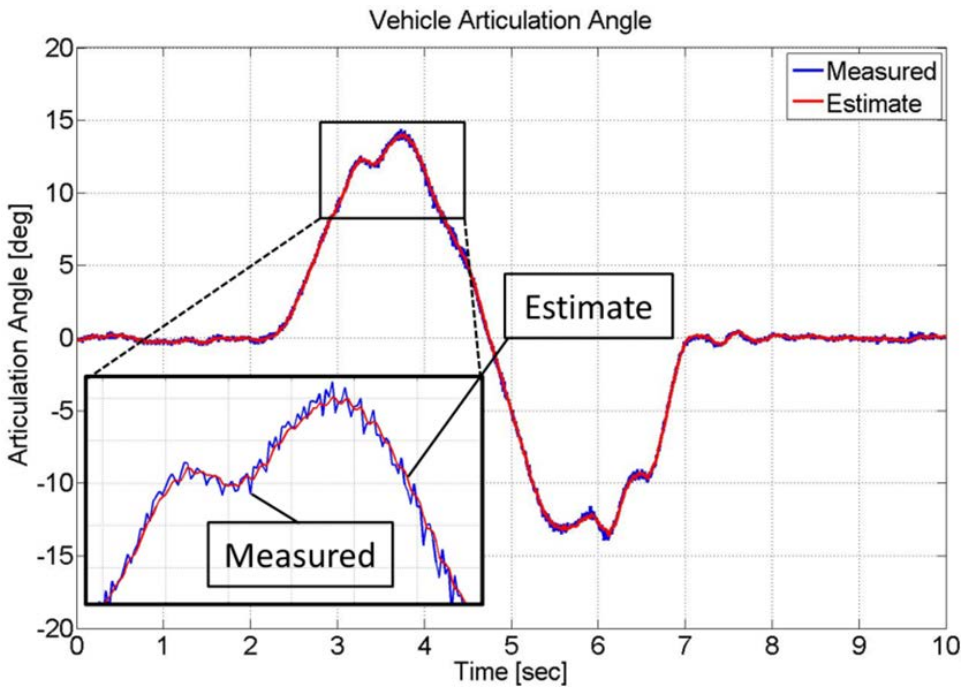

Figure 118: Articulation Angle – SLC on Snow.

Figure 118 demonstrates the effectiveness of the observer in estimating the articulation angle almost seamlessly, while Figure 119 shows a marginal performance relative to estimating the yaw angle rate.

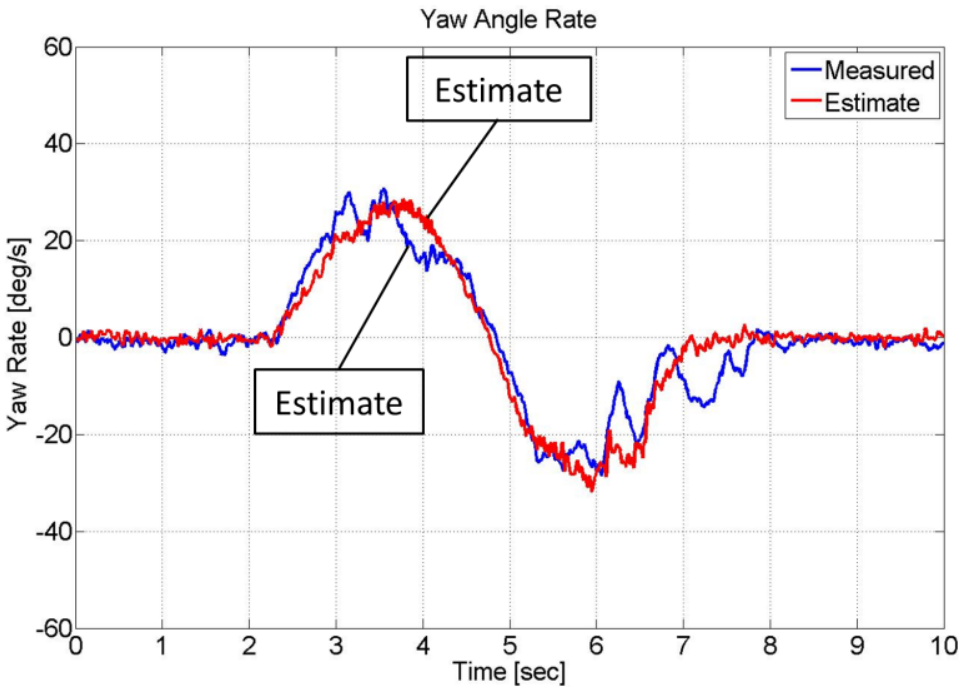

Figure 119: Yaw Angle rate – SLC on Snow.

The yaw rate estimation error is relatively small in steady state operation, which is not the case for instances when the vehicle experiences lateral shuddering due to the tires coming in contact with troughs and ridges along the deformable gravel surface covered with packed snow. This marginal performance can potentially be improved by investigating nonlinear observers, such as sliding mode, or by online linearization of the plant model, such as extended Kalman filter, which are topics for future investigations.

9.6 Results Discussion

The main caveat that is emphasized here is that in both observer design methods, pole placement or LQE, the designer must be cognizant of the overall system operation, performance, and components interaction to be able to reach optimum pole locations in the case of pole placement or matrices weight in the

case of LQE. In this work, the pole placement observer poles are placed at 3.5 times larger than the closed-loop system poles to result in relatively fast and accurate estimation. For the LQE observer, the W_{LQE} and V_{LQE} matrices that yield optimal performance relative to estimation accuracy and control effort are as follows:

$$W_{LQE} = 1. \tag{191}$$

$$V_{LQE} = 1e-3. \tag{192}$$

The obtained results underscore the effectiveness of the designed virtual sensor in estimating the yaw angle rate even in the face of uncertainties and nonlinearities. The results illustrate how an accurately derived and validated linear time-invariant (LTI) plant dynamic model combined with a properly designed linear observer is an effective yet uncomplicated solution. More advanced algorithms should only be pursued if the linear design is deemed inadequate.

9.7 Chapter Summary

- The concept of using a virtual yaw rate sensor based on a minimal collection of state measurements is investigated.
- Two observers are designed and proposed, one based on pole placement technique and the other based on linear quadratic estimation theory.
- Both designs yield accurate estimates when compared with the measurements, but the LQE design has superior performance in the presence of high frequency sensor noise.

- The robustness of the observers in the face of nonlinearities and uncertainties is investigated and deemed acceptable for most operating conditions.
- More advanced observation methods can be considered to further improve the observer robustness.

Acknowledgement

The author would like to acknowledge Elsevier for granting the rights to use the work in this chapter, which was published in the *Control Engineering Practice* Journal:

Daher, N. and Ivantysynova, M. 2014. A Virtual Yaw Rate Sensor for Articulated Vehicles Featuring Novel Electro-Hydraulic Steer-by-Wire Technology. *Control Engineering Practice*, Vol. 30, pp. 45-54.

http://www.sciencedirect.com/science/article/pii/S0967066114001506

CHAPTER 10. CONCLUSIONS AND FUTURE WORK

10.1 Conclusions

The work in this dissertation has confirmed the research aims that were set forth at the onset. The new DC steering system offers a host of advantages over state-of-the-art technologies that employ hydraulic control valves for motion control, such as the baseline hydrostatic steering system considered in this investigation. Under the same testing conditions, the new DC steering system outperformed the stock hydrostatic steering system in the areas of fuel consumption, machine productivity, and overall fuel efficiency. The new system also allows for adjustability in the steering ratio between the hand wheel and the steering angle, as well as variable steering wheel feel relative to the level of torque feedback experienced by the operator. The adaptable modes result in improved operator comfort at low speeds and increased safety at high speeds. The by-wire system also opens the door in front of implementing active safety protocols that continuously monitor and correct, as deemed necessary, critical vehicle states. A yaw stability control system via active steering is designed and validated on a prototype test vehicle. A virtual yaw rate sensor is designed and implemented on the prototype machine, resulting in excellent correlation against a physical yaw rate sensor. An adaptive control algorithm is derived and validated under various

loads, proving the machine's adaptability to varying operating conditions. Last but not least, the new DC steering system provides the potential for remote and autonomous operation since it is a by-wire technology that requires no physical operator input, which is a desirable feature for all modern and future machinery. Future work will focus on researching advanced estimation methods in order to employ virtual sensing techniques for estimating key vehicle parameters, without the need for physical sensors thus reducing cost, maintenance, and increasing machine uptime.

10.2 Future Work

After having investigated the new technology's features and capabilities from a performance standpoint, the safety and reliability of the technology must be assessed. That said however, all by-wire systems face similar challenges when it comes to fail-safe and emergency backup solutions in case of a main power failure or interruption, fault detection and tolerance, and sensor redundancy to ensure robust operation and minimal downtime. Naturally, future work will focus on these areas as outlined below.

10.2.1 Fail-safe

Emergency backup solutions in the case of power loss will be researched and proposed, in order to ensure that the steering function is not completely lost resulting in hazardous machine operation. Multiple fail-safe strategies can be employed to provide an emergency backup system, which depend on the level of steering functionality required by safety standards and machine manufacturers. Three backup solutions are briefly described to give an overview of the available

options. One solution can be similar to hydrostatic steering systems, in which a manual (gear type) pump can be added to the steering wheel/column assembly, where the operator can manually turn the steering wheel to rotate the pump and provide an adequate flow rate to induce steering down to slower speeds that are deemed safe. A second solution can employ a separate power-pack subsystem with a dedicated pump (gear type for cost effectiveness) and a DC motor, which activates when a failure is detected to provide the necessary power to steer the machine until a safe stop is reached. A third solution can make use of the moving vehicle's inertia to drive a pump, which is coupled to the wheels/axles via a clutch that activates when a failure is sensed.

The above solutions are not unique to this research and can be pursued based on the requirements, preferences, packaging constraints, and cost effectiveness.

10.2.2 Sensor Redundancy

Future research will evaluate the sensor redundancy required to meet the safety standards of the vehicles under consideration. For instance, the steering wheel angle sensor must have dual outputs that are completely independent, which ensures that the operator's input is always sensed and fed back to the controller. At the same time, the pump swash plate angle sensor must possess similarly redundant outputs, or the computer software must allow for open-loop control when closed-loop control is not available. A complete examination of all remaining sensors will be carried for completeness and comprehensiveness.

10.2.3 Fault Tolerance

A thorough investigation will be conducted to assess the fault tolerance of the new SbW system and define suitable strategies, which enable the system to stay operational even if some of its components malfunction. The operating quality is allowed to decrease, but the loss of functionality is proportional to the severity of the failure, as compared to a simply designed system that completely shuts down even when a minor failure occurs. A fault-tolerant scheme enables the steering system to resume its anticipated operation, albeit at a reduced level, rather than completely losing steering control of the vehicle. A comprehensive fault insertion exercise will be performed by artificially injecting the system with potential faults, and check its robustness against the number and severity of simulated faults.

.

LIST OF REFERENCES

LIST OF REFERENCES

Abd-Elaziz, M. (2007). *Fault tolerance steer-by-wire electrohydraulic system with haptic interface for articulated vehicles.* Chicago, IL, USA: University of Illinois at Chicago.

Ackermann, J. (1994). Robust decoupling, ideal steering dynamics and yaw stabilization of 4WS cars. *Automatica, 30*(11), 1761-1768.

Ackermann, J. (1997). Robust Control Prevents Car Skidding. *Control Systems, IEEE, 17*(3), 23-31.

Astrom, K., & Wittenmark, B. (2008). *Adaptive Control.* Mineola, New York, USA: Dover.

Azad, N. (2006). *Dynamic Modelling and Stability Controller Development for Articulated Steer Vehicles.* Ph.D. dissertation, University of Waterloo. Waterloo, Ontario, Canada.

Berbuer, J. (1988). *Neuartige Servoantriebe mit primärer Verdrängersteuerung.* Ph.D. Thesis. RWTH Aachen. Aachen, Germany.

Bobrow, J., & Lum, K. (1996). Adaptive, High Bandwidth Control of a Hydraulic Actuator. *Journal of Dynamic Systems, Measurement, and Control, 118*(4), 714-720.

Bonchis, A., Corke, P., Rye, D., & Ha, Q. (2001). Variable structure methods in hydraulic servo systems control. *Automatica, 37*(4), 589-595.

Chen, C., & Tomizuka, M. (1997). Modeling and Control of Articulated Vehicles. *California Partners for Advanced Transit and Highways, Institute of Transportation Studies. Report number UCB-ITS-PRR-97-42*.

Chen, L., & Shieh, Y. (2011). Jackknife Prevention for Articulated Vehicles Using Model Reference Adaptive Control. *Journal of Automobile Engineering, 225*(1), 28-42.

Cheng, C., Roebuck, R., & Cebon, D. (2011). High-speed optimal steering of a tractor-semi-trailer. *Vehicle System Dynamics, 49*(4), 561-593.

Crolla, D. (2009). *Automotive Engineering: Powertrain, Chassis System and Vehicle Body.* Burlington, MA: Elsevier Science & Technology Books.

Crolla, D., & Horton, D. (1983). The steering behaviour of articulated body steer vehicles. *I. Mech. E. Conference on Road Vehicle Handling*, (pp. 139-146). Nuneaton, U.K.

Daher, N., & Ivantysynova, M. (2012). Electro-hydraulic energy-saving power steering systems of the future. *Proceedings of the 7th FPNI PhD Symposium*, (pp. 929 – 952). Reggio Emilia, Italy.

Daher, N., & Ivantysynova, M. (2013a). Novel Energy-Saving Steer-by-Wire System for Articulated Steering Vehicles: A Compact Wheel Loader Case Study. *Proceedings of the 13th Scandinavian International Conference on Fluid Power, SICFP2013.* Linkoping, Sweden.

Daher, N., & Ivantysynova, M. (2013a). Novel Energy-Saving Steer-by-Wire System for Articulated Steering Vehicles: A Compact Wheel Loader Case Study. *Proceedings of the 13th Scandinavian International Conference on Fluid Power, SICFP2013.* Linkoping, Sweden.

Daher, N., & Ivantysynova, M. (2013b). Pump Controlled Steer-by-Wire System. *SAE 2013 Commercial Vehicle Engineering Congress* (pp. SAE Technical Paper 2013-01-2349). Rosemont, IL, USA: Society of Automotive Engineers.

Daher, N., & Ivantysynova, M. (2013c). System Synthesis and Controller Design of a Novel Pump Controlled Steer-By-Wire System Employing Modern Control Techniques. *ASME/Bath Symposium on Fluid Power and Motion Control.* Sarasota, FL, USA: American Society of Mechanical Engineers.

Daher, N., & Ivantysynova, M. (2014). A Virtual Yaw Rate Sensor for Articulated Vehicles Featuring Novel Electro-Hydraulic Steer-by-Wire Technology. *Control Engineering Practice, 30*, 45-54.

Daher, N., & Ivantysynova, M. (2014). An Indirect Adaptive Velocity Controller for a Novel Steer-by-Wire System. *ASME Journal of Dynamic Systems, Measurement, and Control, 136*(5), TBD.

Daher, N., & Ivantysynova, M. (2014). Energy Analysis of an Original Steering Technology that Saves Fuel and Boosts Efficiency. *Energy Conversion and Management*.

El-Gindy, M., Mrad, N., & Tong, X. (2001). Sensitivity of rearward amplification control of a truck/full trailer to tyre cornering stiffness variations. *Journal of Automobile Engineering, 215*(5), 579-588.

Fancher, P., Winkler, C., Ervin, R., & Zhang, H. (1998). Using Braking To Control the Lateral Motions of Full Trailers. *International Journal of Vehicle Mechanics and Mobility, 29*(1), 462-478.

Goodwin, G., Graebe, S., & Salgado, M. (2000). *Control System Design.* Valparaiso: Prentice-Hall, Inc.

Grabbel, J. (2003). *Robust control strategies of a displacement controlled joint rotary actuator using vane type motor.* Hamburg, Germany: TUHH Hamburg, Ph.D. Dissertation.

Habibi, S., & Goldenberg, A. (1999). Design of a New High Performance. *Proceedings of the 1999 IEEE/ASME International Conference on Advanced Intelligent Mechatronics.* Atlanta, GA, USA.

Hac, A., Fulk, D., & Chen, H. (2008). Stability and control considerations of vehicle–trailer combination. *SAE*, 2008-01-1228.

Haggag, S. (2002). *Development of fault-tolerant steer-by-wire system for earth moving equipment.* Chicago, IL, USA: University of Illinois at Chicago.

He, J. (2005). *Integrated vehicle dynamics control using active steering, driveline and braking.* Leeds, UK: University of Leeds - PhD Dissertation.

He, Y., Khajepour, A., McPhee, J., & Wang, X. (2005). Dynamic modeling and stability analysis of articulated frame steer vehicles. *International Journal of Heavy Vehicle Systems, vol. 12, no. 1*, 28-59.

Hewett, A. (1994). *Patent No. 5329767.* United States of America.

Hisseine, D. (2005). Robust tracking control for a hydraulic actuation system. *IEEE Conference on Control Applications.* Toronto, Ontario, Canada.

Horton, D., & Crolla, D. (1986). Theoretical analysis of the steering behaviour of articulated frame steer vehicles. *Vehicle System Dynamics, vol. 15*, 211-234.

Ivantysynova, M., Weber, J., & Grabbel, J. (2011). *Patent No. 7,786,125 B2.* USA.

Lawrence, P., Salcudean, S., Sepehri, N., Chan, D., Bachmann, S., Parker, N., . . . Frenette, R. (1995). Coordinated and Force-Feedback Control of Hydraulic. *Symposium on Experimental Robotics.* Stanford, CA, USA.

Li, G., & Khajepour, A. (2005). Robust control of a hydraulically driven flexible arm using backstepping technique. *Journal of Sound and Vibration, 280*(3-5), 759-775.

Liu, Y., & Handroos, H. (1999). Technical note Sliding mode control for a class of hydraulic position servo. *Mechatronics, 9*(1), 111-123.

Lodewyks, J. (1994). *Der Differentialzylinder im geschlossenen hydrostatischen Kreislauf.* Ph.D. Thesis. RWTH. Aachen, Germany.

Lumkes Jr., J. H., & Van Doorn IV, W. (2008). Design and Testing of a Dual-Path Front Hydrostatic Drive-By-Wire Control System for an Off-Road Vehicle. *Transactions of the ASABE, 51*(4), 1165-1175.

Merritt, H. E. (1967). *Hydraulic Control Systems.* Cincinnati, Ohio, USA: John Wileys and Sons.

Milliken, W., & Milliken, D. (1995). *Race Car Vehicle Dynamics.* SAE International.

Odhams, A., Roebuck, R., Jujnovich, B., & Cebon, D. (2011). Active steering of a tractor–semi-trailer. *Journal of Automobile Engineering, 225*(7), 847-869.

Palkovics, L., & El-Gindy, M. (1996). Examination of different control strategies of heavy-vehicle performance. *ASME Journal of Dynamic Systems, Measurement, and Control, 118*(3), 489-498.

Pastrakulijic, V. (1995). *Design and Modeling of a New Electro Hydraulic Actuator.* M.S. Thesis. University of Toronto. Toronto, Canada.

Phillips, B., & Spencer, Jr., B. (2012). *Model-Based Framework for Real-Time Dynamic Structural Performance Evaluation.* NSEL Report Series Report No. NSEL-031. University of Illinois at Urbana-Champaign.

Plummer, A., & Vaughan, N. (1996). Robust Adaptive Control for Hydraulic Servosystems. *Journal of Dynamic Systems, Measurement, and Control, 118*(2), 237-244.

Rahmfeld, R. (2002). *Development and Control of Energy Saving Hydraulic Servo Drives for Mobile Systems.* Ph.D. Thesis, Dept. of Aircraft Systems, Technical University of Hamburg-Harburg. Hamburg, Germany.

Rahmfeld, R., & Ivantysynova, M. (1998). Energy Saving Hydraulic Actuators for Mobile Machines. *Proceedings of 1st Bratislavian Fluid Power Sysmposium*, (pp. 47-57). Častá – Píla, Slovakia.

Rahmfeld, R., & Ivantysynova, M. (2003). New Displacement Controlled Linear Actuator Technology – A Suitable Control Element for Active Oscillation Damping. *The Eighth Scandinavian International Conference on Fluid Power.* Tampere, Finland.

Rahmfeld, R., & Ivantysynova, M. (2004). Displacement Controlled Wheel Loader – a simple and clever Solution. *4th International Fluid Power Conference Proceedings*, (pp. 183-196). Dresden, Germany.

Rajamani, R. (2005). *Vehicle Dynamics and Control.* Springer.

Scholl, R., & Klein, R. (1971). Stability Analysis of an Articulated Vehicle Steering System. *Earthmoving Industry Conference*, (p. S.A.E. Paper 710527). Illinois, USA.

Stephenson, D., & Rajput, P. (2010). *Patent No. WO 2010/115018 A1.* USA.

Tabatabaei Oreh, S., Kazemi, R., & Azadi, S. (2014). A sliding-mode controller for directional control of articulated heavy vehicles. *Journal of Automobile Engineering, 228*(3), 245-262.

Tabatabaei Oreh, S., Kazemi, R., & Shahram, A. (2013). Directional Control of Articulated Heavy Vehicles. *SAE International Journal of Commercial Vehicles, 6*(1), 143-149.

Tsao, T., & Tomizuka, M. (1994). Robust Adaptive and Repetitive Digital Tracking Control and Application to a Hydraulic Servo for Noncircular Machining. *ASME Journal of Dynamic Systems, Measurement, and Control, 1*(116), 24-32.

Vossoughi, G., & Donath, M. (1995). Dynamic Feedback Linearization for Electrohydraulically Actuated Control System. *Journal of Dynamic Systems, Measurement, and Control, 117*(4), 468-477.

Williamson, C., & Ivantysynova, M. (2007). The Effect of Pump Efficiency on Displacement-Controlled Actuator Systems. *Proceedings of the Tenth Scandinavian International Conference on Fluid Power.* Tampere, Finland.

Williamson, C., & Ivantysynova, M. (2010). Power Optimization for Multi-Actuator Pump-Controlled Systems. *Proceedings of the 7th International Fluid Power Conference Aachen 2010 (7IFK)*, (pp. 91-102). Aachen, Germany.

Williamson, C., Lee, S., & Ivantysynova, M. (2009). Active Vibration Damping For an Off-Road Vehicle with Displacement Controlled Actuators. *International Journal of Fluid Power*, 5-16.

Williamson, C., Zimmerman, J., & Ivantysynova, M. (2008). Efficiency Study of an Excavator Hydraulic System Based on Displacement-Controlled Actuators. *ASME/Bath Workshop on Fluid Power and Motion Control (FPMC08).* Bath, UK.

Yao, B., Bu, F., Reedy, J., & Chiu, G. (2000). Adaptive Robust Motion Control of Single-Rod Hydraulic Actuators: Theory and Experiments. *IEEE/ASME TRANSACTIONS ON MECHATRONICS, 5*(1), 79-91.

Yao, B., Chiu, G., & Reedy, J. (1997). Nonlinear adaptive robust control of one-dof electro-hydraulic servo systems. *ASME International Mechanical Engineering Congress and Exposition.* Dallas, TX, USA.

Yih, P. (2005). *STEER-BY-WIRE: IMPLICATIONS FOR VEHICLE HANDLING AND SAFETY.* Stanford, CA, USA: Stanford University.

Zheng, S., Tang, H., Han, Z., & Zhang, Y. (2006). Controller design for vehicle stability enhancement. *Control Engineering Practice, 14*(12), 1413-1421.

Ziegler, R. (1990). *Auslegung und Optimierung schneller Servopumpen.* Ph.D. Thesis. Universitat Karlsruhe. Karlsruhe, Germany.

Zimmerman, J. (2008). *Design and Simulation of an Energy Saving Displacement-Controlled Actuation System for a Hydraulic Excavator.* West Lafayette, IN, USA.

Zong, C., Zhu, T., Wang, C., & Liu, H. (2012). Multi-objective stability control algorithm of heavy tractor semi-trailer based on differential braking. *The Chinese Journal of Mechanical Engineering, 25*(1), 88-97.

APPENDICES

Appendix A Dynamic Model Matrices

$$M_{11} = m_f + m_r$$
$$M_{12} = -bm_r - cm_r$$
$$M_{13} = cm_r$$
$$M_{14} = 0$$
$$M_{21} = -bm_r - cm_r$$
$$M_{22} = m_r b^2 + 2m_r bc + m_r c^2 + I_f + I_r$$
$$M_{23} = -m_r c^2 - m_r bc - I_r$$
$$M_{24} = 0$$
$$M_{31} = cm_r$$
$$M_{32} = -m_r c^2 - m_r bc - I_r$$
$$M_{33} = m_r c^2 + I_r$$
$$M_{34} = 0$$
$$M_{41} = 0$$
$$M_{42} = 0$$
$$M_{43} = 0$$
$$M_{44} = 1$$
$$C_{11} = \frac{-N_f C_{\alpha f} - N_r C_{\alpha r}}{u_f}$$
$$C_{12} = \frac{-aN_f C_{\alpha f} - (b+c+d) N_r C_{\alpha r}}{u_f} - (m_f + m_r) u_f$$
$$C_{13} = -\frac{N_r C_{\alpha r} (c+d)}{u_f}$$
$$C_{14} = -N_r C_{\alpha r}$$
$$C_{21} = \frac{-aN_f C_{\alpha f} + (b+c+d) N_r C_{\alpha r} + N_f C_{M\alpha f} + N_r C_{M\alpha r}}{u_f}$$
$$C_{22} = \frac{\begin{pmatrix} -a^2 N_f C_{\alpha f} - (b+c+d)^2 N_r C_{\alpha r} \\ +aN_f C_{M\alpha f} - (b+c+d) N_r C_{M\alpha r} \end{pmatrix}}{u_f} + m_r (b+c) u_f$$

$$C_{23} = \frac{(b+c+d)(c+d)N_r C_{\alpha r} + (c+d)N_r C_{M\alpha r}}{u_f}$$

$$C_{24} = (b+c+d)N_r C_{\alpha r} + N_r C_{M\alpha r}$$

$$C_{31} = \frac{-(c+d)N_r C_{\alpha r} - N_r C_{M\alpha r}}{u_f}$$

$$C_{32} = \frac{(c+d)(b+c+d)N_r C_{\alpha r} + N_r C_{M\alpha r}(b+c+d)}{u_f}$$

$$C_{33} = \frac{-(c+d)^2 N_r C_{\alpha r} - N_r C_{Mr}(c+d)}{u_f} - m_r c u_f - C_{aj}$$

$$C_{34} = -(c+d)N_r C_{\alpha r} - N_r C_{M\alpha r} - K_{aj}$$

$$C_{41} = 0$$

$$C_{42} = 0$$

$$C_{43} = 1$$

$$C_{44} = 0$$

Appendix B Baseline Machine Wiring Diagram.

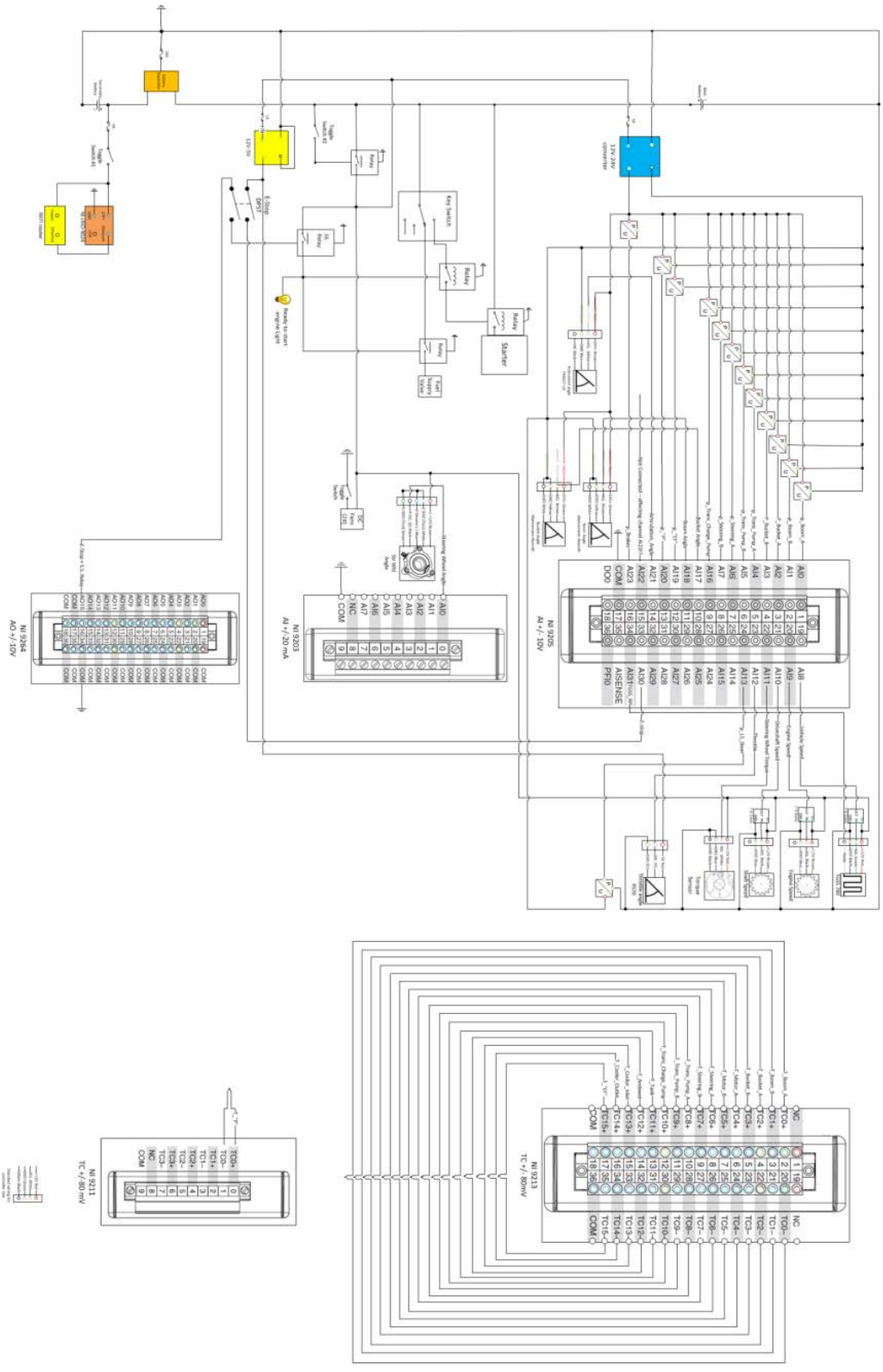

Appendix C Baseline Machine Power Logic Switches

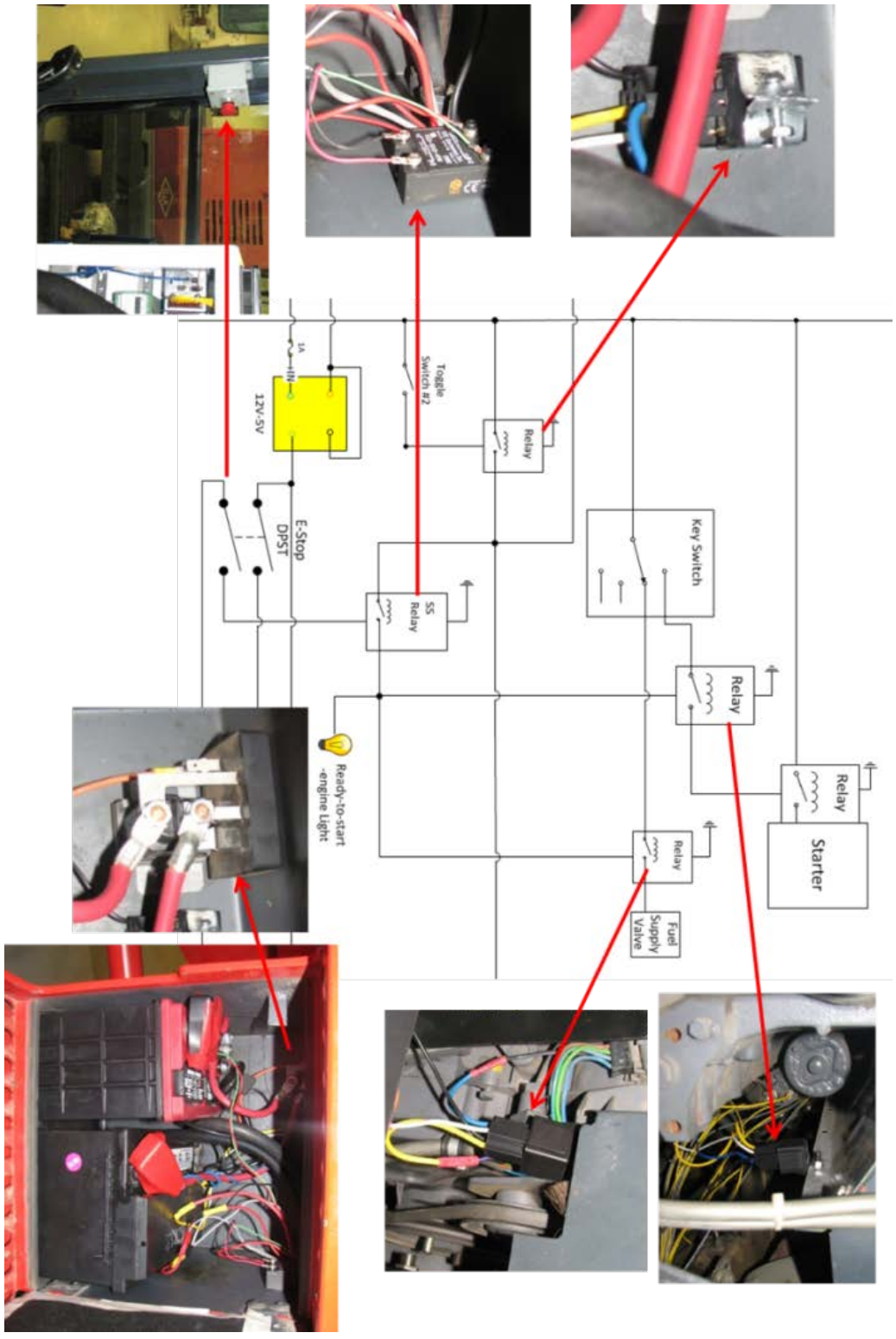

Appendix D Start-up and Shut-down Procedures

The procedures below are followed during start-up and shut-down of the prototype test vehicle.

Startup:

a. With the E-stop in the un-depressed position, the user toggles two manual switches on the dashboard, which turn on both the control unit and the power sources for the sensors and electronics. The controller initializes and all sensors 'wake-up' in approximately 1-2 minutes. When the controller is ready, it sends a signal via its analog-output module to a solid-state relay switch, which illuminates a light alerting the user that the engine is ready to start.
b. The solid-state relay switch powers both the relay switch for the fuel supply solenoid valve and the engine starter relay switch, which makes it possible to start and run the engine.
c. When the user sets the ignition switch to the "Crank" position, electric power flows through the engine starter relay switch to start the engine. After the engine starts and the user sets the ignition switch to the "Run" position, electric power flows through the fuel supply solenoid valve relay switch allowing the engine to stay running.

Shutdown:

The shut-down procedure is performed by following the startup steps but in a reverse order.

Emergency Shutdown:

Two cases for emergency shutdown are possible. A first *manual* mode is when the user physically depresses the E-stop switch, which interrupts power to the engine fuel supply solenoid valve and stops the engine. A second *automatic* mode is when the controller detects pre-programmed fault(s) and cuts off power to the solid-state relay, which in turn de-energizes the fuel supply solenoid valve and stops the engine. In both modes, power to the controller is maintained in order to allow for corrective actions to be taken and data recording to remain active, in spite of the engine being stopped.

Appendix E New Steering System Wiring Diagram

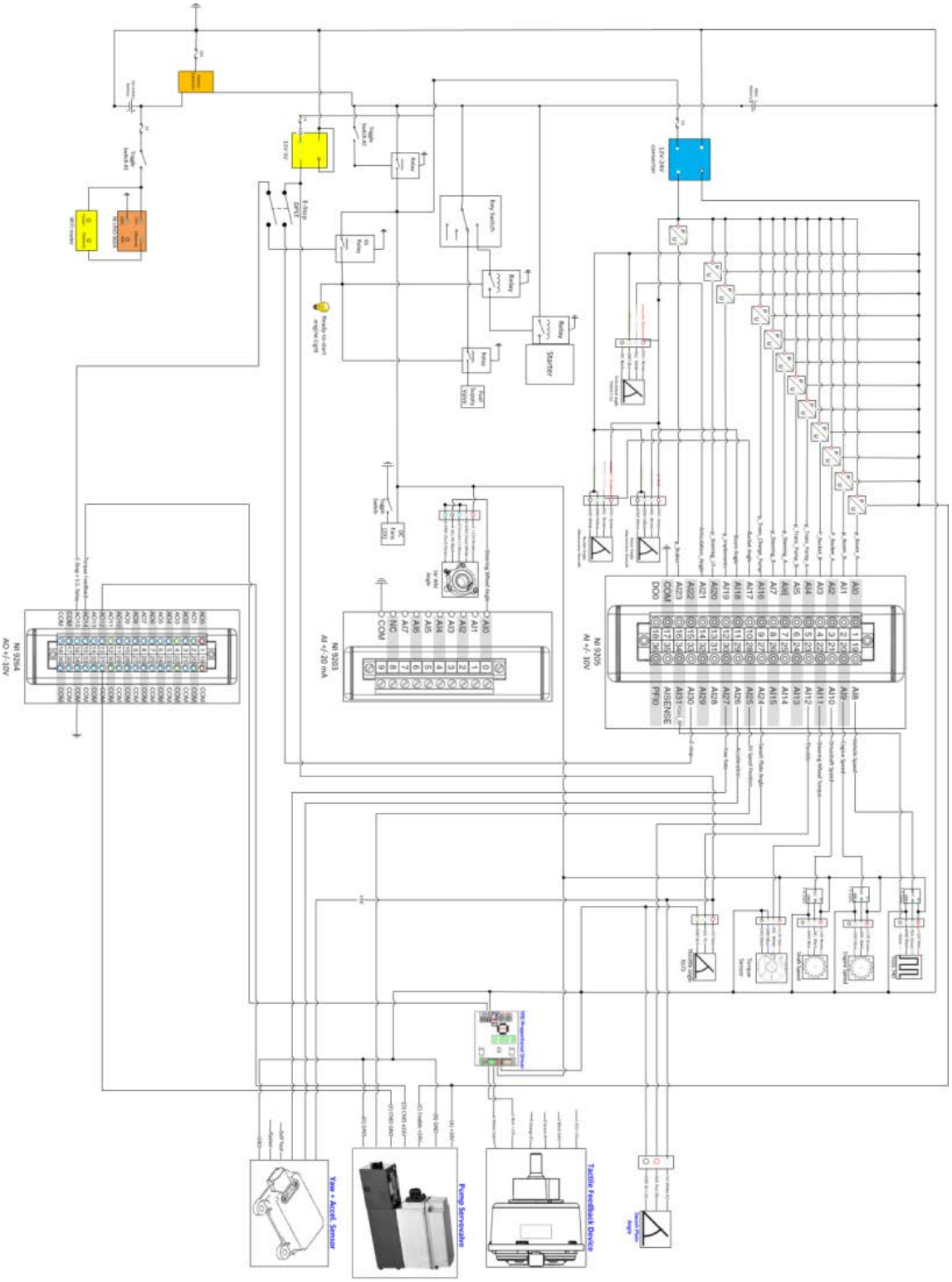

VITA

VITA

Naseem Daher
School of Mechanical Engineering, Purdue University

Education

B.S.M.E., May 2006, Lawrence Technological University, Southfield, Michigan
M.S.M.E., Dec. 2008, Lawrence Technological University, Southfield, Michigan
Ph.D., Dec. 2014, Mechanical Engineering, Purdue University, West Lafayette, Indiana

Graduate Certificates

Hybrid Vehicle Systems Certificate, Dec. 2013, School of Mechanical Engineering, Purdue University, West Lafayette, Indiana

Research Experience

Graduate Research Assistant, Maha Fluid Power Research Center, Purdue University, Lafayette, Indiana, USA 2011-2014

Industrial Experience

TRW Automotive Livonia, Michigan, USA

Principal Engineer, Slip Control Systems	2010-2011
Senior Engineer, Advanced Braking Control Systems	2008-2010
Product Engineer, New Braking Products Development	2005-2008

Research Interests

Dynamic Systems and Control Engineering
Vehicle Dynamics and Active Safety Systems
Mechatronics
Hybrid Vehicle Systems

PUBLICATIONS

PUBLICATIONS

Journal

Daher, N. and Ivantysynova, M. (2014). “An Indirect Adaptive Velocity Controller for a Novel Steer-by-Wire System.” *ASME Journal of Dynamic Systems, Measurement, and Control*. Vol. 136, Issue 5, pp. 051012.

Daher, N. and Ivantysynova, M. (2014). “A Virtual Yaw Rate Sensor for Articulated Vehicles Featuring Novel Electro-Hydraulic Steer-by-Wire Technology.” *Control Engineering Practice.* Vol. 30, pp. 45-54.

Daher, N. and Ivantysynova, M. (2014). “Energy Analysis of an Original Steering Technology that Saves Fuel and Boosts Efficiency.” *Energy Conversion and Management.* Vol. 86, pp. 1059-1068.

Daher, N. and Ivantysynova, M. (2014). “Yaw Stability Control of Articulated Frame Off-Highway Vehicles via Displacement Controlled Steer-by-Wire.” *Control Engineering Practice.* Manuscript No. CONENGPRAC-D-14-00439 (in review)

Conference

Daher, N. and Ivantysynova, M. (2014). “A Steer-by-wire System that Enables Remote and Autonomous Operation.” *SAE 2014 Commercial Vehicle Engineering Congress*, Rosemont, IL, USA. SAE Technical Paper No. 2014-01-2404.

Daher, N. and Ivantysynova, M. (2014). “New Steering Concept for Wheel Loaders.” *Proceedings of the 9th International Fluid Power Conference (9IFK)*, Aachen, Germany, Vol. 1. pp.224-235

Daher, N. and Ivantysynova, M. (2013). “System Synthesis and Controller Design of a Novel Pump Controlled Steer-By-Wire System Employing Modern Control Techniques.” *ASME/Bath Symposium on Fluid Power and Motion Control*, Sarasota, FL, USA. Paper No. FPMC2013-4410.

Daher, N. and Ivantysynova, M. (2013). "Pump Controlled Steer-by-Wire System." *SAE 2013 Commercial Vehicle Engineering Congress*, Rosemont, IL, USA. SAE Technical Paper No. 2013-01-2349. **Excellence in Oral Presentation Award.**

Daher, N., Wang, N., and Ivantysynova, M. (2013). "Novel Energy-Saving Steer-by-Wire System for Articulated Steering Vehicles: A Compact Wheel Loader Case Study." *Proceedings of the 13th Scandinavian International Conference on Fluid Power*, Linkoping, Sweden.

Daher, N. and Ivantysynova, M. (2012). "Electro-hydraulic energy-saving power steering systems of the future." *Proceedings of the 7th FPNI PhD Symposium*, Reggio Emilia, Italy, pp. 929 – 952.

Magazines

Resource Magazine, Jan./Feb. 2014 Edition, pp. 17-19
American Society of Agricultural and Biological Engineers
http://bt.e-ditionsbyfry.com/publication/?i=190183

Tribology & Lubrication Technology Magazine, Jan. 2014 Edition, pp. 10-11
Society of Tribologists and Lubrication Engineers
http://onlinedigitalpublishing.com/publication/?i=188982

News Articles

Purdue News Sep. 2013
"New steering tech for heavy equipment saves fuel, ups efficiency"
http://www.purdue.edu/newsroom/releases/2013/Q3/new-steering-tech-for-heavy-equipment-saves-fuel,-ups-efficiency.html

Design News Oct. 2013
"Valveless Hydraulics Cuts Fuel Consumption in Construction Vehicles"
http://www.designnews.com/author.asp?section_id=1386&doc_id=269044

MyCarma Nov. 2013
"Fuel-Efficiency in the Construction Industry"
http://blog.mycarma.com/2013/11/29/fuel-efficiency-in-the-construction-industry/